

Synthesis, Functionalization and Catalytic Application of Porous Hybrid Materials

Thesis Submitted to

**Academy of Scientific and Innovative Research (AcSIR) for the
Degree of Doctor of Philosophy
in Chemical Sciences**



By

Sushma Kumari

Registration Number: 10CC12A26057

Under the guidance of

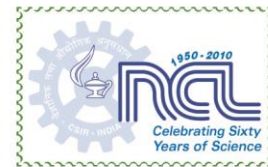
Dr. Sayam Sen Gupta

Chemical Engineering and Process Development Division

CSIR-National Chemical Laboratory

Pune-411008, India

June 2015



CERTIFICATE

This is to certify that the work incorporated in the thesis entitled “**Synthesis, Functionalization and Catalytic Application of Porous Hybrid Materials**”, submitted by **Sushma Kumari**, for the degree of Doctor of Philosophy to **Academy of Scientific & Innovative Research (AcSIR)**, has been carried out by her under my supervision at Chemical Engineering and Process Development Division, CSIR-National Chemical laboratory, Pune-411008, India. All the materials from the other sources have been duly acknowledge in the Thesis.

Sayam Sen Gupta

Dr. Sayam Sen Gupta

(Research supervisor)

Chemical Engineering and Process Development Division,

CSIR-National Chemical laboratory,

Pune-411008,

India.

Date: 26. 06. 2015

DECLARATION

I hereby declare that the thesis entitled “**Synthesis, Functionalization and Catalytic Application of Porous Hybrid Materials**” submitted to the **Academy of Scientific and Innovative Research** for Award of the **Degree of Doctor of Philosophy in Chemistry**, has been carried out by me at CSIR-National Chemical laboratory, Pune-411008, India, under the supervision of Dr. Sayam Sen Gupta. The work is original and has not been submitted in part or full by me for any other degree or diploma to this or any other University.

Pune

June 2015



Sushma Kumari

*This Dissertation is dedicated
to my Beloved Parents*

ACKNOWLEDGEMENT

Studying at CSIR-National Chemical Laboratory has been one of the most memorable experiences. I am very grateful to have the opportunity of conducting research here and meet many great and eminent scientists.

First and foremost, I want to express my heartfelt gratitude to my research supervisor Dr. Sayam Sen Gupta for his invaluable guidance, innumerable discussions, constructive suggestions and continuous support throughout my doctoral journey. He has been the source of inspiration and role model in many aspects of my life; whether scientific or non-scientific and these innumerable discussions helped me to build my character. I sincerely thank him for the care and affection that I received for the entire period of my doctoral research. My deepest regards and reverence are always due for his wonderful personality.

I take this wonderful opportunity to thank Dr. Guruswamy Kumaraswamy for believing me and giving me an opportunity to work in his self-assembly projects and sharing his enthusiastic, supportive, creative ideas, and research expertise which tremendously enhanced my skills.

I am also thankful and indebted to my DAC committee members Dr. P. A. Joy, Dr. Guruswamy Kumaraswamy and Dr. Nandini Devi for their constructive and innovative suggestions.

I would like to thank the Council of Scientific and Industrial Research, New Delhi, for award of research fellowship. I am thankful to Dr. S. Sivaram, Ex-Director, Dr. B. D. Kulkarni, Ex-Deputy Director, Dr. S. Pal, Ex-Director, Dr. V. K. Pillai, Director and Dr. V. V. Ranade, Deputy Director, CSIR-National Chemical Laboratory for extending all possible infrastructural facilities to complete my research work. I would also like to express my gratitude to all the scientific members of our CEPD Division, especially, Dr. A. Kulkarni, Dr. (Mrs.) M. Gadgil and Dr. A. Orpe for their helping nature and fruitful discussions. I would like to extend my thanks to the support group (Patane kaka, Kamble kaka, Subbi, Ravi & Radha) and all the staff members of our division, especially Mr. Raheja for being modest and helping me to finish the official work.

Special thanks to Dr. H. V. Thulasiram, Dr. D. Satyanarayana and Dr. B. L. V. Prasad from NCL for their outreach and scientific discussions. I would like to acknowledge Dr. R. Banerjee and his research group for their help with gas adsorption-desorption studies. Special thanks to Dr. Nandini devi and her research group for providing powder XRD instrumentation. I shall also acknowledge the outreach from Mrs. D. Dhoble, Mrs. P. Purohit for help regarding FT-IR, UV-Vis spectroscopy and TGA analysis. I would like to thank Dr. S. Bhatt and his research group for their help with confocal microscopy. I would like to thank Dr. Ajithkumar and his research group from NMR division and Mr. A. Gaikwad, Mr. R. Gholap, Mr. Ketan, Mr. Anuj, Mr. Pandiraj and Mr. Pankaj from Centre for Materials characterization for their help in characterizations with NMR, SEM and TEM. I am also very thankful to Vijay from IISER Pune for helping me to learn and image biological samples.

I sincerely thank Dr. Bharmana Malvi and Dr. Kamendra Sharma for teaching me the experimental techniques and scientific skills in porous materials which helped me to construct my doctoral research.

I must say that it's a great privilege for me to work under Dr. Sayam Sen Gupta and his group. I would like to thank all my colleagues and ingenious labmates (past and present) for their helpful and cheerful attitude that had made my research experience much more easy and enjoyable. I am highly indebted to my seniors, Malvi, Mrityunjoy, Debasis, Anal and Chakadola for their incessant help and support during my junior years. I personally thank my labmates Munmun, Soumen, Vinita, Kundan, Santanu, Praveen, Bhawana, Nimisha, Sandipan, Bittu, Nikhil, Maria, Basudeb, Anagh, and Mayur. I hope they achieve the best in their research. My Special thanks goes to Dr. Basab Bijayi Dhar, Pool Officer for his scientific contributions to my research work. It has been a great and enjoyable experience to mentor undergraduates Akshay, Swapna, Neenu, Anu, Abhishek, Nikhil and Sandeep. I truly believe they will be very successful in the future. Special thanks to my best friend Munmun for being helpful and caring all the time. I would like to acknowledge Anindita for her support and encouragement during my doctoral research. I am thankful to Pallavi and Sauyana for being modest with me. I would like to thank Pankaj, Vishal, Joyashish, Vishwa, Soumyajyoti, Manoj, Kartikha, Deepika, Ajeet, Nivedita, Vannur, Neha, and Sandeep for their help and support at NCL.

Acknowledgement

It has been great and galvanizing work atmosphere in the D-wing of PAML building, CSIR-NCL. I had a very good time with Tamas da, Kaushal, Shubhadeep, Sharath, Suman, Maria, Arjun and Mayur in my seating place. I have really enjoyed my research work with all the members of D-wing. I am thankful to all the members of D-wing and wish them a great success ahead.

I offer my sincere regards to people, teachers who have inspired me directly or indirectly in research carrier.

Last but not the least, my most pious and deepest gratitude from my heart goes to my parents. I credit them for whatever I am today. They are the nucleus of my existence and I owe them each and every bit of the good I have in me. Their immense love, care, support was the foundation for all my accomplishments and my doctoral work would not have been possible without them. From my heart I say “Pranam” and thank them for everything. I also thank my elder sister Manju and elder brother Arvind for their incessant love and encouragement.

Sushma Kumari

Table of Contents

<u>Particulars</u>	Page
Acknowledgement	
List of Figures	vii
List of Tables	xi
List of Abbreviations	xii
Abstract of the thesis	xiii
Chapter 1 Introduction and Literature Survey	
1.1 Introduction	2
1.2 Organic-Inorganic Hybrid Materials	3
1.3 Porous Materials	4
1.4 Mesoporous Silica based Materials	5
1.4.1 Organically Functionalized Mesoporous Silica Phases	7
1.4.1.1 Grafting Method (post synthetic functionalization of silica)	7
1.4.1.2 Co-Condensation Method (one pot synthesis)	8
1.5 Macroporous Materials	9
1.5.1 Template Directed Synthesis of 3D Macroporous Materials	10
1.5.1.1 Hard Templates	11
1.5.1.2 Soft Templates	11
1.5.1.3 Colloidal Organization by Templating	11
1.5.1.4 Ice Templating Method to create Macroporous Materials	12
1.5.1.5 Dynamic Templating of Surfactant Hexagonal Domains	13
to create Porous Structure	
1.6 Click Chemistry	14
1.6.1 CuAAC Click Chemistry	15
1.6.2 Thiol-Ene Click Chemistry	16
1.6.2.1 Radical based Thiol-Ene Click Reactions	16
1.6.2.2 Michael Addition Reactions	17
1.7 Physico-Chemical Characterization	18
1.7.1 Powder X-Ray Diffraction	18

1.7.2	Scanning Electron Microscopy.....	19
1.7.3	Transmission Electron Microscopy.....	20
1.7.4	Gas adsorption-desorption studies.....	21
1.7.5	Thermogravimetric analysis (TGA).....	24
1.7.6	Fourier Transform Infrared Spectroscopy.....	24
1.7.7	Cross-polarization magic angle spinning NMR spectroscopy.....	24
1.8	Motivation and Objective of the Present Work	25
1.9	References.....	26

Chapter 2 Functionalized Mesoporous Hybrid Materials using “Thiol-Ene Click”

2.1	Introduction	34
2.2	Experimental Details	
2.2.1	Materials	36
2.2.2	Synthesis	36
2.2.2.1	Synthesis of SBA-15	36
2.2.2.2	Synthesis of Methacrylate-Functionalized SBA-15	37
2.2.2.3	Modification of Methacrylate Functionalized SBA-15 (SBA-ACL) by Thiol-Ene “Click” Reaction	37
2.2.2.4	Synthesis of Biotin NHS ester	38
2.2.2.5	Synthesis of Biotin-Cystine (6)	38
2.2.2.6	Modification of SBA-ACL with Biotin-cystine (6) by Thiol-ene “Click” Reaction	38
2.2.2.7	Labeling of SBA-SR-6 with Phycoerythrin-Labeled Streptavidin	38
2.3	Analytical and Characterisation Methods	39
2.4	Results and Discussion	
2.4.1	Synthesis of Methacrylate Functionalized SBA-15	40
2.4.2	Thiol-Ene Click Reaction of SBA-ACL with various Thiol-Containing Substrates	41
2.5	Characterisations	
2.5.1	Small Angle X-ray Scattering (SAXS)	45
2.5.2	Scanning and Transmission Electron Microscopy	46

2.5.3	Thermo Gravimetric Analysis	47
2.5.4	Nitrogen Adsorption-Desorption Studies	48
2.5.5	FT-IR spectroscopy	49
2.5.6	Solid State CP-MAS NMR Spectroscopy	
2.5.6.1	¹³ C CP-MAS NMR Spectroscopy	50
2.5.6.2	²⁹ Si CP-MAS NMR Spectroscopy	51
2.5.7	Cyclic Voltammetry	53
2.6	Conclusions	53
2.7	References	54

Chapter 3 Fe-TAML Encapsulated Inside Mesoporous Silica Nanoparticles for Ultra-Sensitive Detection of Proteins

3.1	Introduction	59
3.2	Experimental Details	
3.2.1	Materials	61
3.2.2	Synthesis	
3.2.2.2	Synthesis of 3-azidopropyltriethoxysilane, AzPTES.....	62
3.2.2.3	Synthesis of Azide Functionalized MSN (x-N ₃ -MSN).....	62
3.2.2.3	Synthesis of 1-Fe-MSN, 5-Fe-MSN and 10-Fe-MSN.....	63
3.2.2.4	Synthesis of Amine Functionalized MSN (NH ₂ -N ₃ -MSN).....	64
3.2.2.5	Modification of NH ₂ -N ₃ -MSN with Biuret Modified Fe-TAML by Cu(I) Catalyzed Azide-Alkyne Cyclo- addition Reaction (CuAAC) (NH ₂ -Fe-MSN).....	64
3.2.2.6	Synthesis of Biotin Immobilized MSN (biotin-Fe-MSN).....	65
3.2.2.7	Synthesis of Maleimide Functionalized MSN (maleimide-Fe-MSN).....	65
3.2.2.8	Conjugation of Antibodies to Maleimide-Fe-MSN (antihuman IgG-5-Fe-MSN).....	66
3.2.2.9	Kinetics of TMB Oxidation.....	66
3.2.2.10	Experimental methodology for kinetics of TMB oxidation.....	67
3.2.2.11	Colorimetric Assay of Streptavidin	67
3.2.2.12	Detection of Human IgG Using Antihuman IgG-Fe-MSN.....	68

3.2.2.13	Detection of Human IgG in CHO-S and CHO-IgG	68
3.2.2.14	Determination of the concentration of 1-Fe-MSN and 5-Fe-MSN in a stock solution of 1.00 mg/mL.....	69
3.3.	Characterisation Techniques.....	69
3.4	Results and Discussion	
3.4.1	Design and Synthesis of Biuret Modified Fe-TAML Immobilized MSN.....	71
3.4.2	Evaluation of Kinetic Parameters for TMB Oxidation by Fe-TAML Encapsulated in MSN.....	74
3.4.3	Biotin conjugated Fe-MSN for detection of Streptavidin.....	78
3.4.4	Antihuman IgG Conjugated Fe-MSN for Detection of Human IgG in Cells.....	79
3.5	Characterisations	
3.5.1	Scanning and Transmission Electron Microscopy.....	82
3.5.2	Powder X-ray Diffraction.....	83
3.5.3	Thermogravimetric Analysis.....	84
3.5.4	Nitrogen Adsorption-Desorption studies.....	85
3.5.5	FT-IR Spectroscopy.....	85
3.5.6	Solid State ¹³ C CP-MAS NMR Spectroscopy.....	86
3.6	Conclusions.....	87
3.7	References.....	88

Chapter 4 Macroporous Scaffold from Transition Metal Nanoparticles for Continuous Flow Reactions

4.1	Introduction	93
4.2	Experimental Section	
4.2.1	Materials	95
4.2.2	Synthesis	
4.2.2.1	Ferritin Modification	
4.2.2.2	General Procedure for the Synthesis of Macroporous..... Hydrogel Using Ferritin Based Nanoparticles	95
4.2.2.3	Synthesis of Apo-ferritin Scaffold from Ferritin Scaffold.....	96

4.2.2.4	Synthesis of Palladium Nanoparticle Encapsulated Apo-ferritin Scaffold (Pd@apo-ferritin).....	96
4.2.2.5	Control Experiment in Absence of Surfactant	96
4.2.2.6	General Procedure for Oxidation of 2, 3, 6-trimethylphenol to trimethyl-1, 4-benzoquinone Using Ferritin Scaffold	97
4.2.2.7	General Procedure for Suzuki-Miyaura Cross-Coupling Reaction Using Pd@apo-ferritin Scaffold	97
4.2.2.8	Oxidation of TMB (3, 3', 5, 5'-Tetramethylbenzidine) Using Ferritin Scaffold in the Continuous Flow	97
4.2.2.9	Calculation	98
4.3	Characterisation Techniques	98
4.4	Results and Discussion	
4.4.1	Synthesis and Characterization of Large Centimeter-Sized Macroporous Ferritin Scaffold.	100
4.4.2	Synthesis of Pd Nanoparticle Embedded Apo-Ferritin Scaffold.....	104
4.4.3	Catalytic Activity of Ferritin for Oxidation Reaction.....	105
4.4.4	Catalytic Activity Pd@apo-ferritin Scaffold for Suzuki–Miyaura Cross Coupling Reaction.....	107
4.4.5	Macroporous Scaffold for Continuous Flow Synthesis.....	108
4.5	Conclusion.....	110
4.6	References.....	110

Chapter 5 Soft Colloidal Macroporous Scaffolds by Ice Templating Method

5.1	Introduction.....	117
5.2	Experimental Section	
5.2.1	Materials.....	119
5.2.2	Synthetic Methods	
5.2.2.	Synthesis of 10% silica scaffolds	120
5.2.2.2	Synthesis of 20% silica scaffolds.....	120
5.2.2.	Synthesis of 30% silica scaffolds.....	120
5.2.2.5	Synthesis of 10% fluorescent polystyrene scaffold.....	121
5.2.2.5	Synthesis of scaffold from 300nm silica	121

5.2.2.6	Synthesis of 10% silica scaffolds from Ludox TM (26 nm silica nanoparticles) using poly(ethyleneglycol) diglycidyl ether as a crosslinker	121
5.2.2.7	Synthesis of hydrophobised scaffold.....	121
5.2.2.8	Synthesis of scaffold by variation of crosslinker concentration....	122
5.2.2.9	Control experiment.....	122
5.2.2.10	Preparation of patchy particles on glass slide.....	122
5.2	Analytical and Characterization methods.....	122
5.3	Procedure for estimation of porosity and density.....	123
5.4	Results and Discussion	
5.4.1	Structural characterization of monolithic scaffolds.....	124
5.4.2	Mechanical response of monolith to compression	126
5.4.3	Entropic origin of monolith mechanical response.....	132
5.4.4	Elastic mechanical response of ice-templated monoliths is chemistry independent.....	137
5.5	Conclusions.....	139
5.6	References.....	140

Chapter 6 Conclusions and Future Work

6.1	Summary and Conclusions	144
6.2	Scope of future work	146

List of Figures

Figure 1.1	(a) bio mineralisation of the nacre shell (b) hybrid (organic–inorganic) composition available using nanostructured chemicals.....	4
Figure 1.2	Structures of three categories of nanoporous materials.....	5
Figure 1.3	Structures of M41S materials	6
Figure 1.4	Functionalization of mesoporous materials by the grafting method.....	8
Figure 1.5	Functionalization of mesoporous materials by co-condensation method	9
Figure 1.6	Different methodologies for fabrication of three-dimensionally ordered macroporous (3DOM) materials by colloidal crystal templating	12
Figure 1.7	Schematic diagram of the ice-templating process	12
Figure 1.8	Schematic illustration of assembling nanoparticles using non-ionic surfactant C ₁₂ E ₉	14
Figure 1.9	Mechanism of the CuAAC reaction	16
Figure 1.10	The mechanism for the hydrothiolation of a C=C bond in the presence of a photoinitiator and $h\nu$	17
Figure 1.11	Anionic chain mechanism for the hydrothiolation of an acrylic C=C bond	18
Figure 1.12	Types of physisorption isotherms.....	22
Figure 1.13	Types of hysteresis loops	23
Figure 2.1	Synthesis of methacrylate-functionalized SBA-15 materials.....	41
Figure 2.2	Thiol-ene click reaction of methacrylate functionalized SBA-15 with various thiols.....	42
Figure 2.3	Confocal image of SBA-SR-6 with labeled phycoerythrin streptavidin....	45
Figure 2.4	SAXS patterns of different SBA-15 samples,.....	46
Figure 2.5	SEM images and TEM micrographs of SBA-ACL material	47
Figure 2.6	TGA graphs of various modified SBA-15 materials.....	47
Figure 2.7	Nitrogen adsorption-desorption isotherms for various SBA-15 materials and pore size distribution of these various materials	48

Figure 2.8	Comparative FT-IR spectra of the different SBA-15 materials.....	50
Figure 2.9	¹³ C CP MAS NMR spectra of the different functionalized SBA-15 materials.....	51
Figure 2.10	²⁹ Si CP-MAS NMR spectra of the different functionalized SBA-15 materials.....	52
Figure 2.11	Cyclic voltammogram of ferrocene labeled SBA-15 (SBA-SR-4) and methacrylate labeled SBA-15 (SBA-ACL).....	53
Figure 3.1	Schematic representation of signal amplification.....	60
Figure 3.2	Synthesis of (a) biuret modified Fe-TAML functionalized MSN (Fe-MSN); (b) biotin conjugated Fe-MSN; (c) antihuman IgG conjugated Fe-MSN.....	73
Figure 3.3	UV-vis spectra of quenched reaction mixture for TMB oxidation using 5-Fe-MSN and H ₂ O ₂	75
Figure 3.4	Michaelis-Menten fit for H ₂ O ₂ and TMB variation.....	76
Figure 3.5	Application of biuret modified Fe-TAML MSN in direct immunosorbent assay.....	78
Figure 3.6	Synthesis of antihuman IgG-Fe-MSN	80
Figure 3.7	Human IgG detection in CHO-S and CHO-IgG cells	81
Figure 3.8	SEM and TEM images of 1-N ₃ -MSN	82
Figure 3.9	SEM and TEM images of 5-N ₃ -MSN	82
Figure 3.10	TEM image of NH ₂ -N ₃ -MSN and Ninhydrin test	83
Figure 3.11	Powder XRD patterns of 1-N ₃ -MSN, 5-N ₃ -MSN and 5-Fe-MSN.	83
Figure 3.12	TGA for MSN before and after azide grafting.....	84
Figure 3.13	Nitrogen adsorption-desorption isotherms for 5-N ₃ -MSN	85
Figure 3.14	FT-IR spectra of 5-N ₃ -MSN, 5-Fe-MSN and NH ₂ -Fe-MSN.....	86
Figure 3.15	¹³ C CPMAS-NMR for as synthesized 1-N ₃ -MSN.NMR and after template removal 1-N ₃ -MSN	87
Figure 4.1	Synthesis of porous ferritin scaffold proceeds via ferritin cationisation using N, N'- dimethyl-1, 3-propanediamine followed by dynamic templating to assemble the ferritin nanoparticles into a three dimensional macroporous scaffold	101
Figure 4.2	(A) SAX scattering curves for native ferritin 5 wt%, ferritin scaffold and apparent structure factor.	

	(B) Frequency sweep of Ferritin @0.75% strain.....	102
Figure 4.3	FT-IR spectra of ferritin scaffold.....	103
Figure 4.4	TEM image of Pd nanoparticles inside scaffold.....	104
Figure 4.5	Synthesis of Pd@apo-ferritin scaffold and its application in catalysis.....	106
Figure 4.6	Schematic representation for the continuous flow hydrogenation reaction of different substrates with immobilized Pd@apoferritin scaffold using H ³ system (Thales Nano Ltd).....	109
Figure 5.1	One pot synthesis proceeds via MSN synthesis using structure directing agents (SDA); followed by dynamic templating to assemble the MSN particles into a macroporous scaffold.....	118
Figure 5.2	Schematic of the ice-templating process.....	124
Figure 5.3	TGA of a scaffold prepared from 1 μm silica particles and a control scaffold prepared using the same 1 μm silica particles.....	126
Figure 5.4	Compression study of an ice-templated monolith of 1 μm silica colloids.	128
Figure 5.5	Confocal microscopy of scaffolds prepared from 1 μm fluorescent polystyrene colloidal latex, ice-templated with PEI and diepoxide cross-linker.	129
Figure 5.6	Photographs showing the compression, frequency sweep and confocal microscopy on 1 μm fluorescent polystyrene latex scaffold	130
Figure 5.7	SEM micrographs of 1 micron silica scaffolds prepared by ice templating	131
Figure 5.8	Photographs that show the compression and recovery of scaffolds prepared by ice templating 10% , 20 % and 30% w/v dispersions of 1 μm silica particles, with 25 kDa PEI and poly(ethyleneglycol) diglycidyl ether as the cross-linker.....	132
Figure 5.9	Temperature dependence of Young's modulus (E*) and solid shear modulus (G') of solvated scaffolds prepared by ice-templating 1 μm silica colloids.....	133
Figure 5.10	FE-SEM image of scaffold prepared from a φ = 10% w/v dispersion of 1 μm silica colloids	135
Figure 5.11	Trajectory of motion for a single 1 μm silica colloid cross-linked through its PEI coating to a glass slide.	136

Figure 5.12	Mechanical response of scaffolds in shear and in compression, prepared by ice-templating 10% w/v aqueous dispersions of silica particles.....	137
Figure 5.13	Photographs that show the compression of scaffold prepared by ice templating a 10% w/v dispersion of 1 μm silica particles, with 25 kDa PEI and poly(ethyleneglycol) diglycidyl ether as the crosslinked and subsequently hydrophobized by chemical modification	139
Figure 6.1	Ice templating for the preparation of silk-silica composite scaffold.....	148

List of Tables

Table 2.1	Summary of thiol-ene reaction with different thiol substrates.....	43
Table 2.2	Properties of various SBA-15 materials	49
Table 3.1	Physical Properties of x-N ₃ -MSN.....	74
Table 3.2	Comparison of the Kinetic Parameters of 1-Fe-MSN, 5-Fe-MSN, HRP, 30 nm Fe ₃ O ₄ MNPs, and Au@Pt 0.25.....	77
Table 4.1	Oxidation and Suzuki-Miyaura cross coupling reaction with ferritin and Pd@apo-ferritin.....	107
Table 4.2	Hydrogenation of Alkenes Using Pd@apo-ferritin under Continuous Flow Reactions.....	109

List of abbreviations

AzPTES	3-azidopropyltriethoxysilane
BET	Braunauer-Emmett-Teller
BJH	Barrett-Joyner-Halenda
C₁₂E₉	Poly(ethylene glycol) diglycidyl ether
CP-MAS	Cross-Polarization Magic Angle Spinning
CLSM	Confocal Laser Scanning Microscopy
CuAAC	Cu (I) catalyzed azide-alkyne cycloaddition
CTAB	Cetyltrimethyl ammonium bromide
HRTEM	High Resolution Transmission Electron Microscopy
ICP	Inductively Coupled Plasma
LC-MS	Liquid Chromatography-Mass Spectrometer
MCM	Mobil's Composition Material
NMR	Nuclear Magnetic Resonance
SBA	Santa Barbara Amorphous
SEM	Scanning Electron Microscopy
TEOS	Tetraethyl orthosilicate
TEM	Transmission Electron Microscopy
TGA	Thermo Gravimetric Analysis
UV-Vis	Ultraviolet-Visible
XRD	X-Ray Diffraction

Abstract of the thesis

Organic-inorganic hybrid materials represent a class of very exciting materials that have applications in diverse fields such as: optics, electronics, ionics, mechanics, energy, environment, biology, medicine for example as membranes and separation devices, functional smart coatings, fuel and solar cells, catalysts, sensors, etc. These materials can be broadly defined as composites with intimately mixed organic and inorganic components to generate hybrid materials with remarkable properties not found in either organic or inorganic phase. Inorganic materials bring thermal stability, greater modulus, strength, and porosity to the hybrids; while their organic counterparts bring toughness, elasticity, optical properties, and chemical functionality to the hybrids. Hybrid materials are tougher than a normal ceramic and more thermally stable than an organic polymer. Thus research and development in this area brings together a variety of communities that have research interests spanning across multiple discipline such as organometallics, colloids, soft matter and polymers, sol-gel, catalysis and surfaces, nanocomposites, mesoporous and macroporous materials, biomaterials, biochemistry and engineering.

In addition to having inherent properties characteristic of a hybrid organic-inorganic material, high porosity is also an essential requirement for a wide spread application. Porosities are defined at multiple length scales such as, micropores (< 2 nm), mesopores (2-50 nm) and macropores (>50 nm). Porous materials can be easily synthesised by templating methods such as spray drying, dynamic templating using breath figures, polymerization induced phase separation, adsorption on an interface or substrate (layer by layer, LbL, technique), etc. These organic inorganic hybrid porous materials have found widespread application in technologically important areas such as catalysis, separation, drug delivery, chromatography, catalysis, filtration, sensor design, insulation and as biomedical scaffolds.

In my thesis, I have focused on the synthesis of hybrid porous materials and their application in catalytic reactions. I have been involved in the synthesis of both mesoporous and macroporous hybrid materials. Hybrid mesoporous silica based materials were synthesized and then post-functionalized using both copper-catalyzed [3+2] alkyne-azide cycloaddition (CuAAC) and thiol-ene Michael addition. Using a molecular hook strategy I have successfully immobilized a variety of catalysts and enzymes among other things. Functionalized porous nanoparticles were also self-assembled into free-standing porous materials using dynamic templating of surfactant H₁ hexagonal domains and ice templating method to demonstrate its application in continuous flow synthesis and biomedical

applications. The dissertation is presented in six chapters; a brief summary of each chapter is given below.

Chapter 1: Introduction of organic-inorganic hybrid materials

This chapter provides general introduction to the organic inorganic hybrid porous materials including synthetic strategies for mesoporous and macroporous hybrid materials along with their applications. Different approaches for the synthesis of hybrid organic-inorganic mesoporous materials by incorporation of functional organic groups onto surface of these materials have been discussed. An introduction to Cu(I) catalyzed azide-alkyne click chemistry (CuAAC) and thiol-ene click chemistry have been discussed in brief. This chapter also discusses the top down and bottom up approaches for the synthesis of macroporous materials. Basic principles of various analytical techniques used for the characterization of porous hybrid materials are also described. Finally, the motivation for the development of porous hybrid materials from functionalised porous materials and templating method is discussed.

Chapter 2: Functionalized Mesoporous Hybrid Materials using “Thiol-Ene Click”

This chapter describes a new methodology for the successful attachment of functional molecules onto mesoporous silica. Methacrylate-labeled SBA-15 was synthesized from calcined SBA-15 and commercially available 3-trichlorosilyl propylmethacrylate. This material underwent very efficient thiol-ene “click reaction” with a variety of both thiol and disulfide-containing functional molecules in both aqueous and organic media. The products were thoroughly characterized by a variety of analytical techniques including multinuclear (^{13}C , ^{29}Si) solid-state NMR, TG-DTA, and nitrogen adsorption desorption studies. Disulfide-containing substrates in which the TCEP-mediated reduction of the disulfide bond and its subsequent addition to the methacrylate group anchored in SBA-15 in one-pot were used to synthesize a silica-protein hybrid material composed of biotin-labeled SBA-15 and streptavidin. This methodology was used to synthesize electrochemically active material from the reaction of ferrocene-containing thiol and the methacrylate-labeled SBA-15. The ease of synthesis for the methacrylate-labeled SBA-15 material together with its ability to undergo efficient chemoselective thiol-ene reaction would make it a very attractive platform for the development of covalently anchored enzymes and sensors.

Chapter 3: Fe-TAML Encapsulated Inside Mesoporous Silica Nanoparticles for Ultra-sensitive Detection of Proteins

This chapter describes the development of a mesoporous hybrid nanoparticle that is a functional mimic of peroxidase enzyme. This material was tested as a replacement of horseradish peroxidase (HRP) for the precise and accurate determination of very low quantities of proteins (fM and lower) via an ELISA type assay. In particular, we have synthesized and developed a second generation hybrid material in which approximately 25 000 alkyne tagged biuret modified Fe tetraamido macrocyclic ligand (Fe-TAML), a very powerful small molecule synthetic HRP mimic, was covalently attached inside a 40 nm mesoporous silica nanoparticle (MSN). Biuret-modified Fe-TAMLS represent one of the best small molecule functional mimics of the enzyme HRP with reaction rates in water close to the native enzyme and operational stability (pH, ionic strength) far exceeding the natural enzyme. The catalytic activity of this hybrid material is around 1000-fold higher than that of natural HRP and 100 fold higher than that of most metal/metal oxide nanoparticle based HRP mimics reported to date. We also show that using antibody conjugates of this hybrid material it is possible to detect and, most importantly, quantify femtomolar quantities of proteins colorimetrically in an ELISA type assay. This represents at least 10-fold higher sensitivity than other colorimetric protein assays that have been reported using metal/metal oxide nanoparticles as HRP mimic. Using a human IgG expressing cell line, we were able to demonstrate that the protein of interest human IgG could be detected from a mixture of interfering proteins in our assay.

Chapter 4: Macroporous Scaffold from Transition Metal Nanoparticles for Continuous Flow Reactions

In this chapter, we illustrate the synthesis of a self-standing macroporous scaffold monolith by the self-assembly of catalytic nanoparticles for application into continuous flow synthesis. As a proof-of-concept, the bionanoparticle ferritin, consisting of iron oxide nanoparticle core and a protein shell, was organized into well-defined large (centimeter-sized) self-standing macroporous scaffold monoliths using dynamic templating of surfactant H₁ domains. These scaffolds comprise three-dimensionally connected strands of ferritin, organized as a porous gel with porosity ~55 μm . The iron oxide inside the ferritin scaffold can be easily replaced with catalytically active monodisperse zerovalent transition metal nanoparticles using a very simple protocol. Since the ferritin is cross-linked in the scaffold, it

is significantly robust with enhanced thermal stability and better tolerance toward several organic solvents in comparison to the native ferritin bionanoparticle. In addition, the scaffold macropores facilitate substrate and reagent transport and hence the monoliths containing active Pd or iron oxide nanoparticles inside apo-ferritin bionanoparticles were used as a recyclable heterogeneous catalyst for the oxidation of 2,3,6-trimethyl phenol to 2,3,6-trimethyl-1,4-benzoquinone (precursor for Vitamin E synthesis) and for Suzuki-Miyaura cross-coupling reaction in both aqueous and organic solvents. The protein shell around the nanoparticles protects them from agglomeration, a phenomenon that otherwise plagues nanoparticles-based catalysis. The presence of macropores allow the ferritin scaffold to act as catalytic monolith for continuous flow reactions having rapid reaction rates, while offering a low pressure drop. Finally, the Pd@apo-ferritin scaffold was immobilized inside a steel cartridge and used for the continuous flow hydrogenation of alkenes to their corresponding alkanes for 15 cycles without any loss of activity.

Chapter 5: Soft Colloidal Macroporous Scaffolds by Ice Templating Method

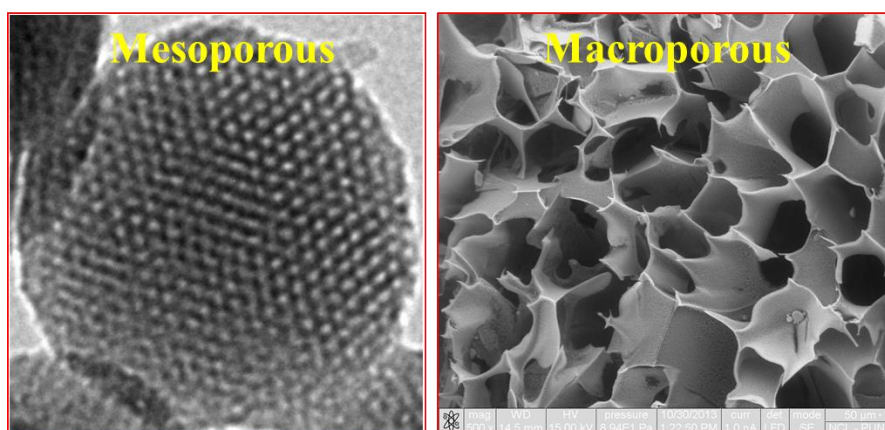
In this chapter, we demonstrated for the first time a general strategy to create centimeter-size macroporous monoliths, composed primarily (>90 wt %) of colloidal particles, that recover elastically after compression to about one-tenth their original size. We employ ice templating of an aqueous dispersion of particles, polymer, and cross-linker such that cross-linking happens in the frozen state. This method yields elastic composite scaffolds for starting materials ranging from nanoparticles to micron-sized dispersions of inorganics or glassy lattices. The mechanical response of the monoliths is also qualitatively independent of polymer type, molecular weight, and even cross-linking chemistry. Our results suggest that the monolith mechanical properties arise from the formation of a unique hybrid microstructure, generated by cross-linking the polymer during ice templating. Particles that comprise the scaffold walls are connected by a cross-linked polymeric mesh. This microstructure results in soft monoliths, with moduli $\sim 10^4$ Pa, despite the very high particle content in their walls. A remarkable consequence of this microstructure is that the monolith mechanical response is entropic in origin: the modulus of these scaffolds increases with temperature over a range of 140 K. We show that interparticle connections formed by cross-linking during ice templating determine the monolith modulus and also allow relative motion between connected particles, resulting in entropic elasticity.

Chapter 6: Conclusions and future work

This chapter presents an overall summary of the work done and describes the major findings of the studies. Future directions based on the work reported in this thesis are also discussed.

Chapter 1

Introduction and Literature Survey



This chapter provides an introduction to the thesis. Salient features of reported synthetic procedures of mesoporous silica and their functionalization procedures are presented. In addition, different methodologies to generate macroporous materials have been discussed. Application of porous materials in catalysis has also been highlighted. Using this discussion as a background, the chapter wise organization of the thesis is presented.

1.1 Introduction

Hybrid materials represent a new field for academic research to design new materials and compounds because of the possibility to combine the organic, inorganic or bio inorganic character.¹⁻⁷ This offers an attractive platform for advanced materials with remarkable new properties. Today, a very large set of accessible hybrid materials offer various applications in extremely diverse fields such as optics, microelectronics, ionic, mechanics, transportation, separation, catalysis, sensing and biomedicine.⁸⁻¹⁰ Hybrid materials that contain cavities, channels or interstices can be regarded as porous. Porous hybrid materials have many useful properties e.g. extremely low thermal conductivity, large adsorption capacity etc. which are derived from its specific porous structure. Such hybrid organic-inorganic material with high porosity finds huge application in technologically demanding areas such as catalysis, sensing, drug delivery, and tissue engineering. In catalysis, macropores and meso/micropores provides complementary benefits since macropores allow enhanced mass-transport, especially for large molecules, while meso/micropores provide high surface areas for active catalytic sites. Porous materials are generally synthesized by using sacrificial templates, space fillers or structure directors around which a solid wall structure forms, followed by removal of the template by either chemical or thermal methods.

This thesis is focused on the synthesis of mesoporous and macroporous hybrid materials for its application in catalysis. In the first part of the thesis, a “molecular hook” has been designed using “click chemistry” on the surface of mesoporous silica nanoparticles like SBA-15 and MSN that allows synthesis of multifunctional organic inorganic hybrid materials. These molecular hooks are utilized to anchor functional molecules to generate novel catalysts, sensors and biocatalysts. Thiol-ene click chemistry is used to prepare electrochemically active materials and silica protein hybrid mesoporous material. Subsequently, Cu(I)-catalyzed azide alkyne click reaction (CuAAC) was used to prepare MSN hybrid material that contained several chemically conjugated peroxidase mimic small molecule inorganic catalysts inside the pores and antibody molecules on its surface. This novel hybrid MSN construct displayed peroxidase activity and was used for the ultra-sensitive detection (fM and lower) and quantification of protein using a colorimetric assay. In the second part of the thesis, macroporous hybrid monoliths have been prepared by using self-assembly. Here, large centimeter size porous ferritin based organic inorganic hybrid monolith, containing catalytically active nanoparticles was synthesized by dynamic

templating of surfactant. This versatile nanoreactor was shown to function as a heterogeneous catalyst for a variety of organic transformations in both batch and continuous mode. Finally silica based hybrid soft and spongy monoliths were prepared by ice templating method. This yields elastic composite macroporous scaffolds predominantly comprising of colloidal silica particles (up to 90 % by weight of inorganic) which can recover their structure completely after compression to 15 % of their original size. These “designer” monoliths based on functional colloids may have applications in several technological areas.

In this chapter we set the platform for the thesis by introducing synthesis and functionalization of porous hybrid materials, application of porous hybrid materials in catalysis and discussed various analytical techniques used for characterization of porous hybrid materials. We have also given a brief introduction to “click chemistry” and the “template directed synthesis”; which has been implemented in this thesis to synthesize novel porous hybrid materials. Finally, this chapter delineates the motivation of our work and objective of this thesis.

1.2 Organic-Inorganic Hybrid Materials

Nature has used organic-inorganic materials to design a new class of materials or compounds with remarkable properties that are not found in either organic or inorganic phase.^{11, 12} For example, calcium carbonate is generally very brittle (chalk), however as a hybrid organic-inorganic composite it has dramatically altered mechanical properties, as in nacre or mother of pearl (Figure 1.1a). Generally inorganic materials like ceramics are stable at high temperature but are often brittle. Polymers, on the other hand are very tough, but not very stable to temperatures above 180 °C. Hybrid materials are advantageous because it allows us to combine the properties of inorganic and organic materials into one composite material. Inorganic materials bring thermal stability, greater modulus, strength, and porosity to the hybrids. Organics impart toughness, elasticity, optical properties, and chemical functionality to the hybrids. Therefore, organic-inorganic hybrid materials are tougher than a normal ceramic and more thermally stable than an organic polymer. The graph shown in Figure 1.1b represents the manner in which the properties of the two constituents can add during the formation of the hybrid.

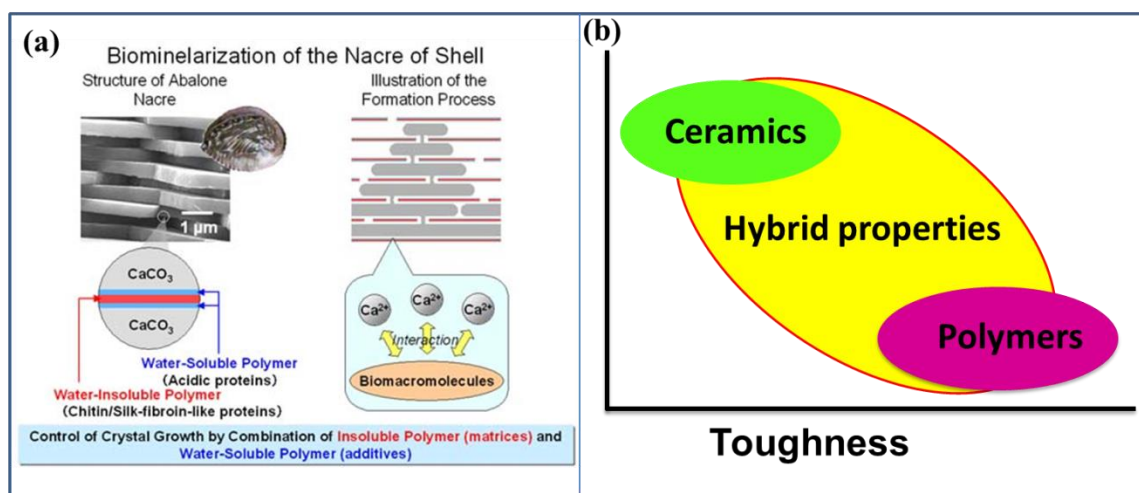


Figure 1.1 (a) bio mineralisation of the nacre shell (b) unique hybrid (organic–inorganic) compositions available using nanostructured chemicals (Figure adapted from ref. 4 (b) with permission).

1.3 Porous Materials

Porous solids are of great interest in scientific and technologically important areas because of their capability to interact with atoms, ions and molecules not only at their surfaces, but all through the bulk of the material. Properties of porous materials like high surface area, pore size distribution, pore volume, adjustable framework, surface properties and volumes of the void spaces in porous materials directly relates to their ability to perform the desired function in a particular application.¹³ The International Union of Pure and Applied Chemistry have classified porous materials into three classes based on the pore diameters: pore sizes in the range of 2 nm and below are called micropores with zeolites and metal-organic frameworks (MOF structures) as the most prominent representatives; mesopores are in the range of 2 nm to 50 nm e.g. aerogels, pillared clays, or M41S phases and the pore sizes above 50 nm are defined as macropores such as foams or glasses.¹⁴

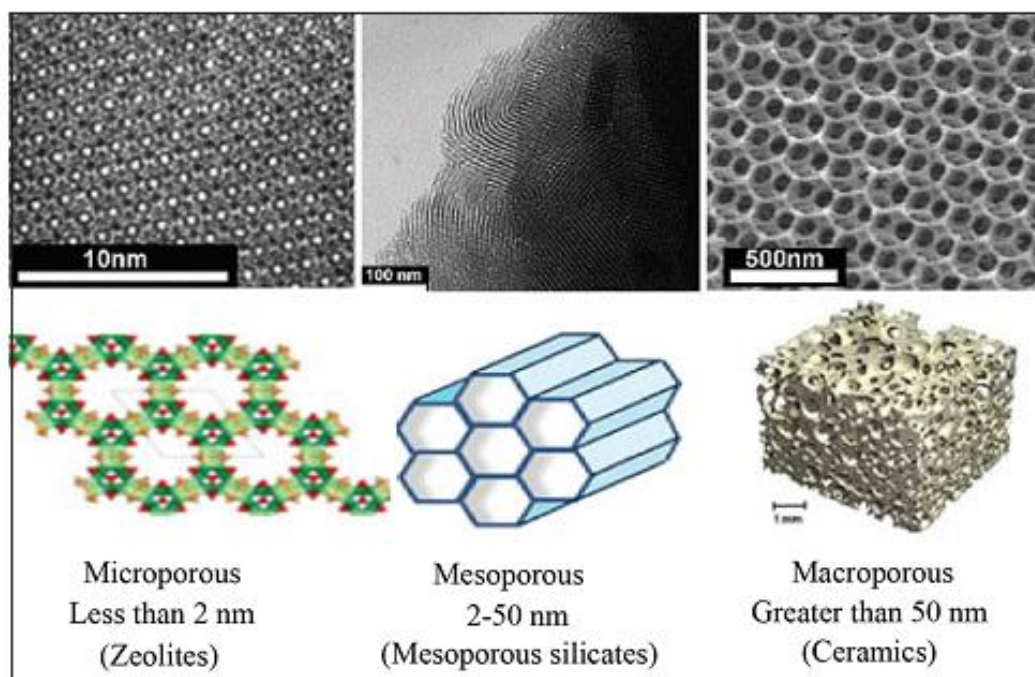


Figure 1.2 The three categories of nanoporous materials and their TEM images (Figure adapted from ref. 13 with permission).

Many synthetic pathways have been reported for the synthesis of porous materials, either with a disordered pore system or ordered with various structures, which can meet the demands of the target application. Among several porous materials, siliceous porous materials are important both from a fundamental and an application point of view. Specifically, tremendous growth for the synthesis of ordered porous materials has been achieved since the discovery of the ordered mesoporous silica of the M41S family or related materials,^{15, 16} which are synthesized with the help of cooperative surfactant templating (Figure 1.2). After these pioneering studies, significant amount of progress has been built in terms of structural, compositional, and morphological control.

1.4 Mesoporous Silica based Materials

Mesoporous materials are attractive candidates for heterogeneous catalysts or as a catalyst support because of its novel properties such as well-defined crystalline structure,

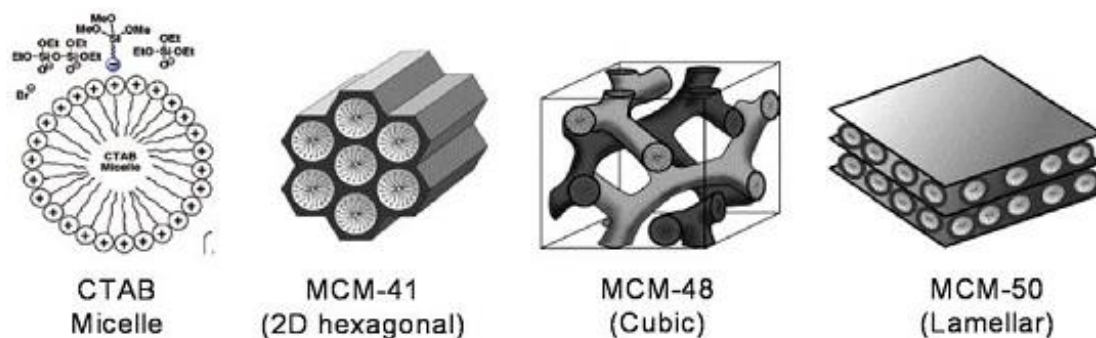


Figure 1.3 Structures of M41S materials (Figure adapted from ref. 16(b) with permission).

high internal surface area, uniform pore sizes, good thermal stability and highly acidic sites in the protonated form. In the early 1990s, the Mobil Oil Company discovered the class of periodic mesoporous silica's known as the M41S phase. The most well-known examples of this class include hexagonal MCM-41, cubic MCM-48, and lamellar MCM-50 (Figure 1.3). MCM is an abbreviation of "Mobil Crystalline Materials". The mesoporous materials are typically synthesized by using supramolecular aggregates of ionic surfactants (long-chain alkyltrimethylammonium halides) as structure-directing agents (SDAs). These SDAs, in the form of a lyotropic liquid-crystalline phase, lead to the assembly of an ordered mesostructured composite during the condensation of the silica precursors such as fumed silica, sodium silicate, or tetra-alkyl oxide of silane under acid or basic conditions. Mesoporous materials are obtained by subsequent removal of the surfactant by extraction or calcination.

Subsequently, Stucky et al. introduced another mesoporous materials using nonionic surfactants in acidic condition, designated as SBA-15 (SBA stands for Santa Barbara Amorphous).^{17, 18} This consists of thermally stable thick walls with large hexagonal mesopores (4-10 nm) which overcame the weak hydrothermal stability encountered by M41S materials. A non-ionic triblock co-polymer, poly (ethylene oxide) poly (propylene oxide) poly (ethylene oxide) (PEO-PPO-PEO) was used as templating agent for the synthesis of SBA-15. This SBA-15 material has been extensively studied for various applications due to its remarkable properties and several features which makes it very exciting. These include tailored pore size, high degree of structural ordering, ease of synthesis, thicker pore walls, higher hydrothermal stability in comparison to M41S and substantial amount of silanol

groups that allow incorporation of high amount of organic groups on its surface. Importantly, the polymer employed to obtain SBA-15, poly (ethylene oxide)-poly (propylene oxide)-poly (ethylene oxide) (PEO-PPO-PEO), is cheap and biodegradable. Later, Stucky and co-workers reported the synthesis of different types of mesoporous materials from the SBA family using non-ionic triblock, star diblock and oligomeric surfactants with various mesophases.

1.4.1 Organically Functionalized Mesoporous Silica Phases

Mesoporous silicates have very high surface area and are covered by silanol groups. Organic functional groups can be easily incorporated on the surface of the mesoporous materials using organo-silane coupling agents. There are two major pathways to functionalize the surface of mesoporous silicates; post-synthesis modification (also known as grafting method) and; one pot synthesis or co-condensation method. Each of these two surface functionalization methods has certain advantages, which have been discussed in the section below. These surface functionalized mesoporous silicates could change the chemical and physical properties of materials dramatically. The immense variation of functional organic chemistry combined with the advantages of a thermally stable and robust inorganic solid matrix affords synthesis of a broad range of novel materials for various applications. Mesoporous materials have already been functionalized with various organic functional groups which include amines,^{19, 20} thiols,²¹ carboxylic acid,²² sulfonic acid,²³ vinyl²⁴ and nitrogen based heterocycles.²⁵ These functional groups present on the surface of mesoporous material have been used to anchor various synthetic catalysts, biomolecules and polymers to generate novel functional materials and have found wide spread applications in catalysis, separation, decontamination, drug delivery and sensor design.

1.4.1.1 Grafting Method (post synthetic functionalization of silica)

Grafting refers to the post synthesis modification of a prefabricated mesoporous silica support. Typically it is carried out by condensation of organosilanes of the type $(R'O)_3SiR$, or less frequently chlorosilanes $ClSiR_3$ or silazanes $HN(SiR_3)_3$ with the free silanol groups of the silica surfaces (Figure 1.4). Using this methodology, functionalization with a variety of

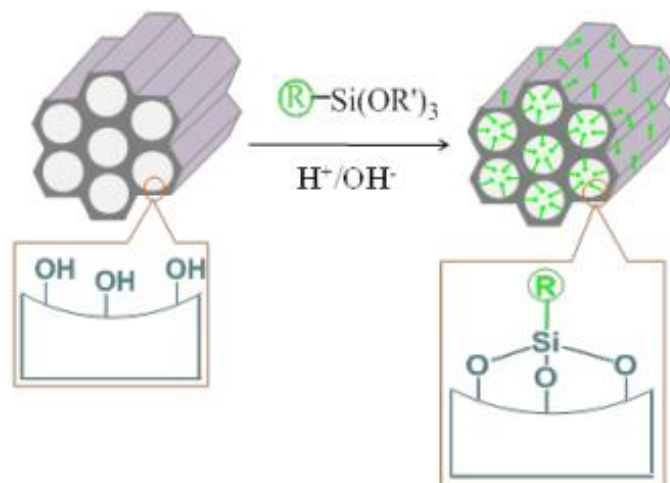


Figure 1.4 Functionalization of mesoporous materials by the grafting method.

organic groups can be achieved by varying the organic residue R in $(R'O)_3SiR$. In this methodology, the particle morphology and pore structure is preserved under the synthetic conditions. However, it should be noted that silanols groups situated on the exterior surface and at the openings of the mesopores are kinetically more accessible than silanols situated on the interior pore walls.^{27, 28} Thus, most organic functional groups that are added to mesoporous materials through this post synthetic grafting method have been shown to be located on the exterior surface or congregated at the mesopore opening. This gives rise to non-uniform distribution of the organic group over the whole material. This methodology is particularly advantageous for selectively functionalizing the exterior surface of silica. However, grafting with very bulky species leads to complete closure of the pores (pore blocking).

1.4.1.2 Co-Condensation Method (one pot synthesis)

Organically functionalized mesoporous silica material can be synthesized using an alternative direct synthesis method known as co-condensation method (one-pot synthesis). In this methodology, mesostructured silica phases are prepared by the co-condensation of tetraalkoxysilanes $(RO)_4Si$ (TEOS or TMOS) with terminal trialkoxyorganosilanes of the type $(R'O)_3SiR$ in the presence of structure-directing agents leading to materials with organic

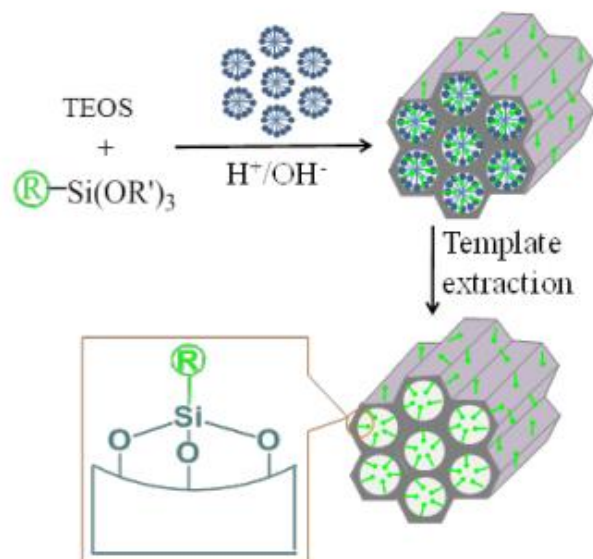


Figure 1.5 Functionalization of Mesoporous materials by co-condensation method.

functional groups anchored covalently on to the pore walls. Since the organic functionalities are direct components of the silica matrix, pore blocking is not a problem in the co-condensation method (Figure 1.5). Furthermore, the organic units are generally more homogeneously distributed than in materials synthesized with the grafting process. However, the disadvantage of this method is that increasing the concentration of $(\text{R}'\text{O})_3\text{SiR}$ can lead to the formation of disordered mesoscopic structure or even loss of order in the final material. Moreover, an increase the concentration of organic functional group leads to the reduction of pore volume and specific surface area. Finally, care must be taken not to destroy the organic functionality during the removal of surfactant. Solvent extraction methods are commonly used for template removal.

1.5 Macroporous Materials

Macro porous materials represent an interesting and technologically important class of material due to its potential application as catalyst support, chromatography, filtration, insulation and biomedical scaffolds. In comparison with microporous and mesoporous materials, macroporous materials have larger interconnected pores (usually from tens to

hundreds of nanometers) and thus have the potential to provide easier molecule transportation through the materials. They are also of particular interest for the transport of large biomolecules (e.g., proteins and cells). Thus, due to the technological importance of macroporous materials, a rich variety of methods have been listed below for the production of macro porous materials. In general, top-down and bottom-up are considered as two main approaches for the synthesis of macroporous materials. (a) Top-down: size reduction from bulk materials. (b) Bottom-up: material synthesis from atomic level.

The top-down manufacturing approach often uses the traditional workshop or microfabrication methods where externally controlled tools are used to cut, mill, and shape materials into the desired shape and order. This can be done by using techniques such as precision engineering, inkjet printing excimer laser micromachining, micro fabrication, and microlithography.

Bottom-up approach refers to the build-up of a material from the bottom: atom-by-atom, molecule-by-molecule or cluster-by-cluster. This approach can be defined into three categories: chemical synthesis, self-assembly and positional assembly. In the bottom-up route, nano to microscale patterned structures are assembled using interactions between molecules or colloidal particles. For bottom-up production, templates are typically used around with atoms/molecules/particles self-assemble to form macroporous materials.

1.5.1. Template Directed Synthesis of 3D Macroporous Materials

Template based synthesis of macroporous materials is one of the main strategies used to fabricate advanced materials. Templated assembly gives rise to complex structures decided by the shape of the template.²⁹ The general route for the synthesis of structured materials using templates includes the following steps: (a) colloidal particles/precursor solution are mixed with the template, (b) the former occupies the empty spaces/voids or adhere to the surface of templates to form an inverse structure and, (c) finally the templates are removed after fixation, for example, by chemical crosslinking of the colloidal structure. Commonly, templates are classified as ‘hard’ and ‘soft’.

1.5.1.1 Hard Templates

Hard templates are usually solid-state materials with particular structure and morphology. They include large-sized substances, such as colloidal crystals,³⁰ inorganic salt,³¹ ice crystals, mesoporous silica materials like MCM-41, MCM-48, SBA-15, and porous polycarbonate.³² Usually hard templates are added in the synthesis to direct the creation of macroporous structures. Harsh acid or alkali leaching processes are usually required to remove these hard templates to generate highly ordered inverse macroporous structures.

1.5.1.2 Soft Templates

Soft templates are generally in a fluid-like state and include surfactant micelles, amphiphilic copolymers or biological molecules like DNA, virus, proteins among others.^{33, 34} These templates usually give rise to mesopores in the material after self-organization. Soft templates can easily be removed by controlled heat treatment or by mild dissolution conditions.

1.5.1.3 Colloidal Organization by Templating

The assembly of colloids using templates involves different methods/strategies such as spray drying,³⁵ dynamic templating using breath figures,^{36, 37} polymerization induced phase separation,^{38, 39} adsorption on an interface or substrate (layer by layer technique)^{40, 41} etc. Also different types of templates are used for assembling nanoparticles which includes emulsion droplets,^{42, 43} bubbles, colloidal crystals,⁴⁴⁻⁴⁷ polymer foam,^{48, 49} membranes,⁵⁰ polymer gels,^{51, 52} biopolymers, and biological templates.⁵³ For example, colloidal crystals have been used to prepare exact replicas of the template. Here, pre-organized larger colloidal spheres template the organization of smaller nanoparticles that fill the cavities of the 3D structure (Figure 1.6a). In another case, colloidal spheres are coated with nanoparticles and then the former are organized by various methodologies as discussed in section 1.3. (Figure 1.6 b). Removal of template leads to the formation of three-dimensionally ordered macroporous (3DOM) materials or hollow sphere array of nanoparticles, respectively.⁵⁴

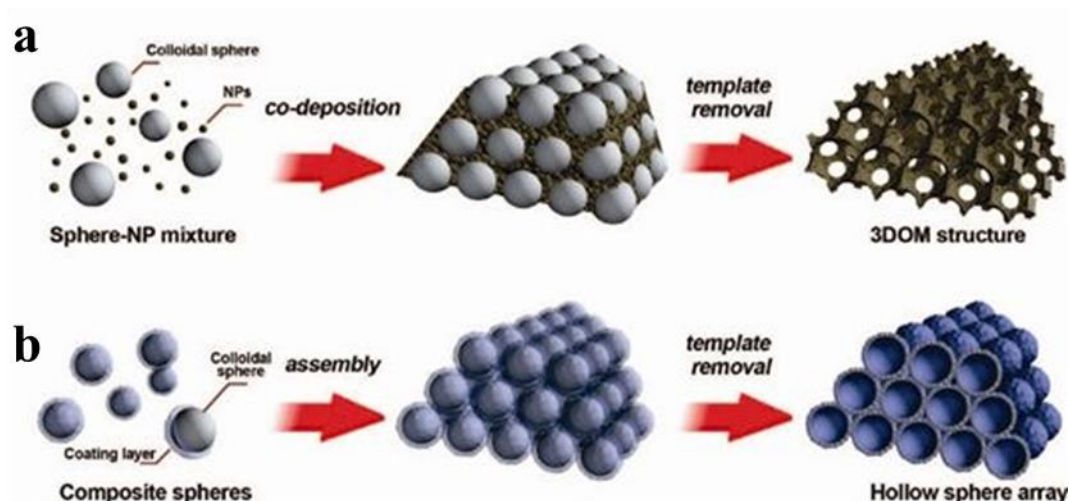


Figure 1.6 Different methodologies for fabrication of three-dimensionally ordered macroporous (3DOM) materials by colloidal crystal templating (Figure adapted from ref. 54 with permission).

1.5.1.4 Ice Templating Method to create Macroporous Materials

In a typical ice templating process, an aqueous solution or dispersion of metal oxides or polymers is frozen by immersing into a cold bath.^{55, 56} This results in the growth of micrometer sized ice spheres due to thermally induced phase separation. This ice templating methodology involves ice spheres as a template to prepare three-dimensionally interconnected

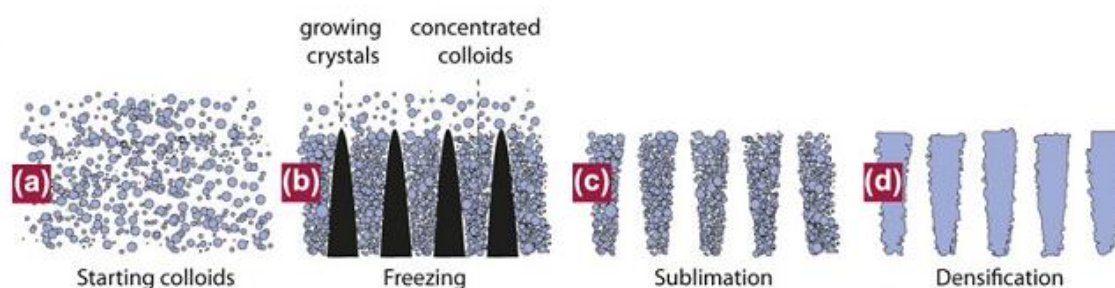


Figure 1.7 Schematic diagram of the ice-templating process (Figure adapted from ref. 56 with permission)

macroporous metal oxide or polymers and can be easily removed simply through thawing and drying. This ice templating methodology neither requires a special template material nor a special removal process of the template. It is an inexpensive, environmentally friendly and can produce highly pure materials with interconnected spherical macropores.

1.5.1.5 Dynamic Templating of Surfactant Hexagonal Domains to create Porous Structure

Dispersion of colloids in an ordered matrix results in their self-assembly, driven by colloid-matrix interactions, and by matrix-mediated particle-particle interactions. Templating of nematic domains, by particles expelled to domain boundaries, results in the formation of particulate networks. In such systems, chain-like linear arrays of colloids with dipolar interactions, mediated by a nematic matrix have been reported, as well as two-dimensional crystals of colloids with quadrupolar interactions. Recently, Guruswamy *et.al.* reported the synthesis of macroporous materials and hierarchically porous monolith scaffolds using dynamic templating of non-ionic surfactant $C_{12}E_9$ (H_1) mesophases.⁵⁷⁻⁵⁹ They have demonstrated that particles over a wide size range (diameter, d , greater than 10 nm and up to about 500 nm; $d > a$, characteristic length scale of the surfactant mesophase H_1 ; $a = 5.7$ nm,) form particulate networks in surfactant-water systems. This network formation of particles in 1:1 mixtures of nonionic surfactant $C_{12}E_9$ and water is reversible, and the particles redisperse on heating above the isotropic phase at a temperature $T_{HI} \approx 40$ °C. On cooling from the isotropic phase into the hexagonal, the particles are expelled from the growing hexagonal domains and forms networks of particles that are jammed at the H_1 domain interfaces. Cross-linking the particles followed by removal of surfactant template by extensive water washing results in the formation of macroporous scaffolds. This technique involves near ambient temperatures, and a benign water wash for template removal. The network mesh size can be varied from the sub-micron to tens of microns by controlling the cooling rate. Thus it represents a general methodology that allows preparing a wide variety of self-standing porous materials from nanoparticles dispersion.

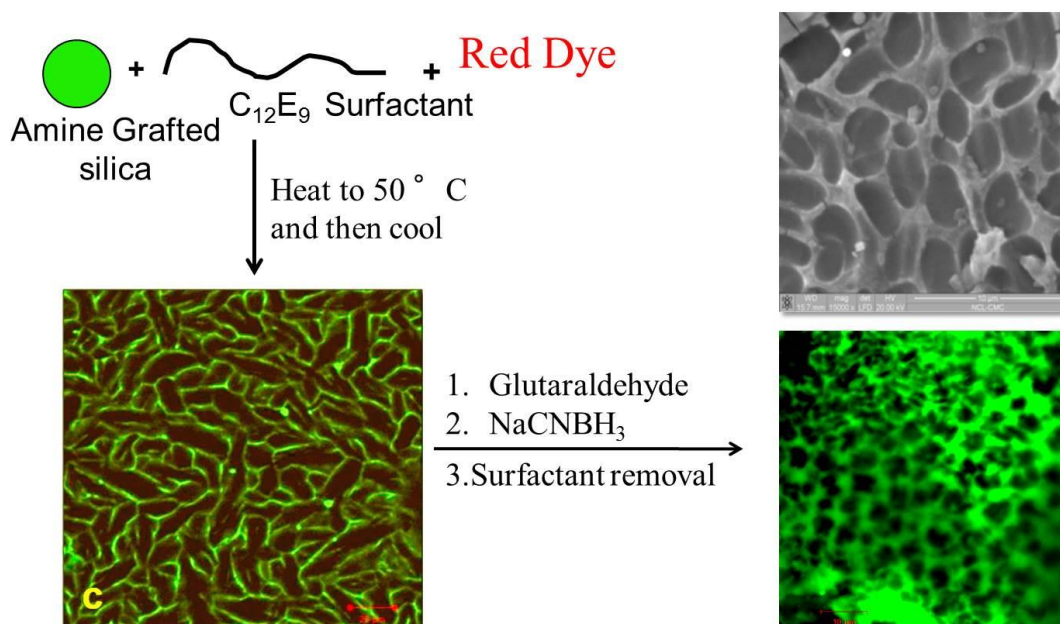


Figure 1.8 Schematic illustration of assembling nanoparticles using non-ionic surfactant $C_{12}E_9$. (A) Confocal micrograph of fluorescently tagged silica particles in surfactant dispersion. (B) SEM of Scaffold (C) Confocal image of the scaffold. (Figure adapted from ref. 58 with permission)

1.6 Click Chemistry

The introduction and progress of the “click chemistry” to design and prepare complex, highly functional molecules was first highlighted by Sharpless and co-workers in 2001.⁶⁰ This has made a huge impact on the synthesis of polymers and materials, small organic molecules and in drug discovery. The characteristics of modular click reactions as defined by Sharpless *et. al.* includes a) high yields with by-products (if any) that are removable by non-chromatographic processes, b) regioselectivity and stereoselectivity, c) insensitivity to water or oxygen, d) mild, solvent less (or aqueous) reaction conditions, e) orthogonality with other common organic synthesis reactions, and f) amenability to a wide variety of readily available starting materials and reagents. Although meeting the requirements of a ‘click’ reaction is a tall order, several reactions have been identified which step up to the mark : (i) cycloadditions of unsaturated species, especially 1,3-dipolar cycloaddition reactions, but also the Diels-Alder family of transformations; (ii) nucleophilic substitution chemistry, particularly ring-opening reactions of strained heterocyclic electrophiles such as epoxides, aziridines, aziridinium ions, and episulfonium ions; (iii) carbonyl chemistry of the “non-aldol” type, such as formation of ureas, thioureas, aromatic

heterocycles, oxime ethers, hydrazones, and amides; and (iv) additions to carbon-carbon multiple bonds, especially oxidative cases such as epoxidation, dihydroxylation, aziridination, and sulfenyl halide addition, but also Michael additions of Nu-H reactants.

1.6.1 CuAAC Click Chemistry

While a series of click reactions reported so far, the most widely studied or which has been termed as the “cream of the crop” of click reactions is Huisgen [3+2] cycloaddition, between a terminal alkyne and an azide to yield substituted 1, 2, 3-triazoles (Figure 1.9).^{61, 62} This is due to its general ease of execution, facile reaction conditions and impressive orthogonality. The highly efficient copper (I)-catalyzed Huisgen 1, 3-dipolar cycloaddition, is broadly known as the azide/alkyne “click”-reaction or CuAAC-reaction. The great success of the Cu(I) catalyzed reaction is rooted in the fact that it is a virtually quantitative, very robust, insensitive, general, and orthogonal ligation reaction, suitable for even biomolecular ligation and in vivo tagging or as a polymerization reaction for synthesis of long linear polymers. The triazole formed is essentially chemically inert to reactive conditions, e.g. oxidation, reduction, and hydrolysis, and has an intermediate polarity with a dipolar moment of ~5D. A mechanistic picture of the copper catalyzed reaction was first proposed by Meldal, Sharpless and co-workers. However, the proposed catalytic mechanism (calculated by density functional theory (DFT) calculations) that relied on the initial formation of a Cu acetylide between the CuI species and the terminal alkyne which subsequently proceeded by an initial π -complex formation between the CuI and the alkyne, to lead to a lowering of the pK_a of the terminal acetylene by up to 9.8 units, thus enabling the attack onto the C–H bond, especially in aqueous systems, has been recently revised in favor of a binuclear mechanism as shown in Figure 1.9.

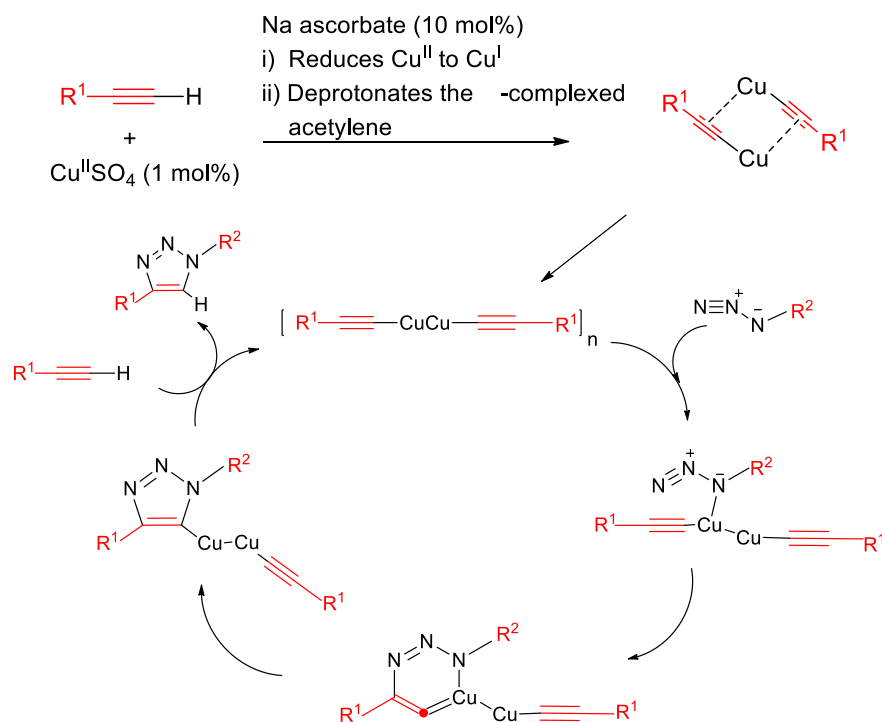


Figure 1.9 Mechanism of the CuAAC reaction.

1.6.2 Thiol-Ene Click Chemistry

The broad utility of the Cu(I)-mediated alkyne-azide reaction has encouraged researchers to more closely evaluate the potential of other reactions that possess “click” characteristics. In this perspective, reactions of thiols with reactive carbon-carbon double bonds, or simply “enes”, were noted as highly efficient reaction in 1905. Historically, in the area of polymer and materials, thiol-ene reaction has been most widely employed as a means of preparing near-perfect networks and films as exemplified by the work of Hoyle, Bowman and co-workers.⁶³⁻⁶⁴ More significantly, thiol-ene coupling reactions have been proposed to proceed via either the (i) anti-Markovnikov's radical addition or the (ii) base/nucleophile-catalyzed Michael addition reaction.

1.6.2.1 Radical based Thiol-Ene Click Reactions

Generally the thiol-ene reactions conducted under radical conditions are photochemically induced. Under such conditions it proceeds via a typical chain process with

initiation, propagation and termination steps as shown in Figure 1.10.⁶⁵⁻⁶⁷ Initiation involves the treatment of a thiol with photoinitiator, under irradiation, resulting in the formation of a thiyl radical, RS^\bullet , plus other byproducts. Propagation is a two-step process involving first the direct addition of the thiyl radical across the $C=C$ bond yielding an intermediate carbon-centred radical followed by chain transfer to a second molecule of thiol to give the thiol-ene addition product, with anti-Markovnikov orientation, with the concomitant generation of a new thiyl radical. Finally the termination reactions involves a typical radical-radical coupling processes.

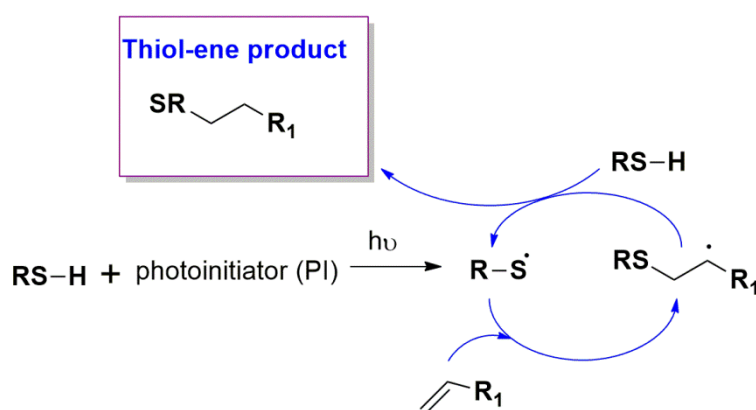


Figure 1.10 The mechanism for the hydrothiolation of a $C=C$ bond in the presence of a photoinitiator and $h\nu$.

1.6.2.2 Michael Addition Reactions

In contrast to the traditional thiol-ene free-radical reaction, thiol-vinyl reactions between a thiol and an electron-deficient ene also occur readily (Figure 1.11).^{68, 69} This click reaction can also be simply referred as a thiol-Michael addition reaction, with the condition that the ene is electron-deficient, such as (meth) acrylates, maleimides, α , β -unsaturated ketones, fumarate esters, acrylonitrile, cinnamates, and crotonates. The primary/secondary amine and phosphine nucleophilic catalysts are particularly efficient and provide a simple, highly efficient process for catalyzing thiol-ene reactions between thiols and acrylates and other electron-deficient enes. The reactions proceed with the nucleophilic attack at the activated ene generates the intermediate, strong (zwitterionic) enolate base that is responsible for deprotonating thiol, generating the thiolate anion. Once the thiolate is formed, the anionic

chain process begins with rapid formation of the thiol-ene product by a subsequent proton abstraction of the thiol. In contrast to the thiol-ene radical process, there are no anionic coupling processes that terminate the chains for the thiol-Michael reactions once they are initiated. Another salient feature of this proposed anionic chain process for hydrothiolation mediated by amines or phosphines is that no special precautions need to be taken such as exclusion of moisture and O_2 . The combination of the typically low pK_a 's of thiols coupled with the high reactivity of the thiolate towards conjugate addition enables such reactions to be performed with 100% efficiency in the presence of other protic species, including water.

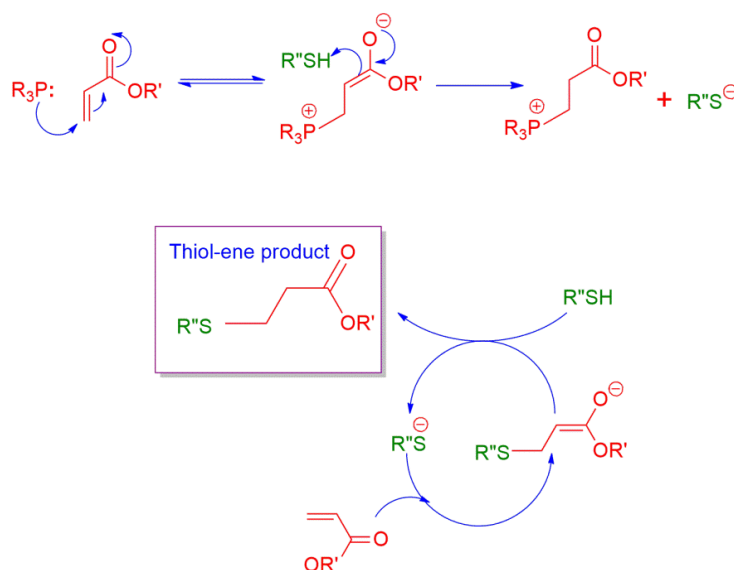


Figure 1.11 Anionic Chain mechanism for the hydrothiolation of an acrylic C=C bond.

1.7 Physico-Chemical Characterization

The inorganic-organic hybrid mesoporous materials can be characterized by various techniques, which provide important information about different physico-chemical properties of these materials. In this section, a brief introduction to the theory and principle of various characterization techniques employed in the present study are discussed.

1.7.1 Powder X-Ray Diffraction

Powder X-ray diffraction is a rapid analytical technique used to identify and measure the uniqueness of structure, phase purity, degree of crystallinity and unit cell parameters of

crystallite materials. The mesoporous materials exhibit characteristic high intensity peaks in the low angle region between $2\theta = 0.5-10^\circ$. The XRD patterns are recorded by the measurements of the angles at which the X-ray beams are diffracted by the sample. The relation between the distance between two hkl planes (d) and angle of diffraction (2θ) is given by Bragg's equation as follows (Eq. 1.1):

$$n\lambda = 2d \sin\theta \quad (\text{Eq. 1.1})$$

Where λ = wavelength of X-rays, n = an integer known as the order of reflection (h , k , and l represent Miller indices of respective planes). From the diffraction patterns, the uniqueness of mesoporous structures, phase purity, degree of crystallinity, and unit cell parameters of the semi crystalline hybrid materials can be determined. The identification of phase is based on a comparison of a set of reflections of the sample with that of pure reference phases distributed by International Center for Diffraction Data (ICDD). Unit cell parameter (a_0) of a cubic lattice can be determined by the following equation: $a_0 = d_{hkl}(h^2 + k^2 + l^2)^{1/2}$, where d = distance between two consecutive parallel planes having Miller indices h , k , and l . The unit cell dimensions determined by XRD are also used to calculate the wall thickness of mesoporous materials in combination with pore size data determined from gas adsorption-desorption studies.

1.7.2 Scanning Electron Microscopy

Scanning electron microscopy (SEM) is an important technique for characterization of size and morphology of mesoporous materials. This technique provides not only topographical information like optical microscopes do, but also information on the chemical composition near the surface. SEM creates the magnified image by using electrons instead of light waves. It generates very detailed three-dimensional image at much higher magnification than is possible with an optical microscope. A scanning electron microscope can generate an electron beam scanning back and forth over a solid sample. The interaction between the beam and the sample produces different types of signals providing detailed information about the surface structure and morphology of the sample. When an electron from the beam encounters a nucleus in the sample, the resultant Coulombic attraction leads to a deflection in the electron's path, known as Rutherford elastic scattering. A fraction of these electrons will be

completely backscattered, reemerging from the incident surface of the sample. Since the scattering angle depends on the atomic number of the nucleus, the primary electrons arriving at a given detector position can be used to produce images containing topological and compositional information. The high-energy incident electrons can also interact with the loosely bound conduction band electrons in the sample. However, the amount of energy given to these secondary electrons as a result of the interactions is small, and so they have a very limited range in the sample. Hence, only those secondary electrons that are produced within a very short distance from the surface are able to escape from the sample. As a result, high resolution topographical images can be obtained in this detection mode. SEM is non-destructive to samples although some electron beam damage is possible. SEM scans over a sample surface with a probe of electrons (5-50 kV) and detects the yield of either secondary or back-scattered electrons as a function of the position of the primary beam. Magnification of 10-500,000 times is possible with a resolution of about 1 nm. Sample requirements are minimal; they should be vacuum compatible and invariably be coated with a conducting film to avoid sample charging during the measurement.

1.7.3 Transmission Electron Microscopy

Transmission electron microscopy (TEM) is a major analytical tool in a range of scientific fields including materials and biological sciences. TEM is typically used for high resolution imaging of thin sections of solid samples for nanostructural and compositional analysis. The technique involves: (i) irradiation of a very thin sample by a high energy electron beam, which is diffracted by the lattice of a crystalline or semi crystalline material and propagated along different directions. (ii) imaging and angular distribution analysis of the forward-scattered electron (unlike SEM where backscattered electrons are detected), and (iii) energy analysis of the emitted X-rays. A beam of accelerated electrons can interact with an object in a conventional transmission electron microscope in one of two ways. Usually elastic scattering takes place, whereby the electrons change their path in the specimen without a loss of energy. Inelastic scattering can also occur, resulting in a loss of energy due to an interaction of the impinging electrons with the orbital electrons surrounding the nucleus of each atom in the object. Those electrons, which are not or hardly scattered, contribute positively to the image. However, considerably deflected electrons are prevented from doing so by apertures in the optical path. As a result, differences in light intensity (contrast) are created in the final image, which relate to areas in the object with different scattering

potentials. As the atomic number increases, their scattering efficiency will also increase. Hence, heavy metals can form images with good contrast. The imaging system consists of an objective lens and one or more projector lenses. The chief lens in transmission microscopes is the objective. It determines the degree of resolution in the image. It forms the initial enlarged image of the illuminated portion of the specimen in a plane that is suitable for further enlargement by the projector lens. The projector lens, as it implies, serves to project the final magnified image on the screen or photographic emulsion. The great depth of focus provides the high magnification of the sample. The topographic information obtained by TEM in the vicinity of atomic resolution can be utilized for structural characterization and identification of various phases of mesoporous materials, viz., hexagonal, cubic or lamellar. TEM also provides real space image on the atomic distribution in the bulk and surface of a nanocrystal. The modern TEM machines can achieve resolution below 0.5 angstroms (50 pm) at magnifications above 50 million times.

1.7.4 Gas adsorption-desorption studies

Gas adsorption-desorption studies is one of the widely used technique for evaluating the surface area, pore size, pore volume and pore size distribution of porous solid materials. In this technique, the amount of gas adsorbed by a solid is measured, which in turn is directly related to the porous properties and pore structure of the material. Depending on the nature of the adsorbent solid and information required, various gases like Nitrogen (N₂), Carbon dioxide (CO₂) and Argon (Ar) are used as adsorbates. The volume of gas adsorbed by the solid is measured over a wide range of relative pressures, and a plot of the volume adsorbed with varying relative pressure (p/p_o) is called the adsorption isotherm. N₂ adsorption isotherm at sub-atmospheric pressures and -196 °C is routinely used for determining pore information and pore size distributions in microporous, mesoporous and macroporous range. Surface area is determined from the Brauner-Emmett-Teller (BET) equation (Eq. 1.2), based on monolayer adsorption of gases.

$$\frac{p}{v(p_o - p)} = \frac{1}{v_m c} + \frac{c-1}{v_m c} X \frac{p}{p_o} \quad (\text{Eq. 1.2})$$

where, v = volume of N₂ adsorbed by the sample under pressure p , p_o = saturated vapor pressure at the same temperature, v_m = volume of N₂ adsorbed when the surface is covered with monolayer, and c = BET constant for a given adsorbate.

The equation suggests that the plot of $p/v/(p_0 - p)$ versus p_0/p should be linear, and from the intercept $1/v_m c$ and slope $(c-1)/v_m c$, the values of v_m and c can be determined. Thus the specific surface area (S) of a sample can be determined as follows (Eq. 1.3):

$$S = \frac{N_0 v_m A}{22414 m} \quad (\text{Eq. 1.3})$$

where N_0 = Avogadro number, m = mass of solid adsorbent, A = cross-section of the gas molecules (16.2 \AA^2 for N_2), and S is expressed in $\text{cm}^2 \text{ g}^{-1}$ unit.

Several computational procedures are available for the derivation of pore size distribution of mesoporous samples from physisorption isotherms. Most popular among them is the Barrett-Joyner-Halenda (BJH) model, which is based on speculative emptying of the pores by a stepwise reduction of p/p_0 , and allowance being made for the contraction of the multilayer in those pores already emptied by the condensate. The mesopores size distribution is usually expressed as a plot of dV_p/dr_p versus r_p , where V_p = mesopore volume, and r_p = pore radius. It is assumed that the mesopores volume is completely filled at high p/p_0 .

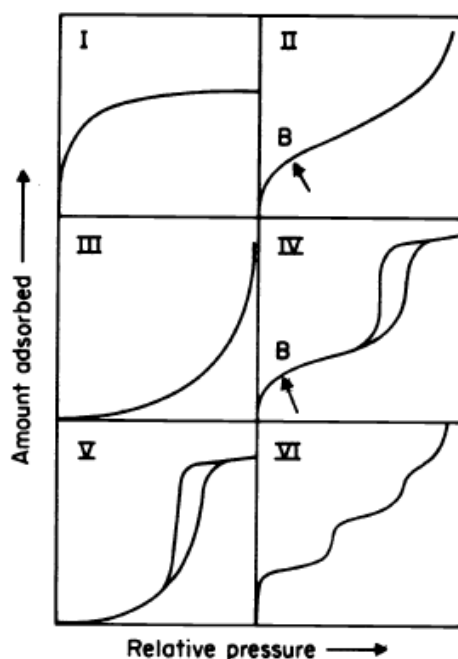


Figure 1.12: Types of physisorption isotherms.

The physisorption isotherms have been classified into six distinct types by IUPAC (Fig 8): Type I reversible isotherms exhibited by microporous solids; Type II reversible

isotherms exhibited by nonporous and macroporous solids; Type III isotherm, which is rarely seen; Type IV isotherm with hysteresis loop, exhibited by mesoporous solids; Type V isotherm which is rarely seen and arises due to weak adsorbent-adsorbate interactions. Type VI isotherm arising from stepwise multilayer adsorption on a uniform nonporous solid. The different isotherms are shown in Figure 1.7. The hysteresis loop exhibited in the type IV isotherm is classified into 4 distinct types: H1, usually exhibited by pores with regular shape and narrow pore size distribution; H2, usually associated with pores with narrow necks and wide bodies; H3, usually associated with plate like particles; H4, usually associated with slit-like pores. The shapes of the different hysteresis loops are shown in Fig. 9.

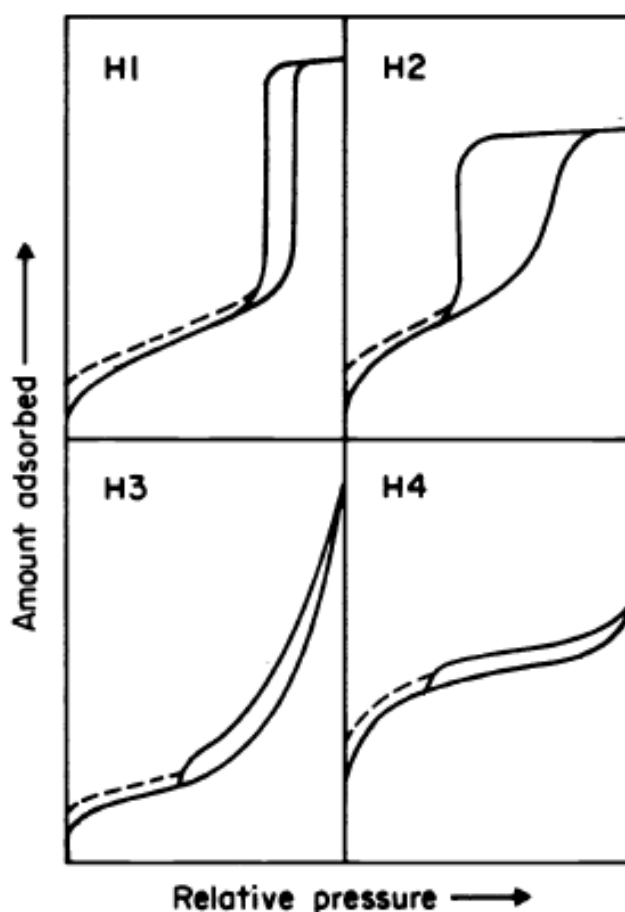


Figure 1.13: Types of hysteresis loops.

1.7.5 Thermogravimetric analysis (TGA)

Thermogravimetric analysis or TGA is a technique in which the weight loss of a sample is studied with increasing temperature. It is a highly sensitive technique, which provides information about the weight percentage of moisture, volatiles, solvent, organic /inorganic contents, etc in a samples. It is done by placing the sample in a weighing balance and heating the sample at a controlled rate. The weight loss is studied in various ambient atmospheres like nitrogen or air. TGA is widely used for studying the weight percentage of templates in mesoporous material synthesis and to estimate the organic /inorganic contents in modified mesoporous materials.

1.7.6 Fourier Transform Infrared Spectroscopy

Fourier transform infrared (FTIR) spectroscopy deals with the vibration of chemical bonds in a molecule at various frequencies depending on the elements and types of bonds. After absorbing electromagnetic radiation the frequency of vibration of a bond increases leading to transition between ground state and several excited states. These absorption frequencies represent excitations of vibrations of the chemical bonds and thus are specific to the type of bond and the group of atoms involved in the vibration. The energy corresponding to these transitions corresponds to the infrared region ($4000\text{--}400\text{ cm}^{-1}$) of the electromagnetic spectrum. The term Fourier transform (FT) refers to a recent development in the manner in which the data are collected and converted from an interference pattern to an infrared absorption spectrum that is like a molecular "fingerprint". In the case of porous silicates, the FTIR spectra in the $400\text{--}1300\text{ cm}^{-1}$ region provides information about the structural details, for example, peaks at 466 , 800 , 1070 and 1220 cm^{-1} are typical of Si-O-Si bands that are associated with formation of silica framework. Whereas the bands in the $3000\text{--}4000\text{ cm}^{-1}$ region allows to determine different organic functional groups present on the surface of the materials, Bronsted and Lewis acid sites and silanol groups.

1.7.7 Cross-polarization magic angle spinning NMR spectroscopy

Nuclear magnetic resonance (NMR) spectroscopy is one of the most powerful tools to investigate structure and dynamics of a molecular system in liquid phase. Atomic nuclei

consisting of odd number of protons and/or neutrons possessing a nuclear spin $I \neq 0$ and consequently a magnetic moment $\mu = \gamma \hbar I$ ($\gamma =$ gyromagnetic ratio), when placed in a magnetic field of strength B_0 , Zeeman interaction results in quantized orientations of the nuclear magnetic moments. The nucleus can adopt $2I + 1$ Eigen states with energies $E(m) = -m\gamma \hbar B_0$, where $m = (I, I-1, \dots, -I)$. Transitions between neighbouring energy states ($\Delta m = \pm 1$) can be induced by electromagnetic radiation (energy $E = h\nu$) of frequency $\nu_0 = \gamma B_0/2\pi$. The chemical shift interaction arises from secondary local magnetic fields induced by the interaction of the electrons surrounding the nucleus. The induced local field opposes B_0 and hence shields the nucleus under observation. The shielding is spatially anisotropic due to the nonspherical electron distribution around the nucleus.

In solid-state NMR, the line shape is determined by dipolar and quadrupolar interactions. The lines are usually broader because the rigid structure of the solid phase prevents the averaging of the dipolar interaction by motions. Since, the first order quadrupolar and dipolar interactions are proportional to $(3 \cos^2\theta - 1)$, where, θ is the angle between an internuclear vector and the magnetic field, these interactions can be removed, to a first order approximation, by spinning the sample around the so-called magic angle β with respect to the external magnetic field, for which $3 \cos^2\beta - 1 = 0$, i.e. $\beta = 54.74^\circ$. This technique is known as Magic Angle Spinning (MAS).

Cross-polarization (CP) involves indirect excitation of the less abundant nucleus through magnetization transfer from an abundant spin system (e.g. ^1H) i.e., to increase the signal to noise ratio (SNR) of the spectra of nuclei with low natural abundance (e.g. ^{13}C , ^{29}Si , ^{31}P etc.), and to monitor the spatial proximity of nuclei. CP technique does not affect the line width of the spectra, but is applied to improve the sensitivity.

1.8 Motivation and Objective of the Present Work

Although organic-inorganic porous hybrid materials have emerged as one of frontier research areas in the field of advanced functional materials, the potential for their application in areas such as catalysis, adsorption, sensing, and biotechnology has not been fully realized. This requires development of newer hybrid inorganic-organic materials with improved properties. For example in the field of catalysis, meso-macroporous materials have been demonstrated as catalyst supports because the combination of multiple functionalities allow

them to function both as catalytic materials in addition to facilitating transport of reactant. Hierarchically porous materials that afford control of pore characteristics at each length scale, and allow chemical functionalization, have significant potential for applications in areas as diverse as catalysis and tissue engineering.

In my thesis I have attempted to synthesize mesoporous, macroporous and meso-macroporous hybrid materials for possible applications in catalysis and biotechnology. This involved both development of new synthetic methodology, characterization of such materials and evaluation of their function. By keeping the above objectives in mind, the following specific work was selected for the present thesis:

1. Development of new post-synthesis functionalization methods for generation of mesoporous hybrid materials using “thiol-ene click” Michael addition reaction
2. Synthesis of silica based hybrid materials as an oxidation catalyst for ultra-sensitive detection of proteins via signal amplification
3. Synthesis of transition metal nanoparticle based hybrid macroporous material using dynamic templating of surfactant H₁ domains and its application as catalysts in continuous flow reactions
4. Synthesis of soft and spongy macroporous scaffolds using ice templating method for applications in biotechnology.

1.9 References

- 1) Mann, S.; Burkett, S. L.; Davis, S. A.; Fowler, C. E.; Mendelson, N. H.; Sims, S. D.; Walsh, D.; Whilton, N. T., Sol--Gel Synthesis of Organized Matter. *Chem. Mater.* **1997**, 9 (11), 2300-2310.
- 2) Soler-Illia, G. J. d. A. A.; Sanchez, C.; Lebeau, B.; Patarin, J., Chemical Strategies To Design Textured Materials: from Microporous and Mesoporous Oxides to Nanonetworks and Hierarchical Structures. *Chem. Rev.* **2002**, 102 (11), 4093-4138.
- 3) Sanchez, C.; Boissière, C.; Grosso, D.; Laberty, C.; Nicole, L., Design, Synthesis, and Properties of Inorganic and Hybrid Thin Films Having Periodically Organized Nanoporosity. *Chem. Mater.* **2008**, 20 (3), 682-737.
- 4) Sanchez, C.; Rozes, L.; Ribot, F.; Laberty-Robert, C.; Grosso, D.; Sassoie, C.; Boissiere, C.; Nicole, L., “Chimie douce”: A land of opportunities for the designed

- construction of functional inorganic and hybrid organic-inorganic nanomaterials. *Comptes Rendus Chimie* 2010, 13 (1-2), 3-39. (b) Zhu, F.; Nishimura T.; Sakamoto, T.; Tomono, H.; Nada, H.; Okumura, Yasushi.; Kikuchi, H.; Kato, T. Tuning the Stability of CaCO₃ Crystals with Magnesium Ions for Formation of Aragonite Thin Films on Organic Polymer Templates. *Chem. Asian J.*, **2013**, **8**, 3002-3009
- 5) Ozin, G. A., Panoscopic materials: synthesis over 'all' length scales. *Chem. Commun.* **2000**, (6), 419-432.
 - 6) Backov, R., Combining soft matter and soft chemistry: integrative chemistry towards designing novel and complex multiscale architectures. *Soft Matter* **2006**, 2 (6), 452-464.
 - 7) Antonietti, M.; Göltner, C., Superstructures of Functional Colloids: Chemistry on the Nanometer Scale. *Angew. Chem., Int. Ed.* **1997**, 36 (9), 910-928.
 - 8) Gómez-Romero, P.; Sanchez, C., Hybrid Materials, Functional Applications. An Introduction. In Functional Hybrid Materials, *Wiley-VCH Verlag GmbH & Co. KGaA*: **2005**; pp 1-14.
 - 9) Kickelbick, G., Introduction to Hybrid Materials. In Hybrid Materials, *Wiley-VCH Verlag GmbH & Co. KGaA*: **2007**; pp 1-48.
 - 10) Sanchez, C.; Julian, B.; Belleville, P.; Popall, M., Applications of hybrid organic-inorganic nanocomposites. *J. Mater. Chem.* **2005**, 15 (35-36), 3559-3592.
 - 11) S. Mann, Biomimetic Materials Chemistry, Wiley-VCH, Weinheim, **1997**
 - 12) Clay Minerals and the Origin of Life, ed. A. G. Cairns-Smith and H. Hartman, Cambridge University Press, Cambridge, 1986
 - 13) (a) Fayed, T.; Shaaban, M.; El-Nahass, M.; Hassan, F., Hybrid organic-inorganic mesoporous silicates as optical nanosensor for toxic metals detection. **2014**; Vol. 1, p 74-94. (b) Handbook of Heterogeneous Catalysis, Vol. 1 (Eds: G. Ertl, H. Knözinger, J. Weitkamp), *Wiley-VCH, Weinheim, Germany* **1997**.
 - 14) K.S.W. Sing, D.H. Everett, R.A.W. Haul, L. Moscou, R.A. Pierotti, J. Rouquerol and T. Siemieniewska, Reporting Physisorption Data Gas/Solid Systems with Special Reference to the Determination of Surface Area and Porosity. *Pure and applied chemistry*, **1985**, 57, 603-619
 - 15) Kresge, C. T.; Leonowicz, M. E.; Roth, W. J.; Vartuli, J. C.; Beck, J. S., Ordered mesoporous molecular sieves synthesized by a liquid-crystal template mechanism. *Nature* **1992**, 359 (6397), 710-712

- 16) Beck, J. S.; Vartuli, J. C.; Roth, W. J.; Leonowicz, M. E.; Kresge, C. T.; Schmitt, K. D.; Chu, C. T. W.; Olson, D. H.; Sheppard, E. W., A new family of mesoporous molecular sieves prepared with liquid crystal templates. *J. Am. Chem. Soc.* **1992**, *114* (27), 10834-10843 (b) Hoffmann, F.; Cornelius, M.; Morell, J.; Fröba, M., Silica-Based Mesoporous Organic–Inorganic Hybrid Materials. *Angew. Chem., Int. Ed.* **2006**, *45* (20), 3216-3251.
- 17) Zhao, D.; Feng, J.; Huo, Q.; Melosh, N.; Fredrickson, G. H.; Chmelka, B. F.; Stucky, G. D., Triblock Copolymer Syntheses of Mesoporous Silica with Periodic 50 to 300 Angstrom Pores. *Science* **1998**, *279* (5350), 548-552.
- 18) D. Zhao, Q. Huo, J. Feng, B.F. Chmelka, and G.D. Stucky, "Nonionic Triblock and Star Diblock Copolymer and Surfactant Syntheses of Highly Ordered, Hydrothermally Stable, Mesoporous Silica Structures," *J. Am. Chem. Soc.*, **120**, 6024-6036 (1998).
- 19) Wang, X.; Lin, K. S. K.; Chan, J. C. C.; Cheng, S., Preparation of ordered large pore SBA-15 silica functionalized with aminopropyl groups through one-pot synthesis. *Chem. Commun.*, **2004**, 0, (23), 2762-2763.
- 20) Wang, X.; Lin, K. S. K.; Chan, J. C. C.; Cheng, S., Direct Synthesis and Catalytic Applications of Ordered Large Pore Aminopropyl Functionalized SBA-15 Mesoporous Materials. *J. Phys. Chem. B*, **2005**, *109*, (5), 1763-1769.
- 21) Wei, Q.; Nie, Z.; Hao, Y.; Chen, Z.; Zou, J.; Wang, W., Direct synthesis of thiol-ligands functionalized SBA-15: Effect of 3-mercaptopropyltrimethoxysilane concentration on pore structure. *Materials Letters*, **2005**, *59*, (28), 3611-3615.
- 22) Yang, C.-m.; Zibrowius, B.; Schuth, F., A novel synthetic route for negatively charged ordered mesoporous silica SBA-15. *Chem. Commun.*, **2003**, 0, (14), 1772-1773.
- 23) Marschall, R.; Rathousky, J.; Wark, M., Ordered Functionalized Silica Materials with High Proton Conductivity. *Chem. Mater.*, **2007**, *19*, (26), 6401-6407.
- 24) Wei, Q.; Chen, H.-Q.; Nie, Z.-R.; Hao, Y.-L.; Wang, Y.-L.; Li, Q.-Y.; Zou, J.-X., Preparation and characterization of vinyl-functionalized mesoporous SBA-15 silica by a direct synthesis method. *Materials Letters*, **2007**, *61*, (7), 1469-1473.
- 25) Li, J.; Qi, T.; Wang, L.; Liu, C.; Zhang, Y., Synthesis and characterization of imidazole-functionalized SBA-15 as an adsorbent of hexavalent chromium. *Materials Letters*, **2007**, *61*, (14-15), 3197-3200

- 26) Huang, Y.; Xu, S.; Lin, V. S. Y., Bifunctionalized Mesoporous Materials with Site-Separated Brønsted Acids and Bases: Catalyst for a Two-Step Reaction Sequence. *Angew. Chem., Int. Ed.* **2011**, 50, (3), 661-664
- 27) Slowing, I.; Trewyn, B. G.; Lin, V. S. Y., Effect of Surface Functionalization of MCM-41-Type Mesoporous Silica Nanoparticles on the Endocytosis by Human Cancer Cells. *J. Am. Chem. Soc.* **2006**, 128, (46), 14792-14793.
- 28) Huh, S.; Wiench, J. W.; Trewyn, B. G.; Song, S.; Pruski, M.; Lin, V. S. Y., Tuning of particle morphology and pore properties in mesoporous silicas with multiple organic functional groups. *Chem. Commun.*, **2003**, 0, (18), 2364-2365.
- 29) Grzelczak, M.; Vermant, J.; Furst, E. M.; Liz-Marzán, L. M., Directed Self-Assembly of Nanoparticles. *ACS Nano*, **2010**, 4, (7), 3591-3605.
- 30) Yang, P.; Deng, T.; Zhao, D.; Feng, P.; Pine, D.; Chmelka, B. F.; Whitesides, G. M.; Stucky, G. D., Hierarchically Ordered Oxides. *Science*, **1998**, 282, (5397), 2244-2246.
- 31) Gutiérrez, M. a. C.; Ferrer, M. a. L.; del Monte, F., Ice-Templated Materials: Sophisticated Structures Exhibiting Enhanced Functionalities Obtained after Unidirectional Freezing and Ice-Segregation-Induced Self-Assembly. *Chem. Mater.*, **2008**, 20, (3), 634-648.
- 32) Kar, M.; Pauline, M.; Sharma, K.; Kumaraswamy, G.; Sen Gupta, S., Synthesis of Poly-L-glutamic Acid Grafted Silica Nanoparticles and Their Assembly into Macroporous Structures. *Langmuir*, **2011**, 27, (19), 12124-12133.
- 33) Yuan, Z.-Y.; Su, B.-L., Insights into hierarchically meso-macroporous structured materials. *J. Mater. Chem.*, **2006**, 16, (7), 663-677
- 34) Tsukamoto, R.; Muraoka, M.; Seki, M.; Tabata, H.; Yamashita, I., Synthesis of CoPt and FePt₃ Nanowires Using the Central Channel of Tobacco Mosaic Virus as a Biotemplate. *Chem. Mater.*, **2007**, 19, (10), 2389-2391.
- 35) Iskandar, F.; Mikrajuddin; Okuyama, K., In Situ Production of Spherical Silica Particles Containing Self-Organized Mesopores. *Nano Letters*, 2001, 1, (5), 231-234.
- 36) Bunz, U. H. F., Breath Figures as a Dynamic Templating Method for Polymers and Nanomaterials. *Adv. Mater.*, **2006**, 18, (8), 973-989.
- 37) Sakatani, Y.; Boissière, C. d.; Grosso, D.; Nicole, L.; Soler-Illia, G. J. A. A.; Sanchez, C. m., Coupling Nanobuilding Block and Breath Figures Approaches for the Designed Construction of Hierarchically Templated Porous Materials and Membranes. *Chem. Mater.*, **2007**, 20, (3), 1049-1056.

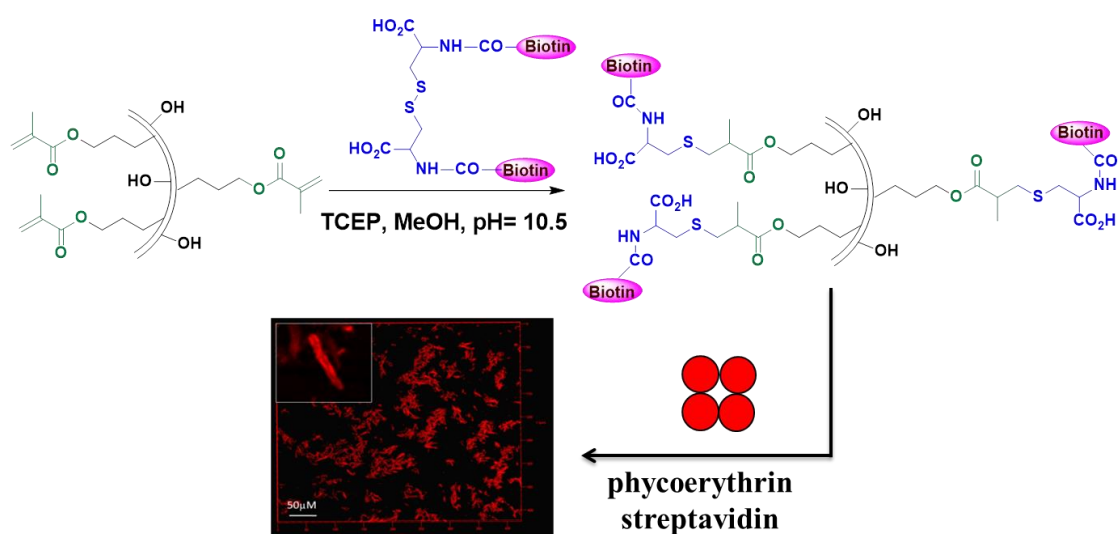
- 38) Amatani, T.; Nakanishi, K.; Hirao, K.; Kodaira, T., Monolithic Periodic Mesoporous Silica with Well-Defined Macropores. *Chem. Mater.*, **2005**, 17, (8), 2114-2119.
- 39) Nakanishi, K.; Kobayashi, Y.; Amatani, T.; Hirao, K.; Kodaira, T., Spontaneous Formation of Hierarchical Macro-Mesoporous Ethane-Silica Monolith. *Chem. Mater.*, **2004**, 16, (19), 3652-3658.
- 40) Boker, A.; He, J.; Emrick, T.; Russell, T. P., Self-assembly of nanoparticles at interfaces. *Soft Matter*, **2007**, 3, (10), 1231-1248.
- 41) Lin, Y.; Skaff, H.; Emrick, T.; Dinsmore, A. D.; Russell, T. P., Nanoparticle Assembly and Transport at Liquid-Liquid Interfaces. *Science*, **2003**, 299, (5604), 226-229.
- 42) Imhof, A.; Pine, D. J., Ordered macroporous materials by emulsion templating. *Nature*, **1997**, 389, 948-951.
- 43) Zhang, H.; Hardy, G. C.; Khimyak, Y. Z.; Rosseinsky, M. J.; Cooper, A. I., Synthesis of Hierarchically Porous Silica and Metal Oxide Beads Using Emulsion-Templated Polymer Scaffolds. *Chem. Mater.*, **2004**, 16, (22), 4245-4256.
- 44) Velev, O. D.; Kaler, E. W., Structured Porous Materials via Colloidal Crystal Templating: From Inorganic Oxides to Metals. *Adv. Mater.*, **2000**, 12, (7), 531-534.
- 45) Davis, S. A.; Breulmann, M.; Rhodes, K. H.; Zhang, B.; Mann, S., Template-Directed Assembly Using Nanoparticle Building Blocks: A Nanotectonic Approach to Organized Materials. *Chem. Mater.*, **2001**, 13, (10), 3218-3226.
- 46) Rhodes, K. H.; Davis, S. A.; Caruso, F.; Zhang, B.; Mann, S., Hierarchical Assembly of Zeolite Nanoparticles into Ordered Macroporous Monoliths Using Core-Shell Building Blocks. *Chem. Mater.*, **2000**, 12, (10), 2832-2834.
- 47) Stein, A.; Li, F.; Denny, N. R., Morphological Control in Colloidal Crystal Templating of Inverse Opals, Hierarchical Structures, and Shaped Particles. *Chem. Mater.*, **2007**, 20, (3), 649-666.
- 48) Zhang, Y.; Zha, S.; Liu, M., Dual-Scale Porous Electrodes for Solid Oxide Fuel Cells from Polymer Foams. *Adv. Mater.*, **2005**, 17, (4), 487-491.
- 49) Huerta, L.; Guillem, C.; Latorre, J.; Beltran, A.; Beltran, D.; Amoros, P., Large monolithic silica-based macrocellular foams with trimodal pore system. *Chem. Commun.*, **2003**, 0, (12), 1448-1449.
- 50) Caruso, R. A.; Antonietti, M., Sol-Gel Nanocoating: An Approach to the Preparation of Structured Materials. *Chem. Mater.*, **2001**, 13, (10), 3272-3282.

- 51) Breulmann, M.; Davis, S. A.; Mann, S.; Hentze, H. P.; Antonietti, M., Polymer–Gel Templating of Porous Inorganic Macro-Structures Using Nanoparticle Building Blocks. *Adv. Mater.*, **2000**, 12, (7), 502-507.
- 52) Caruso, R. A.; Giersig, M.; Willig, F.; Antonietti, M., Porous "Coral-like"• TiO₂ Structures Produced by Templating Polymer Gels. *Langmuir*, **1998**, 14, (22), 6333-6336.
- 53) Valtchev, V.; Smaïhi, M.; Faust, A.-C.; Vidal, L., Biomineral-Silica-Induced Zeolitization of Equisetum Arvense. *Angew. Chem., Int. Ed.* **2003**, 42, (24), 2782-2785.
- 54) Vlasov, Y. A.; Yao, N.; Norris, D. J., Synthesis of Photonic Crystals for Optical Wavelengths from Semiconductor Quantum Dots. *Adv. Mater.* **1999**, 11 (2), 165-169.
- 55) Deville, S.; Saiz, E.; Nalla, R. K.; Tomsia, A. P., Freezing as a Path to Build Complex Composites. *Science* **2006**, 311 (5760), 515-518
- 56) Deville, S., Ice-templating, freeze casting: Beyond materials processing. *J. Mater. Res.* **2013**, 28 (17), 2202-2219
- 57) Sharma, K. P.; Kumaraswamy, G.; Ly, I.; Mondain-Monval, O. Self-Assembly of Silica Particles in a Nonionic Surfactant Hexagonal Mesophase. *J. Phys. Chem. B* **2009**, 113, 3423-3430.
- 58) Sharma, K. P.; Ganai, A. K.; Gupta, S. S.; Kumaraswamy, G. Self-Standing Three-Dimensional Networks of Nanoparticles With Controllable Morphology by Dynamic Templating of Surfactant Hexagonal Domains. *Chem. Mater.* **2011**, 23, 1448-1455.
- 59) Ganai, A. K.; Kumari, S.; Sharma, K. P.; Panda, C.; Kumaraswamy, G.; Gupta, S. S. Synthesis of Functional Hybrid Silica Scaffolds with Controllable Hierarchical Porosity by Dynamic Templating. *Chem. Comm.* **2012**, 48, 5292-5294.
- 60) Kolb, H. C.; Finn, M. G.; Sharpless, K. B., Click Chemistry: Diverse Chemical Function from a Few Good Reactions. *Angew. Chem., Int. Ed.* **2001**, 40 (11), 2004-2021.
- 61) Buckley, B.R.; Dann, S.E.; Heaney, H. Experimental evidence for the involvement of dinuclear alkynylcopper(I) complexes in alkyne-azide chemistry. *Chem. Eur. J.*, **2010**, 16, 6278-6284.
- 62) Rostovtsev, V. V.; Green, L. G.; Fokin, V. V.; Sharpless, K. B., A Stepwise Huisgen Cycloaddition Process: Copper(I)-Catalyzed Regioselective "Ligation" of Azides and Terminal Alkynes. *Angew. Chem., Int. Ed.* **2002**, 41 (14), 2596-2599.

- 63) Lowe, A. B. Thiol-Ene “Click” Reactions and Recent Applications in Polymer and Materials Synthesis. *Polym. Chem.* **2010**, *1*, 17–36.
- 64) Li, G.-Z.; Randev, R. K.; Soeriyadi, A. H.; Rees, G.; Boyer, C.; Tong, Z.; Davis, T. P.; Becer, C. R.; Haddleton, D. M. Investigation into Thiol-(Meth)Acrylate Michael Addition Reactions Using Amine and Phosphine Catalysts. *Polym. Chem.* **2010**, *1*, 1196–1204
- 65) Hoyle, C. E.; Lee, T. Y.; Roper, T., Thiol-enes: Chemistry of the past with promise for the future. *Journal of Polymer Science Part A: Polymer Chemistry* **2004**, *42* (21), 5301-5338.
- 66) Morgan, C. R.; Magnotta, F.; Ketley, A. D., Thiol/ene photocurable polymers. *Journal of Polymer Science: Polymer Chemistry Edition* **1977**, *15* (3), 627-645.
- 67) Griesbaum, K., Problems and Possibilities of the Free-Radical Addition of Thiols to Unsaturated Compounds. *Angew. Chem., Int. Ed.* **1970**, *9* (4), 273-287
- 68) Yu, B.; Chan, J. W.; Hoyle, C. E.; Lowe, A. B., Sequential thiol-ene/thiol-ene and thiol-ene/thiol-yne reactions as a route to well-defined mono and bis end-functionalized poly(N-isopropylacrylamide). *Journal of Polymer Science Part A: Polymer Chemistry* **2009**, *47* (14), 3544-3557.
- 69) Chan, J. W.; Hoyle, C. E.; Lowe, A. B., Sequential Phosphine-Catalyzed, Nucleophilic Thiol-Ene/Radical-Mediated Thiol-Yne Reactions and the Facile Orthogonal Synthesis of Polyfunctional Materials. *J. Am. Chem. Soc.* **2009**, *131* (16), 5751-5753.

Chapter 2

Functionalized Mesoporous Hybrid Materials using “Thiol-Ene Click”



In this chapter, Methacrylate-labeled SBA-15 has been successfully synthesized from calcined SBA-15 and commercially available 3-trichlorosilyl propylmethacrylate. This hybrid material undergoes efficient thiol-ene “click reaction” with a variety of both thiol and disulfide-containing substrates in aqueous and organic media. Disulfide-containing substrates in which the TCEP-mediated reduction of the disulfide bond and its subsequent addition to the methacrylate group anchored in SBA-15 in one-pot were used to synthesize a silica-protein hybrid material composed of biotin-labeled SBA-15 and streptavidin.

This chapter is adapted from the following publication:

“Functionalization of SBA-15 Mesoporous Materials using “Thiol-Ene Click” Michael Addition Reaction” S. Kumari, B. Malvi, A. K. Ganai, V. K. Pillai, S. Sen Gupta, *The Journal of Physical Chemistry C*, **2011**, *115*, 17774-17781.

2.1 INTRODUCTION

Surface-functionalized mesoporous materials have found widespread applications in technologically important areas such as catalysis,¹⁻³ separation,^{4, 5} decontamination,⁶ drug delivery⁷ and sensor design.⁸ In particular, the development of mesoporous material based biocatalysts⁹ and biosensors⁸ has attracted much attention because of their high specific surface areas (up to 2 000 m²/g) and pore volumes (up to 1.5 cm³/g), which render them ideal hosts for biomolecules. Syntheses of such functional materials typically involve covalent immobilization of the enzymes into the pores of the mesoporous channels. This is necessary to achieve long-term stability of these materials because enzymes immobilized by simple physical adsorption tend to leach out, especially in certain types of solvents. Typically, enzymes have been covalently immobilized by chemically attaching them to an organo-functionalized mesoporous material bearing aldehyde or amine functional groups. For example, enzymes can be covalently attached by cross-linking the amine side-chain of the lysine to the amino propyl group of modified mesoporous materials via glutaraldehyde.¹⁰⁻¹² However, there are several limitations of this method including limited control of the spatial orientation of the immobilized enzyme within the pores. Hence, there is a strong need to generate functional mesoporous materials that can provide a platform to perform bio-orthogonal chemoselective ligation. Recently, we and others have reported the synthesis of a “clickable” azide-labeled SBA-15 mesoporous material that could be successfully functionalized with alkyne containing compounds in a chemoselective manner using the Cu(I)-catalyzed azide-alkyne cycloaddition reaction (CuAAC).¹³⁻¹⁵ This material has also been used to immobilize enzymes covalently.¹⁴ However, in reactions involving the CuAAC, the removal of residual amounts of ligand and copper still remains a challenge, which sometimes limits its scope for biological applications. Hence, development of “metal free” bio-orthogonal chemoselective reactions would be very important for immobilization of biomolecules.

Recently, the thiol-ene click reaction has attracted the attention of researchers worldwide and has been utilized in the synthesis of novel materials in various fields including polymer chemistry and nanotechnology.¹⁶ This reaction is chemoselective and also has several desirable attributes that are characteristic of a typical “click” reaction. For example, the reaction is tolerant to most functional groups present and proceeds very well in both aqueous and organic solvents, which is especially significant for a wide range of applications.

More significantly, thiol-ene addition reactions have been proposed to proceed via either the (i) anti-Markovnikov's radical addition¹⁷⁻¹⁹ or the (ii) base/nucleophile-catalyzed Michael addition reaction.^{20, 21} The addition of thiols to alkenes by free radical mechanism has been used extensively in polymer and materials synthesis.¹⁶ However, this methodology requires the addition of an external radical source such as azo or photoinitiators and UV light, which can be unfortunately detrimental for the covalent attachment of biomolecules. Nucleophile-mediated addition of a thiol to an activated C=C bond, described as the thiol-ene Michael-type reaction, has much wider applications because this can be carried out under both aqueous and non-aqueous media using mild reaction conditions.²²⁻²⁴ Such reactions are fairly tolerant to the presence of oxygen/moisture and proceed with near-quantitative formation of the thioether in a region-selective fashion. Furthermore, this reaction is chemoselective and also bio-orthogonal. We envisaged that if an activated C=C can be installed to the surface of a mesoporous silica, then biomolecules such as peptides and proteins having a surface thiol group can be easily attached using this chemistry. Although mesoporous materials have been surface functionalized with activated C=C groups such as propyl methacrylate group,^{25, 26} to the best of our knowledge, no thiol-ene “click” reaction has been reported on these materials. He and co-workers have grafted propyl methacrylate groups on SBA-15 following immobilization of porcine pancreatic lipase; then, the pendant propyl methacrylate groups were polymerized with 3-(trimethoxysilyl) propyl methacrylate to reduce the pore size of SBA-15.^{25, 26} Maleimides, another Michael acceptor with activated C=C bond, have been grafted on mesoporous materials, facilitating the immobilization of biomolecules. These are very reactive, and the reaction proceeds without any added organocatalyst. However, it should be noted that the very high reactivity of maleimide renders it reactive to amino groups of the side-chain lysine at neutral pH, and hence selectivity, an essential requirement to be termed as a “click reaction”, is lost. Furthermore, they are highly potent neurotoxins and should be treated or handled with extreme caution. Recently, vinyl sulphone grafted silica particles have been used for the immobilization of biomolecules.²⁷ However, this reaction is also not specific to thiol groups because the side-chain amino group of lysine was also observed to react.

This chapter reports the synthesis and characterization of an SBA-15 mesoporous material containing an activated ene (methacrylate) group demonstrating its reactions with a number of organic molecules bearing thiol or disulfide functionality using tris-2-carboxyethylphosphine (TCEP) or dimethyl phenyl phosphine (DMPP) as the catalyst.

Specifically, the reaction with the amino acids cysteine and cystine was thoroughly studied because they serve as good model compounds for peptides and proteins. These materials were characterized by using a variety of analytical techniques including FT-IR, SAXS, SEM, TEM, multinuclear (^{13}C , ^{29}Si) solid-state NMR, BET analysis, TGA, ICP, cyclic voltammetry (CV), and confocal microscopy.

2.2 EXPERIMENTAL DETAILS

2.2.1 Materials

Tetraethylorthosilicate (TEOS), poly (ethylene glycol)-block-poly(propyleneglycol)-block-poly(ethylene glycol) (Pluronic P-123, average molecular weight 5800), 3-trichlorosilylpropylmethacrylate (TCSPM), tris(2-carboxy)ethylphosphine (TCEP), dimethylphenyl phosphine (DMPPH), 2-mercaptoethanol, 2-mercaptopropionic acid, cysteine, cystine, 6-(ferrocenyl)hexanethiol, biotin, phycoerythrin-labeled streptavidin, were obtained from Sigma Aldrich. Organic solvents toluene, acetonitrile and acetone were obtained from Merck, India. All the chemicals used were of extra pure for biochemistry or of analytical grade and used as received. For all the experiments, deionized water was used.

2.2.2 Synthesis

2.2.2.1 Synthesis of SBA-15

SBA-15 material was synthesized by following the reported procedure by Zhao et al.²⁸ with slight modifications. Typically for a batch synthesis, 8 g of the nonionic block copolymer Pluronic P-123 was dissolved in 60 mL distilled deionized water using an overhead stirrer (with teflon blades) for 4 h. To this solution, 240 mL of HCl (2 N) was added drop wise and the reaction mixture was stirred for 1 hour at ambient temperature (~28-30 °C). The temperature of the reaction mixture was then raised to 40 °C and stirred for an additional hour. To this warm mixture, tetraethylorthosilicate (TEOS, 18 g, 86.4 mmol) was added drop wise with vigorous stirring and the reaction mixture was stirred for the next 24 h at 40 °C. The synthesized material was kept for aging at 100 °C. After 48 h of aging under static condition, the resulting white solid obtained was isolated by filtration, washing with copious

amount of water and dried in air. Calcined SBA-15 was obtained by calcination of as-synthesized solid material at 500 °C for 6 h in air. (Yield: ~ 4.7 g) This material can be used for further surface modification.

2.2.2.2 Synthesis of Methacrylate-Functionalized SBA-15

To a suspension of 1.0 g of calcined SBA-15 in 80 mL of dry toluene, 3-trichlorosilyl propylmethacrylate (abbreviated as TCSPM; 1.24 g, 4.7 mmol) in 10 mL of dry toluene was added drop wise, and the mixture was stirred for 1 h under inert atmosphere. After the completion of reaction, the contents were filtered and washed with a copious amount of toluene until it became free from unreacted TCSPM. The sample was then washed with deionized water, then dried at 70 °C for 12 h in a vacuum oven and preserved under an argon atmosphere for further use. Yield ~1.0 g. This material will be referred to as SBA-ACL.

2.2.2.3 Modification of Methacrylate Functionalized SBA-15 (SBA-ACL) by Thiol-Ene “Click” Reaction.

In Aqueous Medium: In a typical reaction, SBA-ACL (100 mg, 0.219 mmol) was added to a solution of cysteine (212 mg, 1.752 mmol) and TCEP (25 mg, 0.0876 mmol) in 5 mL of phosphate buffer (100 mM, pH 7) under nitrogen. The mixture was stirred at room temperature for 30 h. After completion of reaction, the mixture was centrifuged, and the residue was washed twice with phosphate buffer (100 mM, pH 7) and then three times with deionized water. The white powder obtained was dried at 80 °C in a vacuum oven for 12 h. Yield: 90 mg

In Organic Solvent: SBA-ACL (25 mg, 0.055 mmol of methacrylate) was incubated with 6-(ferrocenyl)hexanethiol (99 mg, 0.328 mmol) and dimethylphenylphosphine (DMPPH, 47 µL, 0.34 mmol) in dry toluene (5 mL) and stirred for 30 h at room temperature. After completion of reaction, the reaction mixture was centrifuged and the residue was washed with toluene five times until it became free from unreacted thiol. Finally, the dark-orange powder obtained was dried at 70 °C in vacuum oven for 12 h. Yield: 20 mg

2.2.2.4 Synthesis of Biotin NHS ester

The synthesis of Biotin NHS ester was carried out according to reported procedure.²⁹ To a solution of biotin (0.488 g, 2.0 mmol) in DMF (40 mL) was added triethylamine (1 mL, 10.0 mmol) followed by N, N'-disuccinimidyl carbonate (0.614 g, 2.40 mmol). The reaction mixture was stirred at room temperature for 6 h. Solvent was removed by rotary evaporation and the residue was triturated with diethyl ether and ethyl acetate. Filtration and washing with diethyl ether provided rather pure biotin-NHS (1.34 g, 98%) as a solid: m.p. 198–200

2.2.2.5 Synthesis of Biotin-Cystine (6)

To solution of L-Cystine (0.036 g, 0.15 mmol) in 0.1 M NaH₂PO₄ (10 mL) (pH of the solution was adjusted to 10.0 by adding 0.1 M NaOH) was added 15 mL (75 % methanol/water) solution of Biotin NHS (0.100 g, 0.3 mmol) and the resultant reaction mixture was stirred under nitrogen atmosphere at room temperature for 5 h. The reaction mixture was brought to pH 2.0 by adding 1 M HCl and kept for crystallization in the refrigerator for overnight. The resulting crystalline material was filtered and dried under a nitrogen atmosphere (for HR-MS mass see Appendix I, Figure A 4). Yield: 70 mg

2.2.2.6 Modification of SBA-ACL with Biotin-cystine (6) by Thiol-ene “Click” Reaction

To a solution of biotin-cystine (61 mg, 0.0876 mmol) and TCEP (28 mg, 0.0963 mmol) in 2 mL of 70% methanol/phosphate buffer (500 mM, pH 10) was added SBA-ACL (10 mg, 0.0215 mmol) under nitrogen. The mixture was stirred at room temperature for 30 h. After completion of reaction, the reaction mixture was centrifuged, and the residue was washed three times with 70% methanol/PBS buffer (500 mM, pH 11) and then two times with deionized water. Finally, the white powder obtained was dried at 70 °C in a vacuum oven for 12 h. Yield: 8 mg

2.2.2.7 Labeling of SBA-SR-6 with Phycoerythrin-Labeled Streptavidin

We incubated 10 mg of biotin-labeled SBA-15 (SBA-SR-6) or methacrylate-labeled SBA-15 (SBA-ACL) with phycoerythrin-labeled streptavidin (10 μL, 1 mg/mL) in 600 μL of phosphate buffer (500 mM, pH 7.5). After incubation for 30 min, both samples were washed

extensively (5 times) with the buffer. The samples were then dispersed in buffer and analyzed using a laser scanning confocal microscope (LSCM, band pass 543 nm).

2.3 ANALYTICAL AND CHARACTERISATION METHODS

Small-angle X-ray scattering (SAXS) experiments were carried out using Bruker Nanostar equipped with rotating anode and 2D wire detector used over a q range of 0.01 to 0.20 \AA^{-1} . SEM images were obtained on a Leica Stereo scan 440 microscope. HR-TEM images were taken on a FEI Technai F30 operating at 300 kV with FEG. We prepared the samples by dispersing a large number of solid particles in isopropanol by sonication and dropping the resulting suspension (10 μL) on a copper grid of 200 mesh and allowing it to dry in air. Nitrogen adsorption and desorption studies were carried out using a Micromeritics instrument. Samples were preheated to 100 $^{\circ}\text{C}$ for 12 h in the vacuum line. Multipoint BET surface area was obtained from the nitrogen adsorption-desorption data between $P/P_0 = 0.1$ to 0.3. Pore size distributions were calculated using the BJH method. Qualitative FT-IR spectra were recorded on a Perkin-Elmer spectrometer in the diffuse reflectance mode operating at a resolution of 4 cm^{-1} .

^{29}Si and ^{13}C cross-polarization magic-angle spinning (CP-MAS) NMR experiments were carried out on a Bruker AVANCE300 wide bore spectrometer equipped with a superconducting magnet with a field of 7.1 tesla. The operating frequencies for ^{13}C and ^{29}Si were 300, 75.4, and 59.6 MHz, respectively. The samples were packed into a 4 mm zirconia rotor and loaded into a 4 mm BLMAS probe and spun about the magic angle (54.74) at 10 kHz using a standard ramp-CP pulse sequence for both the experiments. The RF powers were 50 and 60 kHz for the ^{29}Si and ^{13}C CPMAS experiments. The contact times were 6 and 3ms for the ^{29}Si and the ^{13}C CPMAS experiments, respectively. All chemical shifts were referenced to TMS. Typically, 10 000–25 000 scans with a recycle delay of 3s were collected depending on the sensitivity of the sample.

Thermogravimetric analysis (TGA) of the silica nanoparticles was carried out using a TA Instrument SDT Q600 analyzer between 30 to 80 $^{\circ}\text{C}$ in air (flow 50 mL min^{-1}) at a heating rate of 5 $^{\circ}\text{C min}^{-1}$. All samples were dried under vacuum at 80 $^{\circ}\text{C}$ overnight prior to TGA runs. The graft density of the grafted moiety on the silica surface was determined by TGA using the following equation as described below.

graft density (mmol/g) =

$$\frac{W_{\text{grafted-SBA15(150-700)}}}{100 - W_{\text{grafted-SBA15(150-700)}}} \times 100 - W_{\text{SBA15(150-700)}}}{M \times 100} \times 10^3$$

Where $W_{\text{grafted-SBA-15(150-700)}}$ is the weight loss between 150 and 700 °C corresponding to the decomposition of the grafted SBA-15 material corrected from the thermal degradation and M is the molecular weight of the grafted silane, whereas $W_{\text{SBA-15(150-700)}}$ represents the determined weight loss of silica before grafting. For grafting of propyl methacrylate group (SBA-ACL), molecular weight of 127 g/mol was considered to determine the graft density. LSM 710 Carl Zeiss LSCM was used to image the fluorescent samples. A He-Ne laser (543 nm) and Argon-ion laser (458 nm) were used for the experiments.

Electrochemical properties were investigated by CV using an Autolab PGSTAT30 (Eco-Chemie) instrument in a conventional three-electrode test cell with glassy carbon as the working electrode (WE), platinum wire as quasi reference electrode (RE), and a platinum foil as a counter electrode (CE). The samples were dispersed in toluene and coated on the tip of a glassy carbon WE. The measurements were carried out in acetonitrile with 0.1 N tetrabutylammonium perchlorate as the supporting electrolyte at a scan rate of 200 mV/s.

ICP experiments were performed on a Thermo IRIS Intrepid spectrum apparatus. The typical procedure used was drying of 5 mg of sample in vacuum overnight, followed by dissolving in 1 mL of 5% KOH for refluxing. This was subsequently acidified with nitric acid and then filtered to make the volume up to 10 mL using Millipore water for the quantitative analysis of Fe using the ICP instrument.

2.4 RESULTS AND DISCUSSION

2.4.1 Synthesis of Methacrylate Functionalized SBA-15

The synthesis of methacrylate-functionalized SBA-15 from calcined SBA-15 material¹⁵ by the postsynthetic grafting method is presented in the Figure 2.1. In short, calcined SBA-15 (CAL-SBA-15) on reaction with TCSPM in dry toluene at room temperature under an inert atmosphere afforded SBA-ACL. However, it was observed that a trace amount of moisture was required for high grafting of the methacrylate moiety. Trace

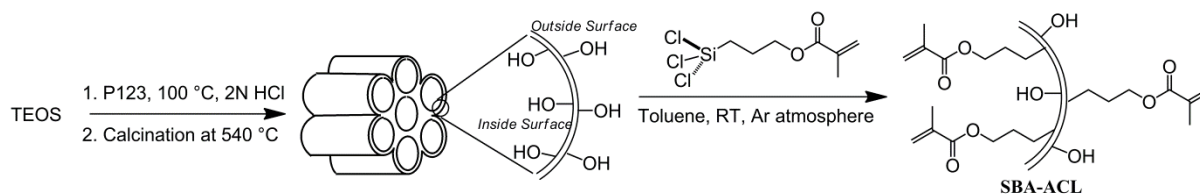


Figure 2.1 Synthesis of methacrylate-functionalized SBA-15 materials

amounts of moisture were critical because toluene dried under rigorous conditions and used in the glove box yielded a very low loading (~ 0.3 mmol/g) of the methacrylate group. The amount of methacrylate group incorporated in the SBA-15 framework, determined by TGA (Figure 2.6), shows the concentration of methacrylate to be 2.19 mmol/g for SBA-ACL. The high loading is probably indicative of a multilayer grafting of the methacrylate moiety. The presence of a trace amount of moisture in toluene probably led to the precondensation of the organotrichlorosilanes in solution, leading to high grafting of methacrylate moiety onto SBA-15. The structure and morphology of SBA-ACL was established unambiguously using SAXS, SEM, TEM, NMR, and N_2 adsorption-desorption isotherms, as discussed in section 2.5.

2.4.2 Thiol-Ene Click Reaction of SBA-ACL with various Thiol-Containing Substrates

The methacrylate functionalized SBA-15 (SBA-ACL) was subjected to phosphine-mediated thiol-ene Michael addition with various organic substrates having either free thiol or disulfide bond (Figure 2.2). Cysteine (**1**) was used as the substrate to optimize the reaction conditions. For example, treatment of SBA-ACL (0.219 mmol of methacrylate) with 8 equiv of cysteine (1.75 mmol) using a catalytic amount of TCEP (0.087 mmol) in pH 7 phosphate buffer for 30 h converted 47 % of the alkene groups into the corresponding thioether SBA-SR-1 (Table 2.1, Figure 2.6). The progress of the reaction was monitored by using DRIFT-IR, where carbonyl stretching vibrations of methacrylate moiety shift from 1700 to 1720 cm^{-1} (Figure 2.8). The amount of TCEP used in this reaction was very carefully optimized because use of excess TCEP (more than 2 equiv with respect to methacrylate) also leads to an addition product with a methacrylate $C=C$ bond. A similar observation was recently reported by Haddleton et al.²⁴ for the functionalization of polymers using thiol-ene reaction. Control reactions for SBA-ACL performed in the absence of either TCEP or cysteine showed no

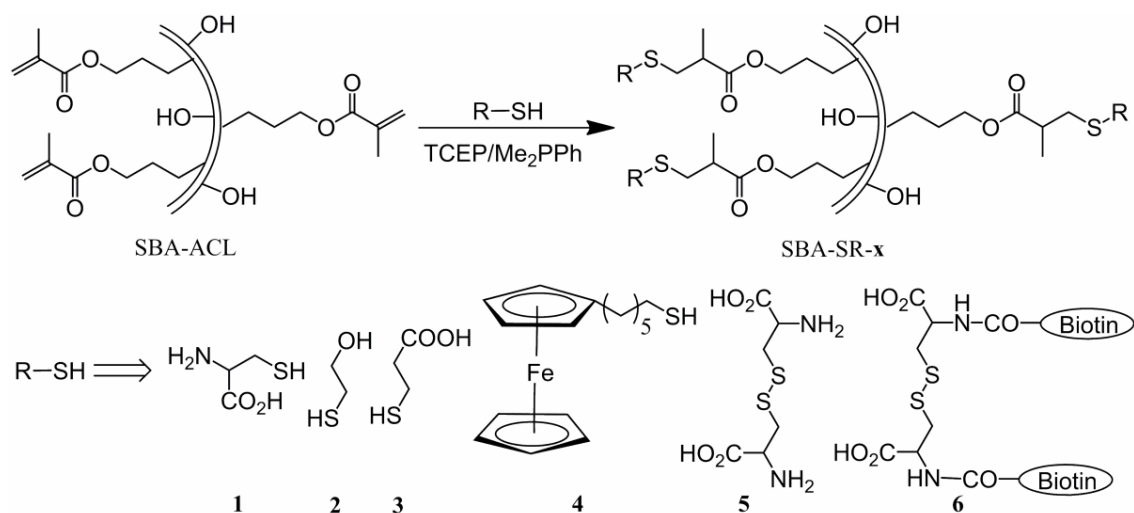


Figure 2.2 Thiol-ene click reaction of methacrylate functionalized SBA-15 with various thiols

change in the IR spectra. To verify that the shift in the IR was due to the attack of the thiol in the cysteine and not the amine present, we performed another control reaction using serine as the substrate in the presence of TCEP. Serine was chosen because it is structurally very similar to cysteine with the only difference that it has a hydroxyl group in its side chain instead of a thiol group. Reaction with serine as a substrate shows no shift in peak for carbonyl stretch, indicating that the presence of amine groups does not interfere with the addition of thiols to the methacrylate C=C bond in SBA-ACL. It is also well known that thiols are ~280 times more reactive than amines for the Michael addition reaction,³² so chances of addition of amine to C=C bond are much less. The addition product SBA-SR-1, formed upon reaction of SBA-ACL and RSH (**1**), was further characterized by SAXS, nitrogen adsorption-desorption, ¹³C NMR, and ²⁹Si NMR as discussed in section 2.5.

The thiol-Michael addition was then extended to other substrates to explore the efficiency of this reaction on methacrylate-functionalized SBA-15. The reaction was carried out with 2-mercaptoethanol (**2**) and 2-mercaptopropionic acid (**3**) in PBS buffer. For both the substrates, shifts in the carbonyl stretching vibrations of methacrylate moiety from 1700 to 1720 cm⁻¹ are observed in IR spectra after thiol-Michael addition. The ¹³C CP-MAS NMR spectra, SAXS, and nitrogen adsorption-desorption data of the resultant material SBA-SR-2 and SBA-SR-3 are also consistent with the observation described above (Figure 2.4, Figure

Table 2.1 Summary of thiol-ene reaction with different thiol substrates

Mesoporous Material	Thiol substrate	Product (SBA-SR-x)	Graft density (mmol/g)	Reaction yield (%)
SBA-ACL	Cysteine (1)	SBA-SR-1	1.02	47 [#]
	2-Mercaptoethanol (2)	SBA-SR-2	1.2	55 [#]
	2-Mercaptopropionic acid (3)	SBA-SR-3	0.98	45 [#]
	6-(Ferrocenyl)hexanethiol (4)	SBA-SR-4	1.1	50 [*]
	Cystine (5)	SBA-SR-5	1.36	62 [#]

[#]Determined by TG-DTA from temperature 150-700 °C ^{*}Determined from ICP analysis

2.8, see Appendix I, Figure A 1- A 3). The extent of the reaction was determined by TGA analysis to be 55% and 45%, respectively (Table 2.1, Figure 2.6).

To elucidate the broad substrate scope for this reaction, we then evaluated the efficiency of the thiol-Michael addition in organic solvents using nonpolar thiols as substrate. For this purpose, we selected 6-(ferrocenyl)hexanethiol (4) as substrate to carry out thiol-Michael addition reaction on methacrylate-functionalized SBA-15 in the nonpolar solvent toluene. This substrate was chosen so that the extent of the reaction can be followed by ICP. Treatment of SBA-ACL (0.0537 mmol of methacrylate) with 6 equiv of 4 using DMPPh (6.2 equiv) as catalyst in dry toluene for 30 h showed the shift of carbonyl stretching vibrations of the starting SBA-ACL from 1700 to 1720 cm⁻¹. No change in the IR spectra was observed for control reactions performed in the absence of either DMPPh or 4. ICP analysis indicates that 35% of the starting alkene in SBA-ACL converted to the corresponding ferrocene containing thioether SBA-SR-4. This was in agreement with the TG-DTA analysis, which indicated that 40% of the alkene in SBA-ACL was converted to the ferrocene thioether (Table 2.1, Figure 2.6). Because ferrocene is electrochemically active, we subjected the ferrocene SBA-15 conjugate SBA-SR-4 to CV in CH₃CN with [n-Bu₄N]ClO₄ as the supporting electrolyte. The

CV of this material displays electrochemical signals with a formal redox potential, $E_{1/2}$, of 0.28 V versus a Pt RE (Figure 2.10). We were therefore able to generate electroactive materials using this thiol-ene reaction.

We then extended this methodology to include compounds containing disulfide bond as the substrate. Phosphines are known to reduce disulfides to their corresponding thiols in a 1:1 ratio, forming the phosphine oxide as the byproduct. Therefore, we envisaged that disulfides can be conjugated by this methodology in which the added phosphine would first reduce the disulfide to the corresponding thiol and then would catalyze the addition of thiol to C=C group of the SBA-ACL in one-pot. To test this hypothesis, we chose cystine, which has a disulfide bond, as the substrate, and its reaction with the methacrylate C=C bond was studied. Because 1 equiv of phosphine was required to reduce the cystine, the reaction was carried out using 1.4 fold excess of TCEP with respect to cystine in pH 10 phosphate buffer for 30 h. This allowed the TCEP to first reduce the disulfide bond into the free thiol and subsequently catalyze the thiol-Michael addition reaction with SBA-ACL to yield the corresponding thioether SBA-SR-5 in one-pot. Similar reaction involving the use of phosphines for the reduction of disulfide linkage into free thiol and then subsequent use in thiol-ene click reaction under homogeneous conditions for polymer synthesis has been previously reported.²² TGA analysis of the product SBA-SR-5 formed showed that 62% of the methacrylate in SBA-ACL is converted to the corresponding thioether (Table 2.1, Figure 2.6). The shift of carbonyl stretching vibrations of the starting SBA-ACL from 1700 to 1720 cm^{-1} was also observed (Figure 2.8).

To prove further the successful attachment of cystine by this one-pot methodology, a biotin-tagged cystine (**6**) was used as the substrate. The product formed after reaction of **6** with SBA-ACL in the presence of TCEP, SBA-SR-6, was then treated with phycoerythrin-labeled streptavidin, a protein specifically known to bind to streptavidin. Commercially available phycoerythrin-labeled streptavidin was incubated with both SBA-SR-6 and SBA-ACL in pH 7.5 phosphate buffer. After incubation for 30 min, both samples were extensively washed with phosphate buffer. The samples were dispersed in the buffer and were then imaged in a confocal microscope using a He-Ne laser (543 nm). Intense fluorescence was observed from the SBA-SR-6 incubated with phycoerythrin-streptavidin, whereas the control sample in which SBA-ACL was used as the scaffold displayed no appreciable fluorescence (Figure 2.11). The fluorescently labeled streptavidin will most likely bind to the biotin on the exterior surface of SBA-SR-5 because it is too large to get inside the channels. The observance of intense fluorescence indicates that cystine-biotin conjugate (**6**) was

successfully conjugated to SBA-ACL to form SBA-SR-6 via this one pot reaction in which the disulfide reduction of cystine-biotin was followed by the thiol-ene Michael addition reaction. This specificity of streptavidin for biotin-labeled SBA-15 can be used in the development of sensors, as has been previously shown.⁸

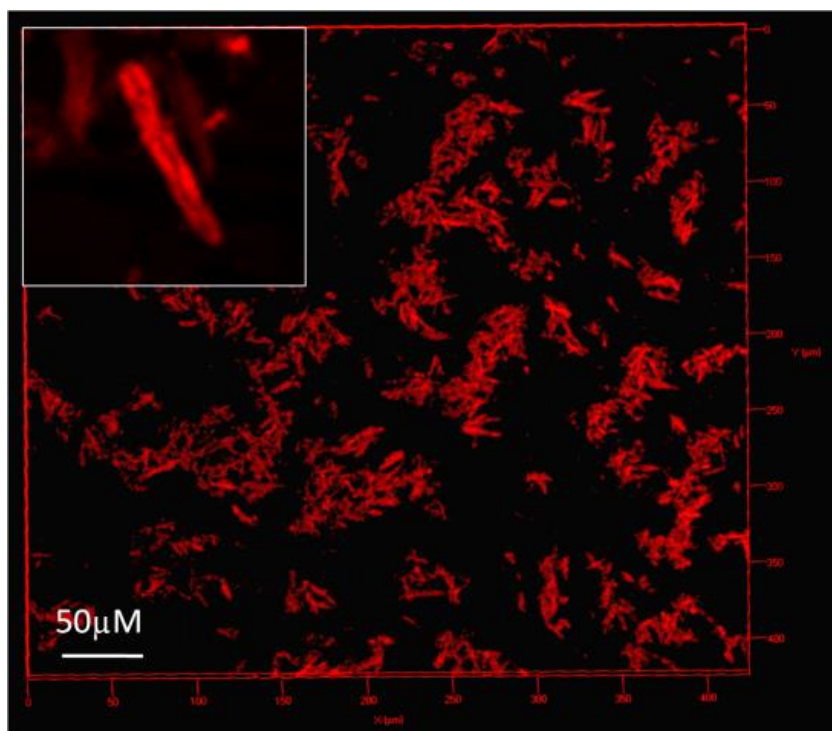


Figure 2.3 Confocal image of SBA-SR-6 with labeled phycoerythrin streptavidin

2.5 CHARACTERISATIONS

2.5.1 Small Angle X-ray Scattering (SAXS)

Small angle X-ray scattering (SAXS) patterns of the mesoporous material were shown in the Figure 4.1. Small angle X-ray scattering (SAXS) patterns of calcined SBA-15 and methacrylate-grafted SBA-15 (SBA-ACL) display their characteristic high intensity 100 peak near the 2θ value of 1° (Figure 2.3). The other significant peaks corresponding to 110 and 200 diffractions are also observed, indicating that well-ordered 1-D hexagonal mesoporous channels of SBA-15 are formed and remained intact under the functionalization environment.

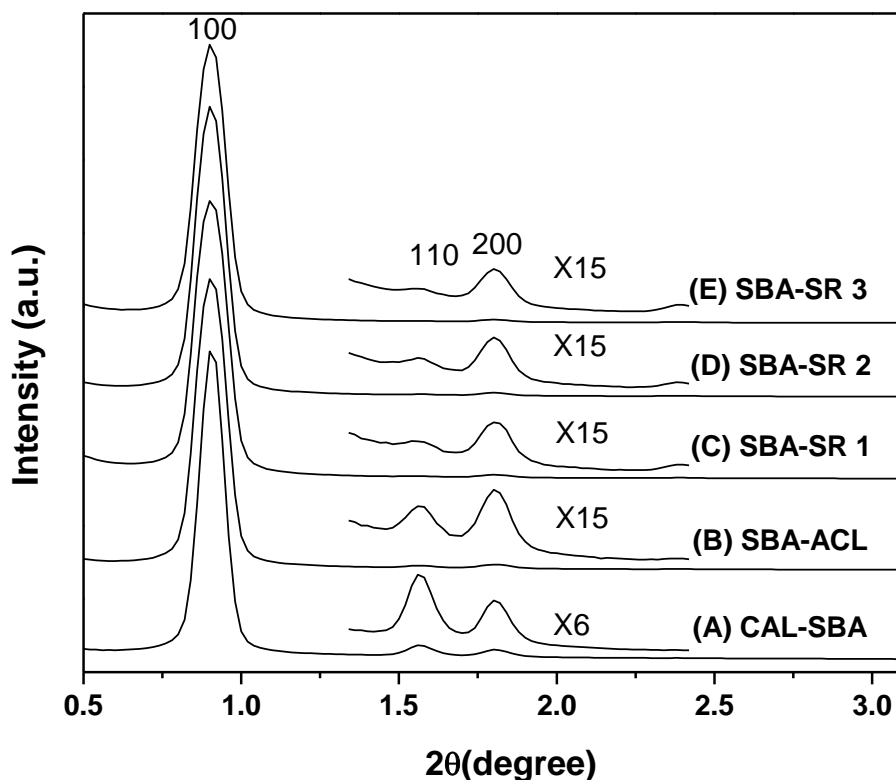


Figure 2.4 SAXS patterns of different SBA-15 samples via post-synthesis grafting [A] CAL-SBA; [B] SBA-ACL; [C] SBA-SR-1; [D] SBA-SR-2; [E] SBA-SR-3

To characterize the click product by SAXS, SBA-ACL clicked with different thiols to obtain SBA-SR and was used to obtain SAXS patterns. The SAXS showed one intense (100) diffraction peak in the proximity of $2\theta=1^\circ$, indicating well-ordered hexagonal arrays and showing that the mesoporosity of the material does not change after undergoing thiol-Michael addition reaction (Figure 2.4).

2.5.2 Scanning and Transmission Electron Microscopy

The SEM images displayed wormlike external morphology whereas the TEM micrographs show the hexagonal pore arrangement with thick walls of the calcined SBA-15 (CAL-SBA) mesoporous material (Figure 2.5).

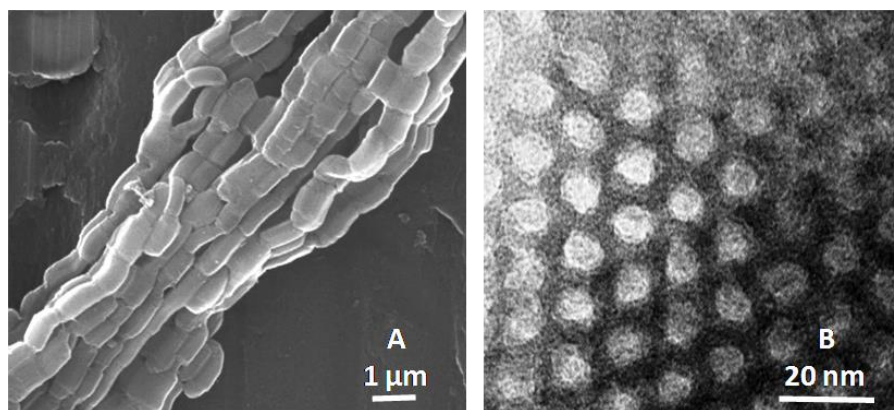


Figure 2.5 (A) SEM images and (B) TEM micrographs respectively of SBA-ACL material.

2.5.3 Thermo Gravimetric Analysis

The TGA graphs of SBA-ACL and the product SBA-SR-x after thiol-ene click reaction are presented in the Figure. 2.6. Samples were heated in air at 5 °C/min to 800 °C so that the organic contents were completely decomposed and removed from the samples.

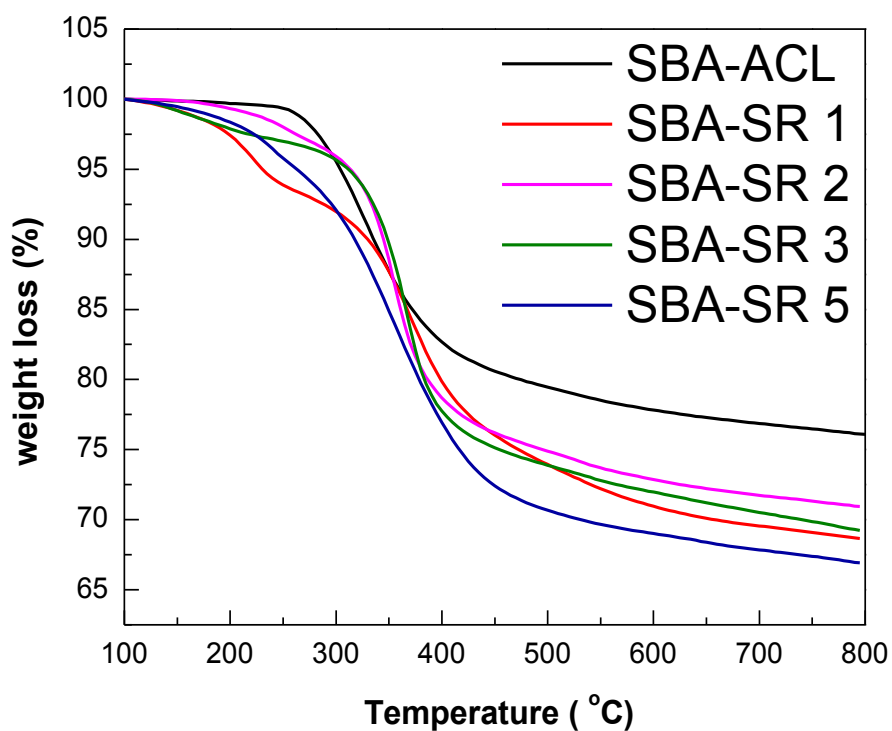


Figure 2.6 TGA graphs of various modified SBA-15 materials

2.5.4 Nitrogen Adsorption-Desorption Studies

The nitrogen adsorption-desorption isotherms for calcined and methacrylate-functionalized SBA-15 materials exhibit a characteristic type IV isotherm with a steep increase in adsorption at $P/P_0 = 0.55$ to 0.75 due to capillary condensation of the nitrogen in the mesopores (Figure 2.7). The BJH pore-size distribution (PSD) analysis for the calcined SBA-15 displays very narrow PSD values in the range of 8 to 9 nm. The methacrylate-grafted SBA-15 material (SBA-ACL) was found to have a narrow PSD value in the range of 6 to 7 nm, and the BET surface area was found to be $265 \text{ m}^2/\text{g}$ (Table 2.2).^{28, 29} The 2 nm decrease in pore diameter is probably due to multilayer grafting of the methacrylate moiety and is also consistent with the high loading obtained from TGA.

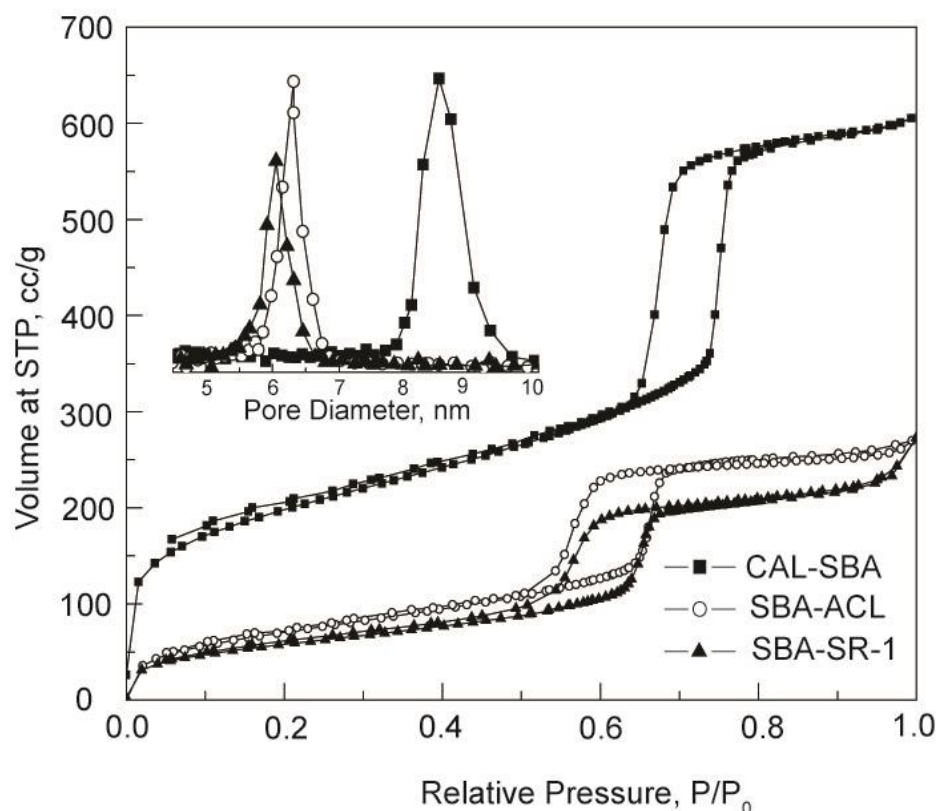


Figure 2.7 Nitrogen adsorption-desorption isotherms for various SBA-15 materials and pore size distribution of these various materials (inset).

N_2 adsorption-desorption isotherm of the clicked product exhibits a characteristic type IV isotherm with a steep increase in adsorption at $P/P_0 = 0.55$ to 0.75 due to capillary

condensation of the nitrogen in the mesopores. The isotherm appears similar to its parent methacrylate grafted SBA-15 material, which indicates that the material did not undergo any physical change during the course of the reaction and its subsequent workup. The pore diameter, BET surface, and the pore volume decreased due to the addition of cysteine to methacrylate C=C bond (Table 2.2).

Table 2.2: Properties of various SBA-15 materials

Sample Name	M_{BET} (m^2/g)	Pore Diameter (nm)	Pore Volume (cm^3/g)
CAL-SBA	685	8.50	0.94
SBA-ACL	265	6.3	0.42
SBA-SR-1	214	6.1	0.41
SBA-SR-2	211	6.1	0.41
SBA-SR-3	244	6.2	0.40

2.5.5 FT-IR spectroscopy

The FT-IR spectra of SBA-ACL display an absorbance at 1700 cm^{-1} , corresponding to a carbonyl group in conjugation with a C=C group (Figure 2.8). The absence of this peak in CAL-SBA shows that the methacrylate group has been successfully incorporated into the SBA-ACL sample.

The FT-IR spectra of SBA-ACL after thiol-ene click reaction displays an absorbance at 1720 cm^{-1} . For all the substrates, shifts in the carbonyl stretching vibrations of methacrylate moiety from 1700 to 1720 cm^{-1} are observed in IR spectra after thiol Michael addition (Figure 2.8). This is expected because the thiol addition onto the double bond will reduce its conjugation to the adjacent carbonyl group.

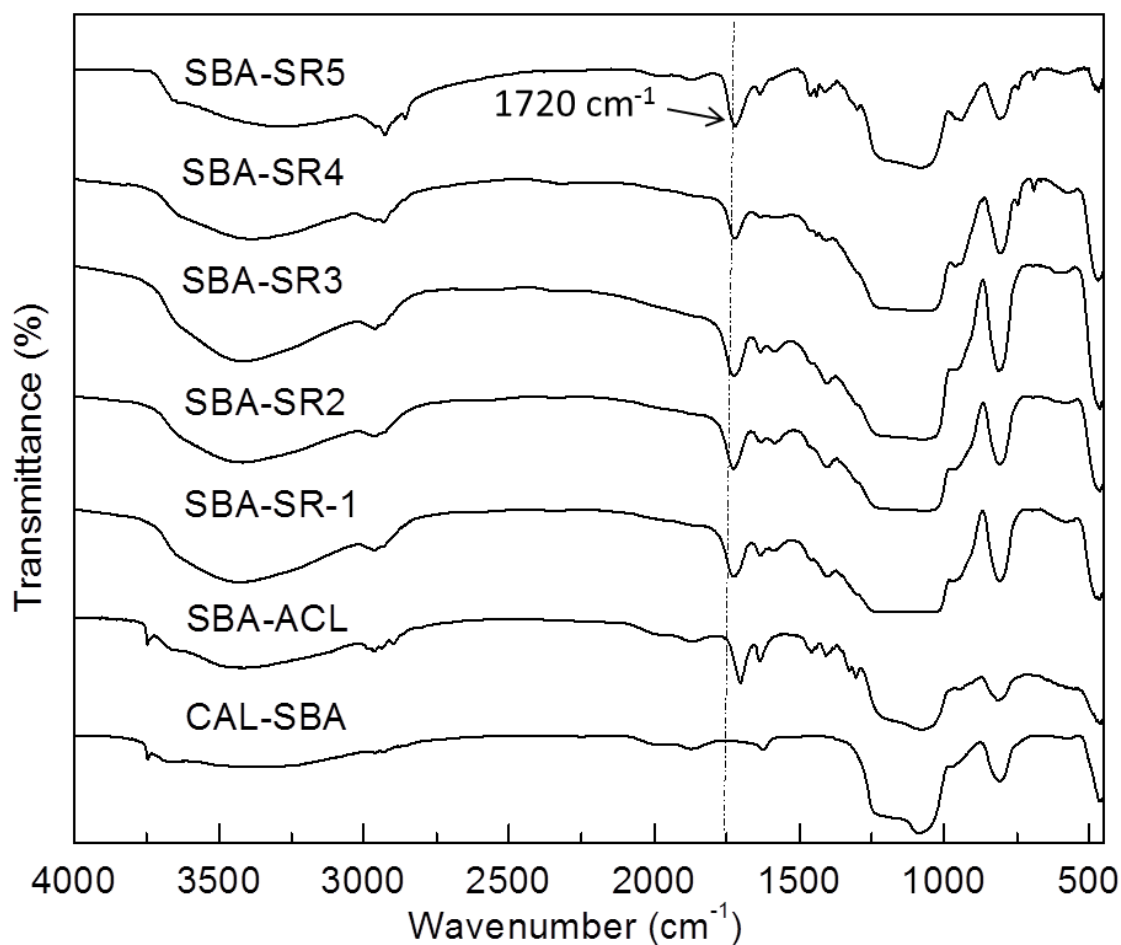


Figure 2.8 Comparative FT-IR spectra of the different SBA-15 materials

2.5.6 Solid State CP-MAS NMR Spectroscopy

2.5.6.1 ^{13}C CP-MAS NMR Spectroscopy

The solid-state ^{13}C CP-MAS NMR spectra of SBA-ACL (Figure 2.8) display peaks at C1 (8 ppm), C2 (22 ppm), C3 (66 ppm), C4 (169 ppm), C5 (136 ppm), C6 (16 ppm), and C7 (124 ppm). These peaks represent the seven C atoms of the propylmethacrylate moiety, as shown in (Figure 2.9b).

The ^{13}C NMR shows extra peaks at 35, 54, and 176 ppm that correspond to the C8, C9 and C10 atoms of the cysteine moiety (Figure 2.9a). The sp^2 hybridized carbon atoms C5 and C7 in methacrylate, which appear at 136 and 124 ppm, respectively, become sp^3 hybridized after thiol-Michael addition and now appear at 44 and 35 ppm, respectively.

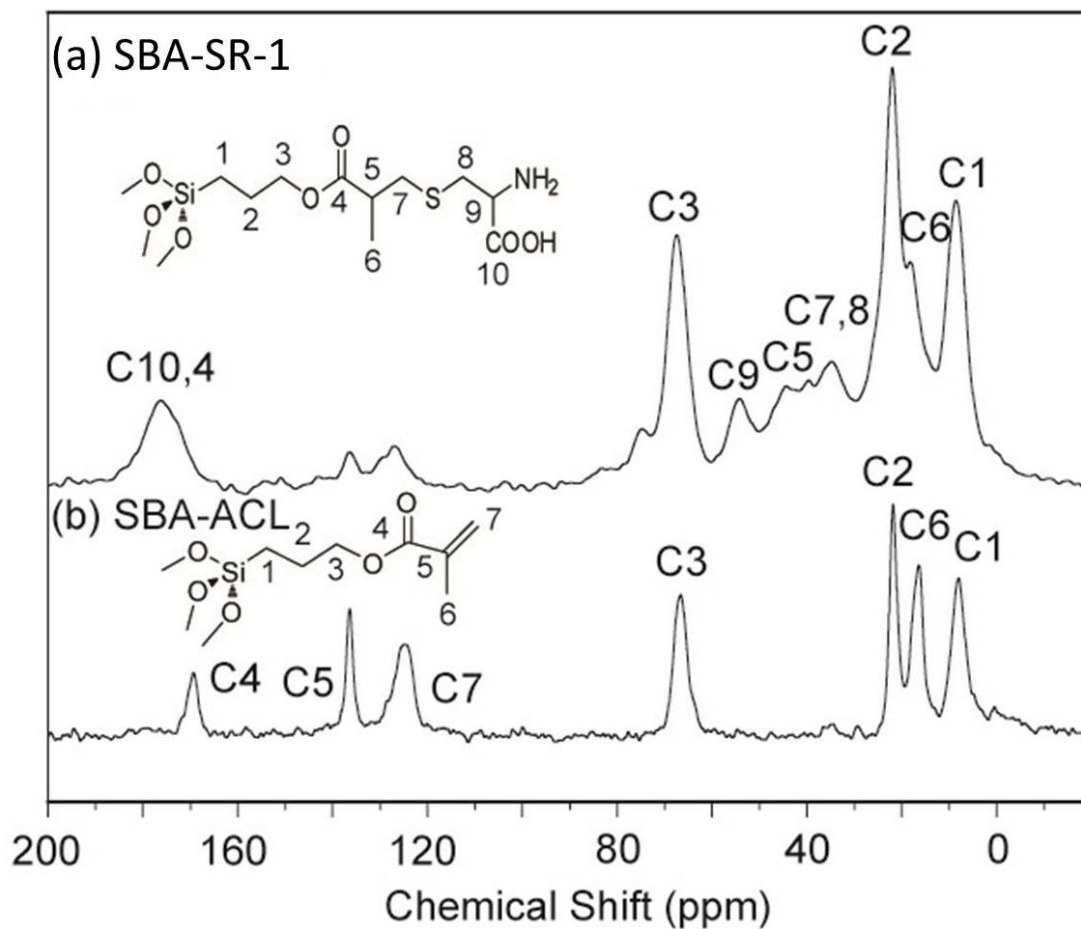


Figure 2.9 ^{13}C CP MAS NMR spectra of the different functionalized SBA-15 materials.

Because peaks corresponding to C5 and C7 olefinic carbon atoms do not completely disappear in the spectrum, it indicates that thiol-Michael addition reaction is not complete. This is consistent with the TG-DTA data, where the reaction yield was estimated to be ~47%.

2.5.6.2 ^{29}Si CP-MAS NMR Spectroscopy

The ^{29}Si CP-MAS NMR spectrum of the methacrylate functionalized SBA-15 material displays prominent peaks at around 91, 101, and 110 ppm, respectively. These are assigned to the different types of the Si-sites, namely, $\text{Q}^2[(\text{SiO})_2\text{Si}(\text{OH})_2]$, $\text{Q}^3[(\text{SiO})_3\text{Si}(\text{OH})]$,

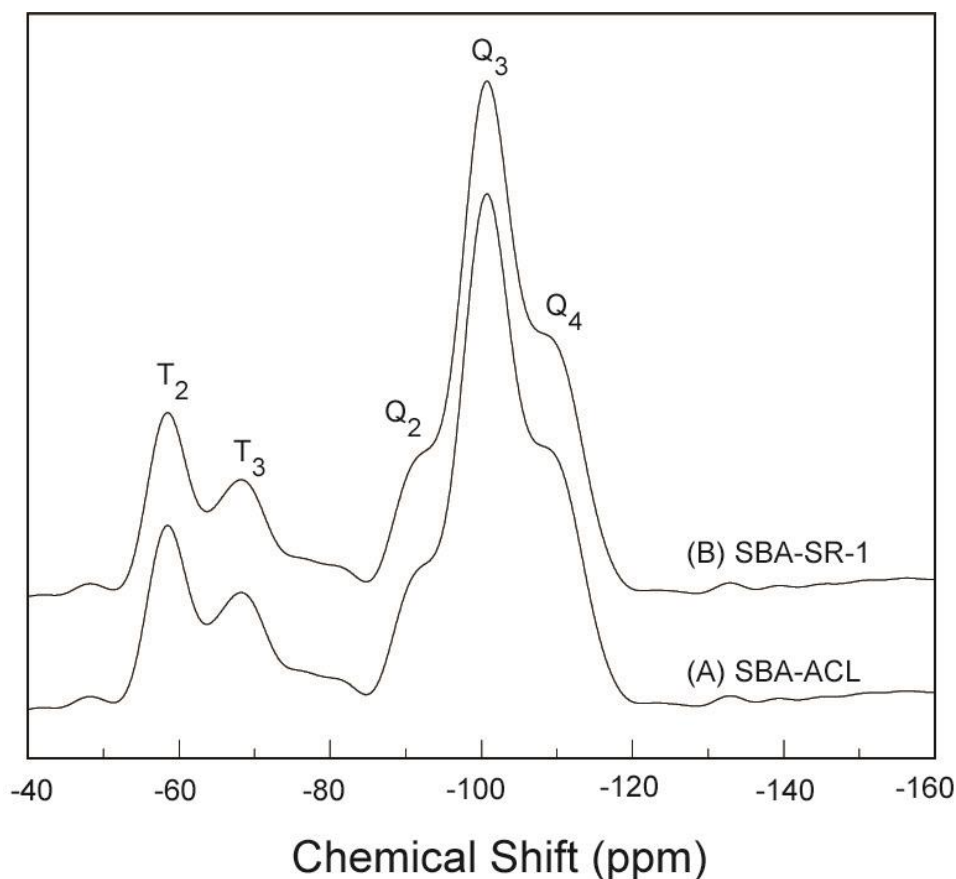


Figure 2.10 ^{29}Si CP-MAS NMR spectra of the different functionalized SBA-15 materials

and $\text{Q}^4[(\text{SiO})_4\text{Si}]$ (Figure 2.10A). Two other distinct peaks that are observed at 58 and 68 ppm are attributed to the functionalized sites of the Si framework, namely, $\text{T}^2[\text{R}(\text{SiO})_2\text{Si}(\text{OH})]$ and $\text{T}^3[\text{R}(\text{SiO})_3\text{Si}]$, respectively, where R is the propylmethacrylate group. The presence of these above mentioned peaks in the ^{13}C and ^{29}Si CP-MAS spectrum unequivocally confirms grafting of propylmethacrylate moiety and is consistent with the N_2 adsorption and FT-IR data as discussed above.

The ^{29}Si CP-MAS spectrum of the SBA-SR-1 material shows little or no change from the starting SBA-ACL, indicating that the Si-sites do not undergo any chemical change during the reaction and its workup (Figure 2.10B). This is expected because the T^2 and T^3 Si-sites are that from the methacrylate-modified silica and should not undergo any change during the course of the reaction.

2.5.7 Cyclic Voltammetry

The CV of this material displays electrochemical signals with a formal redox potential, $E_{1/2}$, of 0.28 V versus a Pt RE (Figure 2.11). The broadness of the peak can be attributed to the insulating nature of the silica framework (causing high ohmic drop) on which the ferrocene moiety is attached. The E_{pa} , E_{pc} , and $E_{1/2}$ values were estimated from the derivative spectra, as has been shown below (inset of Figure 2.11). The CV of the starting methacrylate-labeled SBA-15 (SBA-ACL) displays no discernible electrochemical signal.

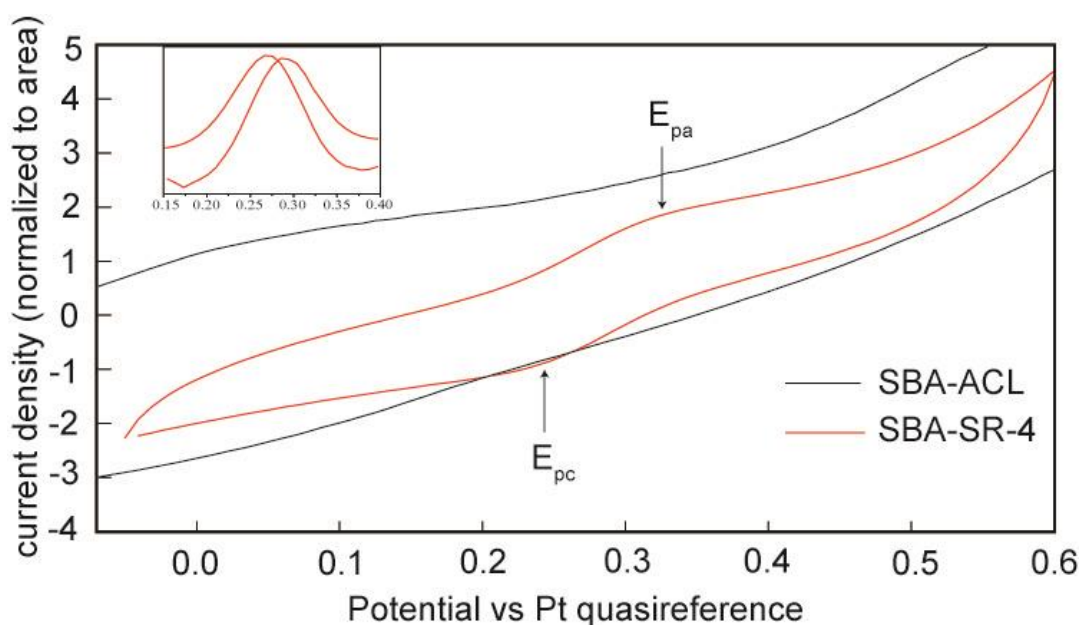


Figure 2.11 Cyclic voltammogram of ferrocene labeled SBA-15 (SBA-SR-4) and methacrylate labeled SBA-15 (SBA-ACL). The derivative spectrum of SBA-SR-4 is shown in the inset.

2.6 CONCLUSIONS

Methacrylate-labeled SBA-15 has been successfully synthesized from calcined SBA-15 and commercially available TCSPM. This material undergoes efficient “thiol-ene click” reaction with a variety of thiol-containing substrates in both aqueous and organic media. The products formed were thoroughly characterized by a variety of analytical techniques such as ^{13}C CP-MAS NMR, SAXS, FT-IR, TG-DTA and nitrogen adsorption desorption studies. A highlight of the reaction was the use of disulfide-containing substrates (cystine) in which the

disulphide bond was reduced to the corresponding thiol and subsequently added to the methacrylate group in one-pot, using TCEP as the catalyst/reducing agent. This strategy was used to synthesize a silica protein hybrid material composed of biotin-labeled SBA-15 and streptavidin. Such hybrid materials may be important in the development of biosensors. Furthermore, electrochemically active material was synthesized from the reaction of ferrocene-containing thiol and the methacrylate-labeled SBA-15. The ease of synthesis for the methacrylate-labeled SBA-15 material together with its ability to undergo efficient chemoselective thiol-ene reaction would make it a very attractive platform for the development of covalently anchored enzymes and sensors. This methodology can also be easily extended to the synthesis of other functional inorganic materials.

2.7 REFERENCES

- 1) Kesanli, B.; Lin, W. Mesoporous Silica Anchored Ru Catalysts for Highly Enantioselective Hydrogenation of β -Ketoesters. *Chem. Commun.* **2004**, *20*, 2284-2285.
- 2) Terry, T. J.; Dubois, G.; Murphy, A.; Stack, T. D. P. Site Isolation and Epoxidation Reactivity of a Templated Ferrous Bis(phenanthroline) Site in Porous Silica. *Angew. Chem. Int. Ed.* **2007**, *46*, 945-947.
- 3) Nozaki, C.; Lugmair, C. G.; Bell, A. T.; Tilley, T. D. Synthesis, Characterization, and Catalytic Performance of Single-Site Iron (III) Centers on the Surface of SBA-15 Silica. *J. Am. Chem. Soc.* **2002**, *124*, 13194-13203.
- 4) Lakhiari, H.; Legendre, E.; Muller, D.; Jozefonvicz, J. High-Performance Affinity Chromatography of Insulin on Coated Silica Grafted with Sialic Acid. *J. Chromatogr., B: Biomed. Sci. Appl.* **1995**, *664*, 163-173.
- 5) Schiel, J. E.; Mallik, R.; Soman, S.; Joseph, K. S.; Hage, D. S. Applications of Silica Supports in Affinity. *Chromatography. J. Sep. Sci.* **2006**, *29*, 719-737.
- 6) Li, J.; Qi, T.; Wang, L.; Liu, C.; Zhang, Y. Synthesis and Characterization of Imidazole-Functionalized SBA-15 as an Adsorbent of Hexavalent Chromium. *Mater. Lett.* **2007**, *61*, 3197-3200.
- 7) Lai, C.-Y.; Trewyn, B. G.; Jeftinija, D. M.; Jeftinija, K.; Xu, S.; Jeftinija, S.; Lin, V. S. Y. A Mesoporous Silica Nanosphere-Based Carrier System with Chemically

- Removable CdS Nanoparticle Caps for Stimuli-Responsive Controlled Release of Neurotransmitters and Drug Molecules. *J. Am. Chem. Soc.* **2003**, *125*, 4451-4459.
- 8) Nozawa, K.; Osono, C.; Sugawara, M. Biotinylated MCM-41 Channels As a Sensing Element in Planar Bilayer Lipid Membranes. *Sens. Actuators, B* **2007**, *126*, 632-640.
- 9) (a) Hartmann, M. Ordered Mesoporous Materials for Bioadsorption and Biocatalysis. *Chem. Mater.* **2005**, *17*, 4577-4593. (b) Zhu, Y.; Shen, W.; Dong, X.; Shi, J. Immobilization of Hemoglobin on Stable Mesoporous Multilamellar Silica Vesicles and Their Activity and Stability. *J. Mater. Res.* **2005**, *20*, 2682-2690.
- 10) Chong, A. S. M.; Zhao, X. S. Design of Large-Pore Mesoporous Materials for Immobilization of Penicillin G Acylase *Biocatalyst. Catal. Today* **2004**, *9395*, 293-299.
- 11) He, J.; Li, X.; Evans, D. G.; Duan, X.; Li, C. a New Support for the Immobilization of Penicillin Acylase. *Journal of Molecular Catalysis B: Enzymatic* **2000**, *11*, 45-53.
- 12) Wang, P.; Dai, S.; Waezsada, S. D.; Tsao, A. Y.; Davison, B. H. Enzyme Stabilization by Covalent Binding in Nanoporous Sol-Gel Glass for Nonaqueous Biocatalysis. *Biotechnol. Bioeng.* **2001**, *74*, 249-255.
- 13) Nakazawa, J.; Stack, T. D. P. Controlled Loadings in a Mesoporous Material: Click-on Silica. *J. Am. Chem. Soc.* **2008**, *130*, 14360-14361.
- 14) Schlossbauer, A.; Schaffert, D.; Kecht, J.; Wagner, E.; Bein, T. Click Chemistry for High-Density Biofunctionalization of Mesoporous Silica. *J. Am. Chem. Soc.* **2008**, *130*, 12558-12559.
- 15) Malvi, B.; Sarkar, B. R.; Pati, D.; Mathew, R.; Ajithkumar, T. G.; Gupta, S. S. "Clickable" SBA-15 Mesoporous Materials: Synthesis, Characterization and Their Reaction with Alkynes. *J. Mater. Chem.* **2009**, *19*, 1409-1416.
- 16) Lowe, A. B. Thiol-Ene "Click" Reactions and Recent Applications in Polymer and Materials Synthesis. *Polym. Chem.* **2010**, *1*, 17-36.
- 17) Campos, L.M.; Meinel, I.; Guino, R. G.; Schierhorn, M.; Gupta, N.; Stucky, G. D.; Hawker, C. J. Highly Versatile and Robust Materials for Soft Imprint Lithography Based on Thiol-ene Click Chemistry. *Adv. Mater.* **2008**, *20*, 3728-3733.
- 18) Chen, G.; Amajjahe, S.; Stenzel, M. H. Synthesis of Thiol-Linked Neoglycopolymers and Thermo-Responsive Glycomicelles As Potential Drug Carrier. *Chem. Commun.* **2009**, 1198-1200.
- 19) Habraken, G. J. M.; Koning, C. E.; Heuts, J. P. A.; Heise, A. Thiol Chemistry on Well-Defined Synthetic Polypeptides. *Chem. Commun.* **2009**, 3612-3614.

- 20) Gauthier, M.; Gibson, M.; Klok, H. A. Synthesis of Functional Polymers by Post-Polymerization Modification. *Angew. Chem.* **2009**, *48*, 48-58.
- 21) Khire, V. S.; Lee, T. Y.; Bowman, C. N. Synthesis, Characterization and Cleavage of Surface Bound Linear Polymers Formed Using Thiol-Ene Photopolymerizations. *Macromolecules* **2008**, *41*, 7440-7447.
- 22) Jones, M. W.; Mantovani, G.; Ryan, S. M.; Wang, X.; Brayden, D. J.; Haddleton, D. M. Phosphine-Mediated One-Pot Thiol-Ene "Click" Approach to Polymer-Protein Conjugates. *Chem. Commun.* **2009**, 5272-5274.
- 23) Chan, J. W.; Hoyle, C. E.; Lowe, A. B.; Bowman, M. Nucleophile-Initiated Thiol-Michael Reactions: Effect of Organocatalyst, Thiol and Ene. *Macromolecules* **2010**, *43*, 6381-6388.
- 24) Li, G.-Z.; Randev, R. K.; Soeriyadi, A. H.; Rees, G.; Boyer, C.; Tong, Z.; Davis, T. P.; Becer, C. R.; Haddleton, D. M. Investigation into Thiol-(Meth)Acrylate Michael Addition Reactions Using Amine and Phosphine Catalysts. *Polym. Chem.* **2010**, *1*, 1196-1204.
- 25) He, J.; Song, Z.; Ma, H.; Yang, L.; Guo, C. Formation of a Mesoporous Bioreactor Based on SBA-15 and Porcine Pancreatic Lipase by Chemical Modification Following the Uptake of Enzymes. *J. Mater. Chem.* **2006**, *16*, 4307-4315.
- 26) He, J.; Xu, Y.; Ma, H.; Zhang, Q.; Evans, D. G.; Duan, X. Effect of Surface Hydrophobicity/Hydrophilicity of Mesoporous Supports on the Activity of Immobilized Lipase. *J. Colloid Interface Sci.* **2006**, *298*, 780-786.
- 27) Ortega-Munoz, M.; Morales-Sanfrutos, J.; Megia-Fernandez, A.; Lopez-Jaramillo, F. J.; Hernandez-Mateo, F.; Santoyo-Gonzalez, F. Vinyl Sulfone Functionalized Silica: A "Ready to Use" Pre-Activated Material for Immobilization of Biomolecules. *J. Mater. Chem.* **2010**, *20*, 7189-7196.
- 28) Zhao, D.; Huo, Q.; J. Feng, Chmelka, B. F.; Stucky, G. D. *J. Am. Chem. Soc.* **1998**, *120*, 6024-6036
- 29) Kang, S.; Mou, L.; Brouillette, W. J.; Prevelige, P. E. Synthesis of Biotin Tagged Chemical Cross-linkers and Their Applications for Mass Spectrometry. *Rapid Commun Mass Spectrom.* **2009**, *23*, 1719-1726.
- 30) Wang, X.; Lin, K. S. K.; Chan, J. C. C.; Cheng, S. Direct Synthesis and Catalytic Applications of Ordered Large Pore Aminopropyl Functionalized SBA-15 Mesoporous Materials. *J. Phys. Chem. B* **2005**, *109*, 1763-1769.

- 31) Wei, Q.; Chen, H.-Q.; Nie, Z.-R.; Hao, Y.-L.; Wang, Y.-L.; Li, Q.-Y.; Zou, J.-X. Preparation and Characterization of Vinyl Functionalized Mesoporous SBA-15 Silica by a Direct Synthesis Method. *Mater. Lett.* **2007**, *61*, 1469-1473.
- 32) Friedman, M.; Cavins, J. F.; Wall, J. S. Relative Nucleophilic Reactivities of Amino Groups and Mercaptide Ions in Addition Reactions with α, β -Unsaturated Compounds 1, 2. *J. Am. Chem. Soc.* **1965**, *87*, 3672-3682.

Chapter 3

Fe-TAML Encapsulated Inside Mesoporous Silica Nanoparticles for Ultra-sensitive Detection of Proteins



In this chapter, peroxidase mimicking hybrid material is described, in which approximately 25 000 alkyne tagged biuret modified Fe-tetraamido macrocyclic ligand (Fe-TAML), a very powerful small molecule synthetic HRP mimic, was covalently attached inside a 40 nm mesoporous silica nanoparticle (MSN). Antibody conjugates of this hybrid material have also been used for the detection and, most importantly, quantify femtomolar quantities of proteins colorimetrically in an ELISA type assay.

This chapter is adapted from the following publication:

“Fe-TAML Encapsulated Inside Mesoporous Silica Nanoparticles as Peroxidase Mimic: Femtomolar Protein Detection” S. Kumari, B. B. Dhar, C. Panda, A. Meena, S. Sen Gupta, *ACS Applied Materials & Interfaces*, **2014**, 6, 13866-13873.

3.1 INTRODUCTION

Peroxidases such as the heme-containing horseradish peroxidase (HRP) is widely used for the detection of biomarker proteins where the key step is the peroxidase catalysed conversion of a colorless substrate into a colored one, thus amplifying the signal many fold.^{1,2} However, HRP conjugated to antibodies that are routinely used for protein detection via conventional enzyme-linked immunosorbent assay (ELISA type assay) has typical limit of detection (LOD) of $\sim 10^{-12}$ M.^{3,4} This LOD is significantly higher than what is necessary for ultrasensitive detection of proteins ($\sim 10^{-15}$ M or lower), which is essential for the early detection of several diseases.^{5,6} It was envisioned that development of synthetic HRP mimics that possess higher K_{cat} values than native HRP could significantly bring down the detection limits, since the final signal amplification would be enhanced several-fold. Out of several synthetic HRP mimics that have been successfully synthesized until date, nanomaterials with peroxidase activity have been quite successful. Ferromagnetic Fe_3O_4 nanoparticles (NPs) were the first that were discovered to possess peroxidase-like activity.⁷ Subsequently, other nanomaterials having similar property such as cupric oxide NPs,⁸ ceria NPs,⁹ graphene oxide NPs,¹⁰ and bimetallic NPs¹¹ such as Au@Pt ¹² and Bi-Au ¹³ have also been reported. Antibodies have been attached on these nanoparticle surfaces and these conjugates have been used for the selective colorimetric detection of proteins with sensitivity limits, which are several fold lower than what can be achieved using their corresponding antibody-HRP conjugates.

Colorimetric detection of proteins in serum or cells is more preferred above other methods since it requires no equipment at all, which is useful for point-of-care (POC) applications⁵ in settings that are resource-limited. Peroxidase mimic such as the 30 nm iron oxide NPs uses the $\text{Fe}^{2+/3+}$ ions⁷ present on the surface to activate H_2O_2 to produce OH radical, which in turn oxidizes a peroxidase substrate such as 3, 3', 5, 5'-tetramethylbenzidine (TMB) to generate a visual signal. In contrast, a single active site in HRP generates a high-valent $\text{Fe}^{\text{IV}}\text{O}$ heme radical cation, which oxidizes TMB to its colored oxidized product. The higher peroxidase activity of 30 nm Fe_3O_4 NPs (~ 100 -fold) is a result of large numbers of catalytically active Fe ions (25 000 $\text{Fe}^{2+/3+}$ ions) present on its surface.¹⁴ On a per-metal atom basis comparison between metal NPs and HRP, the $\text{Fe}^{2+/3+}$ ions in iron NPs oxide are much less efficient peroxidase mimic than the iron-porphyrin complexes in HRP. We had

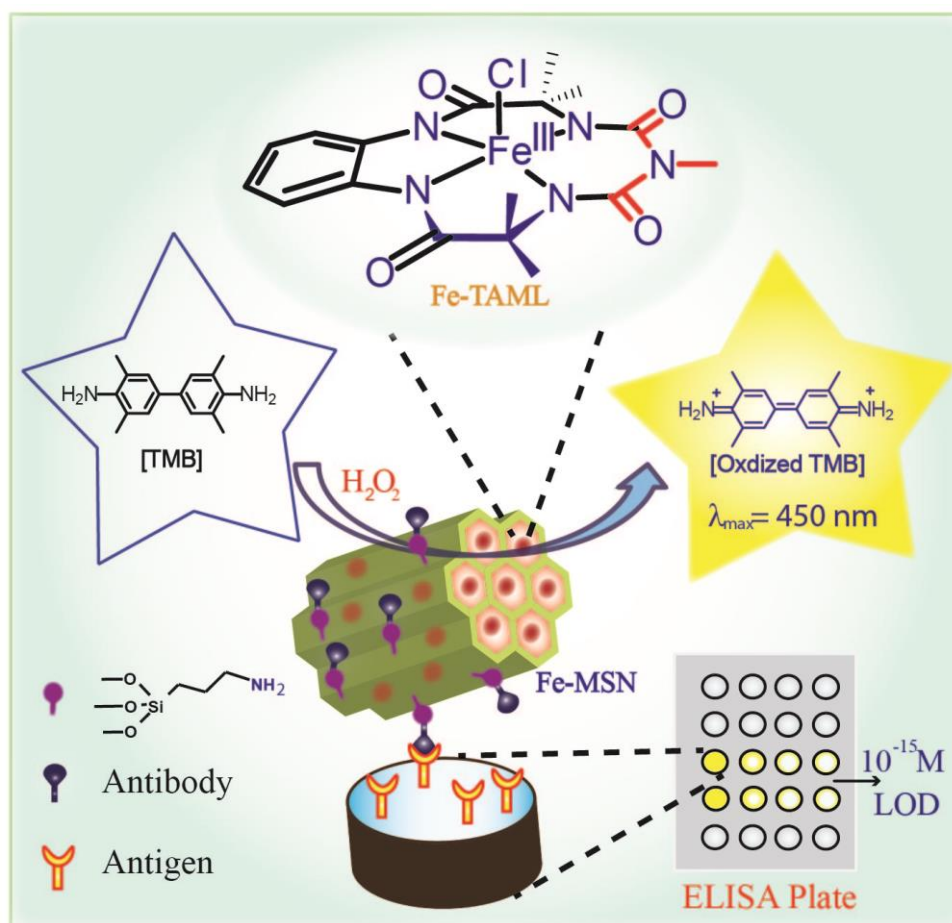


Figure 3.1 Schematic representation of signal amplification.

therefore hypothesized that if we are able to attach large numbers (e.g., ~25 000) of small molecule functional mimic of HRP inside a porous NP, their activity would likely far exceed that of the metal/metal oxide NPs too. Further, outer surface of NPs (especially silica) allows easy chemical modifications to install targeting groups such as antibodies. Such a conjugate can then be used for biomolecule detection in ELISA type assays with detection limits that should be far lower than the corresponding antibody-metal NP conjugates. This would also represent a truly biomimetic system since the HRP mimic embedded inside a NP would resemble an enzymatic system (Figure 3.1).

The choice of an efficient small molecule peroxidase mimic therefore becomes critical in designing such systems discussed above. Fe complex of tetra-amidomacrocyclic ligands (Fe-TAML) developed by Collins,¹⁵⁻¹⁷ represents by far the most efficient small molecule (Mol wt ~500 g/mol) peroxidase mimic having reactivity nearly the native enzymes. We have recently synthesized and reported a biuret modified Fe-TAML complex

which displayed excellent reactivity and very high stability, especially at low pH and high ionic strength in comparison to the prototype Fe-TAML.^{18, 19} This biuret modified Fe-TAML forms the corresponding room temperature stable Fe^V(O) in the presence of oxidant and has been shown to oxidize a variety of alkanes via C-H abstraction.²⁰ A variation of this biuret modified Fe-TAML that was attached inside Mesoporous Silica Nanoparticles (MSN; diameter 100 nm, first generation Fe-MSN) showed good peroxidase activity and was used for selective detection of glucose and cyanide.^{21, 22} In this work, we have synthesized a much improved Fe-TAML embedded^{21, 22} MSN (second generation Fe-MSN) construct that has peroxidase activity that is around 1000-fold higher than that of the particles that has been reported by us before. It's activity is also around 100-fold more than that of metal/metal-oxide NPs that have been reported before.⁵ We also show that the outer surface of these peroxidase mimics can be conjugated to an antibody such as antihuman IgG on the exterior of Fe-MSN thus maximizing the ratio of antibody to biuret modified Fe-TAML. This high ratio allows these particles to detect human immunoglobulin (human IgG) up to concentration of 1 pg/mL ($\sim 10^{-15}$ M) via an ELISA type colorimetric assay. This represents a 1000-fold increase in sensitivity over using commercial antihuman IgG-HRP^{3, 4} conjugate. We also report the selective detection of human IgG from cells that were genetically engineered to express IgG using the whole cell lysate demonstrating that high background proteins do not interfere with our assay.

3.2 EXPERIMENTAL DETAILS

3.2.1 Materials

Tetraethylorthosilicate (TEOS), cetyltrimethylammonium bromide (CTAB), amino guanidine hydrochloride (AG. HCl), 3, 3', 5, 5'-tetramethylbenzidine (TMB), 3-aminopropyl trimethoxy silane (APTES), dithiothreitol (DTT) were obtained from Aldrich. Ethylenediaminetetraacetic acid (EDTA), NaCl, H₂O₂ (30%), streptavidin, antigen hIgG, biotin were obtained from Merck. Human IgG was purchased from Jackson Smith. 96-well ELISA plates were purchased from R&D systems. Econo-Pac® Chromatography Columns, Bio-Gel P-6DG Gel, centrifugal filter tubes (MW = 10K) were purchased from BIO-RAD. CHO-S and CHO-IgG (Chinese Hamster Ovary) cells were obtained from Invitrogen for

research use. In all the assays, deionized water was used. Alkyne tailed biuret modified Fe-TAML,²³ 3-azido-propyltriethoxysilane (AzPTES)²⁴ and tris (3-hydroxypropyl triazolyl methyl) amine (THPTA),²⁵ maleimide NHS,²⁶ and biotin NHS²⁷ were prepared as reported earlier.

3.2.2 Synthesis

3.2.2.1 Synthesis of 3-azidopropyltriethoxysilane, AzPTES

3-Chloropropyltriethoxysilane (abbreviated as Cl-PTES; 2.00 g, 8.30 mmol) was added to a solution of sodium azide (1.08 g, 16.6 mmol) and tetrabutylammonium bromide (0.644 g, 2.00 mmol) in dry acetonitrile (50 mL), under nitrogen atmosphere. The reaction mixture was stirred under reflux for 18 h. After completion of the reaction, the solvent was removed under reduced pressure. The crude mixture was diluted in n-pentane and the suspension was filtered over Celite. Solvent was removed from the resulting filtrate and the crude oil obtained was distilled under reduced pressure of 0.025 mbar at 62 °C to give AzPTES (3-azidopropyltriethoxysilane) as a colorless liquid.²⁴ Yield: 1.52 g, 74%. ¹H NMR (500 MHz, CDCl₃): δ 0.66 (t, 2H, J = 8.25 Hz), 1.21 (t, 3H, J = 6.88 Hz), 1.66 – 1.73 (m, 2H), 3.25 (t, 2H, J = 7.16 Hz), 3.80 (q, 2H, J = 6.88 Hz). ¹³C NMR (50 MHz, CDCl₃) δ 7.59, 18.23, 22.64, 53.8, 58.41 (see Appendix II, Figure B1 and B2).

3.2.2.2 Synthesis of Azide Functionalized MSN (x-N₃-MSN)

The azide functionalized MSN (x-N₃-MSN; x stands for % of azide loading) was synthesized by co-condensation of TEOS with AzPTES (3-azidopropyltriethoxysilane) by following procedure reported in literature^{28, 29} with slight modifications. The density of azidopropyl groups on the surface of MSN was varied by varying the molar ratio of AzPTES with respect to TEOS during one pot co-condensation synthesis.

In a typical batch synthesis for 1% azide loading, CTAB (1.00 g, 2.74 mmol) was dissolved in 640 mL of water and 2 M aqueous NaOH (3.5 mL, 7 mmol). The mixture was stirred thoroughly at 600 rpm for 30 min at 80 °C to dissolve the surfactant completely. To this clear solution, TEOS (4.70 g, 22.60 mmol) was injected rapidly followed by AzPTES (0.06 g, 0.23 mmol). A white precipitate was observed within 1-2 min after the addition was

completed. The resultant reaction mixture was allowed to stir at 600 rpm for 2 h at 80 °C. The hot contents were then filtered and the white residue obtained was washed with copious amounts of water and methanol and dried under vacuum at 100 °C over night (yield ~1.70 g). This azide grafted MSN will be simply denoted as 1-N₃-MSN. Similarly, 5-N₃-MSN and 10-N₃-MSN was synthesized using 0.28 g (1.14 mmol) and 0.60 g (2.30 mmol) AzPTES respectively.

3.2.2.3 Synthesis of 1-Fe-MSN, 5-Fe-MSN and 10-Fe-MSN

Biuret modified Fe-TAML was grafted onto x-N₃-MSN using CuAAC. For CuAAC, 1-N₃-MSN was incubated with 3 equivalents of the alkyne tailed biuret modified Fe-TAML complex in 100 mM phosphate buffer containing THPTA (2.5 equivalent), AG. HCl (4 equivalent), CuSO₄ (0.5 equivalent) and sodium ascorbate (4 equivalent). In a typical click reaction, 1-N₃-MSN (10.00 mg, ~ 1.40 μmol of azide) was incubated with alkyne tailed biuret modified Fe-TAML complex (2.70 mg, 4.20 μmol) in 1 mL of 100 mM phosphate buffer containing THPTA (1.50 mg, 3.50 μmol), AG. HCl (0.62 mg, 5.60 μmol), CuSO₄ (0.18 mg, 0.70 μmol). The reaction mixture was freeze-pump-thawed thrice, sodium ascorbate (1.10 mg, 5.60 μmol) added and the reaction mixture was stirred inside microwave at 55 °C for 15 min and then at room temperature for 24 h. After completion of reaction, the reaction mixture was centrifuged and the residue was first washed with phosphate buffer twice and then sequentially washed with 10 mM N, N-diethyldithiocarbamate sodium solution in 100 mM phosphate buffer and acetone respectively. The last two washings were repeated thrice. Finally, the yellowish white powder obtained was dried at 80 °C in vacuum oven for 8 h (Yield: ~9.00 mg). This biuret modified Fe-TAML functionalized MSN will be denoted as 1-Fe-MSN.

Similarly, CuAAC click reaction was carried out using 5-N₃-MSN (10.00 mg, ~ 5.10 μmol of azide) and was incubated with alkyne tailed biuret modified Fe-TAML complex (10 mg, 15.3 μmol) in 1 mL of 100 mM phosphate buffer containing THPTA (5.50 mg, 12.7 μmol), AG. HCl (2.20 mg, 20.4 μmol), CuSO₄ (0.64 mg, 2.55 μmol). The reaction mixture was freeze-pump-thawed thrice and sodium ascorbate (4.00 mg, 20.4 μmol) was added, and the mixture was stirred inside microwave at 55 °C for 15 min and then at room temperature for 24 h.

In case of synthesis of 10-Fe-MSN, 10-N₃-MSN (10.00 mg, ~ 9.00 μmol of azide)

was incubated with alkyne tailed biuret modified Fe-TAML complex (17.7 mg, 27.00 μmol) in 1 mL, 100 mM phosphate buffer containing THPTA (9.80 mg, 22.5 μmol), AG. HCl (3.96 mg, 36.0 μmol), CuSO_4 (1.10 mg, 4.50 μmol). The reaction mixture was freeze-pump-thawed thrice and sodium ascorbate (7.10 mg, 36.00 μmol) was added. The reaction mixture was stirred inside microwave at 55 $^\circ\text{C}$ for 15 min and then at room temperature for 24 h. The extent of click reaction was estimated by IR spectroscopy and iron content in the 1-Fe-MSN, 5-Fe-MSN and 10-Fe-MSN was determined by ICP.

3.2.2.4 Synthesis of Amine Functionalized MSN ($\text{NH}_2\text{-N}_3\text{-MSN}$)

Using 3-amino-propyltriethoxysilane (APTES) and post synthetic grafting method, amine groups were incorporated selectively on the outer surface of the 5- $\text{N}_3\text{-MSN}$ and the template was removed to yield amine functionalized MSN denoted as ($\text{NH}_2\text{-N}_3\text{-MSN}$). Typically, 1.00 g of 5- $\text{N}_3\text{-MSN}$ was suspended in 200 mL of dry toluene under continuous sonication for 10 minutes. To this APTES (0.36 g, 2.00 mmol) was added, and the reaction mixture was stirred for 18 h at 80 $^\circ\text{C}$ under nitrogen atmosphere. After the completion of reaction, the contents were cooled, filtered and washed with toluene until it became free from APTES. The sample was then dried at 100 $^\circ\text{C}$ for 8 h in a vacuum oven. The template was extracted by stirring the as-synthesized sample (1.00 g) in 200 mL methanol and 2 mL concentrated hydrochloric acid at 60 $^\circ\text{C}$ for 6 h. The resulting template removed solid product, was filtered and washed with methanol (100 mL) and 1% triethyl amine in methanol (50 mL). Then it was again washed with methanol (50 mL) and dried overnight under vacuum at 100 $^\circ\text{C}$ (yield ~0.64 g). This material will be referred as $\text{NH}_2\text{-N}_3\text{-MSN}$. TGA was done to determine the amine incorporation in the $\text{NH}_2\text{-N}_3\text{-MSN}$.

3.2.2.5 Modification of $\text{NH}_2\text{-N}_3\text{-MSN}$ with Biuret Modified Fe-TAML by Cu(I) Catalyzed Azide-Alkyne Cycloaddition Reaction (CuAAC) ($\text{NH}_2\text{-Fe-MSN}$)

For CuAAC, $\text{NH}_2\text{-N}_3\text{-MSN}$ was incubated with 3 equivalents of the alkyne tailed biuret modified Fe-TAML complex in 100 mM phosphate buffer containing THPTA (2.5 equivalent), AG. HCl (4 equivalent), CuSO_4 (0.5 equivalent) and sodium ascorbate (4 equivalent). In a typical click reaction, $\text{NH}_2\text{-N}_3\text{-MSN}$ (10.00 mg, ~ 5.10 μmol of azide) was incubated with alkyne tailed biuret modified Fe-TAML complex (10.00 mg, 15.30 μmol) in

1 mL, 100 mM phosphate buffer containing THPTA (5.50 mg, 12.7 μmol), AG. HCl (2.20 mg, 20.40 μmol), CuSO_4 (0.64 mg, 2.55 μmol). The reaction mixture was freeze-pump-thawed thrice and sodium ascorbate (4.00 mg, 20.40 μmol) was added. The reaction mixture was stirred inside microwave at 55 $^\circ\text{C}$ for 15 min and then at room temperature for 24 h. After completion of reaction, the reaction mixture was centrifuged and the residue was first washed with phosphate buffer twice and then sequentially washed with 10 mM N, N-diethyldithiocarbamate sodium solution in 100 mM phosphate buffer and acetone respectively. The last two washings were repeated thrice. Finally, the yellowish white powder obtained was dried at 80 $^\circ\text{C}$ in vacuum oven for 8 h (Yield: ~9.00 mg). This biuret modified Fe-TAML functionalized MSN will be simply denoted as $\text{NH}_2\text{-Fe-MSN}$. The extent of click reaction was estimated by IR spectroscopy and ICP analysis.

3.2.2.6 Synthesis of Biotin Immobilized MSN (biotin-Fe-MSN)

1.00 mg of 5-Fe-MSN was added to a solution of NHS-Biotin (5.00 mg; 14.00 μmol) in 2 mL of PBS buffer of 100 mM, pH 7.4 and stirred at room temperature for overnight as shown in Figure 3.2(b). After completion of the reaction, the particles were washed extensively (5 times) with the phosphate buffer to afford biotin-Fe-MSN. Ninhydrin test was performed to confirm that the free amine groups on the surface of $\text{NH}_2\text{-Fe-MSN}$ were conjugated with biotin-NHS. $\text{NH}_2\text{-Fe-MSN}$ gives a Ruhemann's purple with ninhydrin test whereas negligible color was observed for biotin-Fe-MSN. The samples were then dispersed in buffer and subsequently used for colorimetric assay.

Biotin modified MSN (no Fe-TAML present) was synthesized in a similar method for control experiments. $\text{NH}_2\text{-N}_3\text{-MSN}$ was used instead of $\text{NH}_2\text{-Fe-MSN}$ for synthesis of Biotin- $\text{N}_3\text{-MSN}$ for control experiments.

3.2.2.7 Synthesis of Maleimide Functionalized MSN (maleimide-Fe-MSN)

To a dispersion of 5-Fe-MSN (1 mg) in PBS buffer was added maleimide NHS (5.00 mg, 19.00 μmol) in acetonitrile: water (1:1) and stirred at room temperature for 12 h. After completion of the reaction, the particles were centrifuged and washed thoroughly several times with acetonitrile-buffer mixture. Ninhydrin test and TGA was performed to confirm that the free amine groups on the surface of $\text{NH}_2\text{-Fe-MSN}$ were conjugated with maleimide-

5-Fe-MSN. NH₂-Fe-MSN gives a Ruhemann's purple with ninhydrin test whereas negligible color was observed for maleimide-5-Fe-MSN. At the end of the centrifugation the particles were dispersed in 100 mM PBS buffer of pH 7.4 and used for the conjugation with reduced antibody.

3.2.2.8 Conjugation of Antibodies to Maleimide-Fe-MSN (antihuman IgG-5-Fe-MSN)

Antihuman IgG antibody was conjugated to maleimide-Fe-MSN using a methodology that is shown in Figure 3.6. The antibodies were first reduced with Dithiothreitol (DTT). Reduced antibody fragments were purified by gel filtration using a desalting resin. Reduced antibody fragments with free sulfhydryl groups were conjugated to maleimide activated Fe-MSN through thiol-maleimide reaction. In a typical reaction, a 2.50 μmol antibody was mixed in 200 μL PBS-EDTA (100 mM, phosphate buffer of pH 7.2, 10 mM EDTA) with 6.50 μmol DTT and incubated at 37 °C for 2 h. Then, 0.10 mg of NH₂-Fe-MSN was mixed with reduced IgG and the solution was incubated at room temperature for overnight. After incubating for 12 h, the solution was centrifuged twice (12 000 rpm, 4 °C and 1 h) and supernatant with unconjugated antibody fragments was discarded. Finally, cysteine was added to the conjugate (0.01 mg, 0.10 μmol) to quench all the unreacted maleimides. The particle antihuman IgG-Fe-MSN was then dispersed in PBS buffer and used for antigen detection in immunoassay.

3.2.2.9 Kinetics of TMB Oxidation

The determination of K_m and K_{cat} values of 1-Fe-MSN and 5-Fe-MSN for the oxidation of TMB in the presence of H₂O₂ was carried out at the physiological pH 7.4. For kinetic runs, primary stock solutions of 1-Fe-MSN (0.50 $\mu\text{g}/\text{mL}$) and 5-Fe-MSN (2.00 $\mu\text{g}/\text{mL}$) was prepared in deionized water. In all kinetic runs the amount of 1-Fe-MSN or 5-Fe-MSN added was kept constant. Concentration of H₂O₂ was calculated by measuring the UV-vis absorbance at 240 nm ($\epsilon = 43.6 \text{ M}^{-1} \text{ cm}^{-1}$). To investigate the peroxidase activity of 1-Fe-MSN, TMB concentration was fixed at $1.6 \times 10^{-4} \text{ M}$ while H₂O₂ was varied from 4.80×10^{-3} to $32.00 \times 10^{-3} \text{ M}$. For TMB variation, the reverse procedure was followed ($[\text{H}_2\text{O}_2] = 10 \times 10^{-3} \text{ M}$; $[\text{TMB}] = 2.40 \times 10^{-5} - 3.20 \times 10^{-4} \text{ M}$). Similarly, for 5-Fe-MSN H₂O₂ was varied from 3×10^{-3} to $40 \times 10^{-3} \text{ M}$ while keeping the TMB concentration fixed at $2.00 \times 10^{-4} \text{ M}$.

TMB was varied from 5.00×10^{-5} - 4.00×10^{-4} M while keeping the $[\text{H}_2\text{O}_2]$ constant at 8.00×10^{-3} M. PBS buffer (pH 7.4; 10 mM) was used for all the kinetic runs.

3.2.3 Experimental methodology for kinetics of TMB oxidation

The determination of K_m and K_{cat} values of 1-Fe-MSN and 5-Fe-MSN for the oxidation of TMB in presence of H_2O_2 was carried out at the physiological pH 7.4. At this pH, upon oxidation TMB forms three products i) one electron oxidized product (TMB^+ ; $\lambda_{max} = 900$ nm), ii) a charge transfer complex consisting of one unreacted TMB and one two electron oxidized species ($\text{TMB}^{2+} : \text{TMB}$; $\lambda_{max} = 650, 370$ nm) and iii) a two electron oxidized product (TMB^{2+} ; $\lambda_{max} = 450$ nm). All these three species remain in equilibrium with each other.³⁰ However, when the pH of the solution is lowered below 2, the equilibrium is shifted towards the complete formation of TMB^{2+} (with characteristic peak at 450 nm; $\epsilon = 59\,000 \text{ M}^{-1}\text{cm}^{-1}$) together with the disappearance of $[\text{TMB}^{2+} : \text{TMB}]$ and TMB^+ . So estimation of rate constants using normal scanning kinetics at any one of the above mentioned λ_{max} (which would represent only one oxidation products of TMB) would not be representative of the “true” rate constants of Fe-MSN. Therefore all kinetic runs the reactions were initiated at pH 7.4 and were quenched to $\text{pH} < 2$ by addition of HCl at different time intervals. The absorbance of the product formed after quenching was measured at 450 nm (Figure 3.3). The initial rate was measured according to absorbance change at 450 nm for different time intervals. For detailed kinetic studies, keeping the catalyst (1-Fe-MSN and 5-Fe-MSN) concentration fixed, $[\text{TMB}]$ or $[\text{H}_2\text{O}_2]$ was varied separately as substrate keeping the other constant. The plots of initial rate vs substrate concentrations were fitted according to Michaelis-Menten equation: $v = V_{max} \times [\text{S}]/(K_m + [\text{S}])$ where “v” stands for initial rate or initial velocity, V_{max} is the maximal velocity, $[\text{S}]$ is the concentration of the substrate and K_m is the Michaelis-Menten constant. K_m and V_{max} values were determined as per fitting (Figure 3.4, Table 3.2) within 10% error limit.

3.2.4 Colorimetric Assay of Streptavidin

In ELISA for the detection of streptavidin, 96-well polystyrene (PS) plates were used. For a typical ELISA experiment, 100 μL of streptavidin with concentrations ranging from 0.001 to 10^5 ng/mL was added to each well and incubated at 4°C overnight. After incubation,

the plate was washed three times with 100 mM, pH 7.4 PBS buffer. Each well was filled with 100 μL of 1% BSA in PBS as blocking agent to prevent nonspecific interaction between the plate and biotin conjugated Fe-MSN. After 2 h, the plate was decanted and washed three times with PBS buffer. In the second step, 50 μL of biotin-Fe-MSN (10^{-2} mg/mL) was added into wells and incubated at 37 $^{\circ}\text{C}$ for another 1 h. After washing three times with wash buffer, 100 μL substrate stock solution containing TMB (4.00×10^{-5} M) and H_2O_2 (16.00×10^{-3} M) was added to each well. After 10 min of incubation, the green color observed was immediately quenched with 0.1 N HCl. ELISA reading was performed in a micro plate reader at 450 nm.

3.2.5 Detection of Human IgG Using Antihuman IgG-Fe-MSN

The detection of human IgG using antihuman IgG-Fe-MSN was performed by the standard sandwich ELISA format included coating a 96-microwell plate with affinity purified rabbit antihuman IgG for capture of IgG. Then, each well was filled with 100 μL of 1% BSA in PBS and incubated at 37 $^{\circ}\text{C}$ for another 2 h to prevent nonspecific interactions between the plate surface and antibody conjugated Fe-MSN, followed by incubating the protein human IgG (100 μL of 10^{-3} to 10^5 ng/mL) at 37 $^{\circ}\text{C}$ for 3 h. After incubation, the plate was washed three times with PBS and then 50 μL of antihuman IgG-Fe-MSN (10^{-2} mg/mL) was added into the wells and incubated for an additional hour. The color development was initiated by addition of 100 μL of TMB (4.00×10^{-5} M) and H_2O_2 (16.00×10^{-3} M). After 10 min of incubation, the green color observed was immediately quenched with 0.1 N HCl. ELISA reading was performed in a micro plate reader at 450 nm.

3.2.6 Detection of Human IgG in CHO-S and CHO-IgG

CHO-S and CHO-IgG cells were grown in suspension under 10% CO_2 atmosphere at 37 $^{\circ}\text{C}$. Cells suspension was centrifuged and washed with an ice-cold PBS to remove the excess media. The cell pellet was lysed by suspension in ice-cold lysis buffer for 15 min, centrifuged and the supernatant was collected for further assay. Supernatant containing CHO-S and CHO-IgG cells were diluted to 10^5 , 10^4 and 10^3 cells/mL and were plated on 96 well plates by incubation at 4 $^{\circ}\text{C}$ for 24 h. The plates were further incubated with antihuman IgG-Fe-MSN for another 1 h, subsequently washed several times and then probed with TMB (4

$\times 10^{-5}$ M) and H_2O_2 (16×10^{-3} M). After 10 min, the reaction was quenched with 0.1 N HCl. ELISA reading was performed in a micro plate reader at 450 nm.

3.2.7 Determination of the concentration of 1-Fe-MSN and 5-Fe-MSN in a stock solution of 1.00 mg/mL

At first the density of particles (N_3 -MSN), that is the ratio of the mass of particle per its volume (excluding the void space between particles), was estimated using:

$$\begin{aligned} \text{Density} &= \text{mass of particles/volume of particles} \\ &= \text{mass of particles/ (volume of walls + volume of internal pores)} \end{aligned}$$

Volume of internal pores: From gas adsorption $0.4 \text{ cm}^3/\text{g}$ (used $p/p_0 = 0.20 - 0.30$ to exclude pore volume contribution from the inter particle porosity)

Volume of walls: mass divided by framework density (silica density of 2.20 g/cm^3 used since it is mostly SiO_2)

Therefore, Density of N_3 -MSN = 1.17 gm/cm^3

This density estimated above and the amount of Fe-TAML loaded onto 1-Fe-MSN and 5-Fe-MSN (as determined by ICP) was used to calculate the concentration of 1-Fe-MSN and 5-Fe-MSN in solution.

The concentration of 1 mg/mL of 1-Fe-MSN was determined to be 3.96×10^{-8} M.

Similarly, the concentration of 1 mg/mL of 5-Fe-MSN was determined to be 2.50×10^{-8} M.

3.3 CHARACTERISATION TECHNIQUES

Powder X-ray diffraction of all the samples was carried out in a PAN analytical X'pert Pro dual goniometer diffractometer. A proportional counter detector was used for low angle experiments and an X'celerator solid state detector was employed in the low angle experiments. The radiation used was $\text{CuK}\alpha$ (1.5418 \AA) with a Ni filter and the data collection was carried out using a flat holder in Bragg–Brentano geometry (0.5 to 10° ; $0.2^\circ \text{ min}^{-1}$). Care was taken to avoid sample displacement effects.

SEM images were obtained on Leica Stereoscan 440 microscope. HR-TEM images were taken on a FEI Technai F30 operating at 300 kV with FEG. The samples were prepared by dispersing a large number of solid particles in isopropanol by sonication, and dropping the

resulting suspension on a copper grid of 400 mesh and allowed to dry in air.

Nitrogen adsorption and desorption studies were carried out using Quantachrome instrument. Samples were preheated at 100 °C for 18 h in the vacuum line. Multi point BET surface area was obtained from adsorption isotherm from P/P₀ 0.1-0.3. Pore size distributions were calculated from adsorption isotherm using the BJH method.

Semi-quantitative FT-IR spectra were recorded on Perkin Elmer FT-IR spectrum GX instrument by making KBr pellets. Pellets were prepared by mixing 3.00 mg of sample with 97.0 mg of KBr. Yields for CuAAC reactions were calculated from corrected area under the curve characteristic for the azide stretch at ~2100 cm⁻¹.

¹³C Cross Polarization Magic Angle Spinning (CPMAS) NMR experiments were carried out on a Bruker AVANCE 300 wide bore spectrometer equipped with a superconducting magnet with a field of 7.1 Tesla operating at 75.4 MHz. The samples were packed into a 4 mm zirconia rotor and loaded into a 4 mm BL MAS probe and spun about the magic angle (54.74) at 10 KHz using a standard ramp-CP pulse sequence was used for the experiment. The RF-powers was 60 KHz ¹³C CPMAS experiments. The contact time was 3 ms for ¹³C CPMAS experiments. All the chemical shifts were referenced to TMS. Typically 10,000 to 25,000 scans with a recycle delay of 3s were collected depending on the sensitivity of the sample.

Confocal laser scanning microscopy (CLSM) images were taken with Carl Zeiss confocal system equipped with a 20 x objective. Optical slices in the center of the particle were selected.

Thermogravimetric analysis (TGA) of the silica nanoparticles were carried out using a TA Instrument SDT Q600 analyzer between 100 and 750 °C in air (flow rate 25 mL min⁻¹) at a heating rate of 10 °C min⁻¹. Prior to TGA runs, all samples were stirred in water overnight, centrifuged and dried under vacuum at 80 °C overnight. The amount of organic content on the silica surface was determined by TGA using the following equation:

$$\text{graft density} \left(\frac{\text{mmol}}{\text{gm}} \right) = \frac{\frac{W_{\text{grafted-MSN}(150-750)}}{100 - W_{\text{grafted-MSN}(150-750)}} \times 100 - W_{\text{MSN}(150-750)}}{M \times 100}$$

Where $W_{\text{grafted-MSN}(150-750)}$ is the weight loss between 150 °C and 750 °C corresponding to the decomposition of the organic substance from MSN corrected from the thermal

degradation, while $W_{MSN (150-750)}$ represents the weight loss between 150 °C and 750 °C from functionalized moiety MSN. M is the molecular weight of the decomposed organic substance.

3.4 RESULTS AND DISCUSSION

3.4.1 Design and Synthesis of Biuret Modified Fe-TAML Immobilized MSN

Detection of biomolecules in femtomolar concentration necessitates development of particles that possess very high peroxidase activity and is also capable of multivalently displaying receptor ligands (e.g., antibodies for protein detection) on its surface. We therefore designed a MSN that contained several chemically conjugated HRP mimic biuret modified Fe-TAML inside the pores and antibody molecules on its surface (Figure 3.1). The presence of large number of biuret modified Fe-TAML complexes inside MSN is expected to have an additive effect to their individual activity and therefore increase the overall peroxidase activity in comparison to HRP enzyme. This high peroxidase activity together with the increased binding affinity of Fe-MSN to the target protein due to multivalent display of antibodies on its surface is expected to bring down the detection limits several folds in comparison to commercial antibody-HRP conjugates.

We have previously reported the synthesis of Fe-(biuret) TAML modified MSN (Fe-MSN) in which 100 nm MSN containing 1% azidopropyl group was used to attach biuret modified Fe-TAML using CuAAC (first generation Fe-MSN).²¹ However, their tendency to aggregate in aqueous solution and the low peroxidase activity (due to low loading of biuret modified Fe-TAML) in comparison to commercial HRP made them unsuitable for usage as catalysts for signal amplification at low nanoparticle concentration conditions that are necessary for ultrasensitive detection of proteins via ELISA type assays. We therefore proceeded to design a second generation Fe-MSN construct that would possess much improved peroxidase activity and will also be amenable to external modification with receptor molecules such as antibodies. We hypothesized that a smaller mesoporous nanoparticle (smaller than first generation Fe-MSN which had 100 nm diameter) and increased amounts of biuret modified Fe-TAML loading (greater 0.05 mmol/g as in first generation Fe-MSN) would probably maximize peroxidase activity and will increase its ability to disperse well in aqueous solutions. Further presence of aminopropyl groups

exclusively on the outer surface would allow easy attachment of receptor molecules such as antibodies on Fe-MSN. Our synthetic strategy is therefore based on a bioorthogonal approach consisting of the following steps: (1) Synthesis of azido-functionalized MSN particles (N_3 -MSN) with average diameter of 30-40 nm using a co-condensation approach so that most of the azidopropyl groups are present inside the MSN; (2) Grafting of amino propyl group on the as-synthesized MSN followed by template removal and (3) Attachment of biuret modified Fe-TAML to N_3 -MSN using CuAAC (Figure 3.2a).

We attempted the synthesis of azide grafted spherical MSN^{21, 31, 32} having average diameter between 30 nm and 40 nm by the co-condensation method. This is likely to result in the organo azide group residing mostly inside the pores. The reasons for this can be attributed to the following: (i) Considering that the azidopropyl group is randomly distributed over the whole material, the higher internal to external surface area ratio (7:1) would lead to the azidopropyl group being located mostly inside the pore; (ii) During initial formation of the first layer of silica during our synthesis, the azidopropyl group (from AzPTES) will be located inside the surfactant as has been discussed before for the synthesis of a related material.^{21b} Condensation of TEOS to form silica walls will then subsequently occur over this first layer. We believe this model to be true for the synthesis of our material as > 95 % azides are available for subsequent conversion into the corresponding triazoles using CuAAC with small molecule alkynes as the substrate. This indirectly shows that the hydrophobic azidopropyl group was embedded inside the surfactant during initial silica condensation thus ending up mostly inside the pores. The amount of azide grafted was varied from 1 to 10 % to allow us to study the effect of biuret modified Fe-TAML loading on peroxidase activity. The resultant azide grafted MSN containing 1, 5, and 10 % azidopropyl groups (1- N_3 -MSN, 5- N_3 -MSN and 10- N_3 -MSN, respectively) obtained after template removal was thoroughly characterized by several physical techniques such as TEM, XRD, SEM, N_2 adsorption-desorption, FT-IR and ^{13}C CP MAS NMR (as discussed in section 3.5 and see Appendix II; Figures B3-B8). The material was found to be very stable in water (pH 4-9) and high ionic strength (phosphate buffer 100 mM). TGA analysis showed the amount of azidopropyl groups incorporated onto 1- N_3 -MSN, 5- N_3 -MSN and 10- N_3 -MSN to be 0.14, 0.51 and 0.90 mmol/g respectively (Table 3.1, Figure 3.12). Biuret modified Fe-TAML containing an alkyne group was then attached to N_3 -MSN using a modified CuAAC procedure. The qualitative and quantitative incorporation of biuret modified Fe-TAML was studied using FT-IR, electron paramagnetic resonance (EPR), and inductively coupled plasma (ICP) analysis

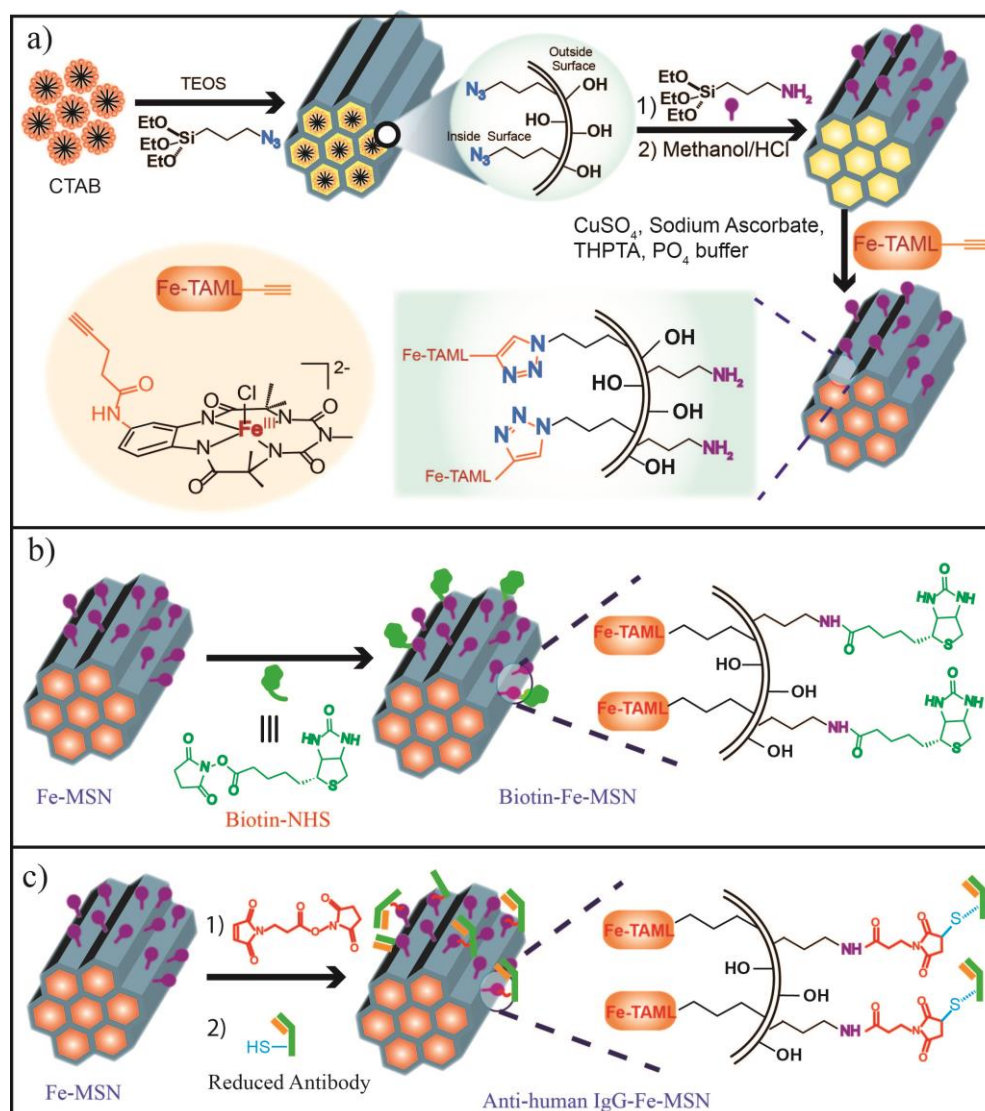


Figure 3.2 Synthesis of (a) biuret modified Fe-TAML functionalized MSN (Fe-MSN); (b) biotin conjugated Fe-MSN; (c) antihuman IgG conjugated Fe-MSN

(as discussed in section 3.5, also see Appendix II; Figures B5, B6, and B9). From ICP analysis, the biuret modified Fe-TAML incorporation was estimated to be 0.15, 0.64 and 0.77 mmol/g of Fe-MSN. The IR results show that the extent of CuAAC for the grafting of biuret modified Fe-TAML onto 1-N₃-MSN and 5-N₃-MSN was greater than 95%. In contrast, for 10-N₃-MSN the extent of CuAAC was found to be only 85% (Figure 3.14; see Appendix II; Figure B5, B6). In fact, the amount of biuret modified Fe-TAML did not increase much when the azide incorporation was increased from 5 to 10% (most likely for steric reasons). In lieu of this, only biuret modified Fe-TAML attached to 1-N₃-MSN and 5-N₃-MSN (1-Fe-MSN

Table 3.1 Physical Properties of x-N₃-MSN

x-N ₃ -MSN	N ₃ Grafting Density (mmol/g)	Surface area M _{BET} (m ² /g)	Pore diameter (nm)	Pore volume (cc/g)
1-N ₃ -MSN	0.14	947	3.54	0.925
5-N ₃ -MSN	0.51	851	3.30	0.779
10-N ₃ MSN	0.90	824	3.18	0.731

and 5-Fe-MSN respectively) was further evaluated for their peroxidase activity (Table 3.2); for K_{cat} values of 10-Fe-MSN see Figure 3.4. Finally, the density of 1-N₃-MSN and 5-N₃-MSN was estimated from the N₂ adsorption-desorption data to evaluate the number of biuret modified Fe-TAMLs incorporated in each nanoparticle. It was estimated that around 25 000 and 5 000 biuret modified Fe-TAMLs were covalently attached inside 5-Fe-MSN and 1-Fe-MSN, respectively.

3.4.2 Evaluation of Kinetic Parameters for TMB Oxidation by Fe-TAML Encapsulated in MSN.

The peroxidase activity of 1-Fe-MSN, 5-Fe-MSN, and 10-Fe-MSN were evaluated by studying their efficiency for the H₂O₂ mediated oxidation of TMB to form colored oxidized products. The oxidation reaction was carried out at the physiological pH of 7.4 and the kinetic parameters V_{max} , K_{cat} and K_m were determined (Table 3.2). These three parameters were chosen so that the activity of the whole particle Fe-MSN can be compared with both HRP and other metal/metal oxide based NPs that have been reported.⁷ At pH 7.4 upon oxidation, TMB forms three products (TMB²⁺, oxidized TMB charge transfer complex and TMB⁺), which remain in equilibrium.³³ However, when the pH of the solution is lowered below 2, the equilibrium is shifted towards the complete formation of TMB²⁺ (characteristic peak at 450 nm; $\epsilon = 59,000 \text{ M}^{-1}\text{cm}^{-1}$) together with the disappearance of oxidized TMB charge transfer complex and TMB⁺ (Figure 3.3). Therefore, for all kinetic runs the reactions were initiated at pH 7.4 but were quenched to pH < 2 by addition of HCl at different time intervals and the absorbance was measured at 450 nm. The plots of initial rate vs substrate

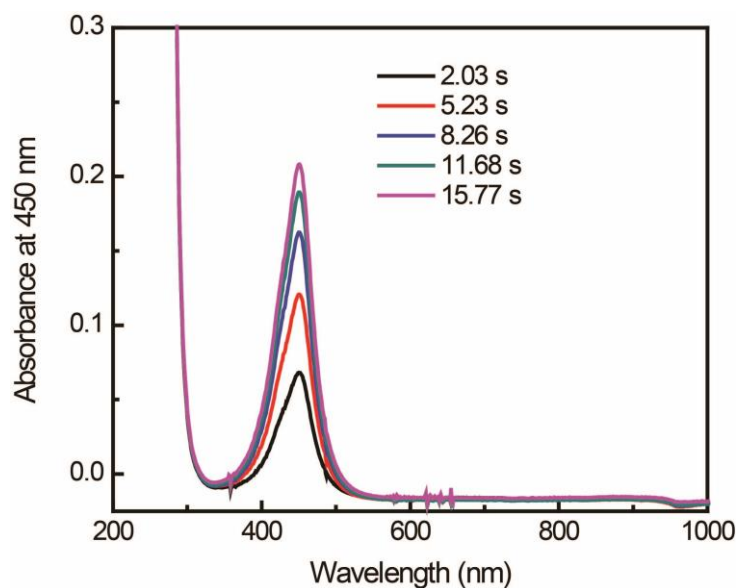


Figure 3.3 UV-vis spectra of quenched reaction mixture for TMB oxidation using 5-Fe-MSN and H_2O_2 . The reaction was quenched at different time intervals' using HCl and the UV-vis spectra was measured. The peak at 450 nm is only observed. Reaction condition: $[\text{TMB}] = 2.00 \times 10^{-4} \text{ M}$, $[\text{H}_2\text{O}_2] = 1.50 \times 10^{-4} \text{ M}$, $[\text{5-Fe-MSN}] = 12.5 \times 10^{-14}$, PBS buffer (pH 7.4, 10 mM).

concentrations were fitted perfectly to a typical Michaelis–Menten curve (Figure 3.4) and the K_m and V_{max} values were determined (Table 3.2). The K_{cat} values of 5-Fe-MSN with TMB as the substrate was found to be 10-folds higher than 1-Fe-MSN. Similarly, the catalytic efficiency (K_{cat}/K_m) of 5-Fe-MSN with TMB as the substrate was found to be 4-folds higher than 1-Fe-MSN. This demonstrated that increasing the loadings of biuret modified Fe-TAML inside MSN led to increased catalytic efficiency. In comparison to our first generation Fe-MSN,²¹ 5-Fe-MSN displayed a K_{cat} value 1000-fold higher. Hence, reduction of nanoparticle size (thereby increasing surface area and dispersibility) and increase in biuret modified Fe-TAML content had a huge positive effect on the catalytic activity for our second generation Fe-MSN. The effect of pH on the catalytic efficiency of the reaction was also studied. It was determined that the amount of oxidized TMB formed at the end of the reaction (responsible for peaks at 450, 650 and 900 nm) was lower at pH 6 and pH 8.4 than at pH 7.4 (see Appendix II, Figure B10). This can be rationalized by careful understanding of the mechanism of Fe-TAML mediated oxidation reactions in water. It is well established that the

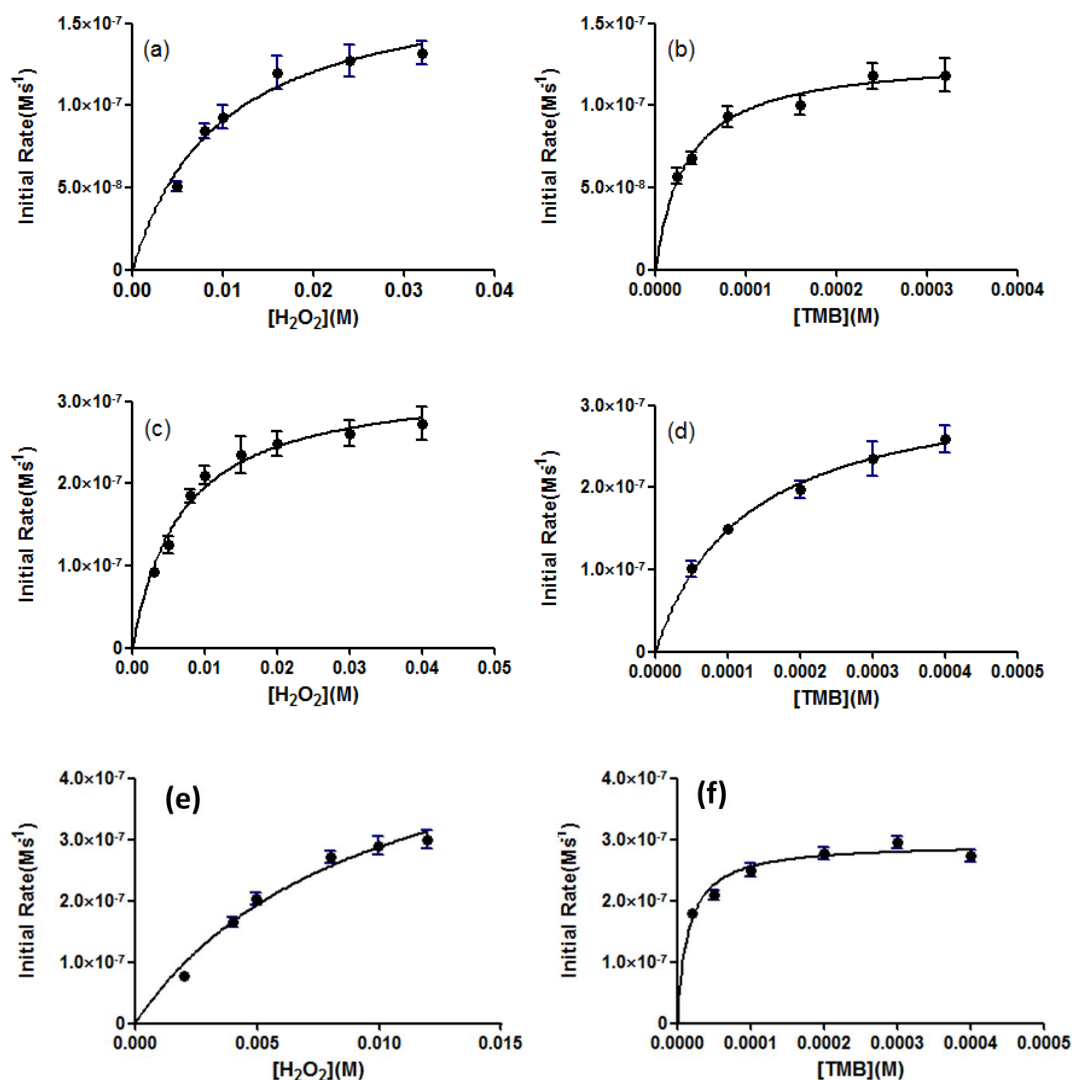


Figure 3.4 Michaelis-Menten fit for H₂O₂ and TMB variation; (a) and (b) for 1-Fe-MSN, (c) and (d) for 5-Fe-MSN, (e) and (f) for 10-Fe-MSN. The K_{cat} values for 10-Fe-MSN with H₂O₂ and TMB as the substrate was found to be 1.00×10^7 and 5.40×10^6 respectively. K_{cat} value has been calculated using formulae $K_{cat} = V_{max}/[E]$. Where $[E] = 5.40 \times 10^{-14}$ and V_{max} for H₂O₂ and TMB was found to be 5.60×10^{-7} and 2.93×10^{-7} . Error bars shown represent the standard error derived from three repeated measurements.

rate of substrate oxidation by Fe-TAML and H₂O₂ increases with increasing pH and hence the activity of 5-Fe-MSN gets reduced at pH 6.³⁴ At pH 7.4 in the presence of peroxide, Fe-TAML forms a μ -O-Fe^{IV} dimer species that is responsible for the 2-electron oxidation of

Table 3.2 Comparison of the Kinetic Parameters of 1-Fe-MSN, 5-Fe-MSN, HRP, 30 nm Fe₃O₄ MNPs, and Au@Pt 0.25.

	[E] (M) ^a	Substrate	K_m (mM)	V_{max} (Ms ⁻¹)	K_{cat} (s ⁻¹)	K_{cat}/K_m (s ⁻¹ M ⁻¹)
1-Fe-MSN	7.92×10^{-13}	TMB	0.033	1.30×10^{-7}	1.64×10^5	4.97×10^9
1-Fe-MSN	7.92×10^{-13}	H ₂ O ₂	9.617	1.79×10^{-7}	2.25×10^5	2.30×10^7
5-Fe-MSN	1.25×10^{-13}	TMB	0.122	3.32×10^{-7}	2.65×10^6	2.17×10^{10}
5-Fe-MSN	1.25×10^{-13}	H ₂ O ₂	6.670	3.27×10^{-7}	2.60×10^6	3.89×10^8
1 st -Fe-MSN ²¹	2.60×10^{-11}	TMB	0.016	1.01×10^{-8}	4.00×10^2	2.47×10^7
HRP ⁷	2.50×10^{-13}	TMB	0.434	10.00×10^{-8}	4.00×10^3	9.22×10^6
30 nm Fe ₃ O ₄ MNPs ⁷	11.40×10^{-13}	TMB	0.098	3.44×10^{-8}	3.02×10^4	3.08×10^8
Au@Pt 0.25 ¹²	12.50×10^{-12}	TMB	0.027	1.81×10^{-7}	1.40×10^4	5.18×10^8

[E] is the enzyme (Au@Pt 0.25 or Fe-MSN or MNPs) concentration, K_m is the Michaelis-Menten constant, V_{max} is the maximal reaction velocity and K_{cat} is the catalytic constant, where $K_{cat} = V_{max}/[E]$. ^aConcentrations have been calculated for 1-Fe-MSN and 5-Fe-MSN from TEM, ICP and N₂ adsorption-desorption data (Figure 3.8, 3.9, and 3.13, see Appendix II , Figure B3, B5)

TMB.³⁵ However, with increasing pH, the μ -O-Fe^{IV} dimer species gets converted to Fe^{IV}(O) which is far more active oxidant.³⁵ Hence at pH 8.4, although oxidized TMB species is formed at faster rates, they undergo subsequent oxidation reactions to form degradation products which are colorless. Fe-TAML is very well-known to completely degrade recalcitrant organic compounds³⁶ at higher pH. Hence, pH 7.4 was considered as the most optimal for obtaining the highest catalytic efficiency.

On comparison of 5-Fe-MSN and 1-Fe-MSN to HRP, it can be seen that K_{cat}/K_m values were 2300 times and 540 times higher than those of commercial HRP, respectively. Among the metal nanoparticles, the highest K_{cat} values have been observed for 30 nm Fe₃O₄ and Au@Pt 0.25 NPs.¹² The K_{cat} value of 5-Fe-MSN is around 100-fold higher than that of both 30 nm iron oxide and Au@Pt 0.25 NPs. This is expected because biuret modified Fe-TAML has peroxidase activity that is far superior to that of the metal ions present on the

nanoparticle surface. This 2300-fold increased peroxidase activity of 5-Fe-MSN in comparison to HRP encouraged us to use this nanoparticle for ultrasensitive detection of proteins.

3.4.3 Biotin conjugated Fe-MSN for detection of Streptavidin.

The detection of streptavidin was attempted using biotin modified 5-Fe-MSN. Streptavidin is known to bind biotin with very high specificity (10^{-14} mol/L).³⁷ We hypothesized that using 5-Fe-MSN that would have biotin displayed on its surface would help us to detect streptavidin in an conventional ELISA assay in which commercially used biotin-HRP would be replaced with our biotin conjugated 5-Fe-MSN. We therefore proceeded to synthesize 5-Fe-MSN having biotin displayed on its surface. This was achieved by first grafting 3-aminopropyl triethoxysilane onto the as synthesized 5-N₃-MSN followed

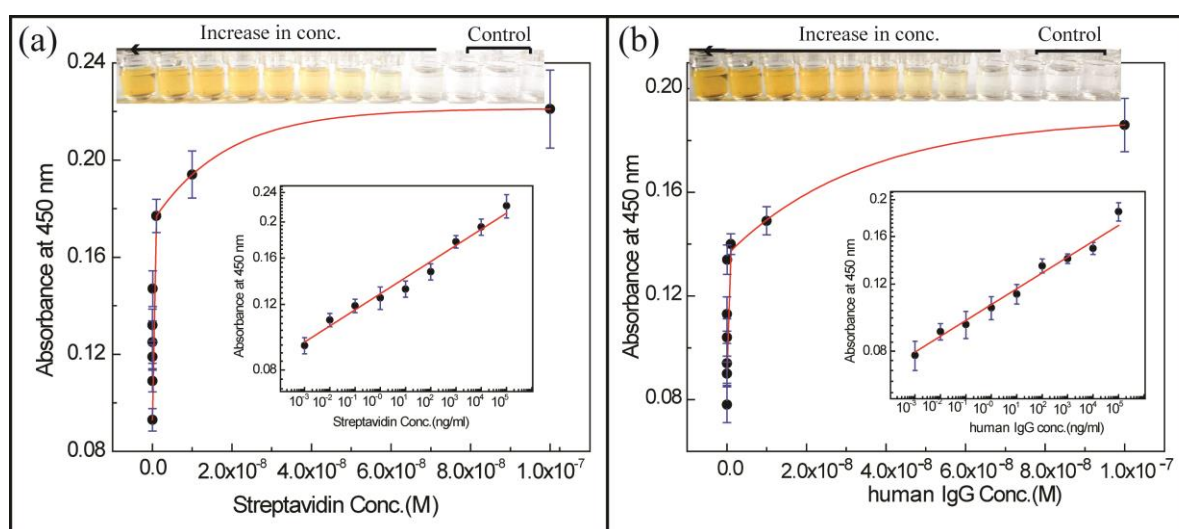


Figure 3.5 Application of biuret modified Fe-TAML MSN in direct immunosorbent assay (a) Calibration curve for the detection of streptavidin in various concentration from 1 pg/mL to 10^6 ng/mL using biotin conjugated Fe-MSN in a 96-well plate (b) Calibration curve of the immunosorbent assay for the detection of human IgG in various concentration from 1 pg/mL to 10^6 ng/mL using antihuman IgG conjugated Fe-MSN. The error bars represent the standard deviation from triplicate measurements.

by template removal (Figure 3.2a). Biuret modified Fe-TAML was then “clicked” onto $\text{NH}_2\text{-MSN}$ using CuAAC and the resultant material $\text{NH}_2\text{-Fe-MSN}$ was characterized by FT-IR, thermogravimetric analysis (TGA), and ICP (Figure 3.14; see Appendix II, Figure B 8). The amount of amine groups grafted was estimated to be 1.04 mmol/g while the amount of biuret modified Fe-TAML grafted was determined to be 0.51 mmol/g.

Additionally, ninhydrin test was done to confirm amine groups on the surface of 5- $\text{N}_3\text{-MSN}$ and TEM image shows the absence of clustering in mesoporous silica nanoparticles after surface modification (Figure 3.10). Finally, $\text{NH}_2\text{-Fe-MSN}$ was reacted with biotin-NHS to yield biotin-Fe-MSN which was then used for the detection of streptavidin (Figure 3.2b).

A 96-well plate was first coated with streptavidin (0.001 to 10^5 ng/mL), then blocked with 1% BSA, and finally incubated with biotin conjugated 5-Fe-MSN for 1 h. After several washes, to remove nonspecific binding, the substrate TMB and H_2O_2 were added such that the biotin conjugated 5-Fe-MSN bound to the streptavidin can utilize H_2O_2 to catalyze the formation of colored oxidized TMB. The reaction was measured using an ELISA plate reader at 450 nm. A linear dependence of absorbance vs analyte concentration was obtained in the range of 1 pg/mL to 10^6 ng/mL (log [absorbance] vs log [streptavidin]) with a limit of detection (LOD) of 19 fM (Figure 3.5a). Control experiments in which $\text{N}_3\text{-MSN}$ or Fe-MSN was used as the probe in place of biotin-Fe-MSN, showed no detectable signal. In the lowest detection limit, the signal was at least twice that was obtained when BSA was used instead of streptavidin as a control. These initial results encouraged us to explore the detection of human IgG in an ELISA format using antihuman IgG conjugated Fe-MSN as the probe.

3.4.4 Antihuman IgG Conjugated Fe-MSN for Detection of Human IgG in Cells.

To evaluate the efficiency of this highly active peroxidase mimic, the ultrasensitive detection (fM) and quantification of human IgG protein was attempted. The amine groups on the surface of $\text{NH}_2\text{-Fe-MSN}$ were converted to maleimides onto which antihuman IgG was attached using the thiol-maleimide chemistry as shown in (Figure 3.2c, 3.6). Any unreacted maleimide on the surface of Fe-MSN was quenched by addition of cysteine.

For colorimetric immunoassay of human IgG, several concentrations of human IgG (0.001 to 10^5 ng/mL) were captured on 96-well plate and then subsequently incubated with antihuman IgG-Fe-MSN for 1 h. After several washes to remove nonspecific binding of

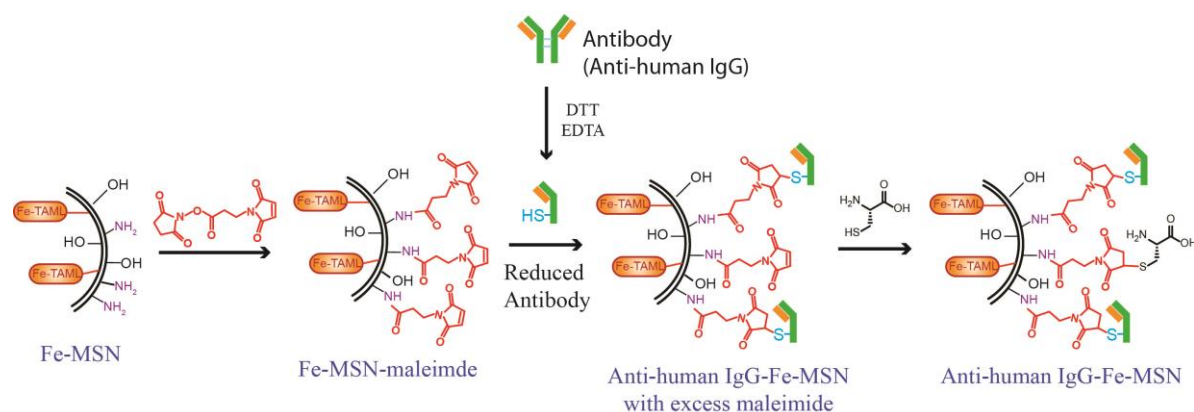


Figure 3.6 Synthesis of antihuman IgG-Fe-MSN

antihuman IgG-Fe-MSN, TMB and H₂O₂ were added. After 10 min, the reaction was quenched with addition of HCl and the absorbance at 450 nm was measured. Figure 3.5b shows the correlation between the signals generated at 450 nm vs human IgG concentration. The results show a linear relationship in the range of 10⁻¹² to 10⁻⁴ g/mL and the limit of detection is 10⁻¹² g/mL (6 × 10⁻¹⁵ M). Control experiments in which N₃-MSN or Fe-MSN was used as the probe in place of antihuman IgG-Fe-MSN showed no detectable signal. In the lowest detection limit, the signal was at least twice that was obtained when BSA was used instead of human IgG as a control. In contrast, when the same assay was carried out with commercially used antihuman IgG-HRP conjugate, linearity was only observed in the range of 10⁻⁸ to 10⁻⁴ g/mL (log [absorbance] vs log [human IgG]) and the LOD was 10⁻⁸ g/mL (6.7 × 10⁻¹¹ M).³⁸ In other words, the use of antihuman IgG-Fe-MSN allows us to probe a dynamic range of human IgG that is at least 4 orders of magnitude higher than that which can be probed with commercial antihuman IgG-HRP. Hence the ultrasensitive detection of human IgG at femtomolar concentrations can be achieved using our designed antihuman IgG-Fe-MSN. In comparison, the LOD for metal NP based peroxidase mimic (eg. Au@Pt 0.25) for the detection of mouse interleukin 2 (IL-2) has been reported to be ~ 10⁻¹¹ g/mL, which was 10-fold higher than that has been achieved by our system. In another approach, MSN with antibody immobilized on the outer surface and the enzyme glucose oxidase (GO) immobilized inside was used for detection of proteins.³⁹ The LOD for this system was observed to be 100 pg/mL. This is also 100 times higher than our reported construct. The low detection limit for our antihuman IgG-Fe-MSN is results of 25 000 extremely efficient

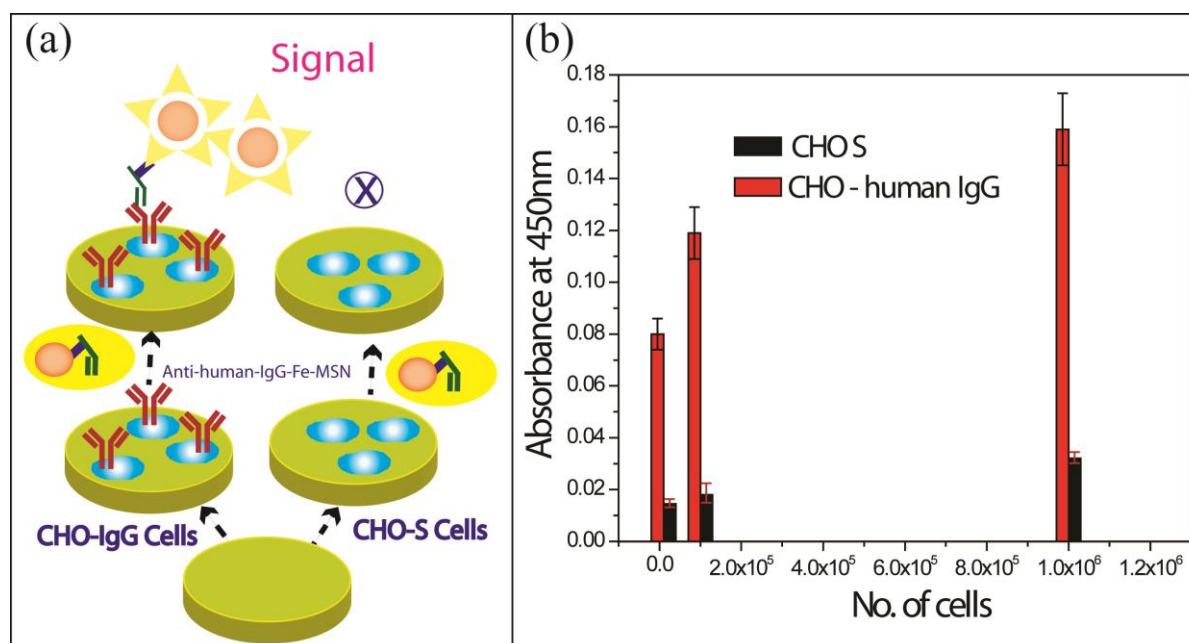


Figure 3.7 Human IgG detection in CHO-S and CHO-IgG cells (a) Schematic representation of the proposed strategy for cell detection in a 96-well plate. (b) Specificity and sensitivity of antihuman IgG-Fe-MSN for CHO-S and CHO-IgG cells were evaluated by assaying 10^5 , 10^4 and 10^3 cells/mL in a 96-well plate format. The error bars represent the standard deviation from triplicate measurements.

peroxidase mimic biuret modified Fe-TAML, which was immobilized inside MSN.

A major challenge in ultrasensitive detection of proteins in cells is the identification of specific proteins among a high background of interfering proteins that are present in real samples. To further evaluate if antihuman IgG-Fe-MSN could specifically detect human IgG from a high background of interfering proteins, we attempted the assay using two different cell lines of Chinese hamster ovary cells (CHO-S and CHO-IgG). CHO-IgG cell lines express human IgG while CHO-S cells do not express human IgG.³⁸ Both CHO-S and CHO-IgG cells were grown in suspension under 10% CO₂ atmosphere at 37 °C. Cells suspension was centrifuged and washed with an ice-cold PBS to remove the excess media. The cell pellet was lysed by suspension in ice-cold lysis buffer for 15 min and centrifuged, and the supernatant was collected for further assay. Supernatant containing CHO-S and CHO-IgG cells were diluted to 10^5 , 10^4 and 10^3 cells/mL and were plated on 96 well plates by incubation at 4 °C for 24 h. The plates were further incubated with antihuman IgG-Fe-MSN for another 1 h and

then washed several times to remove unbound antihuman IgG-Fe-MSN. Finally, TMB and H₂O₂ were added, the reaction was subsequently quenched with HCl and the absorbance of the resultant solution measured at 450 nm. The presence of a signal was only absorbed for CHO-IgG cells while for CHO-S cells no signal was observed (Figure 3.7). The signal to noise ratio for 10³ cells is at-least 4 folds. This conclusively demonstrates that antihuman IgG-Fe-MSN was able to detect human IgG selectively from high background of other proteins present in CHO cells.

3.5 CHARACTERISATIONS

3.5.1 Scanning and Transmission Electron Microscopy

Scanning electron microscopy (SEM) and transmission electron microscopy (TEM) images of 1-N₃-MSN, 5-N₃-MSN and NH₂-N₃-MSN are presented in Figures 3.8, 3.9 and 3.10 respectively. SEM and TEM showed formation of well-ordered two-dimensional hexagonal mesoporous particles with a spherical morphology having average particle size of ~40 nm.

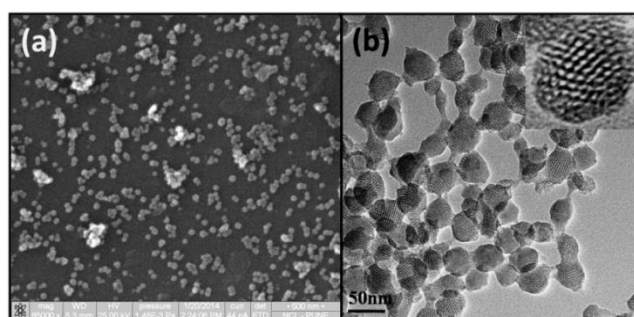


Figure 3.8 (a) SEM and (b) TEM images of 1-N₃-MSN

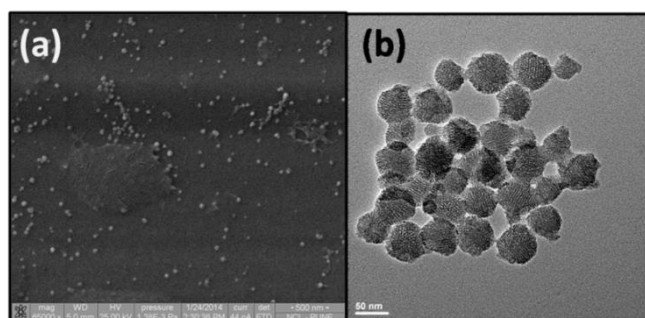


Figure 3.9 (a) SEM and (b) TEM images of 5-N₃-MSN

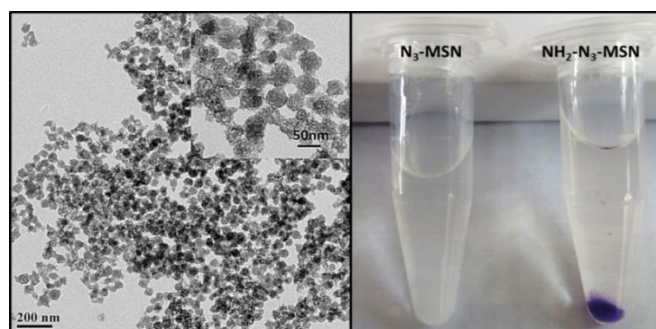


Figure 3.10 (a) TEM image of $\text{NH}_2\text{-N}_3\text{-MSN}$ shows the absence of clustering in mesoporous silica nanoparticles after surface modification. (b) Ninhydrin test before and after amine grafting on MSN. Formation of dark violet color confirms the presence of amine groups on the surface of MSN

3.5.2 Powder X-ray Diffraction

Powder X-ray diffraction patterns of the obtained mesoporous silica materials are shown in the Figure 3.11. All materials showed the characteristic high intensity (100) diffraction peak at $2\theta \sim 2.3^\circ$. The other significant peaks corresponding to (110) and (200) diffractions were also observed indicating that well-ordered one dimensional hexagonal mesoporous channels of MSN were formed and remained intact after functionalization.

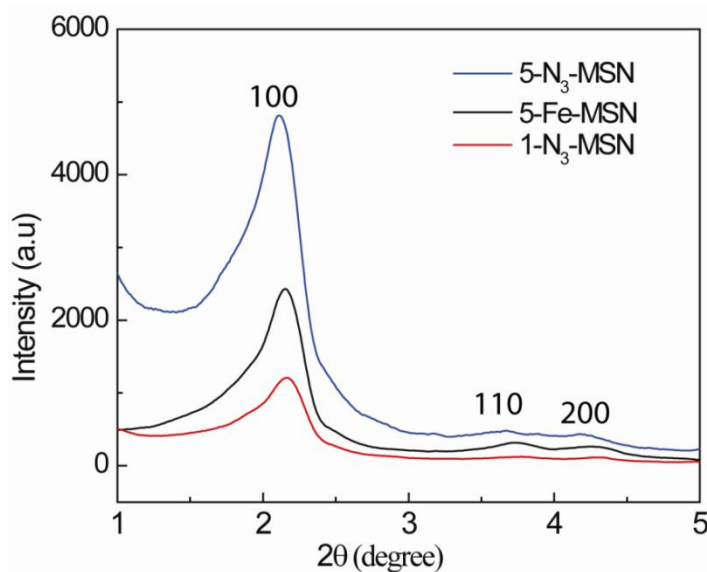


Figure 3.11 Powder XRD patterns of $1\text{-N}_3\text{-MSN}$, $5\text{-N}_3\text{-MSN}$ and 5-Fe-MSN .

3.5.3 Thermogravimetric Analysis

The TGA graphs of various MSNs materials are presented in the Figure 3.12. The amount of azido-propyl groups present in the N_3 -MSN were determined by the weight loss obtained in the thermogravimetric analysis (TGA). The samples were heated in air at $10\text{ }^\circ\text{C}/\text{minute}$ to $800\text{ }^\circ\text{C}$ so that the azidopropyl groups were completely decomposed and removed from the samples. Figure 3.12 b, c, d shows the TGA thermographs of the x - N_3 -MSN sample with the weight loss between $150 - 750\text{ }^\circ\text{C}$. The calcined MSNs (CAL-MSN) show a weight loss of about 14.3% , which can be attributed to the loss of water molecules strongly adsorbed to the silica surface as well as loss of water molecules due to condensation of silanol groups at high temperature. TGA analysis showed the amount of azidopropyl groups incorporated onto 1- N_3 -MSN, 5- N_3 -MSN and 10- N_3 -MSN for grafting of 1, 5 and 10% N_3 on MSN to be 0.14, 0.51 and 0.90 mmol/g respectively (Table 3.1, Figure 3.12).

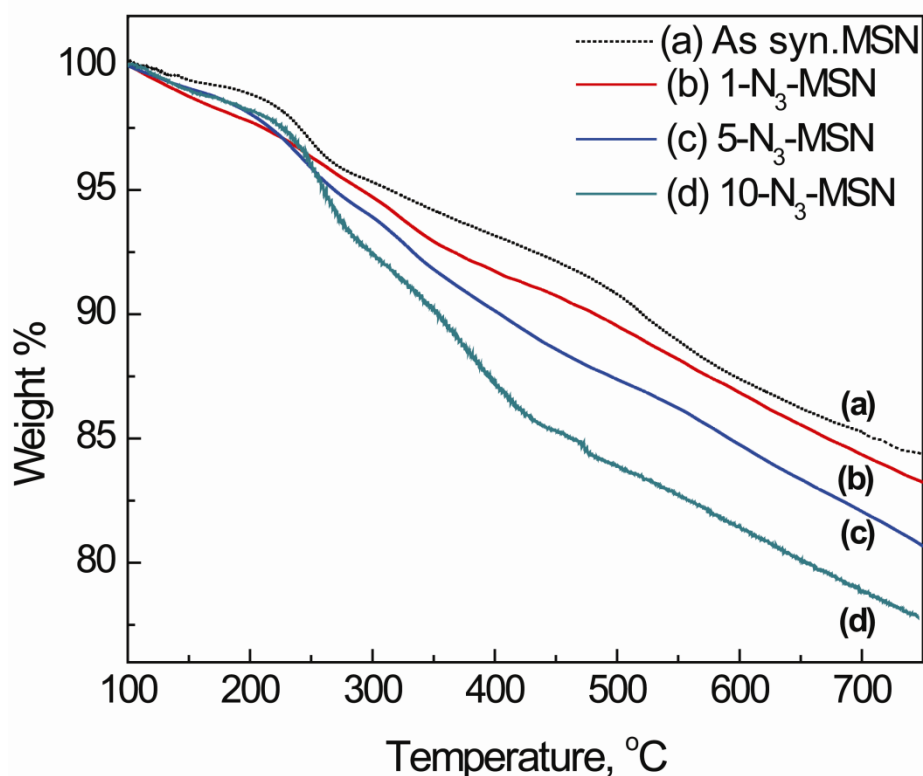


Figure 3.12 TGA for MSN before and after azide grafting. (a) As synthesized MSN, (b) 1- N_3 -MSN (c) 5- N_3 -MSN and (d) 10- N_3 -MSN stand

3.5.4 Nitrogen Adsorption-Desorption studies

The nitrogen adsorption-desorption isotherms of the 5-N₃-MSN is presented in Figure 3.13. Nitrogen adsorption-desorption isotherm of 5-N₃-MSN exhibit the characteristic type IV isotherm with slight increase in adsorption at P/P₀ 0.2-0.4 due to slight capillary condensation of the nitrogen in the mesopores. The BJH pore-size distribution (PSD) analysis shows very narrow PSD values in the range 3-4 nm. The pore diameter, BET surface area and pore volume are listed in Table 3.1.

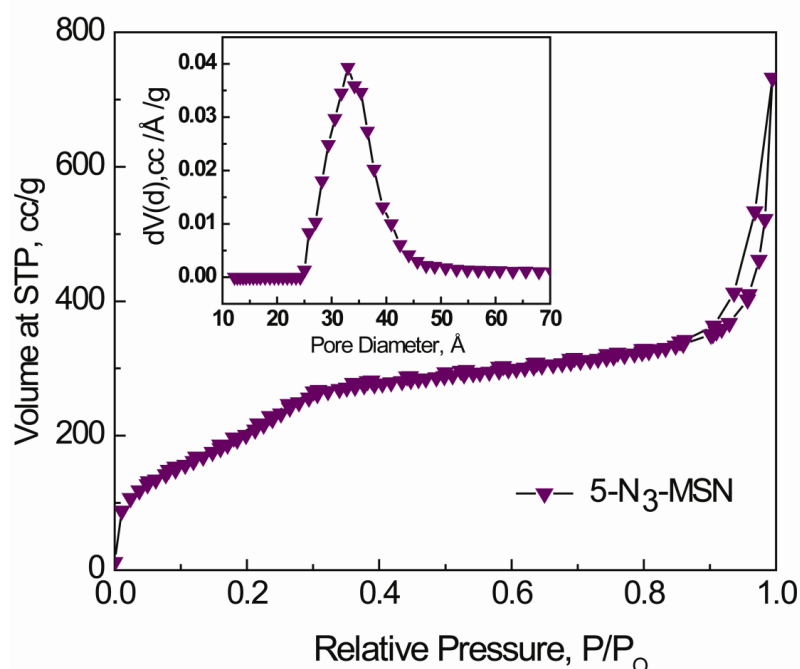


Figure 3.13 Nitrogen adsorption-desorption isotherms for 5-N₃-MSN (*inset* shows pore size distribution)

3.5.5 FT-IR Spectroscopy

The FT-IR spectra of various materials are presented in the Figure 3.13. The spectra of the 5-N₃-MSN display an absorbance at $\sim 2100\text{ cm}^{-1}$, which is the characteristic stretching vibration of an organic azide (Figure. 3.14a). The presence of this peak in the materials shows that the azidopropyl groups were successfully incorporated into N₃-MSN samples. The samples also showed absorbance peaks at 1230, 1080, 805 and 465 cm^{-1} respectively. These peaks are typical of Si-O-Si bands that are associated with the formation of the silica networks. Weak peaks associated with Si-OH groups in the 940-960 cm^{-1} range were also

observed for the functionalized mesoporous materials. The strong peak around 1658 cm^{-1} might be attributed to the bending vibration of H_2O . Thus, the FT-IR spectra indicate that the azido groups were efficiently incorporated in the matrix of the mesoporous silica nanoparticles by the one-pot condensation technique. IR spectroscopy shows about 95% decrease in the integrated intensity $\nu_{\text{as}}(\text{N}_3)$ at 2100 cm^{-1} (Figure. 3.14b and 3.14c).

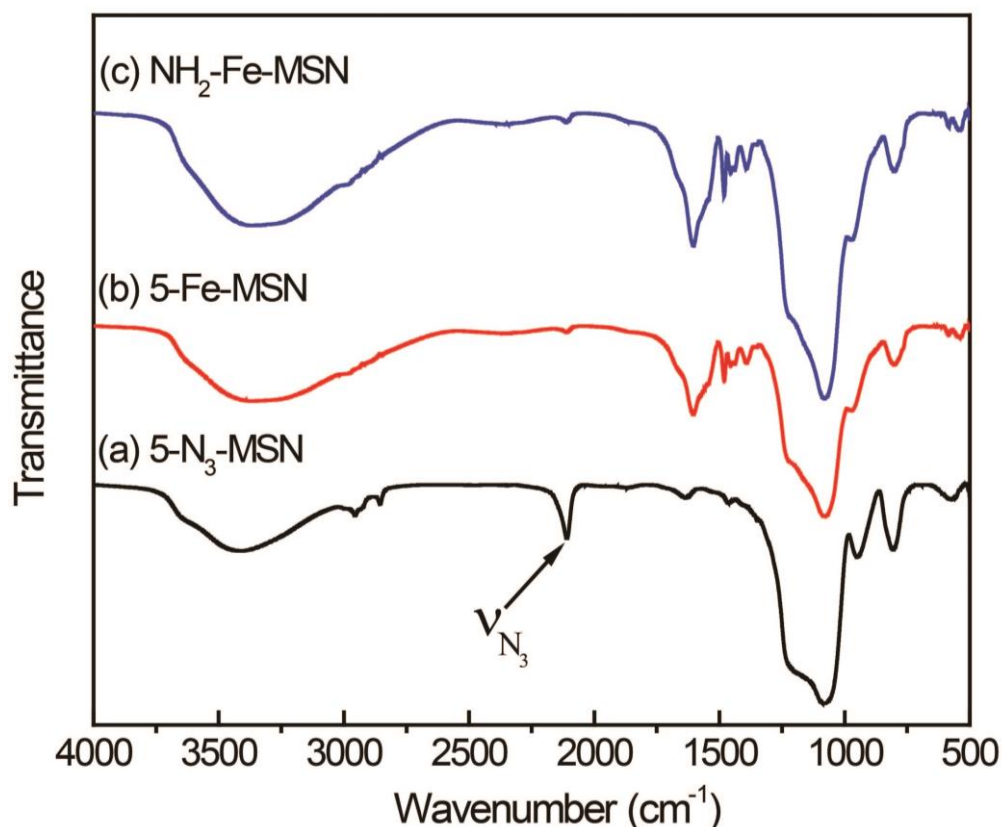


Figure 3.14 FT-IR spectra of (a) 5- N_3 -MSN and (b) 5-Fe-MSN (c) NH_2 -Fe-MSN

3.5.6 Solid State ^{13}C CP-MAS NMR Spectroscopy

The solid state ^{13}C CP-MAS NMR spectrum of the functionalized mesoporous materials has been represented in Figure 3.15. The spectrum of the as-synthesized azido-functionalized mesoporous material (as-synthesized 1- N_3 -MSN, Figure 3.15a) synthesized using co-condensation technique displays signals for the surfactant CTAB group. The peaks at ~ 21 and 78 ppm correspond to the peaks for the surfactant while the three peaks C1 (8.68 ppm), C2 (22 ppm), C3 (53 ppm) represent the three C-atoms of the azido-propyl chain in the

order as presented. ^{13}C CPMAS-NMR for 1- N_3 -MSN. NMR spectrum of 1- N_3 -MSN (a, black) showed three distinct peaks corresponding to the C1, C2 and C3 carbon atoms which is similar to three peaks present in azido-propyl silane (b, red) C1 (8.68 ppm), C2 (22 ppm), C3 (53 ppm).

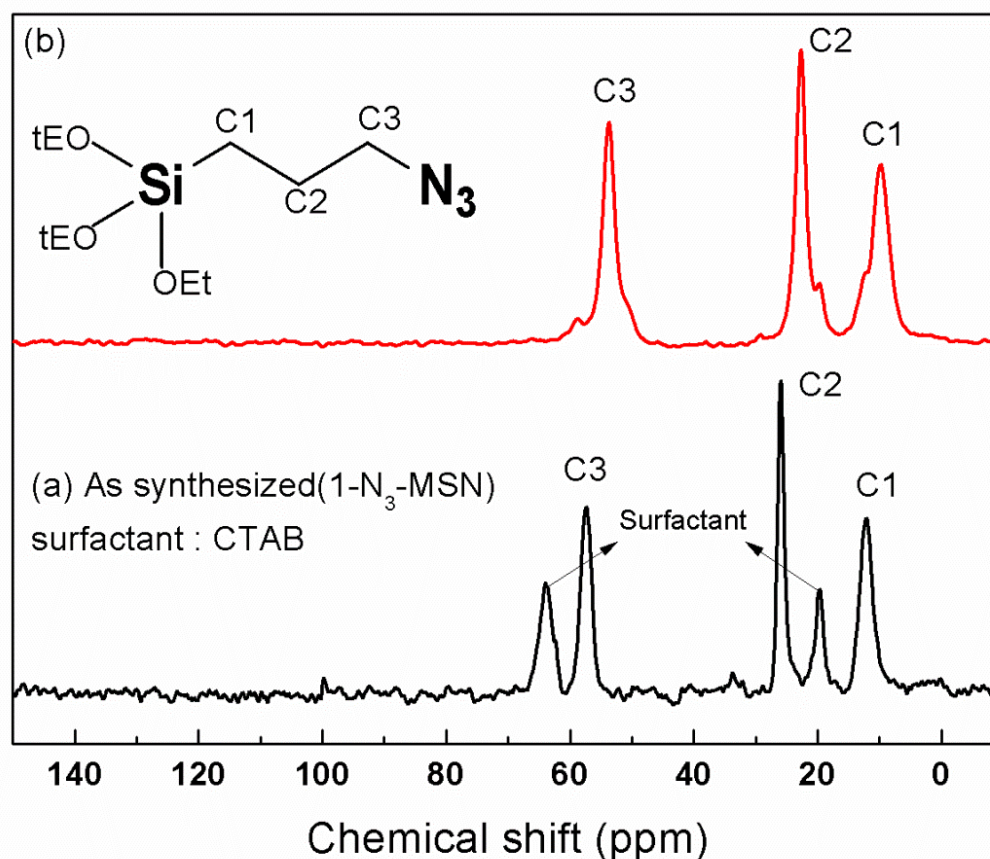


Figure 3.15 ^{13}C CPMAS-NMR for (a) as synthesized 1- N_3 -MSN. NMR (a, black) and (b) after template removal 1- N_3 -MSN (b, red).

3.6 CONCLUSIONS

In a biomimetic approach we have chemically attached ~25 000 highly active small molecule peroxidase mimic biuret modified Fe-TAML inside a 40 nm mesoporous nanoparticle. One of our constructs, 5-Fe-MSN, possess a $K_{\text{cat}}/K_{\text{m}}$ value that is ~2 300 fold higher in comparison to commercial HRP and 100-fold higher than metal/metal oxide NPs that have been reported. The presence of silanol groups in the outer surface of 5-Fe-MSN

allowed easy attachment of biotin and the antibody antihuman IgG. This surface modified 5-Fe-MSN was used for the ultrasensitive detection of proteins. Using antihuman IgG modified 5-Fe-MSN, we were able to detect femtomolar concentration of antihuman IgG. We were also able to quantify human IgG within a dynamic range of nanomolar to femtomolar concentrations. This represents a sensitivity that is 1000-fold higher than commercial antihuman IgG-HRP and 10-fold higher than any metal/metal oxide peroxidase mimic that has been reported to date. The understanding of the mechanism of the catalytic activity of biuret modified Fe-TAML will allow us to develop a new generation Fe-MSN, which will have increased catalytic efficiency. For example, Fe-TAML, which has a maximal activity at pH 7.4, can be used using design rules that have been developed by Collins.¹⁷ Such systems are currently under development in our laboratory.

3.7 REFERENCES

- 1) Marquez, L. A.; Dunford, H. B., Mechanism of the Oxidation of 3,5,3',5'-Tetramethyl-benzidine by Myeloperoxidase Determined by Transient- and Steady-State Kinetics. *Biochemistry* **1997**, *36*, 9349-9355.
- 2) Whitehead, T. P.; Thorpe, G. H. G.; Carter, T. J. N.; Groucutt, C.; Kricka, L. J., Enhanced Luminescence Procedure for Sensitive Determination of Peroxidase-Labelled Conjugates in Immunoassay. *Nature* **1983**, *305*, 158-159.
- 3) Engvall, E.; Perlmann, P., Enzyme-Linked Immunosorbent Assay (ELISA) Quantitative Assay of Immunoglobulin G. *Immunochemistry* **1971**, *8*, 871-874.
- 4) Nilsson, B., Enzyme-Linked Immunosorbent Assays. *Curr. Opin. Immunol.* **1989**, *2*, 898-904.
- 5) Zhang, Y.; Guo, Y.; Xianyu, Y.; Chen, W.; Zhao, Y.; Jiang, X., Nanomaterials for Ultra-sensitive Protein Detection. *Adv. Mater.* **2013**, *25*, 3802-3819.
- 6) Gopinath, S. C. B.; Tang, T.-H.; Citartan, M.; Chen, Y.; Lakshmipriya, T., Current Aspects in Immunosensors. *Biosens. Bioelectron.* **2014**, *57*, 292-302.
- 7) Gao, L.; Zhuang, J.; Nie, L.; Zhang, J.; Zhang, Y.; Gu, N.; Wang, T.; Feng, J.; Yang, D.; Perrett, S.; Yan, X., Intrinsic Peroxidase-like Activity of Ferromagnetic Nanoparticles. *Nat. Nanotechnol.* **2007**, *2*, 577-583.
- 8) Chen, W.; Chen, J.; Liu, A.-L.; Wang, L.-M.; Li, G.-W.; Lin, X.-H., Peroxidase-Like Activity of Cupric Oxide Nanoparticle. *Chem. Cat. Chem.* **2011**, *3*, 1151-1154.

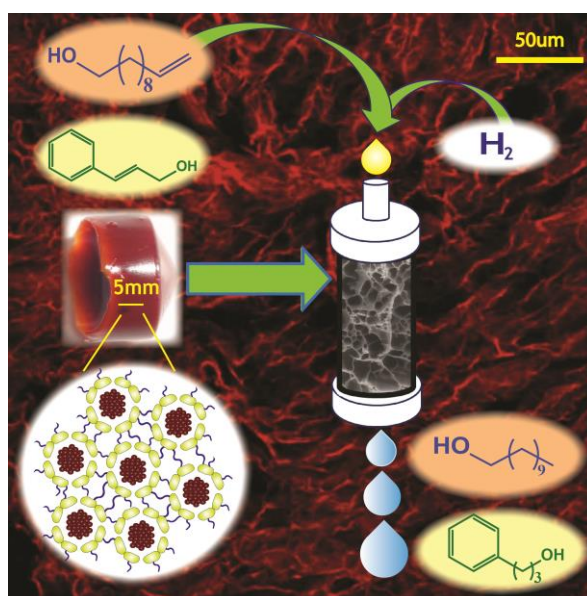
- 9) Asati, A.; Santra, S.; Kaittanis, C.; Nath, S.; Perez, J. M., Oxidase-Like Activity of Polymer-Coated Cerium Oxide Nanoparticles. *Angew. Chem. Int. Ed.* **2009**, *48*, 2308-2312.
- 10) Song, Y.; Qu, K.; Zhao, C.; Ren, J.; Qu, X., Graphene Oxide: Intrinsic Peroxidase Catalytic Activity and Its Application to Glucose Detection. *Adv. Mater.* **2010**, *22*, 2206-2210.
- 11) He, W.; Wu, X.; Liu, J.; Hu, X.; Zhang, K.; Hou, S.; Zhou, W.; Xie, S., Design of AgM Bimetallic Alloy Nanostructures (M = Au, Pd, Pt) with Tunable Morphology and Peroxidase-Like Activity. *Chem. Mater.* **2010**, *22*, 2988-2994.
- 12) He, W.; Liu, Y.; Yuan, J.; Yin, J.-J.; Wu, X.; Hu, X.; Zhang, K.; Liu, J.; Chen, C.; Ji, Y.; Guo, Y., Au@Pt Nanostructures as Oxidase and Peroxidase Mimetics for use in Immunoassays. *Biomaterials* **2011**, *32*, 1139-1147.
- 13) Lien, C.-W.; Huang, C.-C.; Chang, H.-T., Peroxidase-Mimic Bismuth-Gold Nanoparticles for Determining the Activity of Thrombin and Drug Screening. *Chem. Commun.* **2012**, *48*, 7952-7954.
- 14) A sphere of 30 nm Fe₃O₄ was crystallographically drawn and the number of Fe²⁺/Fe³⁺ atoms were estimated to be ~25000.
- 15) Popescu, D.-L.; Chanda, A.; Stadler, M.; de Oliveira, F. T.; Ryabov, A. D.; Münck, E.; Bominaar, E. L.; Collins, T. J., High-Valent First-Row Transition-Metal Complexes of Tetraamido (4N) and Diamidodialkoxido or Diamidophenolato (2N/2O) Ligands: Synthesis, Structure, and Magnetochemistry. *Coord. Chem. Rev.* **2008**, *252*, 2050-2071.
- 16) Ghosh, A.; Mitchell, D. A.; Chanda, A.; Ryabov, A. D.; Popescu, D. L.; Upham, E. C.; Collins, G. J.; Collins, T. J., Catalase–Peroxidase Activity of Iron(III)–TAML Activators of Hydrogen Peroxide. *J. Am. Chem. Soc.* **2008**, *130*, 15116-15126.
- 17) Ellis, W. C.; Tran, C. T.; Denardo, M. A.; Fischer, A.; Ryabov, A. D.; Collins, T. J., Design of More Powerful Iron-TAML Peroxidase Enzyme Mimics. *J. Am. Chem. Soc.* **2009**, *131*, 18052-18053.
- 18) Collins, T. J.; Gordon-Wylie, S. W., Long-Lived Homogenous Oxidation Catalysts. US Patent 5,847,120, December 8th, 1998.
- 19) Panda, C.; Ghosh, M.; Panda, T.; Banerjee, R.; Sen Gupta, S., Fe(III) Complex of Biuret-Amide Based Macrocyclic Ligand as Peroxidase Enzyme Mimic. *Chem. Commun.* **2011**, *47*, 8016-8018.

- 20) Ghosh, M.; Singh, K. K.; Panda, C.; Weitz, A.; Hendrich, M. P.; Collins, T. J.; Dhar, B. B.; Sen Gupta, S., Formation of a Room Temperature Stable Fe^V(O) Complex: Reactivity Toward Unactivated C–H Bonds. *J. Am. Chem. Soc.* **2014**, *136*, 9524–9527.
- 21) Malvi, B.; Panda, C.; Dhar, B. B.; Gupta, S. S., One Pot Glucose Detection by [Fe^{III}(biuret-amide)] Immobilized on Mesoporous Silica Nanoparticles: An Efficient HRP Mimic. *Chem. Commun.* **2012**, *48*, 5289-5291.
- 22) Panda, C.; Dhar, B. B.; Malvi, B.; Bhattacharjee, Y.; Gupta, S. S., Catalytic Signal Amplification using [Fe^{III}(biuret-amide)]-Mesoporous Silica Nanoparticles: Visual Cyanide Detection. *Chem. Commun.* **2013**, *49*, 2216-2218.
- 23) Panda, C.; Ghosh, M.; Panda, T.; Banerjee, R.; Sen Gupta, S., Fe(III) complex of biuret-amide based macrocyclic ligand as peroxidase enzyme mimic. *Chem. Commun.* **2011**, *47*, 8016-8018.
- 24) Malvi, B.; Sarkar, B. R.; Pati, D.; Mathew, R.; Ajithkumar, T. G.; Sen Gupta, S., "Clickable" SBA-15 mesoporous materials: synthesis, characterization and their reaction with alkynes. *J. Mater. Chem.* **2009**, *19*, 1409-1416.
- 25) Hong, V.; Presolski, S. I.; Ma, C.; Finn, M. G., Analysis and Optimization of Copper-Catalyzed Azide–Alkyne Cycloaddition for Bioconjugation. *Angew. Chem. Int. Ed.* **2009**, *48*, 9879-9883.
- 26) Song, H. Y.; Ngai, M. H.; Song, Z. Y.; MacAry, P. A.; Hobley, J.; Lear, M. J., Practical synthesis of maleimides and coumarin-linked probes for protein and antibody labelling via reduction of native disulfides. *Org. Biomol. Chem.* **2009**, *7*, 3400-3406.
- 27) Kang, S.; Mou, L.; Lanman, J.; Velu, S.; Brouillette, W. J.; Prevelige, P. E., Synthesis of biotin-tagged chemical cross-linkers and their applications for mass spectrometry. *Rapid Commun. Mass Spectrom.* **2009**, *23*, 1719-1726.
- 28) Lai, C.-Y.; Trewyn, B. G.; Jeftinija, D. M.; Jeftinija, K.; Xu, S.; Jeftinija, S.; Lin, V. S. Y., A Mesoporous Silica Nanosphere-Based Carrier System with Chemically Removable CdS Nanoparticle Caps for Stimuli-Responsive Controlled Release of Neurotransmitters and Drug Molecules. *J. Am. Chem. Soc.* **2003**, *125*, 4451-4459.
- 29) Mortera, R.; Vivero-Escoto, J.; Slowing, I. I.; Garrone, E.; Onida, B.; Lin, V. S. Y., Cell-induced intracellular controlled release of membrane impermeable cysteine from a mesoporous silica nanoparticle-based drug delivery system. *Chem. Commun.* **2009**, *22*, 3219-3221.

- 30) Josephy, P. D.; Eling, T.; Mason, R. P., The horseradish peroxidase-catalyzed oxidation of 3,5,3',5'-tetramethylbenzidine. Free radical and charge-transfer complex intermediates. *J. Biol. Chem.* **1982**, *257*, 3669-75.
- 31) Schlossbauer, A.; Schaffert, D.; Kecht, J.; Wagner, E.; Bein, T., Click Chemistry for High-Density Biofunctionalization of Mesoporous Silica. *J. Am. Chem. Soc.* **2008**, *130*, 12558-12559.
- 32) Nakazawa, J.; Stack, T. D. P., Controlled Loadings in a Mesoporous Material: Click-on Silica. *J. Am. Chem. Soc.* **2008**, *130*, 14360-14361.
- 33) Josephy, P. D.; Eling, T.; Mason, R. P., The Horseradish Peroxidase-Catalyzed Oxidation of 3,5,3',5'-tetramethylbenzidine. Free Radical and Charge-Transfer Complex Intermediates. *J. Biol. Chem.* **1982**, *257*, 3669-75.
- 34) Ellis, W. C.; Tran, C. T.; Roy, R.; Rusten, M.; Fischer, A.; Ryabov, A. D.; Blumberg, B.; Collins, T. J., Designing Green Oxidation Catalysts for Purifying Environmental Waters. *J. Am. Chem. Soc.* **2010**, *132*, 9774-9781.
- 35) Chanda, A.; Shan, X.; Chakrabarti, M.; Ellis, W. C.; Popescu, D. L.; Tiago de Oliveira, F.; Wang, D.; Que, L.; Collins, T. J.; Münck, E.; Bominaar, E. L., (TAML)Fe^{IV}=O Complex in Aqueous Solution: Synthesis and Spectroscopic and Computational Characterization. *Inorg. Chem.* **2008**, *47*, 3669-3678.
- 36) Gupta, S. S.; Stadler, M.; Noser, C. A.; Ghosh, A.; Steinhoff, B.; Lenoir, D.; Horwitz, C. P.; Schramm, K.-W.; Collins, T. J., Rapid Total Destruction of Chlorophenols by Activated Hydrogen Peroxide. *Science* **2002**, *296*, 326-328.
- 37) Michael Green, N., In *Methods in Enzymology*, eds. Meir, W.; Edward, A. B., Eds. Academic Press: 1990; Vol. 184, pp51-67.
- 38) Pradhan, K.; Gadgil, M., Effect of Addition of 'Carrier' DNA During Transient Protein Expression in Suspension CHO Culture. *Cytotechnology* **2012**, *64*, 613-622.
- 39) Eum, J. Y.; Hwang, S. Y.; Ju, Y.; Shim, J. M.; Piao, Y.; Lee, J.; Kim, H.-S.; Kim, J., A Highly Sensitive Immunoassay using Antibody-Conjugated Spherical Mesoporous Silica with Immobilized Enzymes. *Chem. Commun.* **2014**, *50*, 3546-3548.

Chapter 4

Macroporous Scaffold from Transition Metal Nanoparticles for Continuous Flow Reactions



In this chapter, large (centimeter-sized) self-standing macroporous scaffold monoliths from ferritin bionanoparticles has been synthesized using dynamic templating of surfactant H_1 domains. The iron oxide inside the ferritin scaffold can be easily replaced with catalytically active monodisperse zero valent transition metal nanoparticles. The monoliths containing active palladium or iron oxide nanoparticles inside apo-ferritin bio-nanoparticles were used as a recyclable heterogeneous catalyst.

Part of the work discussed in this chapter has been published in

*“Large Centimeter-Sized Macroporous Ferritin Gels as Versatile Nanoreactors” S. Kumari, A. Kulkarni, G. Kumaraswamy, S. Sen Gupta, *Chemistry of Materials*, **2013**, 25, 4813-4819.*

4.1 INTRODUCTION

In the last several years, bionanoparticles such as the iron storage protein ferritin and the tobacco mosaic virus have emerged as versatile building blocks for the formation of functional nanostructured assemblies.¹⁻³ The nanoparticles have a layered structure comprised of a self-assembled protein shell surrounding a core that can contain nucleic acid, protein and inorganic material. Recent advances in protein engineering, allow incorporation of enzymes,⁴ transition metal catalysts⁵ and zero valent late transition metal nanoparticles^{6,7} into these structures. Such modified bionanoparticles are well suited to perform chemical transformations due to the presence of the catalytically active core while the protein shell modulates the entrance and egress of substrate and products.⁵⁻⁷

The iron-storage protein ferritin represents one of the smallest but most practical of these nanoparticles. Its 24 protein subunits self-assemble to form a 12 nm diameter cage with an interior cavity of 8 nm diameter containing a ≈ 5 nm iron oxide core.⁸ Ferritin has been used for catalysis, biosensing, the template synthesis of nanomaterials, and biomedical applications.^{5, 9, 10}

Organized higher-order assemblies of nanoparticles provide templates that can be exploited for nano-technological applications and ferritin has proven popular in these endeavours due to its ready availability on large scale and the ease of its interior mineralization. Metal ion mediated self-assembled one-dimensional nanostrands of ferritin have shown applications as nanofiltration membranes for ultrafast water permeation.¹¹ Ferritin readily assembles into two-dimensional lattices at the air-water interface¹² and on solid substrates.¹³ Ferritin-polymer conjugates, including ferritin, has also been assembled in oil-in-water (o/w) and water-in-oil (w/o) pickering emulsions to form capsule like structures.¹⁴ Well-defined three-dimensional architectures are more challenging and have attracted considerable recent attention. The first report of chemically cross-linked clusters of ferritin in solution employed biotin-streptavidin linkages to create colloidal aggregates.¹⁵ More recently, composite materials containing ferritin have been shown to have interesting properties.¹⁶⁻¹⁸ Electrospun fibers of polyvinyl alcohol-ferritin composites form nanofibrous hydrogels, that have been used as bioactuators.¹⁹ Vinylated ferritin has also been copolymerized with acrylamide to form a hydrogel.²⁰

The formation of large monolith gels from biomolecular nanoparticles has not been reported till date. Such materials would combine the advantages of cage-like nanoparticles (the ability to sequester a variety of cargo in monodisperse and robust protein cages), with

those afforded by a highly porous three-dimensional architecture, facilitating transport of substrate and products to and from the functional cages. An obvious application for such macroporous, three-dimensional materials is continuous flow biocatalytic chemistry.

Kumarswamy et al. have recently demonstrated a general route to the preparation of macroscopic scaffolds by dynamic templating of surfactant hexagonal phase (H_1) domains.²¹
²² On cooling, below the isotropic- H_1 transition temperature ($T_{HI} \approx 44$ °C), the particle dispersions in 1:1 mixtures of non-ionic surfactant $C_{12}E_9$ and water, forms networks of particles that are jammed at the H_1 domain interfaces. Cross-linking the particles followed by removal of surfactant template by extensive water washing results in the formation of macroporous scaffolds. They have previously demonstrated that macropore dimensions can be varied over 2 orders of magnitude and that pores can be readily oriented by gentle shearing. Thus, dynamic templating is a powerful technique to produce macroporous scaffolds of a variety of nanoparticles.

Previously use of glutaraldehyde cross-linked ferritin in this procedure gave small (~several hundred micrometers in size), brittle and unstable structures in water. Here I am demonstrating a significantly improved protocol that allows the synthesis of large self-standing macroporous monolith gel from ferritin for the first time. These three-dimensionally connected strands of ferritin are robust and demonstrate enhanced thermal stability and tolerance of organic solvents. Organization of ferritin into scaffolds dramatically simplifies the purification protocols associated with replacement of the iron oxide nanoparticle inclusion by catalytically active zerovalent transition metal nanoparticles. Further, I demonstrate heterogeneously catalyzed synthesis of organic compounds using monoliths of Fe_2O_3 or Pd-loaded ferritin. The scaffold macropores minimize pressure drop across the monolith while facilitating substrate and reagent transport. Finally, immobilization of Pd@apo-ferritin scaffolds inside a continuous flow hydrogenation reactor that allows fast hydrogenation of alkenes in quantitative yields has been demonstrated.

4.2 EXPERIMENTAL SECTION

4.2.1 Materials

Ferritin from equine spleen, apo-ferritin, nonionic surfactant, nonaethylene glycol monododecyl ether, C₁₂E₉, N, N'-Dimethyl-1, 3-propanediamine, N-(3-dimethylaminopropyl)-N'-ethylcarbodiimide hydrochloride (EDC-HCl), Poly(ethylene glycol) diglycidyl ether (Mol. wt. 514), potassium tetrachloropallidate, potassium gold(III) chloride and sodium borohydride were used as received from Sigma Aldrich. Dialysis tubing (MWCO 12 KDa) was purchased from Aldrich. All the other chemicals and solvents were purchased from Merck India.

4.2.2 Synthesis

4.2.2.1 Ferritin Modification

Ferritin or apo-ferritin nanoparticles were functionalized with secondary amino groups by conjugation of N, N'-dimethyl-1, 3-propanediamine (DMPA) to aspartic and glutamic acid residues on the external surface of ferritin using carbodiimide activation. Typically, 2 mL of a 2 M aqueous solution of DMPA was adjusted to pH 6 using 6 M HCl, and then added drop wise to a stirred solution of ferritin or apo-ferritin (50 mg/mL). Subsequently 224 mg of N-(3-dimethylaminopropyl)-N'-ethylcarbodiimide hydrochloride (EDC-HCl) was added and pH was maintained using dilute HCl, and then the solution was stirred for further 6 h. After the completion of the reaction, solutions were then centrifuged to remove any precipitate and the supernatant was dialyzed at 4 °C against 1000 mL of 0.15 M NaCl for 24 h and then extensively against Milli-Q quality water to produce stable solutions of cationic DMPA functionalized ferritin or apo-ferritin.

4.2.2.2 General Procedure for the Synthesis of Macroporous Hydrogel Using Ferritin Based Nanoparticles

Typically, a 10% (by weight) 55 mg of aqueous dispersion of ferritin was added to surfactant C₁₂E₉ (45 mg, calculated such that the surfactant to water ratio was 1:1) and homogenized in

a water bath at 50 °C. To this poly(ethylene glycol) diglycidyl ether (4 mg) was added and the sample was then cooled to room temperature in a feedback controlled convective oven. The particle concentration in the overall composite is ~10 wt%. The sample was then allowed to cross-link on standing at room temperature for 24 h. Finally, the scaffold was washed repeatedly with water (6-7 times) to remove the surfactant and afford the free-standing three-dimensional macroporous material.

4.2.2.3 Synthesis of Apo-ferritin Scaffold from Ferritin Scaffold

An apo-ferritin scaffold was prepared by demineralization of ferritin scaffold by following the reported procedure.²³ Ferritin scaffold was placed in 200 mL of sodium acetate buffer 0.1 M, pH 4.5 and purged with nitrogen for 30 min. Then 100 µL of thioglycolic acid (TGA) was added while continuously purging with N₂. After 2 h, further 100 µL of TGA was added, and the N₂ purge was continued for another hour. Finally, fresh buffer was added and the N₂ purge was continued for another hour before the scaffold was taken in 500 mL of 0.15 M NaCl and dialyzed against saline water for a day at 4 °C.

4.2.2.4 Synthesis of Palladium Nanoparticle Encapsulated Apo-ferritin Scaffold (Pd@apo-ferritin)

An apo-ferritin scaffold was incubated with 5 mL of 0.1 M NaCl/H₂O and then the pH was adjusted to 8.5 with 0.01 N NaOH, followed by the addition of aliquots of 500 µL of 30 mM K₂PdCl₄ solution for 2 h. Subsequently, the scaffold was washed with water, followed by immediate reduction with NaBH₄ solution (100 µmol in water) and incubated for an additional 2 h. Finally, the scaffold was extensively washed with deionized water under sonication several times to remove physically adsorbed Pd nanoparticles.

4.2.2.5 Control Experiment in Absence of Surfactant

To an aqueous solution of 100 mg of 8% (by weight) of ferritin or apo-ferritin nanoparticles functionalized with secondary amino groups was added 8 mg of poly(ethyleneglycol)-diglycidyl ether and allowed to crosslink on standing at room temperature for 48 h.

4.2.2.6 General Procedure for Oxidation of 2, 3, 6-trimethylphenol to trimethyl-1, 4-benzoquinone Using Ferritin Scaffold

The oxidation of 2, 3, 6 trimethylphenol (TMP) was performed in a sealed tube containing 1 mg of ferritin scaffold in 1 mL of MeCN at 70 °C for 24 h. The reaction was initiated by adding 0.14 mmol of H₂O₂ to the reaction mixture containing 0.05 mmol TMP. After completion of the reaction, the amount of TMP consumed and product formed was estimated by GC and GC-MS. The scaffold was reused for next cycle after pipetting out the reaction mixture.

4.2.2.7 General Procedure for Suzuki-Miyaura Cross-Coupling Reaction Using Pd@apo-ferritin Scaffold

Suzuki-Miyaura cross-coupling reaction was investigated with Pd@apo-ferritin scaffold at 75 °C for 18 h in water. The reaction was performed in an aqueous solution (1 mL), which contained aryl halide (0.023 mmol), phenylboronic acid (0.048 mmol), NaOH (0.092 mmol) as a base and Pd@apo-ferritin scaffold (3 mg) as a catalyst. The reaction mixture was pipetted out to a separate scaffold, and the product was extracted with chloroform. The amount of starting materials consumed and product formed was estimated by GC and GC-MS. Scaffold was again incubated with fresh batch of reactants to carry out recyclability of the scaffold.

4.2.2.8 Oxidation of TMB (3, 3', 5, 5'-Tetramethylbenzidine) Using Ferritin Scaffold in the Continuous Flow

The scaffold was immobilized inside a glass capillary (2.5 mm i.d.). The porous volume inside the scaffold that was available for flow of liquid was found to be 47.5 µL. The value was obtained based on the area averaged dimensions of the pores from the SEM image. Phosphate buffer (1.5 mL, 50 mM, pH 5.2) containing TMB solution (100 µL of 50 mM), H₂O₂ solution (10 µL of 8 M) was passed through a scaffold having length of 1 cm at a flow rate of 0.5 mL min⁻¹. Catalytic oxidation of TMB by ferritin scaffold in the presence of H₂O₂ yields a blue colored solution 3, 3', 5, 5'-Tetramethylbenzidine diimine.

4.2.2.9 Calculation

(a) Mol% of Pd nanoparticles relative to substrate for Suzuki - Miyaura cross-coupling reaction

$$\begin{aligned}\text{No of atoms in Pd nanoparticles} &= \left(\frac{4}{3}\pi R_{Pd\ np}^3 / \frac{4}{3}\pi R_{Pd\ atom}^3 \right) \times 0.75 \\ &= (1.35)^3 / 0.137^3 \times 0.75 \\ &= 717 \text{ atoms}\end{aligned}$$

$$\begin{aligned}1.17 \mu\text{mol of Pd} &= 1.63 \times 10^{-3} \mu\text{mol of Pd nanoparticles} \\ (1.17 \mu\text{mol Pd from ICP for 3 mg Pd@apo-ferritin scaffold})\end{aligned}$$

$$\begin{aligned}\text{Substrate/ Catalyst} &= 23 \mu\text{mol} / 1.63 \times 10^{-3} \mu\text{mol} \\ &= 14110\end{aligned}$$

$$\text{For mol\% of catalyst / substrate} = (1/ 14110) \times 100 = 0.007 \text{ mol\%}$$

(b) Turnover for hydrogenation of cinnamyl alcohol with Pd@apo-ferritin

$$\begin{aligned}\text{Turnover of substrate per Pd nanoparticles} &= (597 \mu\text{mol} / 35.1 \mu\text{mol}) \times 717 \\ &= 12195\end{aligned}$$

$$\text{Cinnamyl alcohol} = 597 \mu\text{mol}, \text{Pd@apo-ferritin} = 35.1 \mu\text{mol}$$

4.3 CHARACTERISATION TECHNIQUES

Ferritin and Pd@apo-ferritin scaffold were freeze-dried and imaged using a Quanta 200 3D scanning electron microscope (SEM). TEM measurements were done at 100 kV on an FEI Technai F30. An LSM 710 Carl Zeiss laser scanning confocal microscope (LSCM) was used to image the fluorescent samples. FT-IR spectra were recorded on a Perkin-Elmer FT-IR spectrum GX instrument by making KBr pellets. Pellets were prepared by mixing 3 mg of sample with 97 mg of KBr.

Gas chromatography were performed on an Agilent 7890 instrument equipped with a hydrogen flame ionization detector and HP-5 capillary column (30 m × 0.32 mm × 0.25 μm,

J & W Scientific) and nitrogen was used as carrier gas at a flow rate of 1 mL/min. The injector and detector temperature were maintained at 250 °C and operated in splitless mode. GC-MS were performed on Agilent 5975 C mass selective detector interfaced with Agilent 7890A GC in similar conditions using a HP-5-MS capillary column (30 m × 0.32 mm × 0.25 μm, J & W Scientific). Reaction mixtures were quantified from a standard calibration curve that was plot using pure reactants and products.

ICP experiments were performed on a Thermo IRIS Intrepid spectrum apparatus. The typical procedure used was freeze-drying of sample (3 mg) followed by dissolving in 1 mL of aqua regia. The resultant solution was diluted to 50 mL, and the quantitative analysis of Fe and Pd in scaffold was performed using ICP.

The continuous flow experimental setup for TMB (3, 3', 5, 5'-Tetramethylbenzidine) oxidation consisted of the capillary in which the scaffold was immobilized, syringe pump for pumping the fluid at constant flow rate, a digital manometer (AZ-Instruments), diffused light for back illumination and a high resolution camera (Sony α-37 with DT 18–55 mm lens). The inlet of the capillary had a Y-shape such that one segment was connected to the pump while the second segment was attached to an inline digital manometer. The pressure drop across the capillary was measured using a digital manometer and the reaction progress was monitored by visually tracking the color change. The capillary was held vertical and the flow was downward to facilitate sample collection.

Continuous flow hydrogenation was carried out using H³ system of Thales Nano Ltd., where the catalyst (60 mg of Pd@apo-ferritin) was immobilized inside a stainless steel cylindrical cartridge. In a typical hydrogenation reaction, a continuous-flow of alkene cinnamyl alcohol (80 mg in 50 mL methanol) was combined with hydrogen (generated in-situ from the electrolysis of water) and was passed through the cartridge packed with Pd@apo-ferritin at 30 °C and 29 bar pressure. The flow rate of the alkenes was maintained at 0.2 mL/min and the product was collected continuously into a collection tube. The methanol was subsequently removed and the product was quantified using ¹H NMR.

Rheological measurements were made using the ARES, a rotary parallel plate controlled strain rheometer from TA Instruments. Ferritin gel samples were prepared as 8mm disks and were loaded on the rheometer for oscillatory measurements. Measurements were done on wet hydrogels at room temperature (25 °C), and care was taken to minimize the evaporation of water during the experiment. At first, a strain sweep was performed by increasing the strain from 0.5 to 100% at a frequency of 10 rad s⁻¹ and then frequency sweep

from 1 to 100 rad s⁻¹ at a strain amplitude of 0.75% has been performed.

Small angle X-ray scattering was performed on a Bruker-Nanostar, equipped with a rotating anode (Cu K α radiation), three pinhole collimation and a 2D multiwire (HiStar) detector (calibrated using silver behenate standards). Data was collected from the wet ferritin hydrogel loaded in a thin (10 μ m) walled quartz capillary. The data was circularly averaged, and the 1D scattered intensity is presented after background subtraction, corrected for sample transmission. Small-angle X-ray scattering (SAXS) data was analyzed using SASFIT.

4.4 RESULTS AND DISCUSSION

4.4.1 Synthesis and Characterization of Large Centimeter-Sized Macroporous Ferritin Scaffold.

Stable chemical linkages and high cross-linking density are required to make large scaffolds with the mechanical properties required for solid biocatalysts. Because the ferritin surface displays relatively few amine groups (the pI of the particle is 4.5), we hypothesized that the limited mechanical and aqueous stability of ferritin scaffolds prepared using glutaraldehyde followed by NaCNBH₃ treatment was due to low cross-linking density between nanoparticles. We therefore converted the carboxylate groups of aspartic and glutamic acid residues on horse spleen ferritin to secondary amino groups by carbodiimide-mediated conjugation with N, N'-dimethyl-1, 3-propanediamine (DMPA).²⁴ Using this methodology, about 240 secondary amine groups were installed on the surface of the ferritin nanoparticle. The resulting amine functionalized particles (8 wt% aqueous dispersion) was assembled into a macroporous scaffold using dynamic templating by ring-opening of the terminal epoxide groups of a poly(ethylene glycol) diglycidyl ether cross-linker (Figure 4.1), as reported earlier.²²

Removal of the surfactant by extensive water washing gave self-standing 3-D macroporous ferritin scaffolds as soft gels, approximately 1 cm long (Figure 4.1A). No sign of gelation was observed in analogous reactions in which surfactant was omitted, suggesting that protein localization at the H₁ domain boundaries is critical for efficient cross-linking and formation of macroporous materials.

The ferritin-based gel material was characterized in several ways. Scanning electron

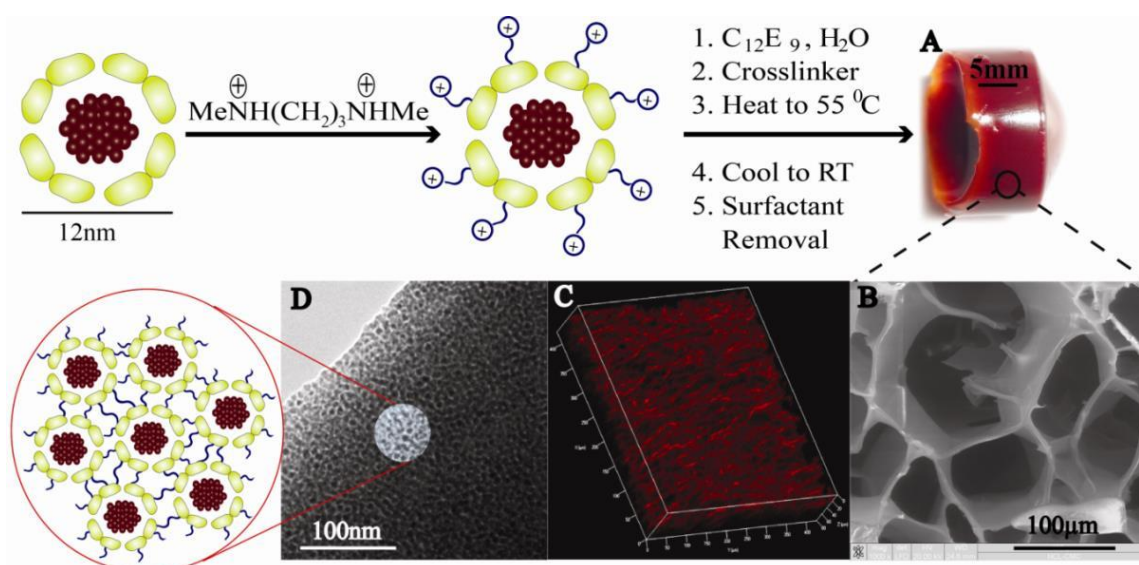


Figure 4.1 Synthesis of porous ferritin scaffold proceeds via ferritin cationisation using N, N'- dimethyl-1, 3-propanediamine followed by dynamic templating to assemble the ferritin nanoparticles into a three dimensional macroporous scaffold (A) Photograph of ferritin scaffold (B) SEM image of cross linked self-standing scaffold after template removal (C) Confocal micrograph image of self standing apo-ferritin scaffold (D) TEM image of a section of scaffold (phosphotungstic acid stained).

microscopy (SEM) obtained after freeze-drying the ferritin scaffold revealed a network structure comprised of a dense mesh of strands, with an average strand thickness of about 4.0 µm (Figure 4.1B). Image analysis of multiple representative SEM micrographs showed an average macropore diameter of ≈55 µm (Figure 4.1B, see appendix III; Figure C 1). To study the bulk three-dimensional structure of the ferritin network, the scaffold was made with apo-ferritin and examined by confocal microscopy using the protein's natural fluorescence. The resulting images showed the apo-ferritin scaffold as thick strands organized into networks with pore dimensions ≈55 µm (Figure 4.1C, Appendix III; Figure C 2).

The organization of the ferritin in the scaffold was investigated using small-angle X-ray scattering (SAXS) (Figure 4.2A). SAXS from a dilute dispersion of ferritin is shown next to that from the scaffold, for ease of comparison (Figure 4.2A). The scattered intensity from the ferritin dispersion was fitted to a model for monodisperse core shell particles with a core radius of 2.6 nm and a shell thickness of 2.8 nm. Details of the fit are provided in the Appendix III; Figure C 3). Scattering from the ferritin scaffolds showed a peak around 0.07

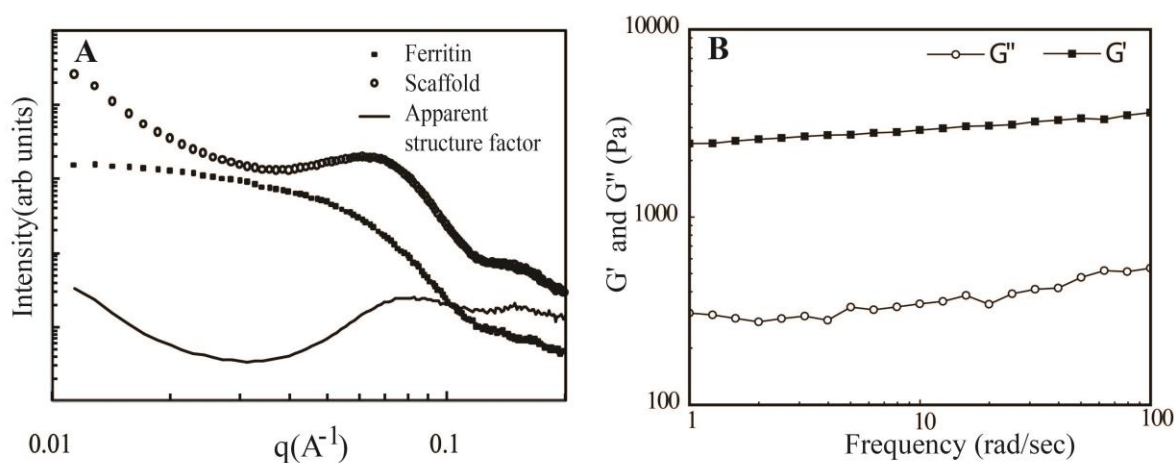


Figure 4.2 (A) SAX scattering curves for native ferritin 5 wt%, ferritin scaffold and apparent structure factor. At low q large increase in the scattering indicates that ferritin nanoparticles are aggregating. (B) Frequency sweep of Ferritin @0.75% strain. Rheology study was done using ferritin scaffold in water.

\AA^{-1} , that arises from the aggregation of individual ferritin units in the network (Figure 4.2A). An apparent structure factor was obtained by dividing the scattering from the scaffold by the scattering from the dilute ferritin dispersion. This apparent structure factor shows a power law decay at low q , with $S_A(q) \sim q^{-3.3}$, suggesting a surface fractal structure for the “walls” of the ferritin network. The correlation peak is modelled using an interference function similar to previous literature reports,²⁵ which gives an interparticle distance of 7.1 nm (see appendix III; Figure C 4). This value is smaller than the ferritin size obtained from the dilute dispersion SAXS (10.3 nm), in accordance with a previous report on metal mediated assemblies of cage-like proteins.²⁶ Transmission electron microscopy (TEM) showed the scaffold walls to be composed of ferritin assemblies, with the protein corona encapsulating dark 4-5 nm iron oxide cores (Figure 4.1D). Energy-dispersive X-ray spectroscopy (EDX) analysis of the ferritin scaffold showed the presence of Fe and P from the iron oxide/phosphate cores of the protein as well as S from the protein (see appendix III; Figure C 5). Dynamic rheological tests indicate the gel-like nature of the ferritin hydrogels. From frequency sweep measurements to characterize the mechanical response of the gel, we observe that the solid modulus (G') exceeds the loss modulus (G'') by about an order of magnitude over the entire experimental frequency range 1-100 rad s^{-1} (Figure 4.2B). This indicates a largely elastic

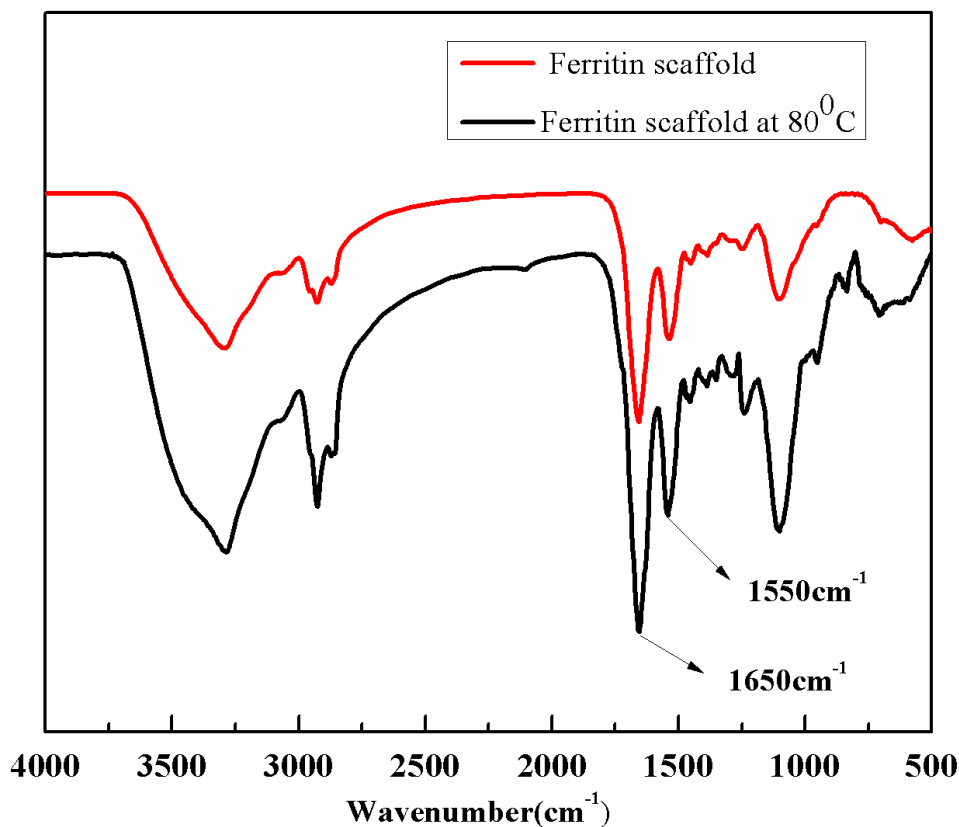


Figure 4.3 FT-IR spectra of ferritin scaffold (1) and ferritin scaffold (2) after 24 h kept at 80 °C in CH₃CN

response to small deformations, characteristic of the network structure of a gel. The solid modulus shows a weak frequency dependence ($G' \sim \omega^{0.08}$), and $\tan \delta = G''/G'$ is approximately frequency independent, as expected for a gel. The solid modulus is around 3000 Pa, indicating that the ferritin network forms a soft hydrogel. The intact nature of the protein shells was suggested by FTIR, which showed peaks at 1650 cm⁻¹ and 1550 cm⁻¹ (amide I and amide II bands) consistent with the retention of ferritin's characteristic α -helical secondary structure^{16, 18} (Figure 4.3). We have also evaluated the stability of this scaffold toward various solvents and elevated temperatures. The macroporous ferritin scaffold was found to be stable toward overnight storage at room temperature in acetonitrile, ethanol, and toluene, and toward incubation in acetonitrile at 80 °C for 24 h (Figure 4.3).

4.4.2 Synthesis of Pd Nanoparticle Embedded Apo-Ferritin Scaffold

Apo-ferritin is known to function in solution as a nanoreactor for the synthesis of encapsulated monodisperse transition metal nanoparticles such as Pd and Au in its core.⁷ A variation of the published metalation procedure was used to install Pd nanoparticles in the macroscopic apo-ferritin gel. Instead of making the gel from the apo-protein, the regular ferritin monoliths were demineralized by incubation with thioglycolic acid.²³ The 3D structure of the resulting colorless material was unchanged by SEM and confocal microscopy; EDX analysis showed complete removal of Fe (see appendix III, Figure C 6). Incubation of the apo-ferritin scaffold with Pd²⁺ salt followed by reduction with NaBH₄ solution led to the formation of encapsulated Pd(0) in the ferritin cages comprising the gel material, indicated by a change in color of the entire scaffold to black. Extensive washing

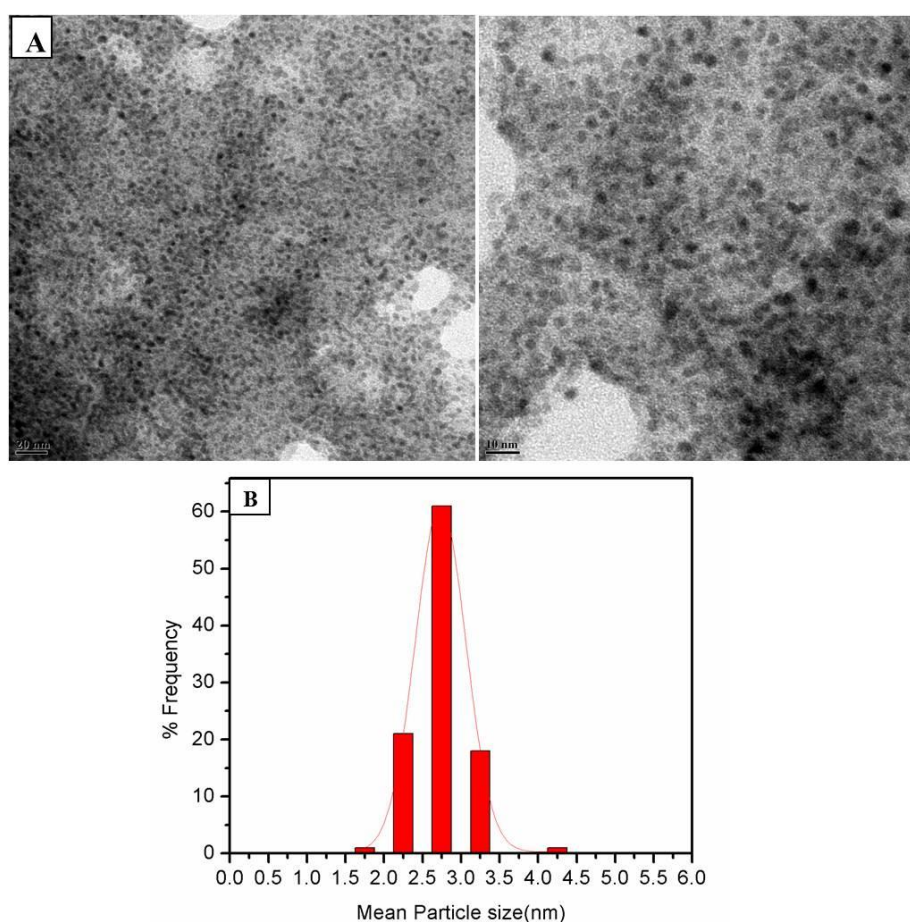


Figure 4.4 (A) TEM image of Pd nanoparticles inside scaffold (B) TEM micrograph of Pd NPs (average size 2.70 ± 0.006 nm) according to *image J* software

with water and organic solvents was performed to remove metallic Pd formed by uncontrolled reduction on the outer surface of the particles. ICP data showed 0.12 mg Pd per mg of scaffold before washing and 0.047 mg per mg of scaffold after washing. TEM of this purified Pd@apo-ferritin composite material showed presence of relatively monodisperse Pd nanoparticles of 2-3 nm diameter inside the apo-ferritin corona (Figure 4.4). The ease and reproducibility of this procedure stands in marked contrast to the preparation of Pd-filled ferritin proteins in solution.⁷ In those cases, purification after Pd encapsulation is laborious and requires several chromatographic purification steps to separate the desired Pd@apo-ferritin from Pd nanoparticles formed in solution.

4.4.3 Catalytic Activity of Ferritin for Oxidation Reaction

Stability of Ferritin scaffold toward various solvents and elevated temperatures, encouraged us to test the applicability of ferritin-encapsulated metal catalysts as heterogeneous catalysts in oxidation and C-C bond formation reactions, previously found to be performed by iron oxide nanoparticles.²⁷ Most of these reactions have been limited to the use of water-soluble substrates since native ferritin protein denatures and precipitates in pure organic solvents. Also, examples of surface modified ferritin which displays stability in nonpolar organic solvent are rare and their catalytic activity has not been studied.²⁸ The organic stability of the cross-linked materials allowed us to test the oxidation of the hydrophobic substrate 2, 3, 6-trimethyl phenol (TMP, only sparingly soluble in water at neutral pH) to its corresponding quinone, trimethyl-1, 4-benzoquinone (TMQ), a key intermediate for the industrial production of vitamin E (Figure 4.5). TMP (0.05 mmol) and H₂O₂ (3 equiv) were added to the ferritin scaffold (1 mg; 2.5 μmol Fe) in acetonitrile and the reaction mixture was heated at 80 °C. The formation of quinone was indicated by a change in solution color to dark yellow. GC and GC-MS analysis of the reaction mixture showed that approximately 80% of the starting TMP was consumed, approximately 72% of which was converted to the desired product TMQ (see Appendix III; Figure C 7, Table 4.1). No TMQ was observed in control reactions omitting either H₂O₂ or the ferritin scaffold. ICP analysis revealed no iron in solution, suggesting that the reaction was catalyzed by the iron oxide nanoparticles present in the scaffold and not by iron salts leached out during the reaction. FT-IR analysis showed the same spectra before and after completion of reaction, showing no gross change in protein secondary structure during the first cycle. There covered ferritin

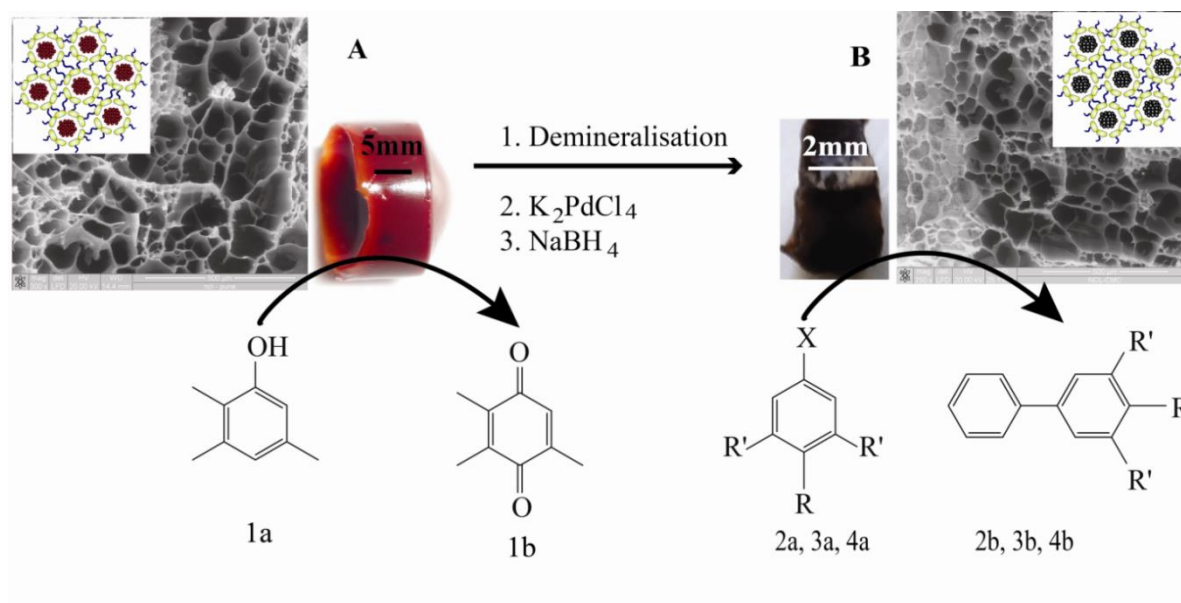


Figure 4.5 Synthesis of Pd@apo-ferritin scaffold via demineralization of ferritin scaffold followed by encapsulation of Pd nanoparticles inside the core of apo-ferritin. The scaffolds were used for the oxidation of **1(a)** 2, 3, 6-trimethylphenol and for the Suzuki-Miyaura cross-coupling reaction. **2a** ($R=NH_2$, $R'=H$, $X=I$), **3a** ($R=OCH_3$, $R'=H$, $X=Br$), **4a** ($R=OCH_3$, $R'=OCH_3$, $X=Br$).

scaffold was then used as a catalyst for two more cycles, with no change in product yield (Table 4.1). In contrast, the attempted oxidation of TMP to TMQ using the native ferritin protein and H_2O_2 (in water at $80\text{ }^\circ\text{C}$), gave rise to $< 10\%$ of the expected amount of TMQ. GC-MS analysis revealed the formation of 2,2',3,3',5,5'-hexamethyl-[1,1'-biphenyl]-4,4'-diol as a side product, indicative of radical based C–C coupling (see Appendix III; Figure C 7).

Furthermore, ferritin protein precipitated during the course of the reaction, indicating denaturation under the reaction conditions. Taken together, these data suggest that the cross-linked macroporous ferritin scaffold is a true reusable heterogeneous catalyst for the synthesis of TMQ with several advantages. It allows the reaction to be carried out in acetonitrile and at a high temperature while retaining the structural integrity of the scaffold.

4.4.4 Catalytic Activity Pd@apo-ferritin Scaffold for Suzuki–Miyaura Cross Coupling Reaction

Similarly, the Pd@apo-ferritin scaffold was evaluated in the Suzuki-Miyaura cross-coupling reaction of p-substituted iodoaniline and phenylboronic acid in water (Figure 4.4), a process known to be catalyzed by other Pd nanoparticles.⁷ Incubation of iodoaniline (2a) with phenylboronic acid in water containing the Pd@apo-ferritin scaffold (1.17 μmol Pd, 0.007 mol % of Pd nanoparticle relative to (2a) at 75 °C overnight gave rise to the product amino-biphenyl (2b) in 87% yield. As in the case of the native ferritin scaffolds, neither leaching of Pd nor a change in the secondary structure of the ferritin coat protein was observed, and at least two addition cycles of catalysis could be performed without change (Table 4.1). As expected, TEM of the scaffold after the reaction showed no agglomeration of the Pd nanoparticles (see Appendix III; Figure C.8), which would otherwise occur if they were not shielded by the cage protein. The Suzuki-Miyaura cross-coupling reaction was also extended to the substituted anilines 3a and 4a with similar product yields (Figure 4.5).

Table 4.1 Oxidation and Suzuki-Miyaura cross coupling reaction with ferritin and Pd@apo-ferritin[‡].

Entry	Reactant	Product	Cycle	Conversion (%)	Yield [†] (%)
1	1a	1b	1 st	79	72
2	1a	1b	2 nd	79	70
3	1a	1b	3 rd	75	70
4	2a	2b	1 st	78	87
5	2a	2b	2 nd	74	83
6	2a	2b	3 rd	72	83
7	3a	3b	1 st	75	81
8	4a	4b	1 st	71	80

[†]Yield was calculated based on % conversion. [‡]For entry 1-3 Ferritin scaffold was used while for entry 4-8 Pd@apo-ferritin scaffold was used.

4.4.5 Macroporous Scaffold for Continuous Flow Synthesis

In the pharmaceutical and fine chemicals industries, process intensification through conversion of traditional batch processes to continuous flow operation is receiving significant attention.²⁹ As in many flow processes, we anticipated that our ferritin-based gels would allow enhanced heat and mass transfer, due to the hydrodynamics of flow through the random pore structure without significant back pressure restrictions, a consequence of the high porosity of the gel microstructure. To test this, oxidation of colorless TMB to its one-electron oxidized blue product was performed in the presence of H₂O₂,³⁰ using the ferritin scaffold immobilized inside a glass capillary, as shown in Appendix III; Figure C 9. The reactant was passed through the capillary at different flow rates using a syringe pump. The pressure drop across the capillary was a modest ≈ 0.0039 atm for a monolith of 1 cm length. The reaction progress was monitored by visually tracking the color change. For the scaffold having >90% porous flow volume, the reaction was seen to proceed even for a residence time of 5.5 s. We were able to carry out these transformations for several hours in continuous flow mode without change in catalyst activity or scaffold structure.

Having established that our ferritin gel monoliths can combine the advantages of continuous flow operation with low pressure drops, we employed Pd@apo-ferritin gels for an industrially important organic transformation, the continuous flow hydrogenation of alkenes (Figure 4.6). Using the H³ system (Thales Nano Ltd.) at 30 °C and 29 bar pressure (see Appendix III, Figure C 10) three substrates were hydrogenated as shown in Table 4.2 were characterised by ¹H NMR (see Appendix III; Figure C 11-13). The use of 60 mg of monolith allowed the quantitative hydrogenation of 80 mg of each substrate in 50 mL methanol (flow rate 0.2 mL min⁻¹), representing approximately 12195 turnovers of substrate per Pd nanoparticles (calculation shown in the section 4.2.2.9).

For cinnamyl alcohol (Table 4.2, entry 2), the yield of the reaction remained unchanged (99%) for an additional 15 reaction cycles. Continuous flow transfer hydrogenation with palladium nanoparticle loaded microreactor monolithic glass/polymer composite has been demonstrated previously.³¹ However, upon progression of the reaction the Pd nanoparticles leached out and the rate of leaching was dependent on the polarity of the solvent and acidity. However, I have demonstrated that Pd nanoparticles inside the Pd@apo-ferritin scaffold does not leach out under demanding reaction conditions and 15 catalytic cycles of hydrogenation, without any loss of reactivity.

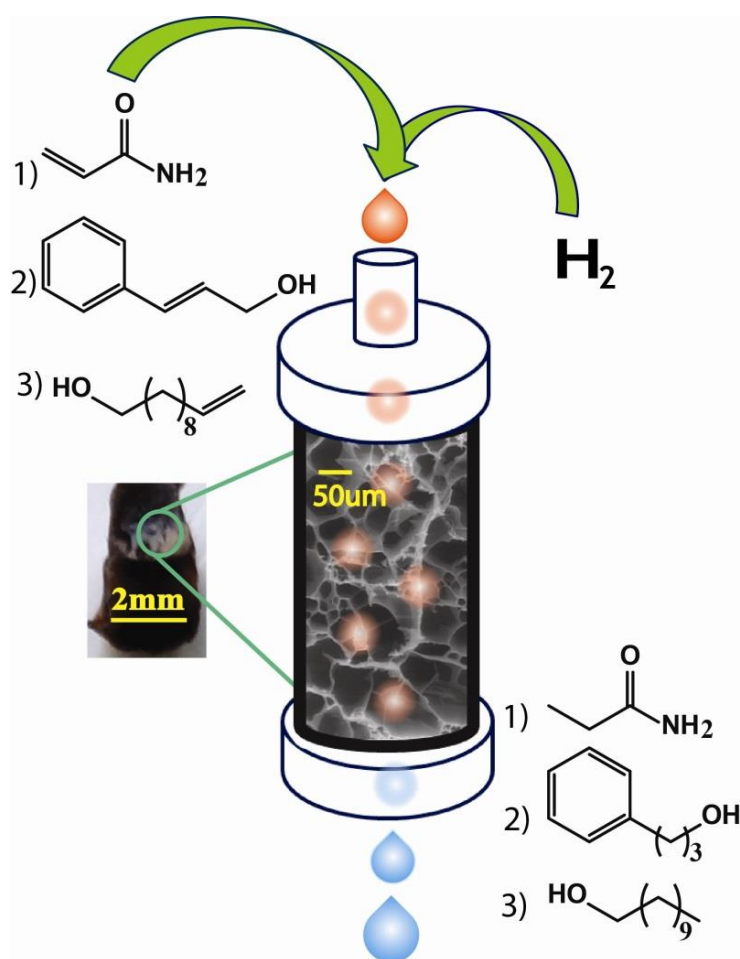


Figure 4.6 Schematic representation for the continuous flow hydrogenation reaction of different substrates with immobilized Pd@apoferritin scaffold using H^3 system (Thales Nano Ltd)

Table 4.2 Hydrogenation of Alkenes Using Pd@apo-ferritin under Continuous Flow Reactions

Entry	Olefins	Alkanes	Yield (%)
1	<chem>CH2=CHCONH2</chem>	<chem>CH3CH2CONH2</chem>	99
2	<chem>PhCH=CHCH2OH</chem>	<chem>Ph(CH2)3OH</chem>	99
3	<chem>CH2=CH(CH2)7OH</chem>	<chem>CH3(CH2)8OH</chem>	99

4.5 CONCLUSION

In summary, I have demonstrated the synthesis of large (centimeter-sized) self standing macroporous scaffold monoliths from ferritin bionanoparticles. The monolith allows easy replacement of iron oxide nanoparticles with other catalytically active late transition metal nanoparticles such as Pd, facilitating the catalysis of several organic transformations both in batch and continuous mode. This demonstration illustrates several practical advantages to solution-phase nanoparticle-based catalysis, including (i) synthesis and metal-swapping procedures performed without the need for tedious chromatographic purification; (ii) high stability of encapsulated metal nano-particles against leaching under the reaction conditions, enabling to use in continuous flow configuration. The methodology for monolith preparation is general and should allow the synthesis of macroporous scaffolds from polymer coated metal nanoparticles as well, although it will be interesting to see what differences may emerge when the component particles are not as monodisperse as the protein nanocages used here.

4.6 REFERENCES

- 1) Uchida, M.; Klem, M. T.; Allen, M.; Suci, P.; Flenniken, M.; Gillitzer, E.; Varpness, Z.; Liepold, L. O.; Young, M.; Douglas, T. Biological Containers: Protein Cages as Multifunctional Nanoplatforms. *Adv. Mater.* **2007**, *19*, 1025-1042. (b) de la Escosura, A.; Nolte, R. J. M.; Cornelissen, J. J. L. M. Viruses and Protein Cages as Nanocontainers and Nanoreactors. *J. Mater. Chem.* **2009**, *19*, 2274-2278. (c) Jutz, G.; Böker, A. Bionanoparticles as Functional Macromolecular Building Blocks-A New Class of Nanomaterials. *Polymer* **2011**, *52*, 211-232.
- 2) Meldrum, F. C.; Wade, V. J.; Nimmo, D. L.; Heywood, B. R.; Mann, S. Synthesis of Inorganic Nanophase Materials in Supramolecular Protein Cages. *Nature* **1991**, *349*, 684-687. (b) Liu, Z.; Qiao, J.; Niu, Z.; Wang, Q. Natural Supramolecular Building Blocks: from Virus Coat Proteins to Viral Nanoparticles. *Chem. Soc. Rev.* **2012**, *41*, 6178-6194.
- 3) Douglas, T.; Young, M. Viruses: Making Friends with Old Foes. *Science* **2006**, *312*, 873-875. (b) Douglas, T.; Strable, E.; Willits, D.; Aitouchen, A.; Libera, M.; Young,

- M. Protein Engineering of a Viral Cage for Constrained Nanomaterials Synthesis. *Adv. Mater* **2002**, *14*, 415-418.
- 4) Comellas-Aragones, M.; Engelkamp, H.; Claessen, V. I.; Sommerdijk, N. A. J. M.; Rowan, A. E.; Christianen, P. C. M.; Maan, J. C.; Verduin, B. J.M.; Cornelissen, J. J. L. M.; Nolte, R. J. M. A Virus-Based Single-Enzyme Nanoreactor. *Nat Nano*. **2007**, *2*, 635-639. (b) Fiedler, J. D.; Brown, S. D.; Lau, J. L.; Finn, M. G. RNA-Directed Packaging of Enzymes within Virus-like Particles. *Angew. Chem. Int. Ed.* **2010**, *49*, 9648-9651.
- 5) Abe, S.; Niemeyer, J.; Abe, M.; Takezawa, Y.; Ueno, T.; Hikage, T.; Erker, G.; Watanabe, Y. Control of the Coordination Structure of Organometallic Palladium Complexes in an Apo-Ferritin Cage. *J. Am. Chem. Soc.* **2008**, *130*, 10512-10514.
- 6) Douglas, T.; Young, M. Host-Guest Encapsulation of Materials by Assembled Virus Protein Cages. *Nature* **1998**, *393*, 152-155. (b) Kramer, R.M.; Li, C.; Carter, D. C.; Stone, M. O.; Naik, R. R. Engineered Protein Cages for Nanomaterial Synthesis. *J. Am. Chem. Soc.* **2004**, *126*, 13282-13286.
- 7) Douglas, T.; Dickson, D. P. E.; Betteridge, S.; Charnock, J.; Garner, C. D.; Mann, S. Synthesis and Structure of an Iron(III) Sulfide-Ferritin Bioinorganic Nano- composite. *Science* **1995**, *269*, 54-57. (b) Ueno, T.; Suzuki, M.; Goto, T.; Matsumoto, T.; Nagayama, K.; Watanabe, Y. Size-Selective Olefin Hydrogenation by a Pd Nanocluster Provided in an Apo-Ferritin Cage. *Angew. Chem. Int. Ed.* **2004**, *116*, 2581-2584. (c) Fan, R.; Chew, S. W.; Cheong, V. V.; Orner, B. P. Fabrication of Gold Nanoparticles Inside Unmodified Horse Spleen Apo-Ferritin. *Small* **2010**, *6*, 1483-1487. (d) Aime, S.; Frullano, L.; Geninatti Crich, S. Compartmentalization of a Gadolinium Complex in the Apo-Ferritin Cavity: A Route To Obtain High Relaxivity Contrast Agents for Magnetic Resonance Imaging. *Angew. Chem. Int. Ed.* **2002**, *41*, 1017-1019.
- 8) Clegg, G. A.; Stansfield, R. F. D.; Bourne, P. E.; Harrison, P.M. Helix Packing and Subunit Conformation in Horse Spleen Apo-Ferritin. *Nature* **1980**, *288*, 298-300.
- 9) Kim, S.-E.; Ahn, K.-Y.; Park, J.-S.; Kim, K. R.; Lee, K. E.; Han, S.-S.; Lee, J. Fluorescent Ferritin Nanoparticles and Application to the Aptamer Sensor. *Anal. Chem.* **2011**, *83*, 5834-5843. (b) Li, K.; Zhang, Z.-P.; Luo, M.; Yu, X.; Han, Y.; Wei, H.-P.; Cui, Z.-Q.; Zhang, X.-E. Multifunctional Ferritin Cage Nanostructures for Fluorescence and MR imaging of Tumor Cells. *Nanoscale* **2012**, *4*, 188-193.

- (c) Zhen, Z.; Tang, W.; Guo, C.; Chen, H.; Lin, X.; Liu, G.; Fei, B.; Chen, X.; Xu, B.; Xie, J. Ferritin Nanocages To Encapsulate and Deliver Photosensitizers for Efficient Photodynamic Therapy against Cancer. *ACS Nano* **2013**.
- 10) (a) Lin, X.; Xie, J.; Niu, G.; Zhang, F.; Gao, H.; Yang, M.; Quan, Q.; Aronova, M. A.; Zhang, G.; Lee, S.; Leapman, R.; Chen, X. Chimeric Ferritin Nanocages for Multiple Function Loading and Multimodal Imaging. *Nano Letters. Nano Letters* **2011**, *11*, 814-819. (b) Uchida, M.; Flenniken, M. L.; Allen, M.; Willits, D. A.; Crowley, B. E.; Brumfield, S.; Willis, A. F.; Jackiw, L.; Jutila, M.; Young, M. J.; Douglas, T. Targeting of Cancer Cells with Ferrimagnetic Ferritin Cage Nanoparticles. *J. Am. Chem. Soc.* **2006**, *128*, 16626-16633.
- 11) Peng, X.; Jin, J.; Nakamura, Y.; Ohno, T.; Ichinose, I. Ultrafast Permeation of Water Through Protein-Based Membranes. *Nat Nano.* **2009**, *4*, 353-357.
- 12) (a) Yamaki, M.; Matsubara, K.; Nagayama, K. A Thin Liquid Layer on the Surface of Mercury as a Matrix of a Flow-Mediated Two-Dimensional Assembly of Proteins. *Langmuir* **1993**, *9*, 3154-3158. (b) Yuan, Z.; Petsev, D. N.; Prevo, B. G.; Velev, O. D.; Atanassov, P. Two-Dimensional Nanoparticle Arrays Derived from Ferritin Monolayers. *Langmuir* **2007**, *23*, 5498-5504.
- 13) Hu, Y.; Chen, D.; Park, S.; Emrick, T.; Russell, T. P. Guided Assemblies of Ferritin Nanocages: Highly Ordered Arrays of Monodisperse Nanoscopic Elements. *Adv. Mater.* **2010**, *22*, 2583-2587.
- 14) (a) van Rijn, P.; Mougin, N. C.; Franke, D.; Park, H.; Boker, A. Pickering Emulsion Templated Soft Capsules by Self-assembling Cross-Linkable Ferritin-Polymer Conjugates. *Chem. Commun.* **2011**, *47*, 8376-8378. (b) Russell, J. T.; Lin, Y.; Böker, A.; Su, L.; Carl, P.; Zettl, H.; He, J.; Sill, K.; Tangirala, R.; Emrick, T.; Littrell, K.; Thiagarajan, P.; Cookson, D.; Fery, A.; Wang, Q.; Russell, T. P. Self-Assembly and Cross-Linking of Bionanoparticles at Liquid-Liquid Interfaces. *Angew. Chem. Int. Ed.* **2005**, *44*, 2420-2426. (c) Mougin, N.C.; van Rijn, P.; Park, H.; Müller, A. H. E.; Böker, A. Hybrid Capsules via Self-Assembly of Thermoresponsive and Interfacially Active Bionanoparticle-Polymer Conjugates. *Adv. Funct. Mater.* **2011**, *21*, 2470-2476.
- 15) Li, M.; Wong, K. K. W.; Mann, S. Organization of Inorganic Nanoparticles Using Biotin-Streptavidin Connectors. *Chem. Mater.* **1998**, *11*, 23-26.
- 16) Lambert, E. M.; Viravaidya, C.; Li, M.; Mann, S. Microemulsion-Mediated Self-Assembly and Silicification of Mesoporous Ferritin Nanocrystals. *Angew. Chem.*

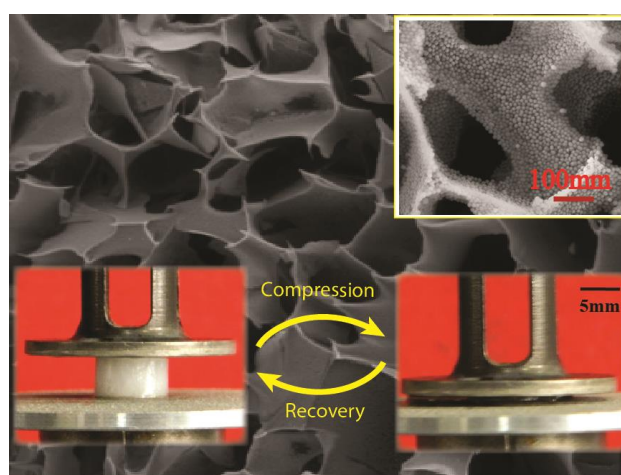
- Int. Ed.* **2010**, *49*, 4100-4103. (b) Sharma, K. P.; Collins, A. M.; Perriman, A. W.; Mann, S. Enzymatically Active Self-Standing Protein-Polymer Surfactant Films Prepared by Hierarchical Self-Assembly. *Adv.Mater.* **2013**, *25*, 2005-2010.
- 17) Srivastava, S.; Samanta, B.; Jordan, B. J.; Hong, R.; Xiao, Q.; Tuominen, M. T.; Rotello, V. M. Integrated Magnetic Bionanocomposites through Nanoparticle-Mediated Assembly of Ferritin. *J. Am. Chem. Soc.* **2007**, *129*, 11776-11780. (b) Kostianen, M. A.; Ceci, P.; Fornara, M.; Hiekkataipale, P.; Kasyutich, O.; Nolte, R.J. M.; Cornelissen, J. J. L.M.; Desautels, R. D.; van Lierop, J. Hierarchical Self-Assembly and Optical Disassembly for Controlled Switching of Magnetoferritin Nanoparticle Magnetism. *ACS Nano* **2011**, *5*, 6394-6402.
- 18) Qu, X.; Kobayashi, N.; Komatsu, T. Solid Nanotubes Comprising α -Fe₂O₃ Nanoparticles Prepared from Ferritin Protein. *ACS Nano* **2010**, *4*, 1732-1738.
- 19) Shin, M. K.; Spinks, G. M.; Shin, S. R.; Kim, S. I.; Kim, S. J. Nanocomposite Hydrogel with High Toughness for Bioactuators. *Adv. Mater.* **2009**, *21*, 1712-1715
- 20) Lee, E. J.; Ahn, K.-Y.; Lee, J.-H.; Park, J.-S.; Song, J.-A.; Sim, S. J.; Lee, E. B.; Cha, Y. J.; Lee, A. Novel Bioassay Platform Using Ferritin-Based Nanoprobe Hydrogel. *Adv. Mater.* **2012**, *24*, 4739-4744.
- 21) Sharma, K. P.; Kumaraswamy, G.; Ly, I.; Mondain-Monval, O. Self-Assembly of Silica Particles in a Nonionic Surfactant Hexagonal Mesophase. *J. Phys. Chem. B* **2009**, *113*, 3423-3430. (b) Sharma, K. P.; Ganai, A. K.; Gupta, S. S.; Kumaraswamy, G. Self-Standing Three-Dimensional Networks of Nanoparticles With Controllable Morphology by Dynamic Templating of Surfactant Hexagonal Domains. *Chem. Mater.* **2011**, *23*, 1448-1455.
- 22) Ganai, A. K.; Kumari, S.; Sharma, K. P.; Panda, C.; Kumaraswamy, G.; Gupta, S. S. Synthesis of Functional Hybrid Silica Scaffolds with Controllable Hierarchical Porosity by Dynamic Templating. *Chem. Comm.* **2012**, *48*, 5292-5294.
- 23) (a) Funk, F.; Lenders, J.-P.; Crichton, R. R.; Schneider, W. Reductive Mobilisation of Ferritin Iron. *Eur. J. Bio.* **1985**, *152*, 167-172. (b) Wong, K. K. W.; Douglas, T.; Gider, S.; Awschalom, D. D.; Mann, S. Biomimetic Synthesis and Characterization of Magnetic Proteins (Magnetoferritin). *Chem. Mater.* **1998**, *10*, 279-285.
- 24) (a) Danon, D.; Goldstein, L.; Marikovsky, Y.; Skutelsky, E. Use of cationized ferritin as a label of negative charges on cell surfaces. *J. Ultrastruct. Res.* **1972**, *38*, 500-510. (b) Perriman, W.; Cölfen, H.; Hughes, R. W.; Barrie, C.L.; Mann, S. Solvent-Free Protein Liquids and Liquid Crystals. *Angew. Chem. Int. Ed.* **2009**, *48*, 6242-6246.

- 25) (a) <http://kur.web.psi.ch/sans1/SANSSoft/sasfit.html>. (b) Peterlik, H.; Fratzl, P. Small-Angle X-Ray Scattering to Characterize Nanostructures in Inorganic and Hybrid Materials Chemistry. *Monatsh. Chem.* **2006**, *137*, 529-543. (b) Fischbach, F. A.; Anderegg, J. W. An X-ray Scattering Study of Ferritin and Apoferritin. *Journal of Molecular Biology* **1965**, *14*, 458-473.
- 26) Broomell, C. C.; Birkedal, H.; Oliveira, C. L. P.; Pedersen, J. S.; Gertenbach, J.-A.; Young, M.; Douglas, T. Protein Cage Nanoparticles as Secondary Building Units for the Synthesis of 3-Dimensional Coordination Polymers. *Soft Matter* **2010**, *6*, 3167-3171.
- 27) (a) Zalomaeva, O. V.; Ivanchikova, I. D.; Kholdeeva, O. A.; Sorokin, A. B. Kinetics and Mechanism of the Oxidation of Alkyl Substituted Phenols and Naphthols with tBuOOH in the Presence of Supported Iron Phthalocyanine. *New. J. Chem.* **2009**, *33*, 1031-1037. (b) Sun, H.; Harms, K.; Sundermeyer, J. Aerobic Oxidation of 2,3,6-Trimethylphenol to Trimethyl-1,4-benzoquinone with Copper(II) Chloride as Catalyst in Ionic Liquid and Structure of the Active Species. *J. Am. Chem. Soc.* **2004**, *126*, 9550-9551. (c) Zhang, N.; Li, F.; Jia Fu, Q.; Tsang, S. C. Naturally Occurring Ferritin as a Novel Catalyst for Selective Hydroxylation of Phenol. *React. Kinet. Catal. Lett.* **2000**, *71*, 393-404
- 28) K. W. Wong, K.; T. Whilton, N.; Douglas, T.; Mann, S.; Colfen, H. Hydrophobic Proteins: Synthesis and characterisation of Organic-Soluble Alkylated Ferritins. *Chem. Commun.* **1998**, 1621-1622.
- 29) Anderson, N. G. Practical Use of Continuous Processing in Developing and Scaling Up Laboratory Processes. *Org. Process. Res. Dev.* **2001**, *5*, 613-621. (b) Charpentier, J.-C. In the Frame of Globalization and Sustainability, Process Intensification, a Path to the Future of Chemical and Process Engineering (molecules into money). *Chem. Eng.* **2007**, *134*, 84-92. (c) Plumb, K. Continuous Processing in the Pharmaceutical Industry: Changing the Mind Set. *Chem. Eng. Res. Des.* **2005**, *83*, 730-738. (d) Schaber, S. D.; Gerogiorgis, D. I.; Ramachandran, R.; Evans, J. M. B.; Barton, P. I.; Trout, B. L. Economic Analysis of Integrated Continuous and Batch Pharmaceutical Manufacturing: A Case Study. *Ind. Eng. Chem. Res.* **2011**, *50*, 10083-10092.
- 30) Zhang, W.; Liu, X.; Walsh, D.; Yao, S.; Kou, Y.; Ma, D. Caged-Protein-Confined Bimetallic Structural Assemblies with Mimetic Peroxidase Activity. *Small* **2012**, *8*, 2948-2953.

- 31) Solodenko, W.; Wen, H; Leue, S; Stuhlmann, F.; Argirusi, G.S; Jas, G; Schonfeld, H; Kunz, U.; Kirsching, A. Development of a Continuous-Flow System for Catalysis with Palladium(0) Particles *Eur. J. Org. Chem.* **2004**, 3601-3610.

Chapter 5

Soft Colloidal Macroporous Scaffolds by Ice Templating Method



In this chapter, the preparation of a macroporous monolith, formed by crosslinking polymer-coated colloids during ice templating is described. This process results in the formation of monoliths with remarkable ability to recover after large compressive strains. Hybrid silica scaffolds, predominantly comprising colloidal particles (up to 90% by weight of inorganic) can be rendered elastic and, can recover their structure completely after compression to 15% of their original size. The link for videos provided in this chapter provides evidence for the elastic mechanical properties of these novel materials, that starkly contrast the brittle response observed for materials such as pumice or polystyrene foam. The mechanical response of the monoliths is also qualitatively independent of polymer type, molecular weight and even crosslinking chemistry.

Part of the work discussed in this chapter has been published in

“Soft Colloidal Scaffolds Capable of Elastic Recovery after Large Compressive Strains” R. Rajamanickam[±], S. Kumari[±], D. Kumar, S. Ghosh, J. C. Kim, G. Tae, S. Sen Gupta, G. Kumaraswamy, *Chemistry of Materials*, 2014, 26, 5161 ([±]equal authorship).

5.1 Introduction

Macroporous materials, both natural and man-made, are ubiquitous,¹ because cellular structure affords the advantage of combining low densities with desirable mechanical, electrical, and thermal properties. Porous materials have been prepared from a wide variety of starting materials, such as polymers, inorganics, and metals.¹ Assembling colloidal particles into macroporous monoliths² offers the exciting possibility of creating multifunctional assemblies that leverage the rapid advances made in particle synthesis. Such porous scaffolds have the potential to open the door for applications of particle-based scaffolds in technologically demanding areas ranging from aerospace³ to electronic materials and from sensors to biomedical implants. However, the utility of porous materials prepared from inorganic or glassy colloids is greatly restricted by their brittleness:^{1, 4} such macroporous materials fail abruptly at low strains. For example, monolith scaffolds of bonded inorganic particles, such as macroporous pumice or mesoporous aerogels,⁴ fail abruptly when subjected to strains on the order of a few percent. Scaffolds of bonded glassy polymer particles, such as macroporous polystyrene foams, exhibit a plastic response beyond small strains. Recently, there has been exciting progress made in the design of ultralight micro-structured porous scaffolds that render them elastic to large compressive strains.⁵ However, the sophisticated fabrication techniques that are required to create such scaffolds are unsuitable for the preparation of scaffolds from colloidal starting materials. Flexible hybrid composites can be created by combining hard colloids with soft organic components. For example, flexible foams can be prepared from polymer nanocomposites⁶ that contain inorganic nanoparticles dispersed in a soft polymer matrix; however, these foams turn brittle when the filler loading exceeds a modest threshold (≈ 5 wt %).

A general route to the preparation of macroscopic scaffolds by dynamic templating of surfactant hexagonal phase (H_1) domains was reported by Sharma *et. al.*² We extended this methodology to develop a one pot strategy for synthesis of hierarchically porous materials using surface functionalized mesoporous silica particles. In these hierarchically porous materials, we demonstrated independent control over nanoparticle mesoporosity and scaffold macroporosity.² In addition, we extended the surfactant templating technique for the synthesis of large (centimeter-sized) self-standing macroporous scaffold monoliths from ferritin bionanoparticles, as shown in the previous chapter.⁹ However, macroporous monoliths prepared by dynamic templating of surfactant H_1 phase by hard, inorganic or glassy colloids are brittle in nature and, this severely restricts their applications.

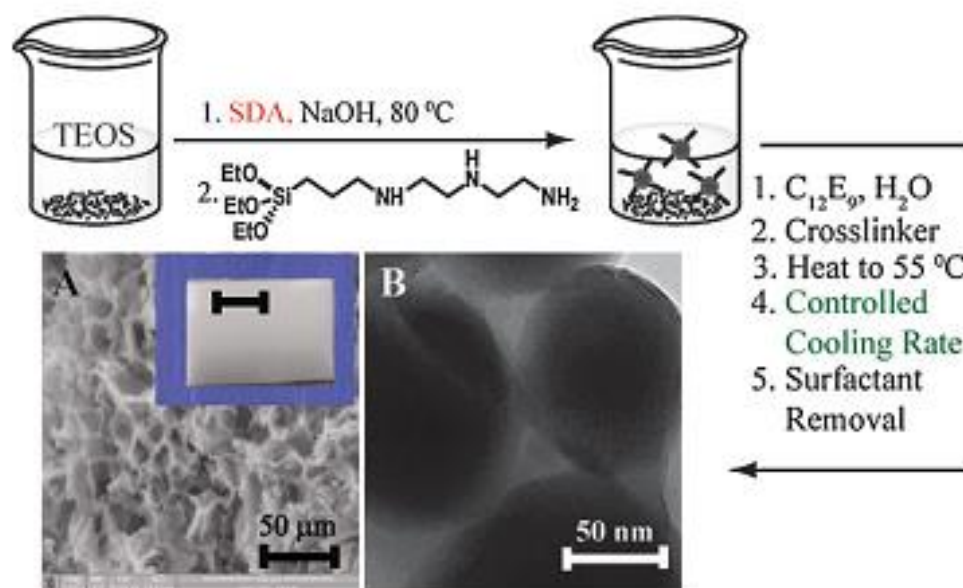


Figure 5.1 One pot synthesis proceeds via MSN synthesis using structure directing agents (SDA); followed by dynamic templating to assemble the MSN particles into a macroporous scaffold. (A) SEM of the freestanding scaffold after surfactant removal (inset: photograph of a scaffold monolith; the bar represents 1 cm). (B) TEM of a section of the scaffold.

Mechanical failure of colloidal assemblies is governed by the nature of interparticle linkages. Therefore, strategies to overcome brittle failure of colloidal assemblies have focused on modification of interparticle linkages. For example, silicate aerogels have been rendered elastic by covalent organic modification⁷ to strengthen interparticle links or by the use of trifunctional alkoxy silanes⁸ in the sol-gel process. Elastic single-layer thick nanoparticle membranes that rely on linkages through organic capping molecules⁹ have been reported. However, three-dimensional assemblies of such nanoparticles show a plastic response.¹⁰ Flexible aerogels prepared by decorating networks of cellulose fibers with cobalt-ferrite nanoparticles synthesized in situ have also been recently reported.¹¹ However, this technique might not be generalizable to other nanoparticle systems. Therefore, a general strategy that can be used to organize a variety of colloidal starting materials into macroscopic porous assemblies that can recover from large compressions remains elusive at this time.

Here, we demonstrate a route to the preparation of large, centimeter-size porous monoliths, primarily comprising rigid colloidal particles that are capable of elastic recovery after compression to nearly one-tenth their original size. This remarkable mechanical

response results from a special micro-structure that is developed in the hybrid colloidal scaffold while cross-linking the minority polymeric component during icetemplating.¹² Large, centimeter-size cellular monoliths can be prepared using a variety of colloids and using different crosslinking chemistries.

The interparticle linkages that characterize this monolith microstructure result in an entropic mechanism that characterizes the elastic recovery, in qualitative contrast with previous reports of macroscopic colloidal assemblies. Our understanding of the microstructural underpinnings of the colloidal scaffold's elastic properties allows us to extend this strategy to a variety of colloids, using different polymers and even different cross-linking chemistries.

5.2 Experimental Section

5.2.1 Materials

N-(3-(Dimethylamino) propyl)-N'-ethylcarbodiimide hydrochloride (EDC-HCl) 98%, polyethylenimine (25 kDa), polyethylenimine (2 kDa) and poly (ethylene glycol) diglycidyl ether ($M_n = 500$) were used as received from Sigma-Aldrich. One micrometer “angstrom sphere” silica particles were obtained from Richen Industry Limited, Hong Kong. Fluorescent PS latex particles (PS-Fluo-Red; Ex = 530 nm, Em = 518 nm) and monodisperse 300 nm silica particles were obtained from Microparticles GmbH, Germany, and were used as received. Glutaraldehyde, calcium nitrate tetrahydrate ($\text{Ca}(\text{NO}_3)_2 \cdot 4\text{H}_2\text{O}$), LudoxTM particles (26 nm silica particles) were obtained as an aqueous dispersion from Sigma-Aldrich and were used as received. We have previously reported detailed characterization of these particles.¹³ Zeta potential for 1 μm silica and 1 μm polystyrene particles before and after amine coating has been given in the Appendix IV; Figure D1 (a-d). Ammonium hydrogen phosphate ($(\text{NH}_4)_2\text{HPO}_4$), and 30% ammonia solution in water were received from Merck and used without further purification. All the other chemicals and solvents were purchased from Merck India.

5.2.2 Synthetic Methods

5.2.2.1 Synthesis of 10% silica scaffolds:

Typically, 60 mg of 1 μm silica particles was dispersed in 530 μL of water by sonication and vortexing for 15 min (corresponding to a concentration of $\phi = 10\%$ w/v). Then, to this aqueous dispersion was added 3 mg (30 μL of 100 mg mL^{-1} stock solution) of PEI (25 kDa), and the mixture was vortexed for 10 min. PEI adsorbs on the silica surface, and literature reports indicate a typical maximum coverage of $\approx 1 \text{ mg m}^{-2}$ (corresponding to a condensed layer of polymer, approximately 1 nm thick, on the silica surface). On the basis of this estimate, 3 mg of PEI added to the 60 mg of 1 μm silica particles represents approximately a 15-fold excess over monolayer coverage. To this was added 4 mg (40 μL of 100 mg mL^{-1} stock solution) of poly(ethylene glycol) diglycidyl ether, and then the sample was frozen at approximately $-10 \text{ }^\circ\text{C}$ for 24 h. The particle concentration in the overall composite is $\approx 10 \text{ wt } \%$ of the volume of water. After 24 h, the scaffold was removed from the refrigerator and allowed to warm to room temperature. Finally, the scaffold was washed multiple times, with excess water, to remove unreacted polymer and poly(ethyleneglycol) diglycidyl ether cross-linker.

5.2.2.2 Synthesis of 20% silica scaffolds:

To 120 mg of 1 μm silica particles dispersed in 460 μL of water, 6 mg (60 μL stock solution) PEI (25 kDa) was added and vortexed for 10 min. To this, 8 mg (80 μL stock solution) of poly(ethyleneglycol) diglycidyl ether was added and then the sample was frozen at $-10 \text{ }^\circ\text{C}$ for 24 h. Then the scaffold was taken out from refrigerator and allowed to reach the room temperature. Finally, the scaffold was washed multiple times with excess water to remove unreacted polymer and poly(ethyleneglycol) diglycidyl ether.

5.2.2.3 Synthesis of 30% silica scaffolds:

To 120 mg of 1 μm silica particles dispersed in 260 μL of water, 6 mg (60 μL stock solution) PEI (25 kDa) was added and vortexed for 10 minutes. To this, 8 mg (80 μL stock solution) of poly(ethyleneglycol) diglycidyl ether was added and then the sample was frozen at $-10 \text{ }^\circ\text{C}$ for 24 h. Finally the scaffold was removed and washed with excessive water to remove unreacted polymer and poly(ethyleneglycol) diglycidyl ether.

5.2.2.4 Synthesis of 10% fluorescent polystyrene scaffold:

To 10% (by weight) dispersion of 1 μm fluorescently labeled PS latex particles in aqueous medium was added 3 mg PEI (25 kDa) and was vortexed for 10 minutes to coat the particles with PEI. To this, 4 mg (40 μL stock solution) of poly(ethyleneglycol) diglycidyl ether was added and then the sample was frozen at $-10\text{ }^{\circ}\text{C}$ for 24 h. Then the scaffold was removed from refrigerator and allowed to reach the room temperature. Finally the scaffold was washed with excessive water to remove unreacted polymer and poly(ethyleneglycol) diglycidyl ether.

5.2.2.5 Synthesis of scaffold from 300nm silica:

To 60 mg of 10% (by weight) aqueous dispersion of 300 nm silica particles was added 3 mg PEI (25 kDa) and vortexed for 15 min. To this 4 mg of poly(ethyleneglycol) diglycidyl ether was added and vortex it to homogenize the sample and immediately frozen at $-10\text{ }^{\circ}\text{C}$ for 24 h. After 24 h, the scaffold was removed from refrigerator and allowed to reach the room temperature. Finally the scaffold was washed with excessive water to remove unreacted polymer and poly(ethyleneglycol) diglycidyl ether.

5.2.2.6 Synthesis of 10% silica scaffolds from Ludox TM (26 nm silica nanoparticles) using poly(ethyleneglycol) diglycidyl ether as a crosslinker:

Typically, to a 10% (by weight) dispersion of nanoparticles was added 10 mg PEI (25 kDa) and was vortexed for 10 minutes to coat the particles with PEI. To this, 5 mg (50 μL stock solution) of poly(ethyleneglycol) diglycidyl ether was added and then the sample was frozen at $-10\text{ }^{\circ}\text{C}$ for 24 h. Then the scaffold was removed from refrigerator and allowed to reach the room temperature. Finally the scaffold was washed with excessive water to remove unreacted poly(ethyleneglycol) diglycidyl ether.

5.2.2.7 Synthesis of hydrophobised scaffold:

A scaffold prepared from a 10% dispersion of 1 μm silica particles with PEI and poly(ethyleneglycol) diglycidyl ether crosslinker, was dried in a vacuum oven at $80\text{ }^{\circ}\text{C}$ for 24 h. Then this scaffold was incubated with 10 mL of dry THF. To this solution 50 μL of triethyl amine and 220 μL of dodecanoyl chloride was added in presence of argon atmosphere and stirred for 24 h at room temperature. After 24 h, the scaffold was washed 4-5 times with THF.

5.2.2.8 Synthesis of scaffold by variation of crosslinker concentration:

To a 10% (by weight) dispersion of silica nanoparticles was added 10 mg PEI (25 kDa) and was vortexed for 10 minutes to coat the particles with PEI. To this, 5 mg (50 μ L of 100 mg/mL stock solution) of glutaraldehyde was added and then the sample was frozen at -10 °C for 24 h. Then the scaffold was removed from refrigerator and allowed to warm to room temperature. Subsequently, sodium cyanoborohydride was added to the gel to reduce the imine groups formed upon crosslinking of PEI and glutaraldehyde. Finally the scaffold was washed with excessive water to remove unreacted glutaraldehyde and sodium cyanoborohydride to afford a self-standing scaffold.

5.2.2.9 Control experiment:

No monolith scaffold was formed in control experiments where an aqueous PEI solution at the same concentration was ice templated, in the absence of colloidal particles. We also performed control experiments where no crosslinker was used during scaffold preparation. Again, no scaffold was observed to form, on thawing.

5.2.2.10 Preparation of patchy particles on glass slide:

Glass slide was first cleaned by treatment with piranha solution and then subsequently coated with 1% PEI solution 25 kDa. This PEI coated glass slide was incubated with a very dilute solution of PEI (25 kDa) coated 1 μ m silica particles for few seconds and then frozen at -10 °C. PEI-coated particles that settled onto the PEI-coated glass slide were allowed to crosslink in the presence of ice. After 24 h, glass slide was removed and used for further characterization.

5.3 Analytical and Characterization methods

Scaffolds were imaged using a Quanta 200 3D scanning electron microscope (SEM) and FE-SEM (Hitachi S-4200). An LSM 710 Carl Zeiss laser scanning confocal microscope (LSCM) was used to image the fluorescent samples. We used a He-Ne laser (543 nm) and an argon-ion laser (488 and 514 nm) for our experiments. Thermogravimetric analysis (TGA) of the silica nanoparticles was carried out using a TA Instruments SDT Q600 analyzer between 30 and 800 °C in air (flow 50 mL min⁻¹) at a heating rate of 10 °C min⁻¹. All samples were dried under vacuum at 80 °C overnight prior to TGA runs.

Rheological measurements were made using a TA-ARES controlled strain rheometer equipped with a normal force transducer. All measurements were repeated several times to confirm the irreproducibility. Ice-templated monoliths were prepared as 8.4 mm cylinders for compression and oscillatory shear measurements. All tests were performed using roughened parallel plates to prevent slippage of the sample. Measurements were done on wet scaffolds at room temperature (25 °C). Compression measurements to determine the increase in normal force with compression were performed using a force-gap test in the transient mode. Nominal compression stress was calculated on the basis of the original cylinder diameter (8.4 mm). We also performed frequency sweep measurements in dynamic mode on the monoliths (frequency range 1 to 100 rad s⁻¹; strain amplitude of 0.25%, sample loaded with normal force = 1 g). Variable temperature measurements were performed using an ARES forced convection oven. We used a 25 mm bottom plate and excess solvent to prevent evaporation of the scaffold during the measurement. Scaffolds were always checked at the end of the measurement to ensure that they were still solvent-swollen.

Compression stress-strain measurements were also performed on a TA Instruments DMA (RSA-III). We used the cylindrical compression geometry to perform tests at various compression rates on the 8.4 mm monoliths. Compression rates of 0.006 to 0.04 mm s⁻¹ were used. Data obtained from the DMA were quantitatively similar to those from the ARES. Therefore, here, we report data obtained using the ARES.

Procedure for estimation of porosity and density:

A wet cylindrical scaffold of known radius, r , and height, h , is taken and the volume calculated as $V = \pi r^2 h$. The mass of this scaffold is determined as m_w . The scaffold is then dried completely in a vacuum oven and is then weighed to determine the scaffold weight, m_s . The volume of water present in the wet scaffold is then determined as $V_w = (m_w - m_s)/\rho$, where ρ is the density of water ($= 10^3 \text{ kg.m}^{-3}$). The void fraction of the scaffold is estimated as V_w/V . The bulk density of the scaffold is estimated as $\rho^* = m_s/V$.

5.4 Results and Discussion

5.4.1 Structural characterization of monolithic scaffolds

Macroporous monolith were prepared by ice-templating¹² an aqueous dispersion containing 10% (weight/volume) of 1 μm silica particles and 0.5% (weight/volume) of

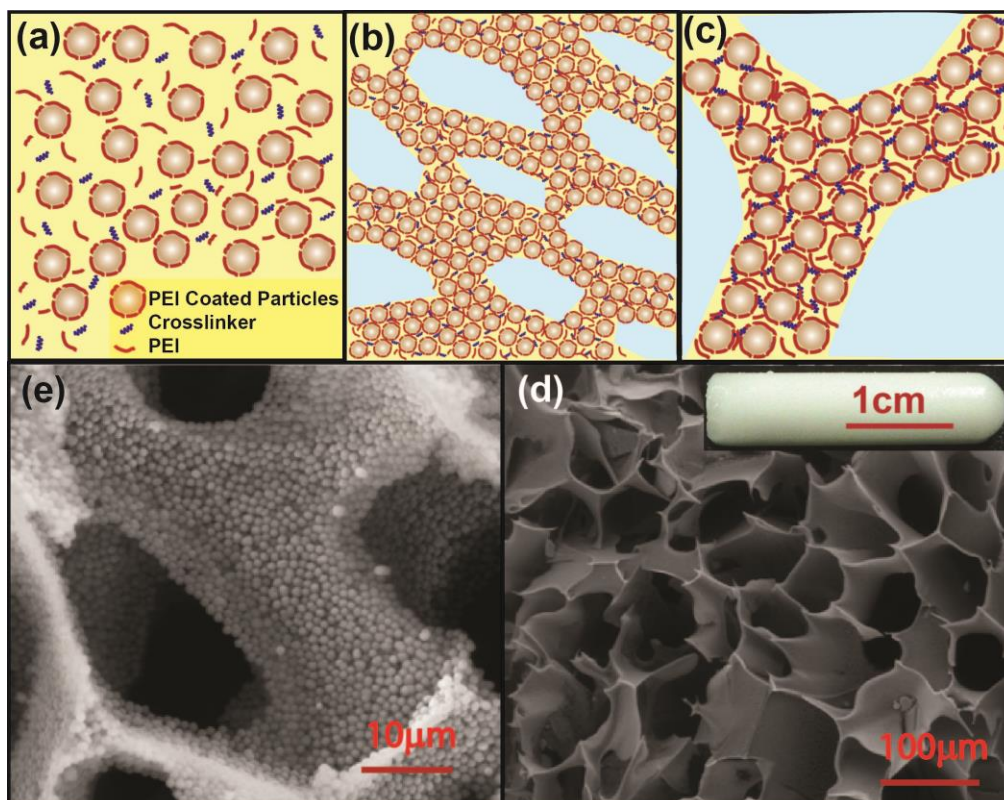


Figure 5.2 Schematic of the ice-templating process. (a) Colloidal particles are dispersed in an aqueous solution containing a cross-linkable polymer, polyethylene imine (PEI; indicated in red) and a telechelic diepoxide cross-linker (indicated in blue). (b) Immediately after addition of the polymer and cross-linker, the dispersion is frozen. (c) Polymer-coated particles, excess polymer, and cross-linker are expelled by the growing ice domains (depicted in light blue) and aggregate where these domains impinge. Crosslinking of the PEI proceeds in the frozen matrix and yields a free standing scaffold on thawing. Large monolith scaffolds that are several centimeters in size can be readily prepared (d, inset). (d) SEM reveals the internal structure of freeze-dried scaffolds prepared using 1 μm silica colloids. (e) At higher magnification, SEM reveals that the cellular monolith is characterized by an open-pore structure with colloids packed together to form the walls.

polyethyleneimine (PEI, of molecular weight 25 000 g/mol) and a telechelic diepoxide crosslinker. In the ice templating process, an aqueous dispersion is frozen such that the growing ice crystals exclude particles and polymers and, consolidate them into the walls of a cellular solid (Figure 5.2a-c). After freezing, the PEI in the hybrid particle-polymer network was crosslinked in the frozen state (viz. at $-18\text{ }^{\circ}\text{C}$), over about a day. A self-standing monolith scaffold was recovered by extensively washing with water after the completion of crosslinking. Several factors affect the amine epoxy cross-linking reaction as has been described before.¹⁴ These include the amine concentration on the particle surface, the chemical identity and concentration of the epoxide in the cross-linker, and finally the reaction temperature and time. In the case of our monoliths, cross-linking of the organic takes place at $-10\text{ }^{\circ}\text{C}$. We anticipate that the low temperature slows down the reaction rates by an order of magnitude. However, this is offset by an increase in local concentration of the cross-linking agent and amine as amine-coated particles and cross-linker are expelled from the ice crystals and concentrated at their boundaries. Thus, this protocol achieves a high degree of cross-linking between the particles.

The monolith is characterized by a TGA weight loss $\approx 10\%$ (Figure 5.3), pore volume $\approx 0.9\text{ cc/cc}$, and bulk density, $\rho^* \approx 0.13\text{ g/cc}$. SEM reveals a foam-like network with interconnected pores (average size $\approx 75\text{ }\mu\text{m}$), having walls comprising primarily of colloidal silica particles (Figure 5.2d, e). The monolith is destroyed by immersion in HF; silica particles dissolve to leave behind a highly viscous material indicative of cross-linked PEI. In a control experiment, where we ice templating a 0.5% PEI/cross-linker solution in the absence of silica particles, we obtain a viscous material, and no monolith is formed (see section 5.2.2.9). Thus, monolith scaffolds are formed only when colloidal particles, PEI and cross-linker are ice-templated and, only when crosslinking proceeds in the frozen state. Scaffolds do not form in the absence of the particles or without crosslinking.

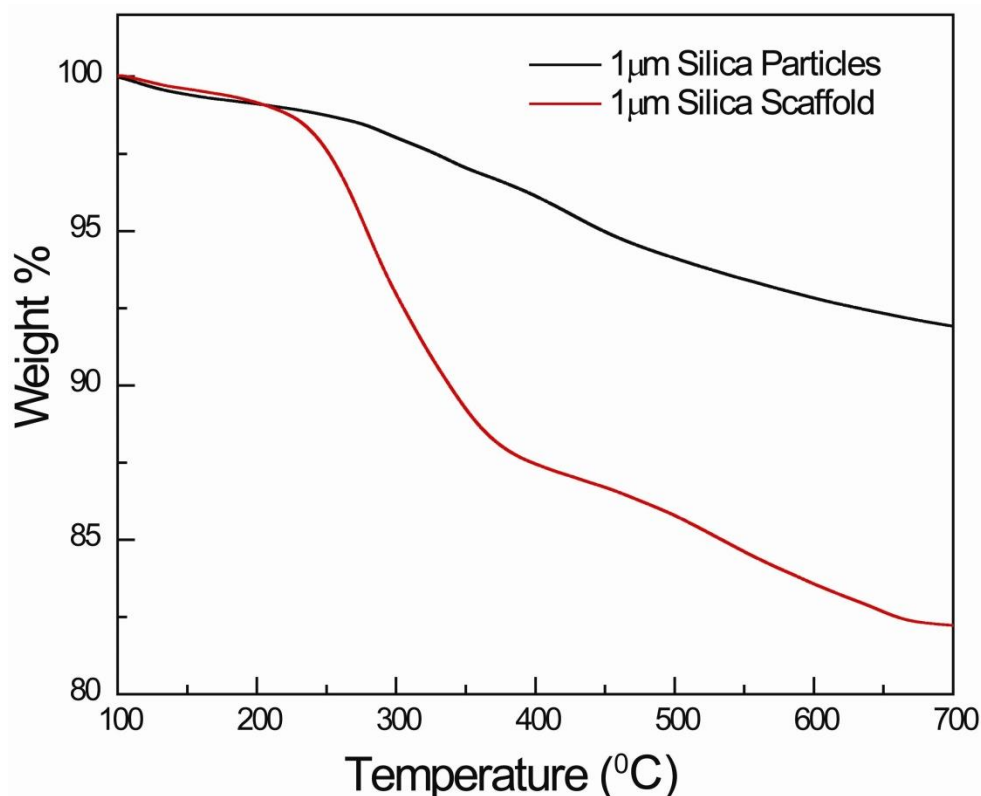


Figure 5.3 TGA of a scaffold prepared from 1µm silica particles and a control scaffold prepared using the same 1 µm silica particles according to procedure 5.2.2.1 and 5.2.2.9. The organic content in the scaffold is obtained as the difference between the weight loss for the scaffold and that for the neat particles.

5.4.2 Mechanical response of monolith to compression

The water-swollen particulate monolith was compressed at room temperature to strains up to $\epsilon = 85\%$ (Figure 5.4a-d) in a rheometer and is able to completely recover its original size when the strain is released. The monolith showed no signs of failure during compression: stress developed during compression did not decay on holding, and remained constant over tens of minutes. During compression, the water contained within the gel was squeezed out, as in a sponge. When the rheometer plates were retracted, the sample rapidly re-absorbed the water that had been squeezed out and recovered its original size (Figure 5.4 a-d; for video see

https://docs.google.com/file/d/0B-D_pJdxFtKjRENldTJwZWNRTTA/edit). Interestingly, there is no measurable change in the diameter of the cylindrical sample during the initial

stages of compression (when reliable measurements of the sample dimensions could be obtained from photographs), viz. the Poisson ratio, $\nu \approx 0$.

The ice-templated silica monolith recovers its original size after being subjected to compressive strains up to 85%. There is no significant compression set (viz. residual compression, relative to the original size, after separation of the rheometer plates), and no change in the mechanical response, over multiple compression cycles for compressive strains up to 85% (Figure 5.4 e). The stress increases linearly with compressive strain at low strain values and, the Young's modulus, $E^* \approx 24\,000$ Pa, is obtained as the slope of the stress-strain curve (Figure 5.4 d). Thus, this monolith gel is very soft when compared with typical porous materials from inorganic materials or glassy polymers that have moduli $\sim O(10^1 - 10^3)$ MPa. The softness of the particle scaffolds, even at such high particle loadings ($\approx 90\%$ by weight of inorganic in the walls), indicates that the modulus is not determined by the silica particles alone but arises from the colloid/polymer hybrid microstructure. The stress-strain curve is independent of the compression rate (for almost 7-fold variation in compression rates; see Appendix IV, Figure D2), indicating that the calculated Young's modulus reflects the response of the colloidal network to deformation, rather than the hydrodynamic force required to squeeze water out of the monolith.

We also obtain the shear modulus, $G' \approx 12\,000$ Pa (Figure 5.4 f), for the monolith from small amplitude oscillatory measurements and observe that it is only very weakly frequency dependent over $0.1 - 100$ rad.s⁻¹, as expected for a cross-linked network. Thus, the Poisson ratio, $\nu = E^*/2G' - 1 \approx 0$. This is in accordance with photographic measurements of sample dimensions, which indicate no change in the diameter of the cylindrical sample during the initial stages of compression. Low values of ν are not unusual¹⁵ for porous foams, since dimensional changes due to compression are accommodated by deformation of the cell walls. While these particulate scaffolds are robust to large compression, they fail readily at low tensile strain. Asymmetry of failure behavior to compressive and tensile loads is well known for a variety of materials: compressive loads suppress fracture while cracks propagate catastrophically under tensile loads.¹

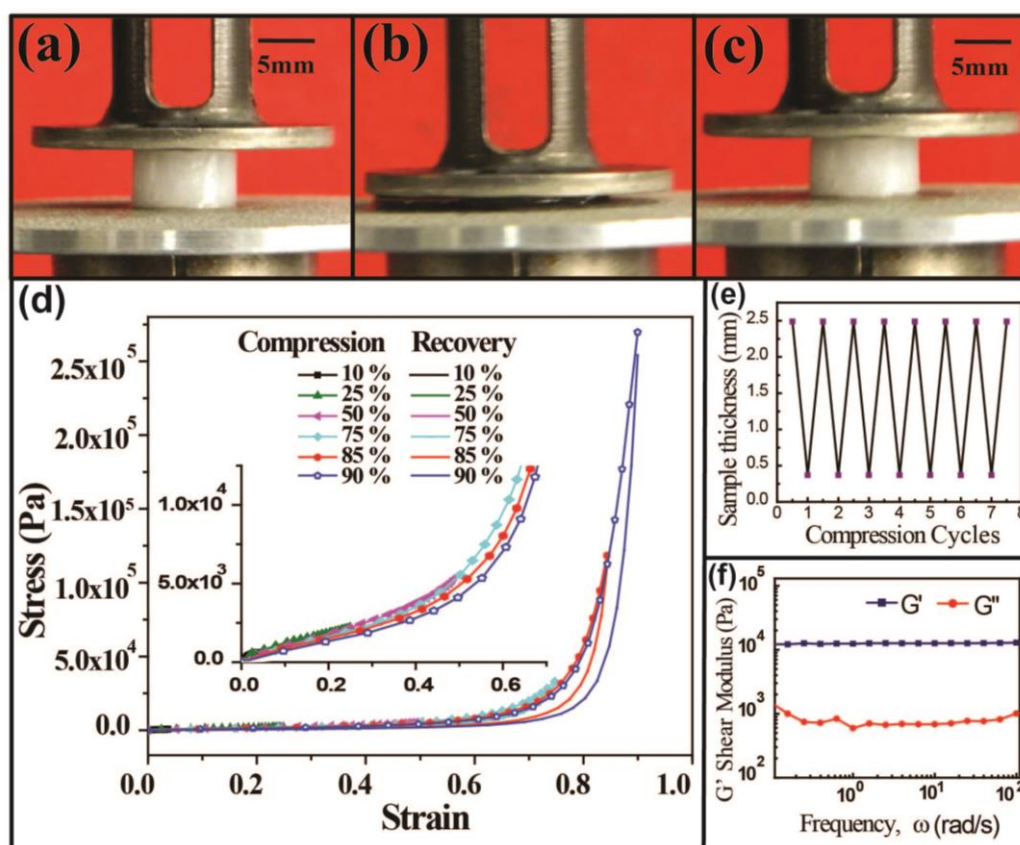


Figure 5.4 Compression of an ice-templated monolith of 1 μm silica colloids. When the water-swollen monolith (a) is compressed to 15% of its original size, (b) water in the pores is squeezed out. However, when the compressive stress is released, (c) the water is reabsorbed as the scaffold regains its original size. (d) Nominal stress (calculated as the normal force, N_1 , by the original cross-sectional area of the scaffold) as a function of nominal strain, ϵ (calculated as the change in sample dimension in the compression axis, normalized by the original dimension), during compression of an ice-templated monolith of 1 μm silica colloids. The compression test is performed in a rheometer using roughened parallel plates to prevent slippage of the sample. Compression is performed at a rate $\approx 2.3 \times 10^{-2} \text{ s}^{-1}$, and the normal force (N_1) measured in the rheometer is used to calculate the nominal stress. (e) The dimensions of the crosslinked colloidal silica gel along the compression axis during cyclic compression to 15% of its original size. We performed 6 compression cycles and note that the scaffold regains its original size after each cycle. (f) The solid shear modulus (G') for the silica scaffold is approximately frequency independent over a range of 10^{-1} to 10^2 rad.s^{-1} and is significantly higher than the loss modulus (G'').

As the compressive strain is increased beyond a few percent, the stress-strain relationship becomes non-linear (Figure 5.4 d). At moderate strains ($< 10\%$), beyond the initial linear region, there is a slower increase in stress with strain. However, at higher strains ($> 50\%$), the stress rapidly increases on compression. The stress-strain curve shows hysteresis in the compression/expansion cycle, indicating loss of energy to dissipative processes. The extent of the hysteresis increases with the imposed compressive strain. For a compressive strain of 25%, the area of the hysteresis loop is about 30% of the area under the stress-strain curve during compression, and this fraction increases to about 40% for a compressive strain of 90%. Remarkably, there is no measurable compression set even when the sample is compressed to a strain of 85%. Even for $\epsilon = 90\%$, the scaffold largely recovers its size on releasing the compressive stress; however, at these high strains, there is a small compression set of about 6% immediately after the stress is released. However, if the monolith is stored in water for a few hours after compression to $\epsilon = 90\%$, we observe that it completely recovers its original size and there is no compression set.

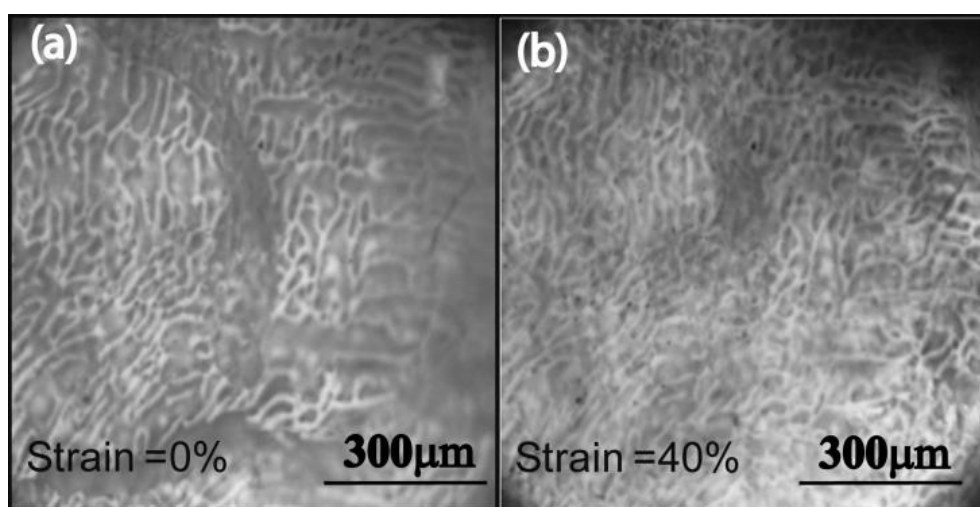


Figure 5.5 Confocal microscopy of scaffolds prepared from 1 μm fluorescent polystyrene colloidal latex, ice-templated with PEI and diepoxide cross-linker. We image the scaffold during compression and present data in a plane normal to the uniaxial compression axis. We observe that the pore structure does not change on increasing the compressive strain from (a) $\epsilon = 0$ to (b) $\epsilon = 40\%$.

Confocal microscopy on a monolith prepared from fluorescent 1 μm polystyrene latex ($\phi = 10\%$ w/v) allows us to examine the change in the pore structure on uniaxial compression. This monolith too exhibits an elastic response to compression, similar to that prepared using silica colloids. We observe no significant change in the pore structure in a plane normal to the uniaxial compression axis for strains up to 40%. Thus, the confocal data indicates that uniaxial compression of the monolith along the z-axis does not result in a change in pore size in the xy plane, consistent with our measurement of $\nu = 0$ (Figure 5.5). Microscopic measurements could not be made beyond $\varepsilon \approx 50\%$ as the pore walls collapsed. Thus, the steep increase in stress beyond $\varepsilon \approx 50\%$ correlates with densification associated with pore wall collapse. Again, remarkably, the scaffolds recover elastically even after such large compressive strains (Figures 5.6).

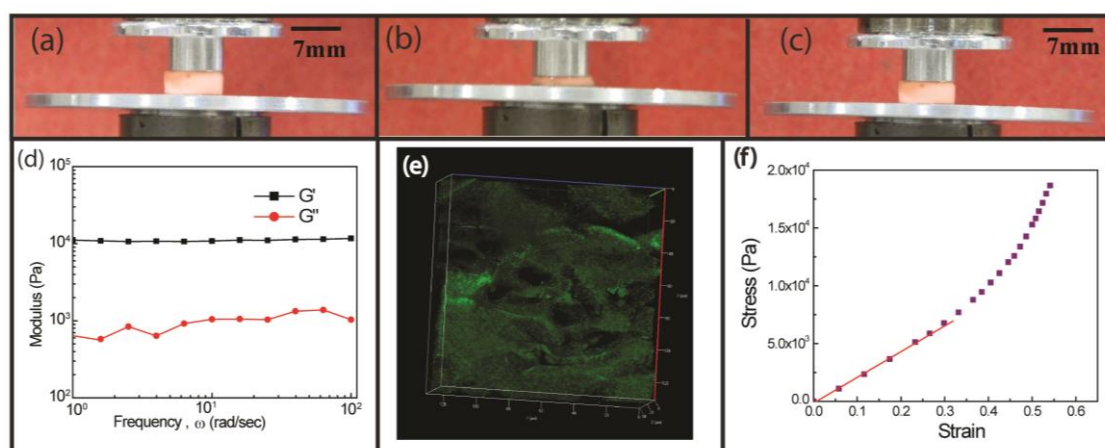


Figure 5.6 Photographs that show the compression of scaffold prepared by ice templating a 10% w/v dispersion of 1 μm fluorescent polystyrene latex, with 25 kDa PEI and poly(ethyleneglycol) diglycidyl ether as the cross-linker. The photographs show (a) the initial state (b) the compressed state (strain = 85%) and (c) recovery on release of stress. (d) Frequency sweep for 1 μm fluorescent polystyrene scaffold. We observe that $G' = 11\,124$ Pa at $\omega = 1$ rad/s. (e) Confocal microscopy of scaffold prepared from 1 μm fluorescent polystyrene latex colloids from a $\phi = 10\%$ w/v dispersion. (f) Stress versus strain for compression test on the same scaffold. The elastic modulus, $E^* = 22\,000$ Pa, is obtained as the slope of the initial linear region in the loading curve of the stress-strain data.

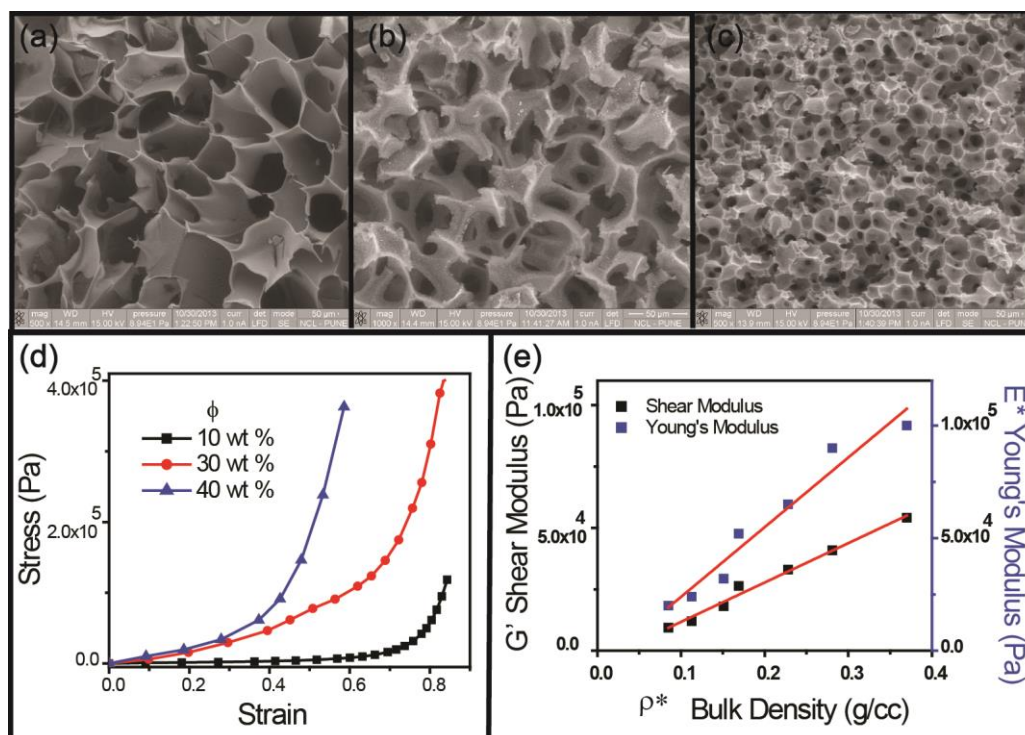


Figure 5.7 SEM micrographs of 1 micron silica scaffolds prepared by ice templating (a) $\phi = 10\%$, (b) $\phi = 20\%$ and (c) $\phi = 30\%$ w/v aqueous dispersions. (d) Nominal stress-nominal strain data for scaffolds prepared from 1 μm silica colloids by varying the colloid fraction ($\phi = 10\%$, 30% and 40% weight/volume) in the original dispersion. (e) Young's modulus (E^*) and solid modulus (G') for scaffolds from 1 μm silica colloids scale linearly with the monolith foam bulk density, ρ^* .

Further insights are obtained by investigation of scaffolds with varying bulk density, ρ^* , prepared from 1 μm silica colloidal dispersions at different ϕ (Figure 5.7). The average pore size of the scaffolds, d , decreases when higher volume fraction (ϕ) dispersions of the 1 μm silica colloids are ice templated (Figure 5.7a-c). SEM micrographs of scaffolds prepared at different ϕ indicates that $d \sim \phi^{-1}$ (Figures 5.7a-c). Confocal microscopy and SEM of samples imaged along different directions confirm that the pores in our monoliths are not anisotropic. Thus, the average number density of pores is $n \sim d^{-3}$ and since, $nd^2t \sim \phi$, we anticipate that the average wall thickness of the pores, t , is independent of the volume fraction of the ice templated dispersion, as confirmed by SEM data (see Appendix, Figure D3). The onset of rapid increase in stress happens at lower ϵ for higher ϕ ; however, the

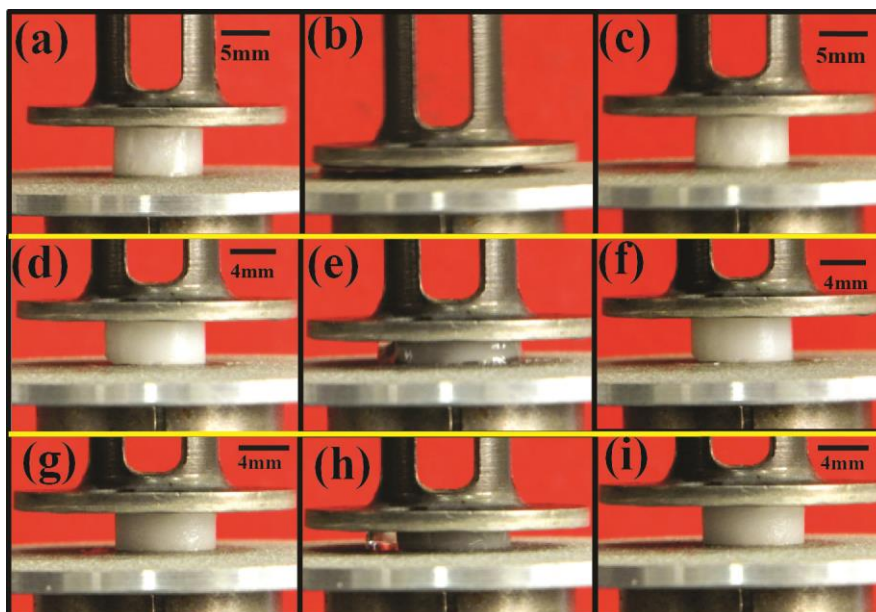


Figure 5.8 Photographs that show the compression and recovery of scaffolds prepared by ice templating (a-c) 10% (d-f) 20 % and (g-i) 30% w/v dispersions of 1 μm silica particles, with 25 kDa PEI and poly(ethyleneglycol) diglycidyl ether as the cross-linker.

For video V1, see: https://docs.google.com/file/d/0B-D_pJdxFtKjRVpLR1JBX3ViRVk/edit

For video V2, see: https://docs.google.com/file/d/0B-D_pJdxFtKjeIB2X1NMY3RITWc/edit

monoliths exhibit elastic recovery from compressive strains of at least 50% (Figure 5.8) and videos (V1 and V2). For the ice-templated scaffolds, we observe that $E^* \sim \rho^*$ and $G' \sim \rho^*$ (Figure 5.7 e). We note that the ratio of colloidal silica, PEI and cross-linker is held constant as we vary ϕ ; therefore, we anticipate that the density of the monolith walls, formed by consolidation of the starting materials during ice-templating, will be constant (ρ_w), independent of ϕ . Therefore, the scaling of the mechanical moduli that we observe can be written as $E^* \sim (\rho^*/\rho_w)$ and $G' \sim (\rho^*/\rho_w)$.

5.4.3 Entropic origin of monolith mechanical response:

Colloid monoliths exhibit elastic mechanical recovery only when swollen with solvent. However, dry scaffolds do not fracture when compressed. Rather, they deform plastically but are able to rapidly recover their original size on immersion insolvent.

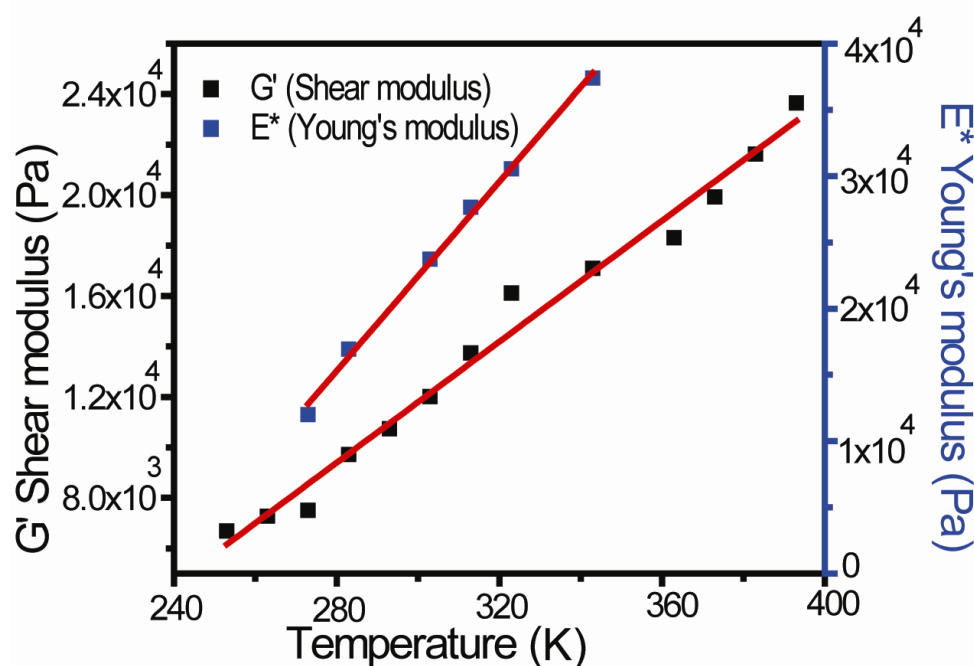


Figure 5.9 Temperature dependence of Young's modulus (E^*) and solid shear modulus (G') of solvated scaffolds prepared by ice-templating 1 μm silica colloids.

Remarkably, the monolith mechanical response is independent of the solvent used to swell the colloidal gel. This enabled us to make measurements G' and E^* for 1 μm silica monoliths ($\phi = 10\%$, PEI, diepoxide) over temperatures from $-20\text{ }^\circ\text{C}$ to $+120\text{ }^\circ\text{C}$. Because we cannot use water as the solvent over this entire temperature range, we performed measurements between $-20\text{ }^\circ\text{C}$ and $+30\text{ }^\circ\text{C}$ using methanol-swollen monoliths, from 10 to $70\text{ }^\circ\text{C}$ in water and from 60 to $120\text{ }^\circ\text{C}$ in DMSO. The same monolith was used for all experiments and was squeezed dry and resolvated (several times) to switch solvents. In qualitative contrast to the reported temperature dependence for inorganic and hybrid scaffolds,^{1,16} we observe an approximately linear increase in modulus with temperature over the entire $140\text{ }^\circ\text{C}$ range of measurement (Figure 5.9). For temperatures above $120\text{ }^\circ\text{C}$, the scaffold exhibited discoloration, probably from oxidative degradation of the organic in the hybrid (despite performing measurements in a nitrogen atmosphere). Also, it was difficult to perform measurements at temperatures lower than $-20\text{ }^\circ\text{C}$ due to excessive condensation on the rheometer oven. Extrapolating the trends in moduli to lower temperatures suggests that the moduli vanish at temperatures near 200 K. We believe that such extrapolation is invalid

and that the mechanical properties of the scaffold might be governed by different physics at temperatures significantly lower than those of our experimental range.

An increase in modulus with temperature is indicative of an entropic origin for mechanical response. Such behavior is well-known for polymeric rubbers.¹⁷ In polymeric rubbers, the flexible polymer strands between cross-links can access a large number of conformational states. Macroscopic deformation of the rubber translates to a corresponding affine deformation of these network strands. Thus, deformation of the rubber changes the equilibrium end-to-end distance of the network strands. This generates a restoring force, because fewer conformations are available to the strands. A natural corollary of this is that the entropic restoring force increases when the rubber is deformed at higher temperatures. Therefore, one possibility is that the entropic elasticity that characterizes the mechanical response arises entirely from the cross-linked polymer in the hybrid. However, our experiments suggest that this is not the case. We observe that the modulus (G') measured for the monolith is largely independent of the solvent that swells it. For example, for the scaffold prepared using 1 μm silica colloids ($\phi = 10\%$, PEI, diepoxide), $G' \approx 12\,000$ Pa when the monolith is swollen in water or methanol (which are good solvents for PEI) or in acetone (which is a bad solvent for PEI). The ability of the monolith to recover elastically from large compression is also independent of the solvent. We have also made measurements on the same monolith in aqueous solutions at high ionic strength (see Appendix IV; Figure D.4), in acidic pH (Appendix IV; Figure D.5), and in basic pH (Appendix IV; Figure D.6), and we find that the mechanical response is quantitatively similar in all cases. This independence of the mechanical response to solvent quality for the polymer¹⁸ suggests that the response is characteristic of the hybrid colloid/polymer architecture of the monolith rather than being merely from the cross-linked PEI. Imaging the details of this microstructure is challenging. We used FE-SEM to observe the microstructure and interparticle connections in the scaffold. Our data (Figure 5.10) reveals that the particles in the scaffold are connected through a thin sheath that we believe is the cross-linked PEI.

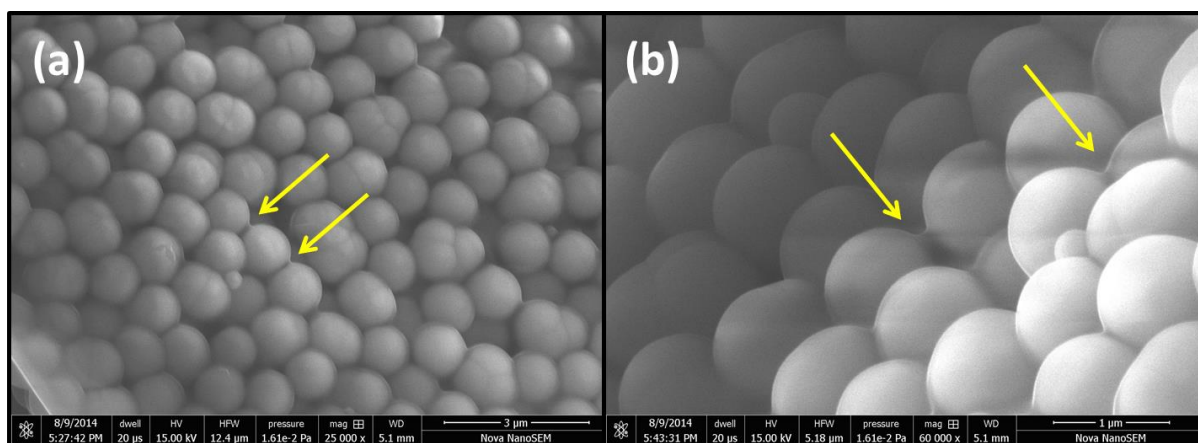


Figure 5.10 (a) FE-SEM image of scaffold prepared from a $\phi = 10\%$ w/v dispersion of $1\mu\text{m}$ silica colloids. (b) Magnified section of the cross-linked scaffold showing interconnected particles.

Entropic elasticity has also been observed for biological gels,¹⁹ where it results from thermal exploration of conformational phase space. Nanoparticle chain-like assemblies, formed by thermal decomposition of precursors, have also been reported to exhibit entropic elasticity²⁰ based on electron microscopy studies. However, these studies were limited to TEM observations of small submicrometer chains, and although a polymer-like entropic origin for this elasticity was speculated, this was not established.

We rationalize that cross linking while ice-templating results in a microstructure that allows several conformational micro-states for the particles comprising the walls. The presence of a solvent appears to be essential for thermalization, enabling exploration of this conformational space. Furthermore, conformational states in these monoliths must arise from relative motion between “bonded” colloids such that compression does not break the links connecting the particles, in contrast to brittle colloidal assemblies that fail when small strains break interparticle links (as indicated earlier). Direct observation of colloid dynamics within ice-templated scaffolds is rendered challenging by strong scattering. Therefore, to model the cross-linked particle/PEI hybrid structure, we suspend $1\mu\text{m}$ silica colloids in an aqueous PEI solution and allow them to gravitationally settle onto a PEI-coated glass slide. This assembly is then frozen, after addition of the same diepoxide cross-linker (see section 5.2.2.10), and cross-linking is allowed to proceed in the frozen state. After a day of cross-linking, the

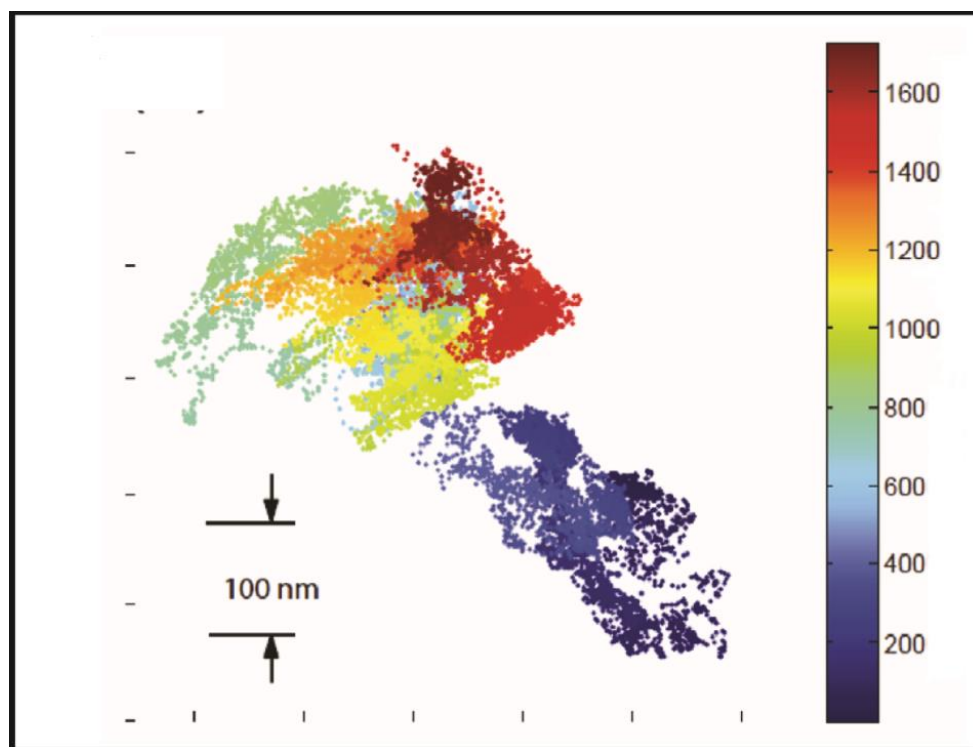


Figure 5.11 Trajectory of motion for a single 1 μm silica colloid cross-linked through its PEI coating to a glass slide. The spatial extent of particle motion is indicated by the scale bar. The time axis (in seconds) is color-coded so that the punctuated dynamics of the colloidal particle is evident.

system is thawed and washed so that the silica particles bonded to the glass slide can be investigated. We use a highly sensitive particle tracking technique²¹. To investigate in-plane motions of the bonded silica particles in an aqueous medium at room temperature. We observe significant center-of-mass motion over a large lateral area, on the order of several hundred nanometers (Figure 5.11). Interestingly, the colloids exhibit punctuated dynamics, viz., and the particle transitions between several spatial locations (“patches, characterized by size, S , and a finite residence time). The typical bonding stiffness associated with the colloid-slide contact at each patch is estimated as $\kappa = k_{\text{B}}T/l^2 \approx 0.5 \mu\text{Nm}^{-1}$. These patches represent discrete spatially separated metastable states, and the punctuated dynamics represent the exploration of the energy landscape by the system in a discrete manner. We hypothesize that the microscopic origin of this patchiness relates to spatial heterogeneity in the polymeric mesh structure enveloping the colloids that develops on cross-linking during ice templating.

Particles hop between these patchy regions, without breaking any chemical bonds. Thus, the macroscopic hybrid manifests an entropic response and remains elastic to large deformations. In cross-linked monoliths, particles are multiply bonded within scaffold walls, and their motion is likely to be more restricted than on a glass slide. However, we believe qualitatively similar colloidal motions in the scaffold could give rise to compression of the walls, resulting in the linear scaling of modulus on bulk density as well as entropic elasticity.

5.4.4 Elastic mechanical response of ice-templated monoliths is chemistry independent:

Elastic recovery after large compression is observed for monoliths prepared for colloids with varying size and chemistry and, is independent both of the molecular

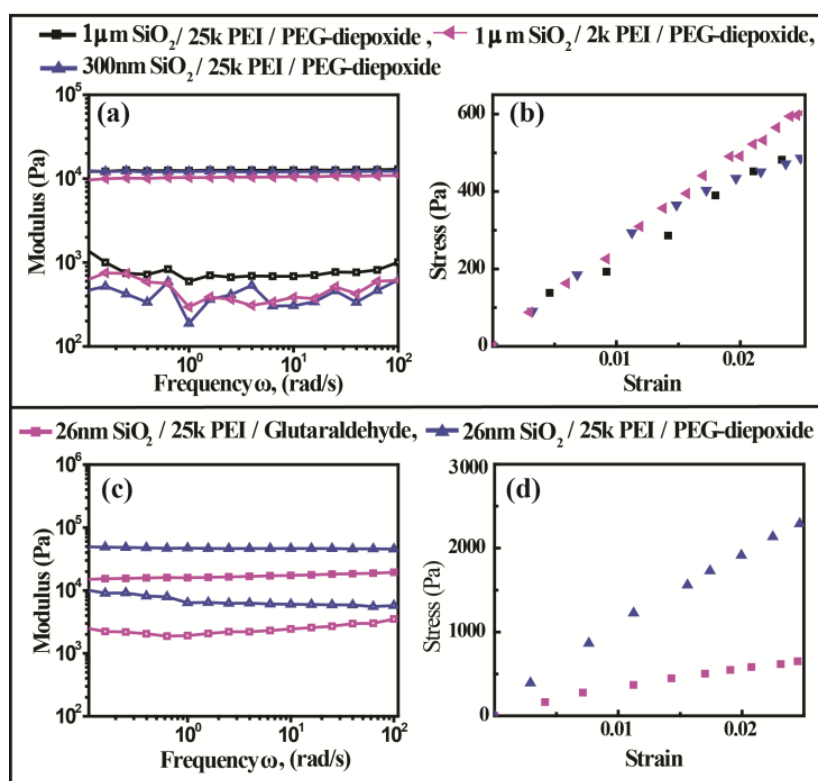


Figure 5.12 Mechanical response of scaffolds (a and c) in shear and (b and d) in compression, prepared by ice-templating 10% w/v aqueous dispersions of silica particles. In the top panels, we show data for scaffolds crosslinked with PEG-diepoxide and comprising 1 micron silica particles/25 kDa PEI; 300 nm silica particles/25 kDa PEI and 1 micron silica particles/2 kDa PEI. In the bottom panels, we show data for scaffolds comprising 26 nm LudoxTM particles, 25 kDa PEI and crosslinked with either glutaraldehyde or PEG-diepoxide.

characteristics of the cross-linkable polymer and of the specific crosslinking chemistry. Macroporous hybrids prepared by ice-templating dispersions of 300 nm silica nanoparticles and PEI, and that are cross-linked with the PEG-diepoxide have essentially the same mechanical properties (Figure 5.12) as scaffolds prepared from 1 μm particles, at the same ϕ . Scaffolds prepared from 26 nm silica nanoparticle/PEI dispersions using the same technique also yield monoliths that recover from compression. However, due to the high specific area of these nanoparticles, we observe that the elastic modulus is marginally higher than scaffolds from 1 μm particles, and the compressive strain for complete recovery is lower ($\approx 60\%$). Changing the molecular weight of the PEI used in preparing the macroporous network from 25 000 $\text{g}\cdot\text{mol}^{-1}$ to 2 000 $\text{g}\cdot\text{mol}^{-1}$ also yields scaffolds with quantitatively identical mechanical response for equivalent scaffolds of 1 μm silica colloids (Figure 5.12). We have also substituted the PEG-diepoxide crosslinker with gluteraldehyde that forms a Schiff base with the primary amine groups on the PEI. After crosslinking using gluteraldehyde during ice-templating, the sample was thawed and NaBH_4 was used to reduce the unstable imines formed by the amine-aldehyde coupling to amines. These water-swollen colloidal scaffolds too recovered from large compressive strains; however, gluteraldehyde cross-linking results in lower values of moduli (Figure 5.12).

Remarkably, for ice-templated scaffolds that are rendered hydrophobic by chemical modification of residual amines from the PEI in the network walls, we observe recovery from compression in apolar solvents such as toluene, in a manner similar to the water-swollen networks (Figure 5.13). Thus, the elastic recovery of the monoliths is independent, even of the characteristics of the fluid used to swell the colloidal gel. Thus, the elastic response of the ice-templated and cross-linked monoliths appears to be inherent to the preparation protocol and is independent of the specific chemistry involved.

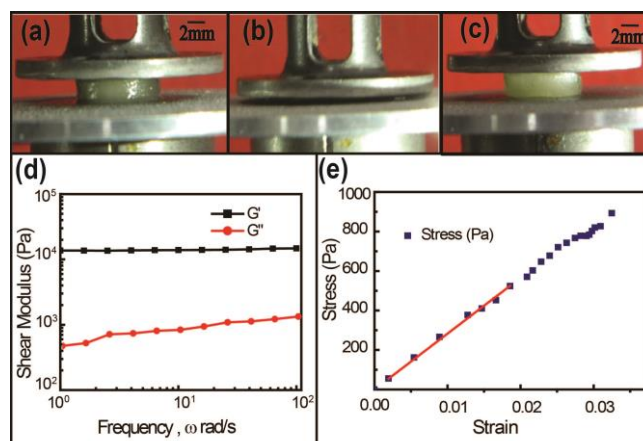


Figure 5.13 Photographs that show the compression of scaffold prepared by ice templating a 10% w/v dispersion of 1 μm silica particles, with 25 kDa PEI and poly(ethyleneglycol) diglycidyl ether (PEG-diepoxyde) as the crosslinker. The scaffold is subsequently hydrophobized by chemical modification and the compression/recovery test is done in toluene. The photographs show (a) the initial state (b) the compressed state (strain = 85%) and (c) recovery on release of stress. (d) Frequency sweep for these scaffolds. We observe that $G' = 13700$ Pa at $\omega = 1$ rad/s. (e) Stress versus strain for compression test on the same scaffold. The elastic modulus, $E^* = 28300$ Pa, is obtained as the slope of the initial linear region of the stress-strain data.

5.5 Conclusions

In summary, ice-templating a colloidal dispersion containing a small fraction of cross-linkable polymer followed by cross-linking in the frozen state results in soft monoliths with a novel microstructure that allows the scaffolds to recover elastically⁵ from large compressive deformations. The microstructure within the colloidal walls enables relative motion between the colloids, creating several conformational states. Recovery happens through an entropic response to the deformation-induced restriction of accessible conformational states. This understanding allows us to create elastic scaffolds from a variety of starting materials, independent of specific chemistry. This opens a route to robust-to-compression “designer” monoliths based on functional colloids for applications in several technological areas. Furthermore, ice freezing during cross-linking could also have implications for the preparation of colloidal models for flexible polymer chains,²⁵ and the monoliths could also

serve as colloidal models for rubber. Combining such colloidal models with the power of confocal microscopy could yield exciting new insights into the structure, dynamics, and phase transitions of flexible polymer systems.

5.6 References

- 1) Gibson, L. J.; Ashby, M. F., *Cellular Solids - Structure and Properties*. 2nd ed.; Cambridge University Press: 1999.
- 2) (a) Iskandar, F.; Mikrajuddin; Okuyama, K., *Nano Letters* 2001, 1 (5), 231; (b) Arachchige, I. U.; Brock, S. L., *Acc.Chem.Research* 2007, 40 (9), 801 (c) Sharma, K. P.; Ganai, A. K.; Gupta, S. S.; Kumaraswamy, G., *Chem. Mater* 2011, 23 (6), 1448; (d) Rhodes, K. H.; Davis, S. A.; Caruso, F.; Zhang, B.; Mann, S., *Chem. Mater.* 2000, 12 (10), 2832; (e) Stein, A.; Schroden, R. C., *Curr. Opin. Solid State Materials Sci.* 2001, 5 (6), 553.
- 3) Leventis, N.; Sotiriou-Leventis, C.; Zhang, G.; Rawashdeh, A.-M. M., 2002, 2 (9), 957.
- 4) (a) Pierre, A. C.; Pajonk, G. M., *Chemical Reviews* 2002, 102 (11), 4243; (b) Hüsing, N.; Schubert, U., *Angew.Chem. Int. Ed.* 1998, 37 (1-2), 22.
- 5) (a) Schaedler, T. A.; Jacobsen, A. J.; Torrents, A.; Soresnen, A. E.; Lian, J.; Green, J. R.; Valdevit, L.; Carter, W. B. *Science* 2011, 334, 962; (b) Jang, D.; Meza, L. R.; Greer, F.; *Nat. Mater.* 2013; (c) Zheng, X.; Lee, H.; Weisgraber, T. H.; Shusteff, M.; DeOtte, J.; Du-oss, E. B.; Kuntz, J. D.; Biener, M. M.; Ge, Q.; Jackson, J. A.; Kucheyev, S. O.; Fang, N. X.; Spadaccini, C. M. *Science*, 2014, 344, 1373.
- 6) Lee, L. J.; Zeng, C.; Cao, X.; Han, X.; Shen, J.; Xu, G., *Composites Sci.Tech.* 2005, 65 (15–16), 2344.
- 7) (a) Nguyen, B. N.; Meador, M. A. B.; Tousley, M. E.; Shonkwiler, B.; McCorkle, L.; Scheiman, D. A.; Palczer, A., *ACS Appl. Mater. & Interf.* 2009, 1 (3), 621. (b) Nguyen, B. N.; Meador, M. A. B.; Medoro, A.; Arendt, V.; Randall, J.; McCorkle, L.; Shonkwiler, B., *ACS Appl. Mater. & Interf.* 2010, 2 (5), 1430.
- 8) (a) Venkateswara Rao, A.; Bhagat, S. D.; Hirashima, H.; Pajonk, G. M., *J. Coll. Interf Sci.* 2006, 300 (1), 279 (b) Kanamori, K.; Aizawa, M.; Nakanishi, K.; Hanada, T., *Adv. Mater* 2007, 19 (12), 1589.

- 9) (a) Lin, Y.; Skaff, H.; Böker, A.; Dinsmore, A. D.; Emrick, T.; Russell, T. P., *J. Am. Chem. Soc.* 2003, 125 (42), 12690 (b) Mueggenburg, K. E.; Lin, X.-M.; Goldsmith, R. H.; Jaeger, H. M., *Nat Mater* 2007, 6 (9), 656.
- 10) (a) Podsiadlo, P.; Krylova, G.; Lee, B.; Critchley, K.; Gosztola, D. J.; Talapin, D. V.; Ashby, P. D.; Shevchenko, E. V., *J. Am. Chem. Soc.* 2010, 132 (26), 8953 (b) Klajn, R.; Bishop, K. J. M.; Fialkowski, M.; Paszewski, M.; Campbell, C. J.; Gray, T. P.; Grzybowski, B. A., *Science* 2007, 316 (5822), 261-264. c) Lee, D.; Jia, S.; Banerjee, S.; Bevk, J.; Herman, I. P.; J. W. Kysar, *Phys. Rev. Lett.* 2007, 98, 026103
- 11) Olsson, R. T.; Azizi Samir, M. A. S.; Salazar Alvarez, G.; Belova, L.; Strom, V.; Berglund, L. A.; Ikkala, O.; Nogues, J.; Gedde, U. W., *Nat Nano* 2010, 5 (8), 584.
- 12) (a) Zhang, H.; Hussain, I.; Brust, M.; Butler, M. F.; Rannard, S. P.; Cooper, A. I., *Nat Mater* 2005, 4 (10), 787. (b) Gutiérrez, M. C.; Ferrer, M. L.; del Monte, F., *Chem. Mater.* 2008, 20 (3), 634. (c) Deville, S.; Saiz, E.; Nalla, R. K.; Tomsia, A. P., *Science* 2006, 311 (5760), 515 (d) Munch, E.; Launey, M. E.; Alsem, D. H.; Saiz, E.; Tomsia, A. P.; Ritchie, R. O., *Science* 2008, 322 (5907), 1516.
- 13) Sharma, K. P.; Kumaraswamy, G.; Ly, I.; Mondain-Monval, O. J. *Phys. Chem. B* 2009, 113, 3423
- 14) Meador, M. A. B.; Fabrizio, E. F.; Ilhan, F.; Dass, A.; Zhang, G.; Vassilaras, P.; Johnston, J. C.; Leventis, N., *Chem. Mater.* 2005, 17 (5), 1085.
- 15) Greaves, G. N.; Greer, A. L.; Lakes, R. S.; Rouxel, T., *Nat Mater* 2011, 10 (11), 823.
- 16) Katti, A.; Shimpi, N.; Roy, S.; Lu, H.; Fabrizio, E. F.; Dass, A.; Capadona, L. A.; Leventis, N., *Chem. Mater.* 2005, 18 (2), 285.
- 17) Treolar, L. R. G., *The Physics of Rubber Elasticity*. 3rd ed.; Oxford University Press: 2005.
- 18) Rubinstein, M.; Colby, R. H. *Polymer Physics*, 2003, Oxford University Press, Oxford
- 19) Storm, C.; Pastore, J. J.; MacKintosh, F. C.; Lubensky, T. C.; Janmey, P. A., *Nature* 2005, 435 (7039), 191.
- 20) (a) Friedlander, S. K.; Jang, H. D.; Ryu, K. H., *App. Phys. Lett.* 1998, 72 (2), 173 (b) Friedlander, S. K., *J. Nanoparticle Res.* 1999, 1 (1), 9 (c) Friedlander, S. K.; Ogawa, K.; Ullmann, M., *J. Polym. Sci. B: Polym. Phys.* 2000, 38 (20), 2658.
- 21) Kumar, D.; Bhattacharya, S.; Ghosh, S., *Soft Matter* 2013, 9 (29), 6618.
- 22) D. Kumar, S. Ghosh, S. Bhattacharya, *J. Chem. Phys.* 2012, 137, 224901.

- 23) (a) Freyman, T. M.; Yannas, I. V.; Gibson, L. J., *Prog.Mater. Sci.* 2001, 46 (3–4), 273
(b) Kanungo, B. P.; Silva, E.; Vliet, K. V.; Gibson, L. J., *Acta Biomater.* 2008, 4 (3), 490
(c) Gaharwar, A. K.; Dammu, S. A.; Canter, J. M.; Wu, C.-J.; Schmidt, G., *Biomacromolecules* 2011, 12 (5), 1641. (d) Song, J.; Xu, J.; Fillion, T.; Saiz, E.; Tomsia, A. P.; Lian, J. B.; Stein, G. S.; Ayers, D. C.; Bertozzi, C. R., *J. Biomed. Mater. Res. Part A* 2009, 89A (4), 1098.
- 24) (a) Engler, A. J.; Sen, S.; Sweeney, H. L.; Discher, D. E., *Cell* 2006, 126 (4), 677. (b) Pek, Y. S.; Wan Andrew, C. A.; Shekaran, A.; Zhuo, L.; Ying, J. Y., *Nat Nano* 2008, 3 (11), 671. (C) Jeong, S. I.; Kwon, J. H.; Lim, J. I.; Cho, S.-W.; Jung, Y.; Sung, W. J.; Kim, S. H.; Kim, Y. H.; Lee, Y. M.; Kim, B.-S.; Choi, C. Y.; Kim, S.-J., *Biomaterials* 2005, 26 (12), 1405. (d) Jung, Y.; Park, M. S.; Lee, J. W.; Kim, Y. H.; Kim, S.-H.; Kim, S. H., *Biomaterials* 2008, 29 (35), 4630.
- 25) (a) Vutukuri, H. R.; Demirörs, A. F.; Peng, B.; van Oostrum, P. D. J.; Imhof, A.; van Blaaderen, A., *Angew.Chem. Int. Ed.* 2012, 51 (45), 11249 (b) Liu, K.; Nie, Z.; Zhao, N.; Li, W.; Rubinstein, M.; Kumacheva, E., *Science* 2010, 329 (5988), 197.

Chapter 6

Conclusions and Future Work

6.1 Summary and Conclusions

This dissertation describes the synthesis and characterization of various porous hybrid mesoporous and macroporous materials for their application in catalysis. It includes development of synthetic methodology for generation of novel functional mesoporous hybrid materials using “click chemistry” reactions such as “activated thiol-ene” and “CuAAC”. This thesis also describes the synthesis of hybrid macroporous material using dynamic templating of surfactant H₁ domains and ice templating method. The application of these porous hybrid materials as catalysts in continuous flow reaction has also been evaluated. This chapter presents the summary and conclusions of all the previous chapters. It also discusses the future scope based on the work reported in this thesis.

Chapter 1 provides a brief review on the literature of porous organic inorganic hybrid materials including synthetic strategies for mesoporous and macroporous materials. This chapter discusses click chemistry based approaches for the synthesis of hybrid organic-inorganic mesoporous materials by incorporation of functional organic groups onto porous materials using thiol-ene and Cu(I) catalyzed azide-alkyne cycloaddition. The top down and bottom up approaches for the synthesis of macroporous materials along with the application of porous organic-inorganic hybrid materials has been discussed in this chapter. The various analytical techniques used for the characterization of mesoporous and macroporous hybrid materials are also described. Finally, the motivation for the development of porous hybrid materials is discussed.

Chapter 2 describes the synthesis of a methacrylate labeled SBA-15 material that undergoes very efficient “thiol-ene click reaction” with a variety of both thiol and disulphide containing substrates in aqueous and organic media. These materials were well characterized by using a variety of analytical techniques including SAXS, SEM, TEM, multinuclear (¹³C, ²⁹Si) solid-state NMR, BET analysis, TGA, ICP, cyclic voltammetry (CV), and confocal microscopy. For example, the incorporation of the organic functionality was confirmed by DRIFT-IR spectroscopy, where carbonyl stretching vibrations of methacrylate moiety shifted from 1700 to 1720 cm⁻¹. A highlight of the reaction was the use of disulphide containing substrates in which the disulphide bond was reduced to the corresponding thiol and subsequently added to the methacrylate group in “one-pot”. This “thiol-ene click reaction” was used to synthesize silica-protein hybrid material and an electrochemically active material. The ease of synthesis

for the methacrylate labeled SBA-15 material together with its ability to undergo very efficient chemoselective thiol-ene reaction would make it a very attractive platform for the development of covalently anchored enzymes and sensors. This methodology is general and can also be extended to the synthesis of other functional inorganic materials.

Chapter 3 describes a peroxidase mimicking hybrid material in which small molecule peroxidase mimic Fe-TAML was chemically conjugated inside a 40 nm mesoporous silica nanoparticle (MSN). Biuret-modified Fe-TAML's represent one of the best small molecule functional mimics of the enzyme HRP with reaction rates in water close to the native enzyme and operational stability (pH, ionic strength) far exceeding the natural enzyme. Using antibody conjugates of this hybrid material, it is possible to detect and most importantly quantify femtomolar quantities of proteins colorimetrically in an ELISA type assay. In a biomimetic approach, ~25 000 biuret modified Fe-TAML were attached inside MSN (possible because of the small size of the mimic). This resulted in a hybrid material with catalytic activity that is 1 000 folds higher than natural HRP and 100 folds higher than most metal/metal oxide nanoparticle based HRP mimics developed till date. This represents an example of one of the most effective peroxidase mimic which allows ultra-sensitive protein detection (fM and lower) and quantification using a colorimetric assay.

Chapter 4 describes the synthesis of large (centimeter-sized) self-standing macroporous scaffold monoliths from ferritin bionanoparticles using dynamic templating of surfactant H₁ domains. These scaffolds represent the first example of macroscopic gels comprised predominantly of bionanoparticles. Such materials combine the advantages of cage-like nanoparticles (namely, the ability to sequester a variety of cargo in monodisperse protein cages), with those afforded by a highly porous three-dimensional architecture (that would facilitate access to the "cargo" in the nanocages, and allow easy transport of substrate and products). The catalytically active metal nanoparticles embedded inside macroporous three-dimensional ferritin gel can be used for both batch and continuous flow chemistry. The presence of macropores allow the ferritin scaffold to act as catalytic monolith for continuous flow reactions having rapid reaction rates, while offering a low pressure drop. The iron oxide nanoparticles inside the scaffold were exchanged with Pd nanoparticles to afford Pd@apo-ferritin scaffold. The Pd@apo-ferritin scaffold was immobilized inside a steel cartridge and used for the continuous flow hydrogenation of alkenes to alkane with a turnover number of

over 12 000 per Pd nanoparticle for each catalytic cycle. The catalytic activity remained unchanged for an additional 14 cycles for the hydrogenation reaction.

Chapter 5 describes the synthesis of macroporous assemblies predominantly comprising colloidal particles (up to 90% by weight of inorganic) that can be rendered elastic and, recovers their structure completely after compression to 15% of their original size. These elastically compressible monoliths can be prepared starting from inorganic colloids, such as silica and hydroxyapatite and glassy polymer colloids, such as polystyrene lattices. The preparation technique is facile: an aqueous dispersion of colloids and a polymer, capable of coating the colloids, is frozen and the polymer is cross-linked in the frozen state. The ice crystals template particles and polymers which are subsequently organized into a macroporous material. Remarkably, the elastic mechanical properties are independent of the specific polymer used in this process and the crosslinking chemistry. Importantly, the route that we have outlined is not limited to a specific class of particles and thus appears to be generally applicable to a wide variety of materials. Therefore, materials prepared using this route is likely to have widespread utility in several applications ranging from aerospace to biomaterials. Further studies provided clear evidence for the mechanistic origin of the observed elasticity. The elastic modulus of the macroporous scaffolds increases approximately linearly with temperature, rather than decreasing as has been shown in all previous reports for inorganic or glassy scaffolds. This indicates that the elastic recovery from compression is entropic in origin. Such elastic scaffolds open a route to robust-to-compression “designer” monoliths based on functional colloids for applications in several technological areas.

6.2 Scope of future work

The work described in the dissertation opens up several new opportunities. Some of them are listed below.

1) Tissue engineering scaffold:

Tissue engineering applications require the development of porous biomaterials that facilitate cell growth by matching the bulk mechanical and structural properties of the target

tissue. Mimicking these properties will enable interactions between the scaffolds and cells to promote tissue healing. Materials based on spider silk are non-immunogenic and cytocompatible, exhibit good mechanical properties, and are thus expected to be well-suited scaffolds for tissue engineering.

In this dissertation, I have prepared macroporous scaffolds from an aqueous dispersion of colloidal particles with > 90 wt % that can recover elastically after compression to about one-tenth their original size. Usually spider silk scaffolds are mechanically strong; the ice templating method will allow to generate soft and flexible macroporous scaffolds in the proposed research as shown in Figure 6.1. Silk-silica composite scaffolds will be prepared by ice templating of an aqueous dispersion of silk coated porous silica particles. MSN have well-defined silanol-containing surface properties that allow an easy functionalization for an effective combination with drugs or growth factors.

Here, I propose to prepare composite scaffold materials made of spider silk proteins and porous inorganic nanoparticles that are bioactive and sponge-type with a three-dimensional (3-D) macroporosity. The preparation of such scaffolds by ice-templating should lead to a soft spongy material containing > 90 wt% of inorganic particles with controllable pore sizes, pore interconnectivity, and the inherent biocompatible properties of silk, all of which are key requirements for soft-tissue engineering. Additionally, the high content of porous inorganic material (exemplary mesoporous silica) within a spider silk 3-D matrix could act as a reservoir for the encapsulation of bioactive molecules like growth factors. The aim is to facilitate cell adhesion, proliferation, and migration over a period of time which is the crucial requirement for the regeneration of tissues. Encapsulating the mesoporous nanoparticles within spider silk should effectively prolong the release of growth factors over weeks to months, providing a nano-carrier platform for a sustained release of growth factors. The biological activity of the scaffold will be investigated by analyzing the proliferation of cells on and within the spider silk-silica composite scaffolds. For application of these materials in tissue engineering, the cytotoxicity, cell proliferation rates and degradability of these scaffolds have to be studied in details.

These composite scaffolds will have various attributes, including: (1) biocompatibility and good biodegradability, (2) lack of immunogenicity and allergenicity, (3) good mechanical properties, (4) adjusted porosities and morphologies for transportation of cells, gases, metabolites, nutrients and signal molecules both within the scaffold and into the scaffold from the local environment, (5) potential growth factors like IGF-1, bFGF, VEGF,

and EGF will be encapsulated inside MSN for proper cell proliferation and growth. Encapsulation of growth factors inside the MSN will also prevent their degradation. Scaffolds made of spider silk and MSN encapsulated growth factors will be studied for soft tissue regeneration.

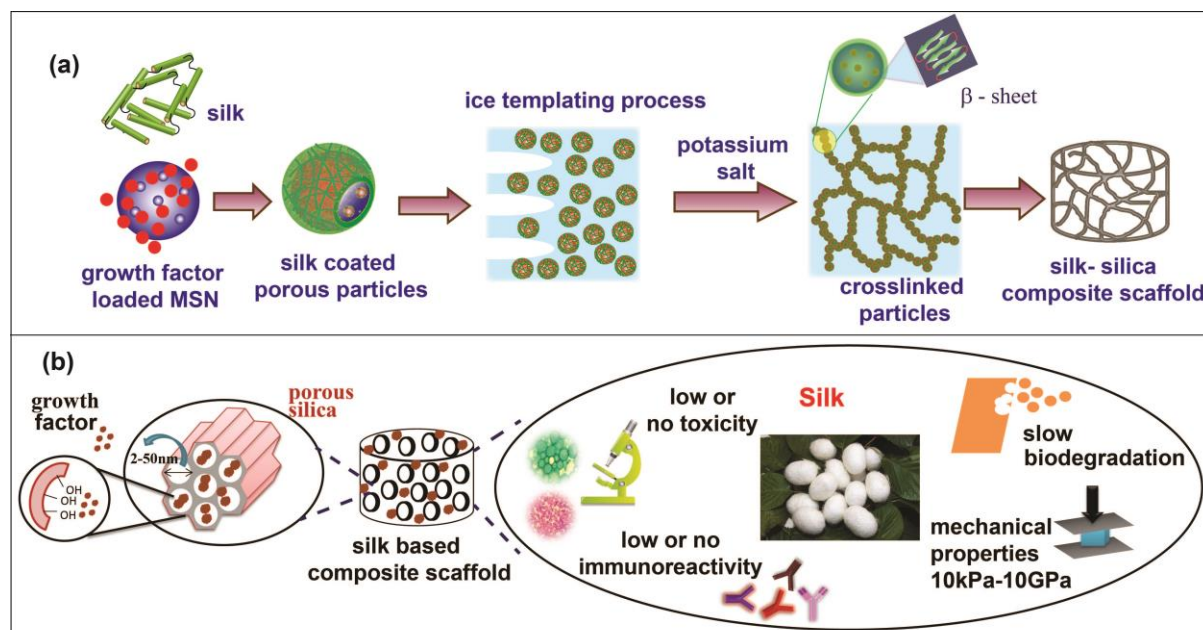


Figure 6.1. (a) Ice templating process for the preparation of a spider silk-silica composite scaffold (b) Properties of a hybrid scaffold based on silk and silica for biomedical applications.

Appendix I

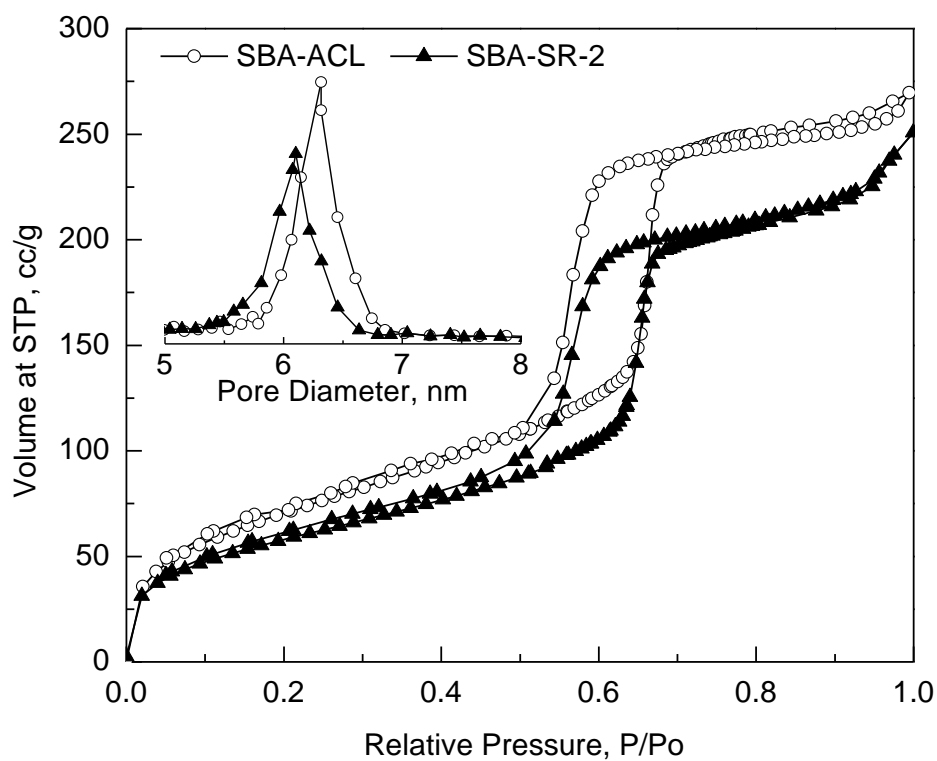


Figure A 1. Nitrogen adsorption-desorption isotherms for various SBA-15 materials (inset) pore size distribution of these various materials

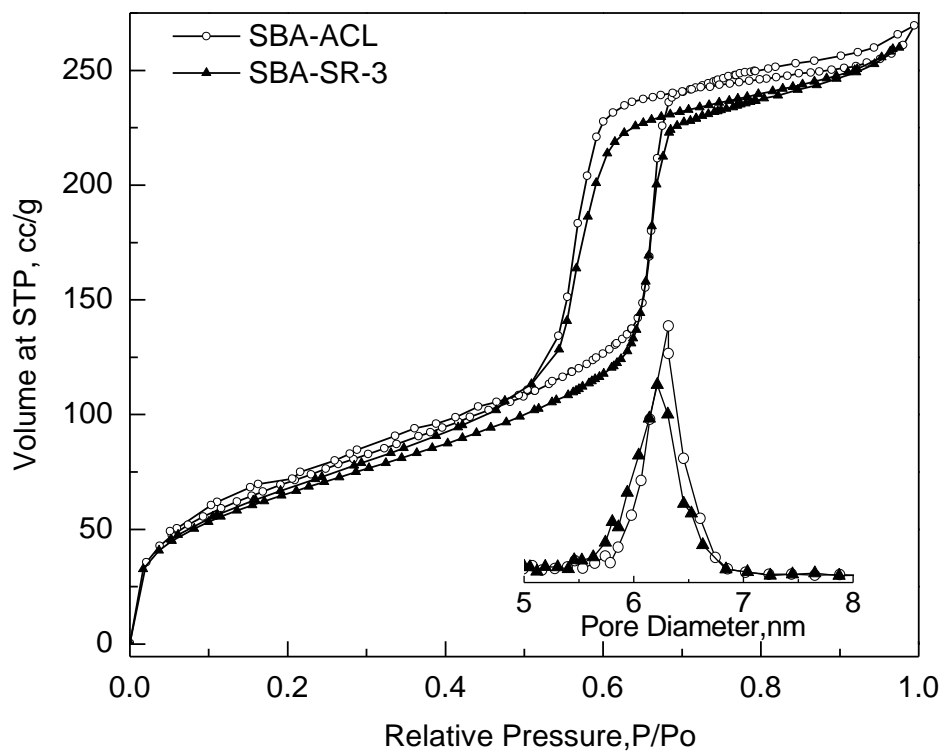


Figure A 2. ^{13}C CP MAS NMR spectra of SBA- SR-2 and SBA-SR-3

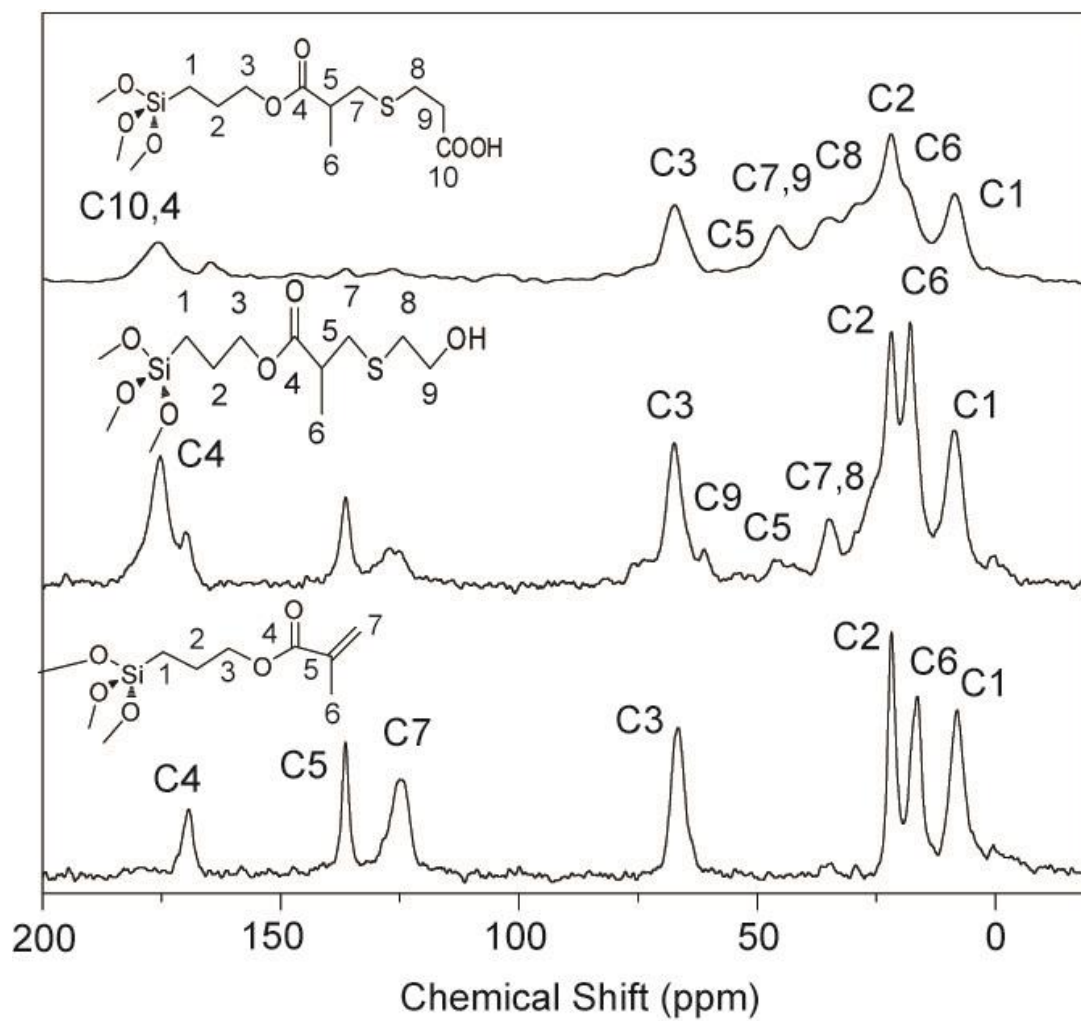


Figure A 3. ^{13}C CP MAS NMR spectra of SBA-SR-2 and SBA-SR-3

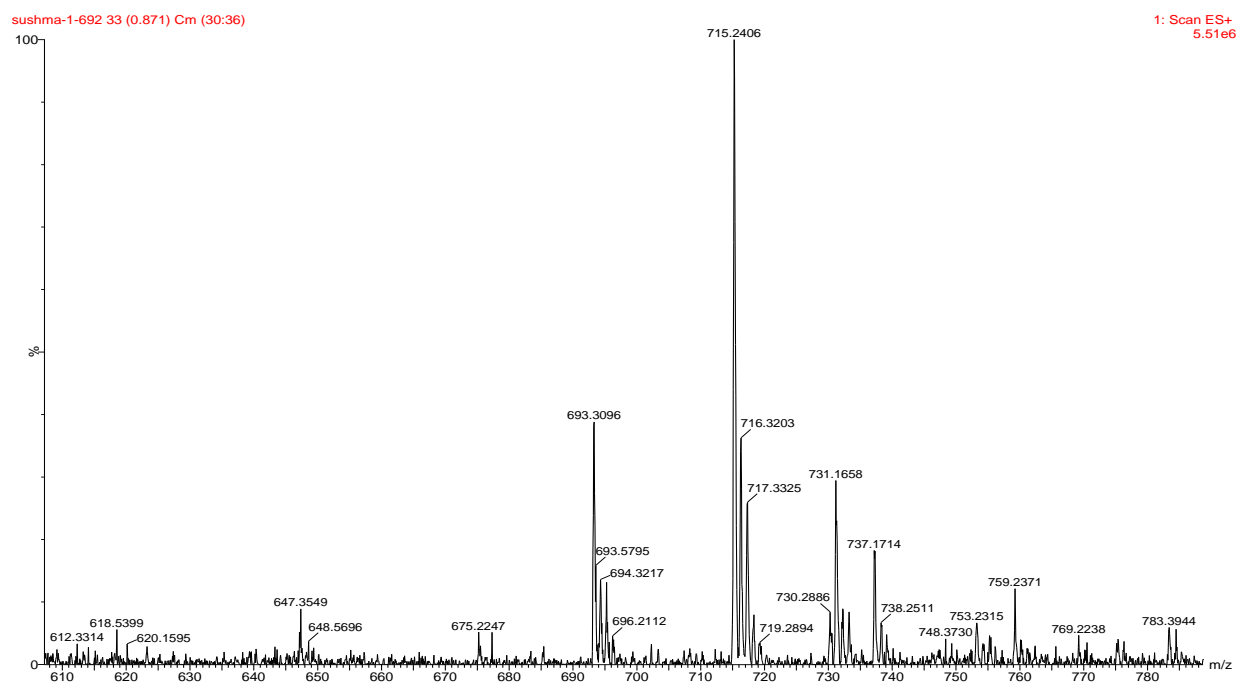


Figure A 4. Mass spectrum of Biotin-NHS-Cystine

Appendix II

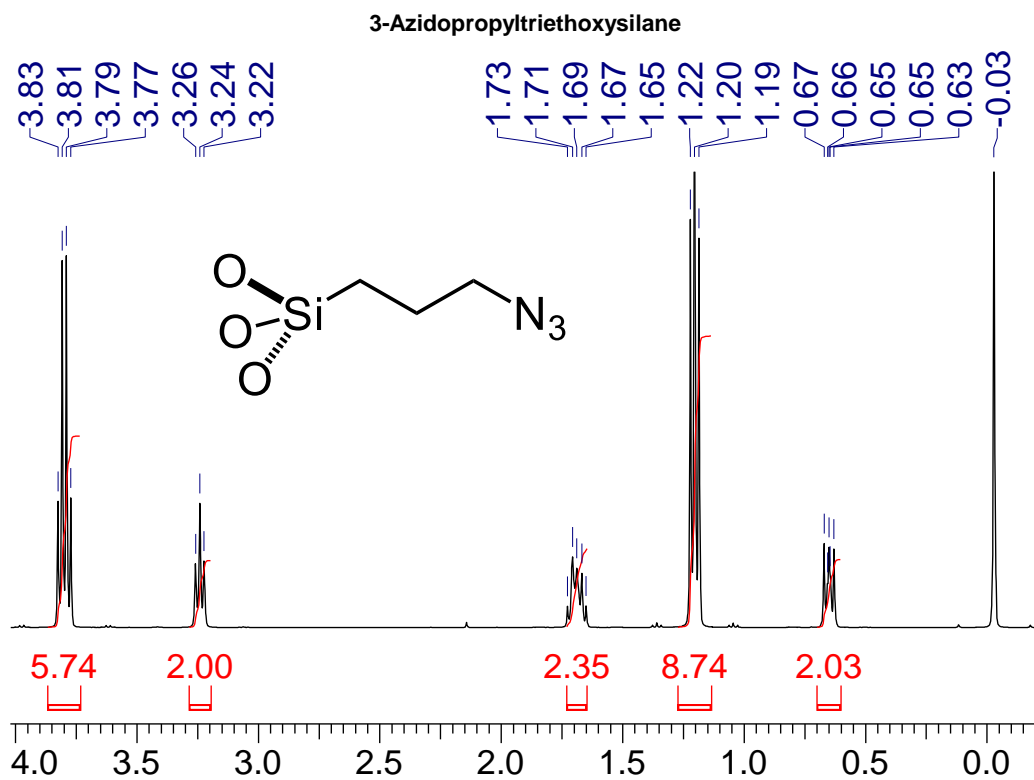


Figure B 1: ^1H NMR spectrum of 3-azidopropyltriethoxysilane

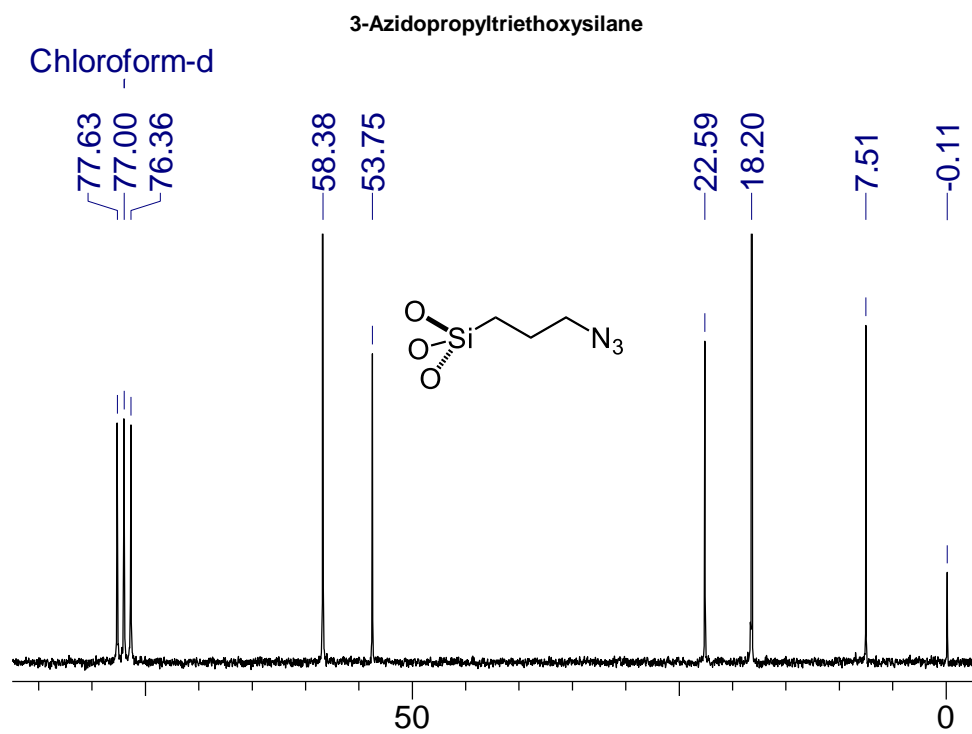


Figure B 2: ^{13}C NMR spectrum of 3-azidopropyltriethoxysilane

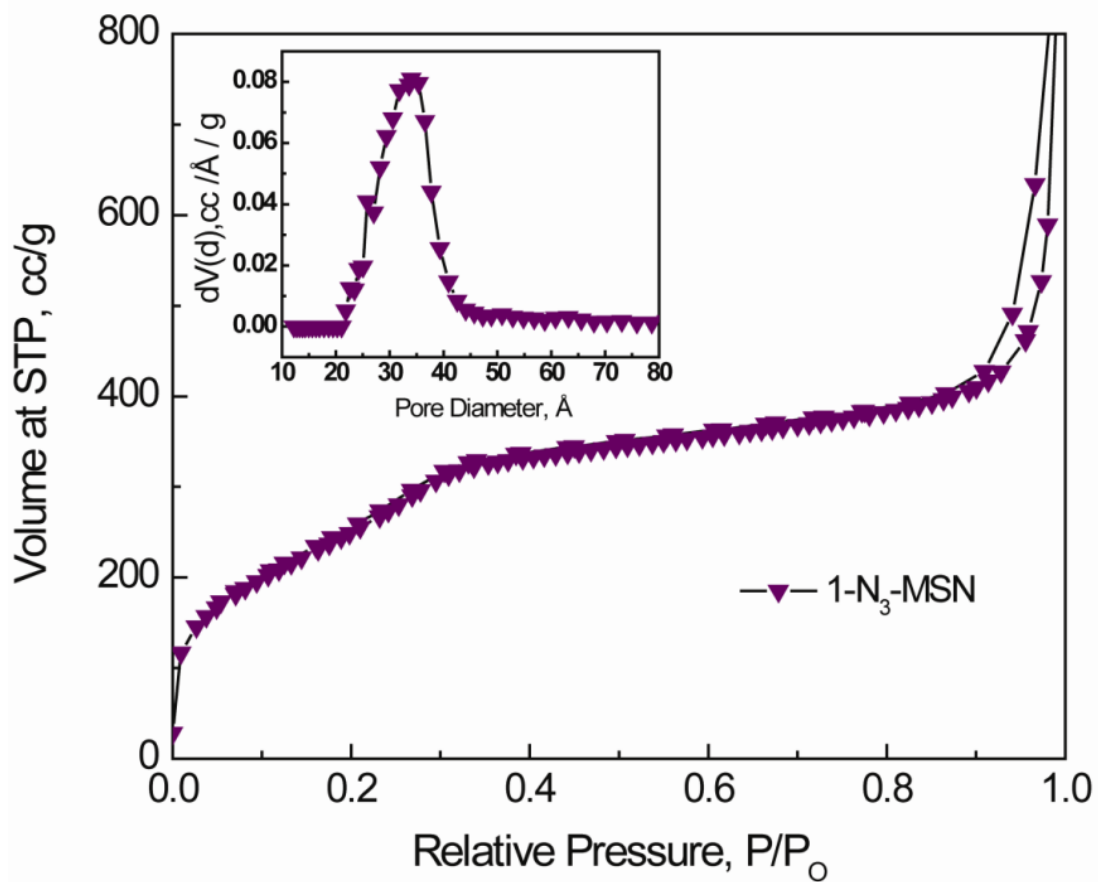


Figure B 3. Nitrogen adsorption-desorption isotherms for 1-N₃-MSN (*inset* shows pore size distribution)

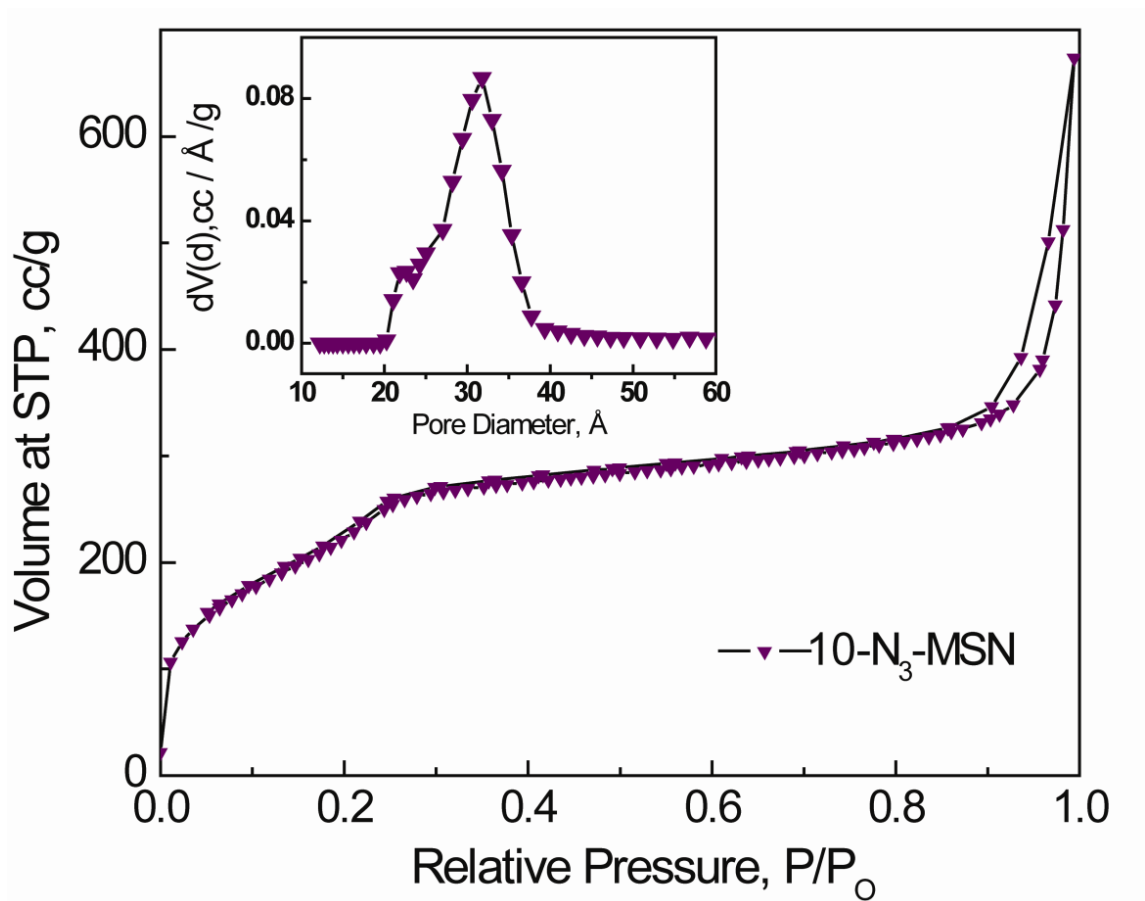


Figure B 4. Nitrogen adsorption-desorption isotherms for 10-N₃-MSN (*inset* shows pore size distribution)

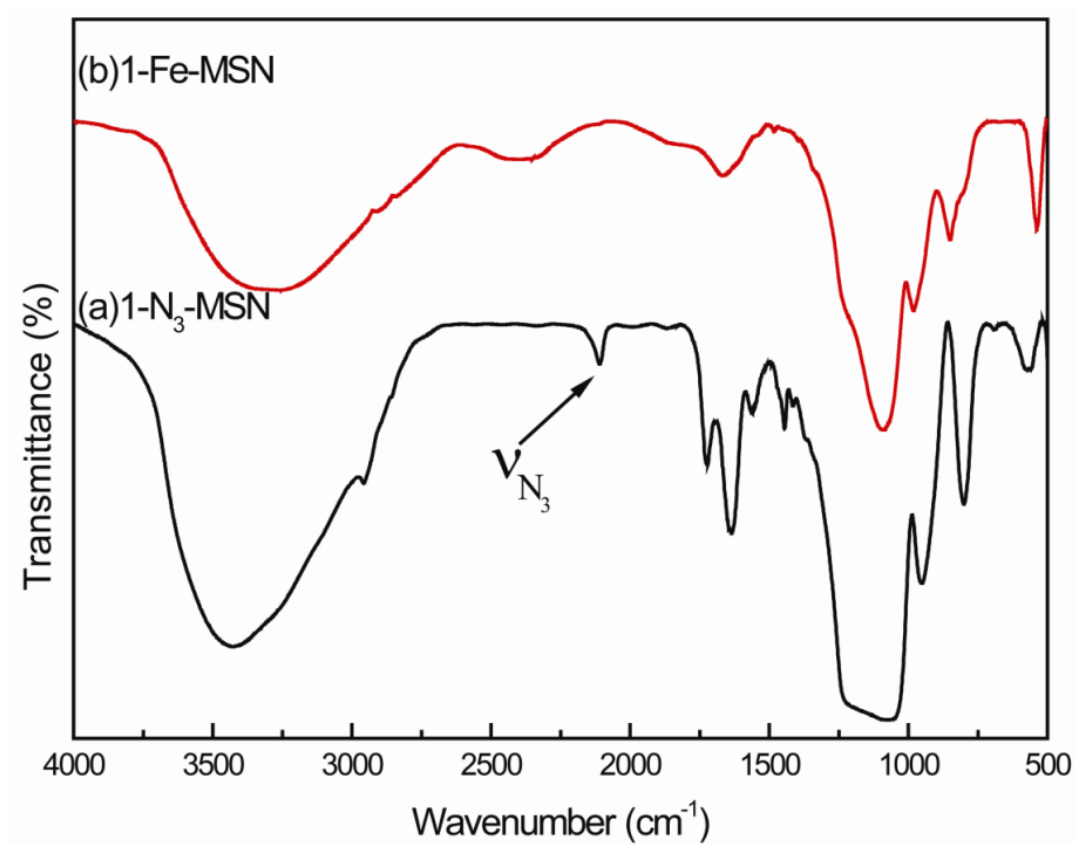


Figure B 5. FT-IR spectra of (a) 1-N₃-MSN and (b) 1-Fe-MSN: IR spectroscopy shows about 98% decrease in the integrated intensity of ν_{N_3} at 2100 cm⁻¹.

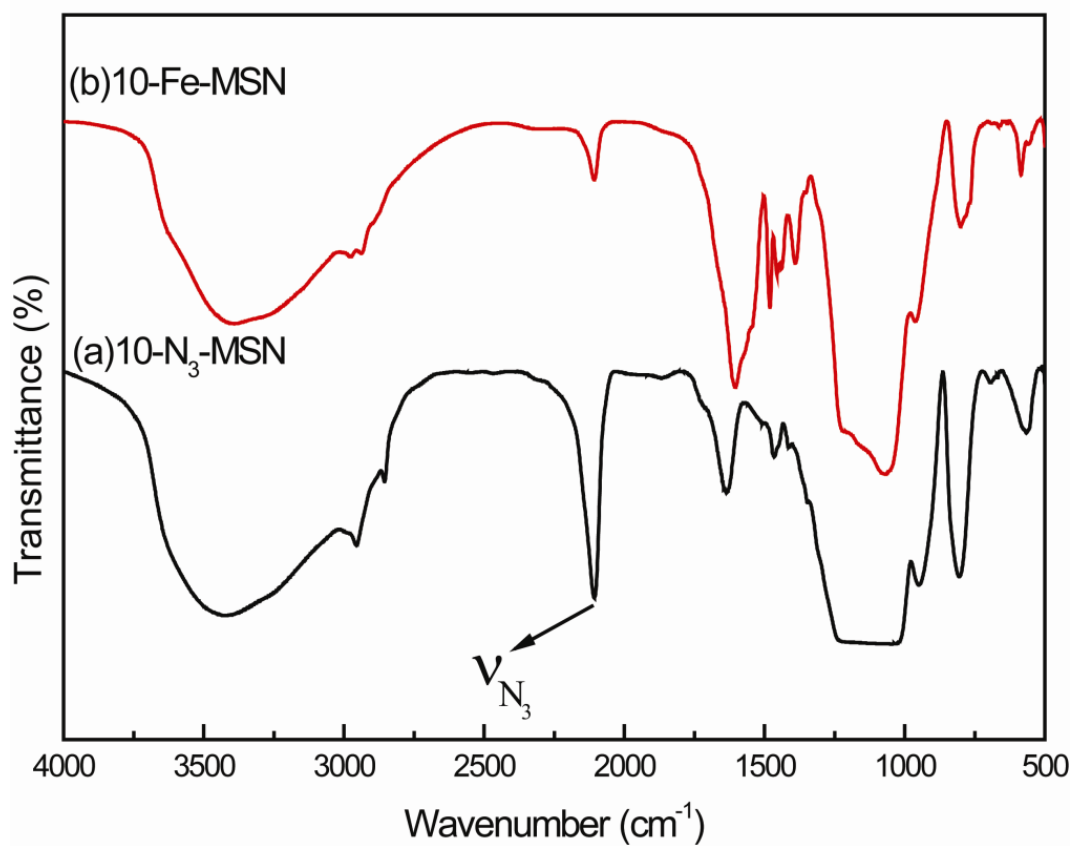


Figure B 6. FT-IR spectra of (a) 10- N_3 -MSN and (b) 10-Fe-MSN: IR spectroscopy shows about 80% decrease in the integrated intensity of ν_{N_3} at 2100 cm^{-1} .

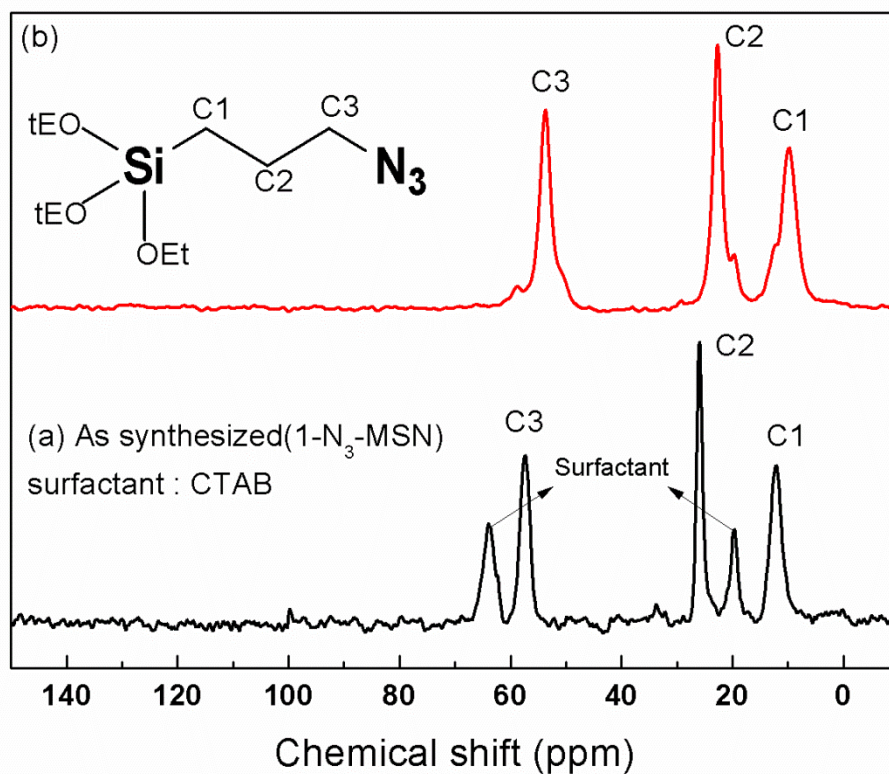


Figure B 7. ^{13}C CPMAS-NMR for 1- N_3 -MSN. NMR spectrum of 1- N_3 -MSN (a, black) showed three distinct peaks corresponding to the C1, C2 and C3 carbon atoms which is similar to three peaks present in azido-propyl silane (b, red) C1 (8.68 ppm), C2 (22 ppm), C3 (53 ppm).

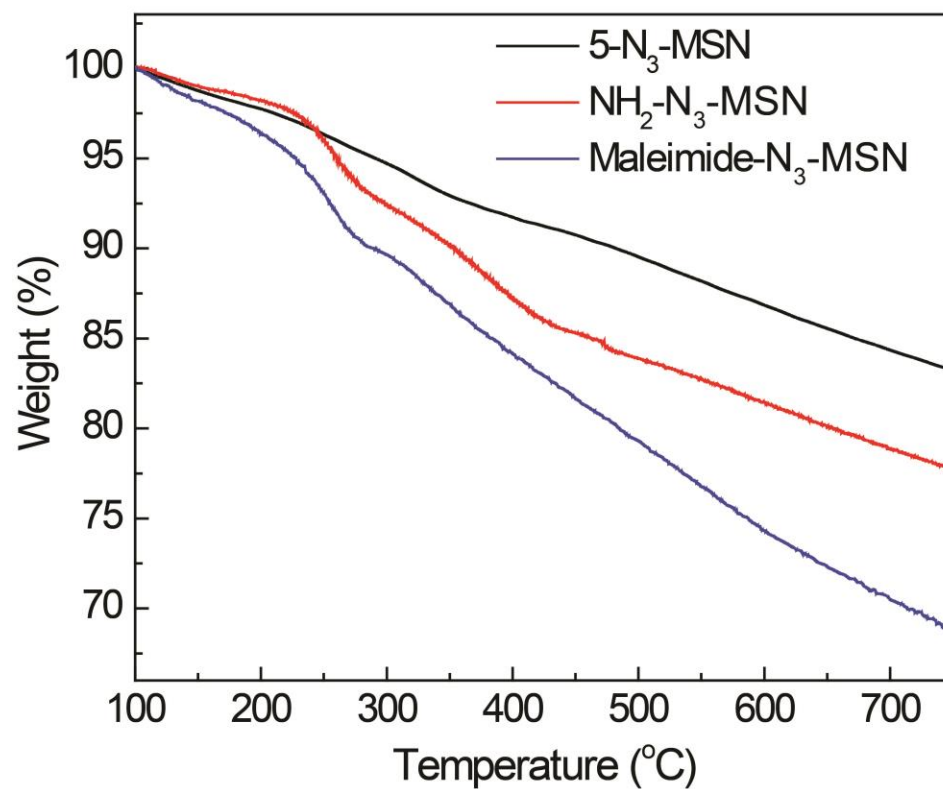


Figure B 8. TGA for NH₂-N₃-MSN and maleimide-N₃-MSN.

Table B. 1. Grafting density of functional moiety for 5-N₃-MSN

Sample	Grafting Density (mmol/g)
5-N ₃ -MSN	0.51
NH ₂ -N ₃ -MSN	1.04
Maleimide-N ₃ -MSN	0.45

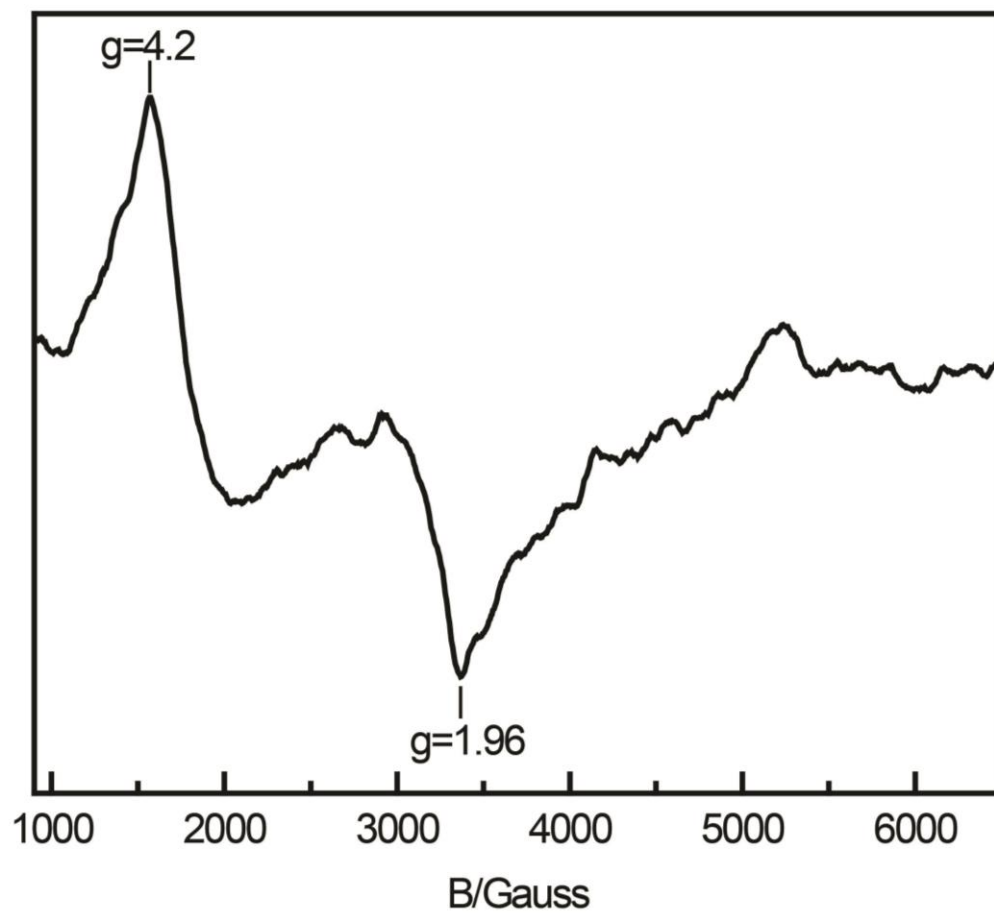


Figure B 9. X-band EPR spectrum of 1-Fe-MSN Solid at 94 K

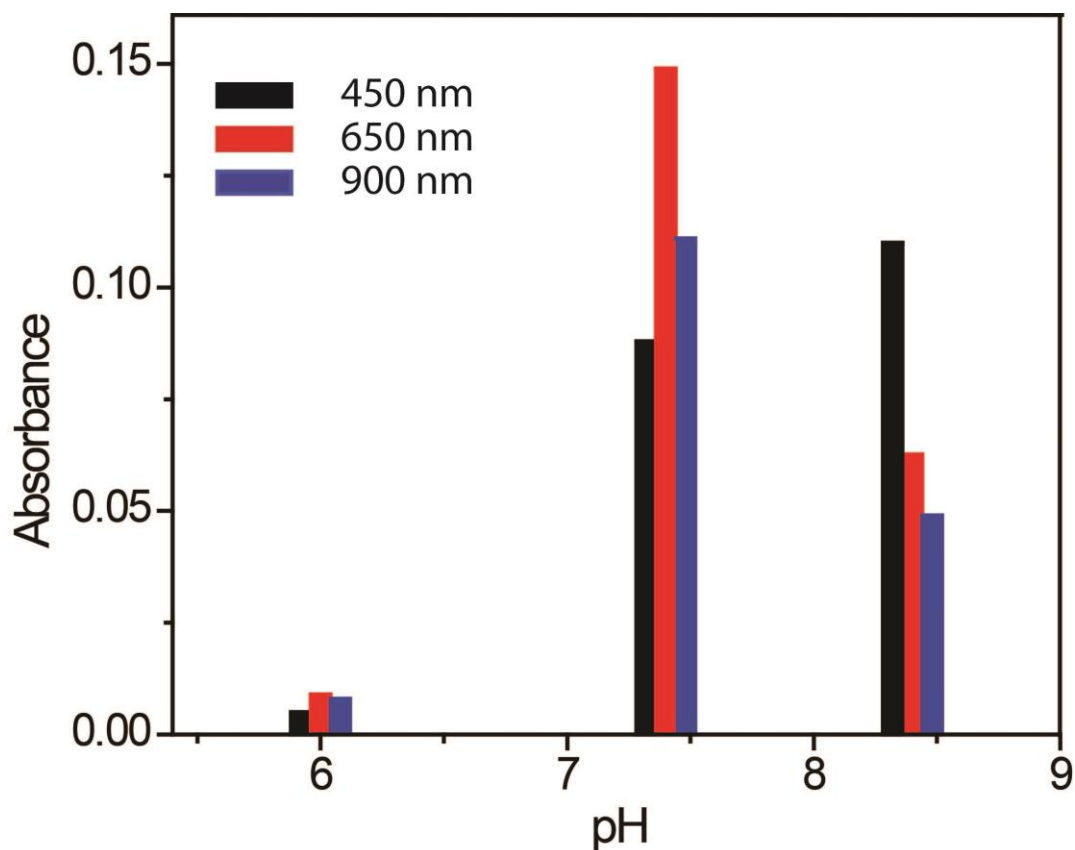


Figure B 10. Absorbance of the three different peaks (450, 650 and 900 nm) generated for TMB oxidation by 5-Fe-MSN and H₂O₂ at pH 6, 7.4 and 8.4. All the absorbance was measured after 60 seconds of the reaction. Reaction condition: [TMB] = 3×10^{-4} M, [H₂O₂] = 1.2×10^{-4} M, [5-Fe-MSN] = 12.5×10^{-14} , PBS buffer of 10mM (pH 6, 7.4 and 8.4).

Appendix III

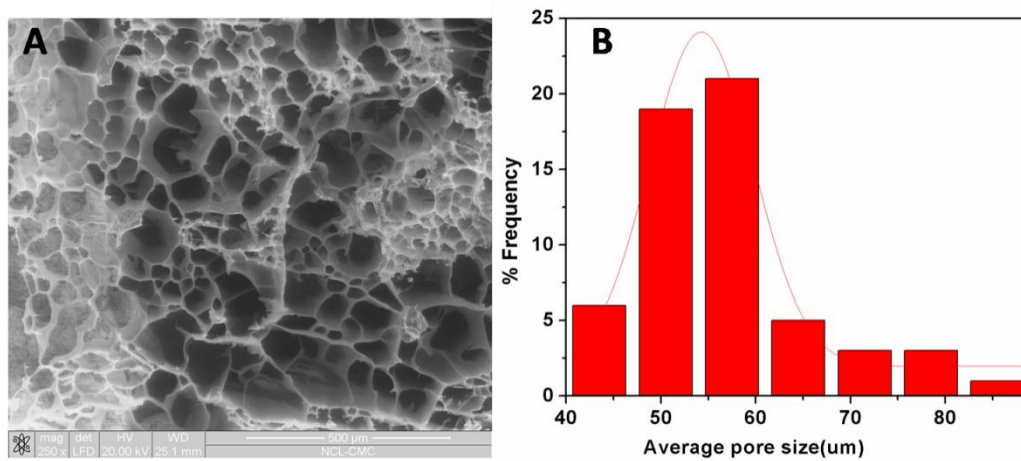


Figure C1. (A) Scanning electron microscope image of ferritin scaffold (B) Pore size distribution of ferritin scaffold (average size $54.25 \pm 0.338 \mu\text{m}$ was estimated using *image J* software)

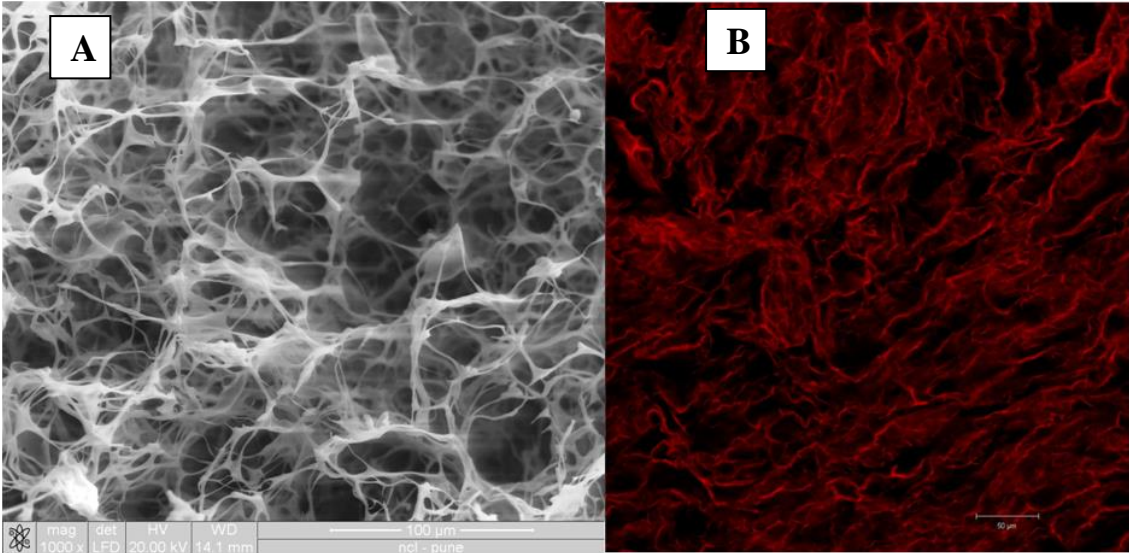


Figure C 2. SEM and Confocal image of scaffold after demineralization

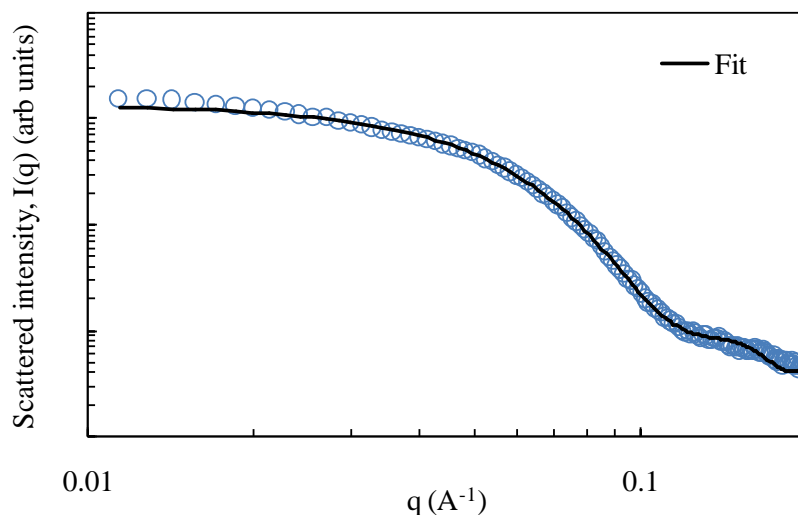


Figure C 3. SAXS data for dispersions of ferritin was obtained, after appropriately subtracting the background scattering. We were unable to fit this data to a model for monodisperse spheres. Introducing polydispersity to this model allowed us to significantly improve the quality of the fit – however, the polydispersity required to achieve this was very large ($\approx 26\%$, with a mean particle radius of 3.4 nm). As such a large polydispersity is inconsistent with our expectations for protein dispersion, we looked for alternate models.¹ We attempted a core shell model for the protein dispersion, as follows:

$$I_s = [K(q, R_o, \Delta\rho_2) - K(q, R_i, \Delta\rho_1 - \Delta\rho_2)]^2$$

where, $[K(q, R_x, \Delta\rho_y)] = \frac{4}{3}\pi R_x^3 \Delta\rho_y (3 \frac{\sin q R_x - q R_x \cos q R_x}{q^3 R_x^3})$, R_o and R_i are the radii of the shell and the core, respectively and $\Delta\rho_2$ and $\Delta\rho_1$ represent the difference in electron densities between the shell and water, and between the core and water, respectively.

Since there are a large number of fit parameters, we constrain the ratio of $\Delta\rho_2$ to $\Delta\rho_1$ using data for the electron densities of water ($0.27 \text{ e}/\text{Å}^3$), the protein coat of the ferritin¹ ($0.41 \text{ e}/\text{Å}^3$) and the core ($\approx 1 \text{ e}/\text{Å}^3$). This yields a good fit to the data, with a core radius of 2.56 nm and a shell thickness of 2.79 nm (see Appendix III, Figure C-4).

¹ Fischbach, F. A.; Anderegg, J. W. *J. Mol. Biol.* **1965**, *14*, 458-473.

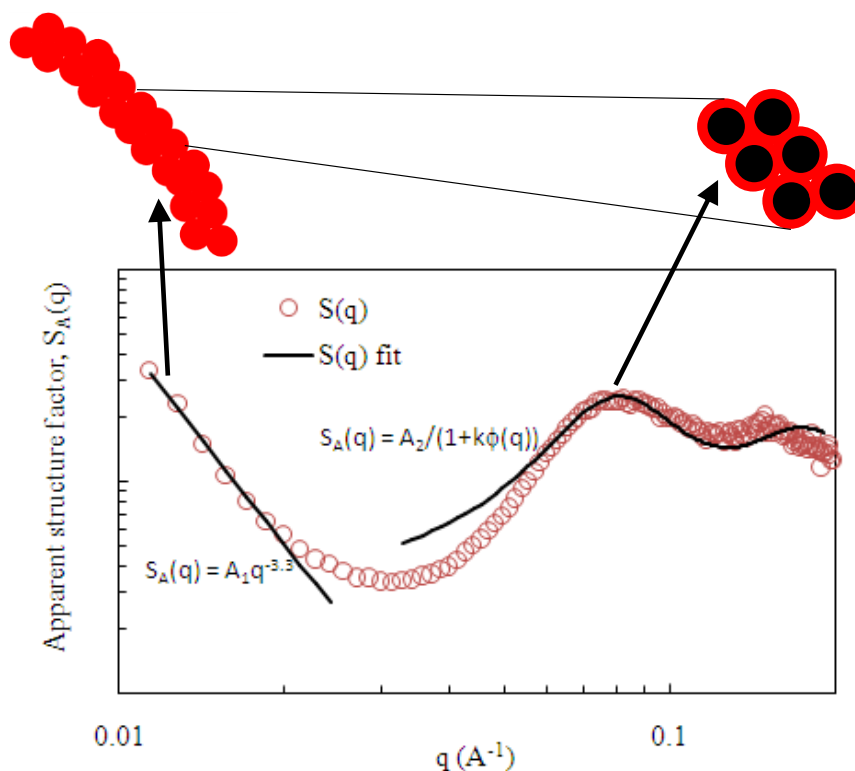


Figure C 4. We obtain an apparent structure factor, $S_A(q)$, by dividing the scattered intensity from the ferritin hydrogel scaffold, by that from the dilute ferritin dispersion. As we do not have an accurate estimate of ferritin concentration in the scaffold, we focus only on the shape of $S_A(q)$, rather than quantitative values. At low q ($<$ around 0.02 \AA^{-1}), we observe a power law decay in $S_A(q)$, that is fitted as $A_1 q^{-3.3}$, where A_1 is a constant. This suggests that the surface of the hydrogel walls are not smooth, possibly due to the particulate nature of the ferritin, and can be described using a surface fractal. At intermediate q , we observe a peak in $S_A(q)$, indicative of the aggregation of ferritin. We model this using as interference function for dense packing, as follows:

$$S_A(q) = A_2 [1 + k\phi(q)]^{-1}$$

where, A_2 is a constant, k is a packing factor, and $\phi = 3 \frac{\sin qd - qd \cos qd}{q^3 d^3}$, where d is the interparticle distance. This yields a reasonable fit to the intermediate q range, and yields $k = 4$ and $d = 7.1 \text{ nm}$.

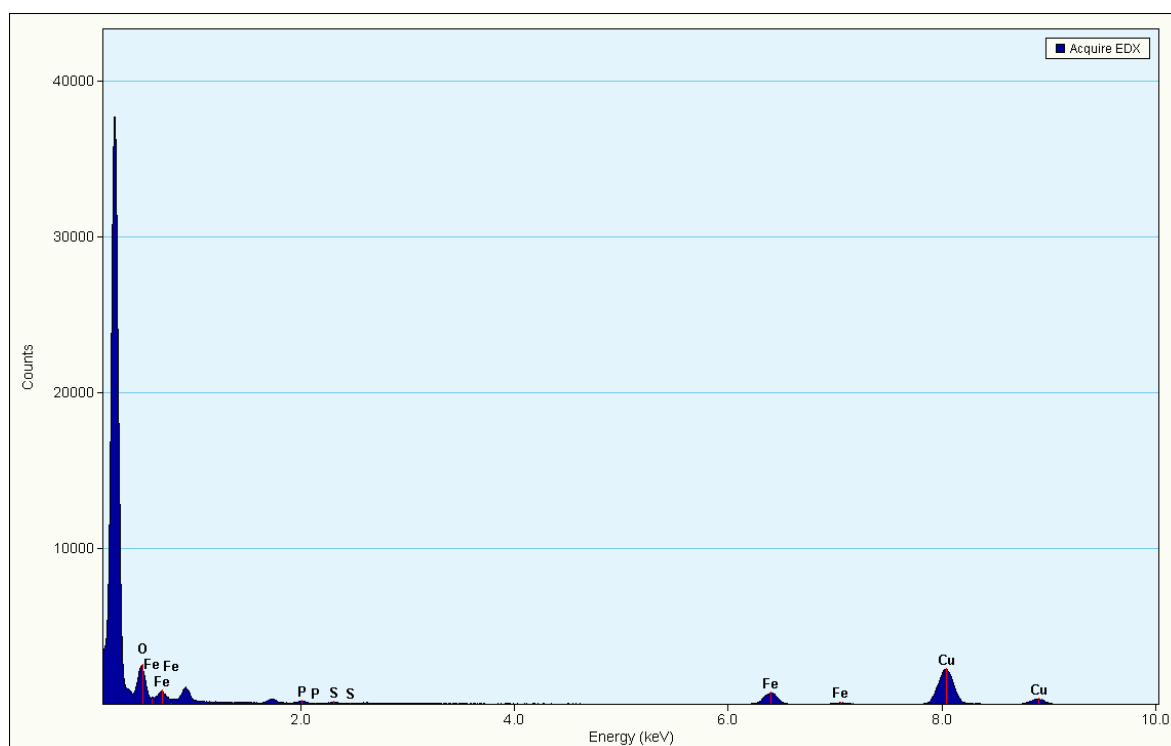


Figure C 5. EDX data for ferritin Scaffold

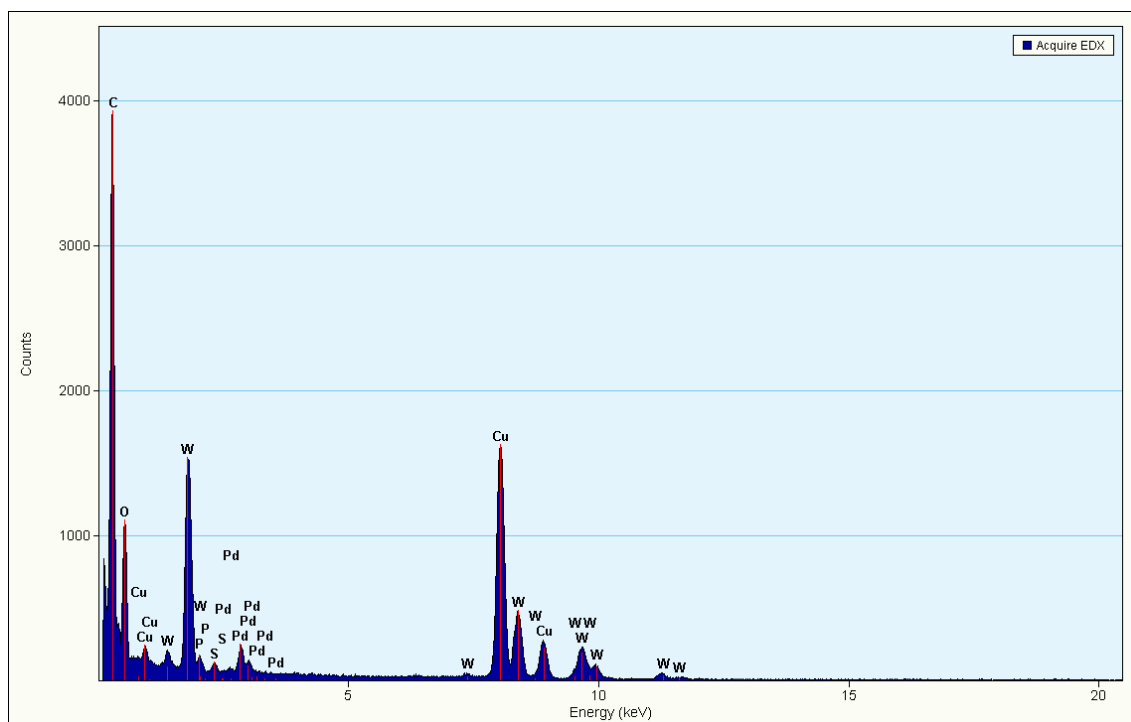
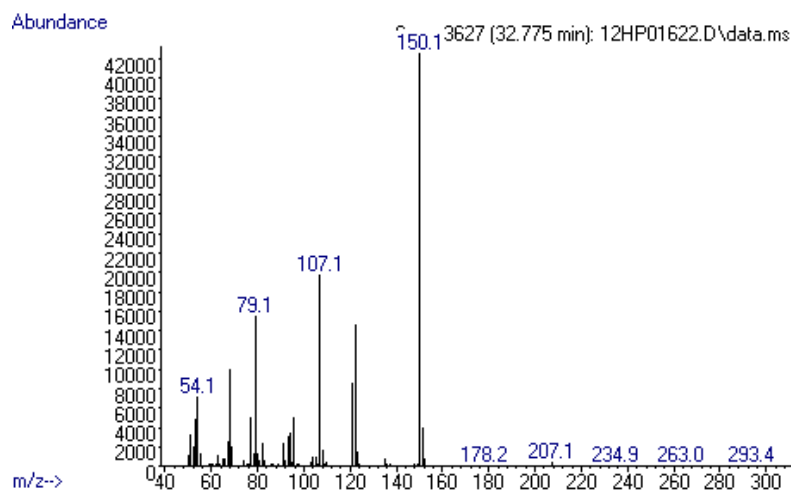
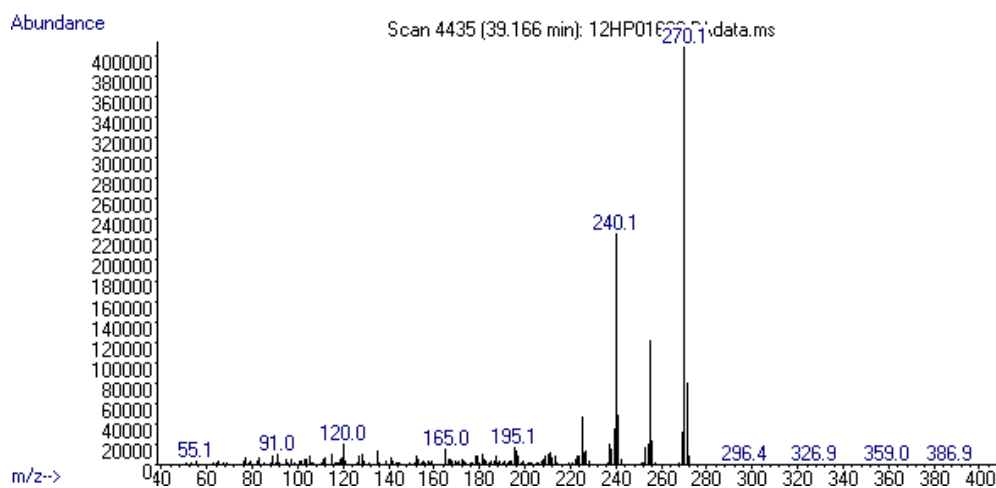


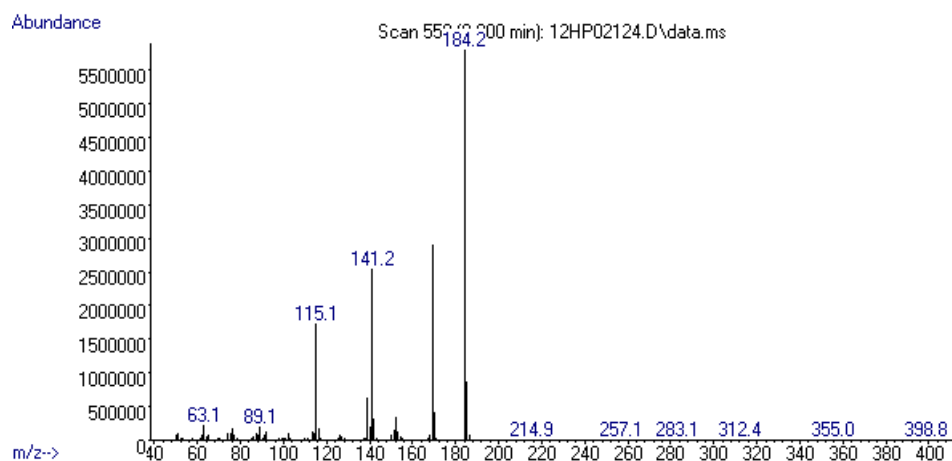
Figure C 6. EDX data for Pd@ apoferritin scaffold

Figure C7. GC-MS Data of various products

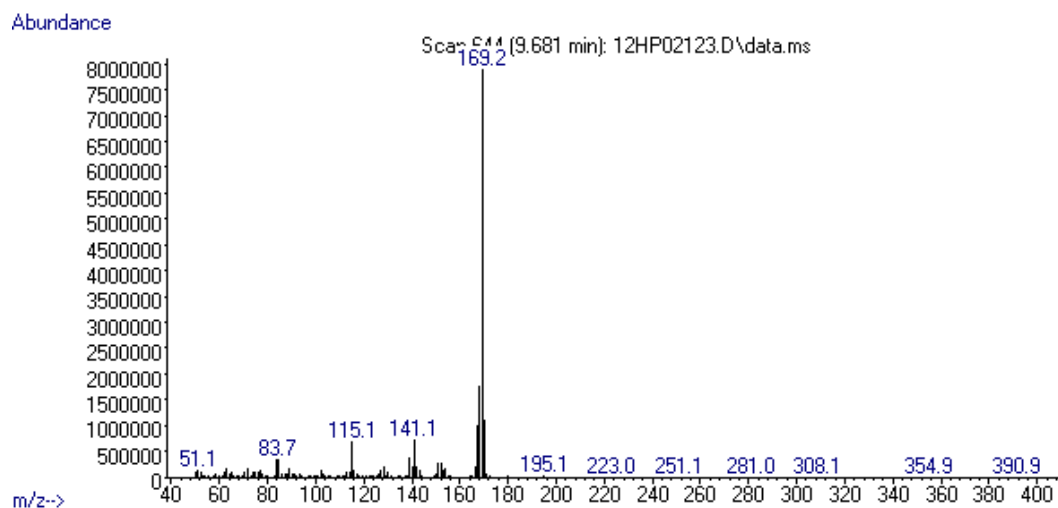
(A) GC-MS Data of 2,3,6 Trimethyl 1,4 benzoquinone



(B) GC-MS Data of 2,2',3,3',5,5'-hexamethyl-[1,1'-biphenyl]-4,4'-diol



(C) GC-MS Data of 4-methoxy-1,1'-biphenyl



(D) GC-MS Data of [1,1'-biphenyl]-4-amine

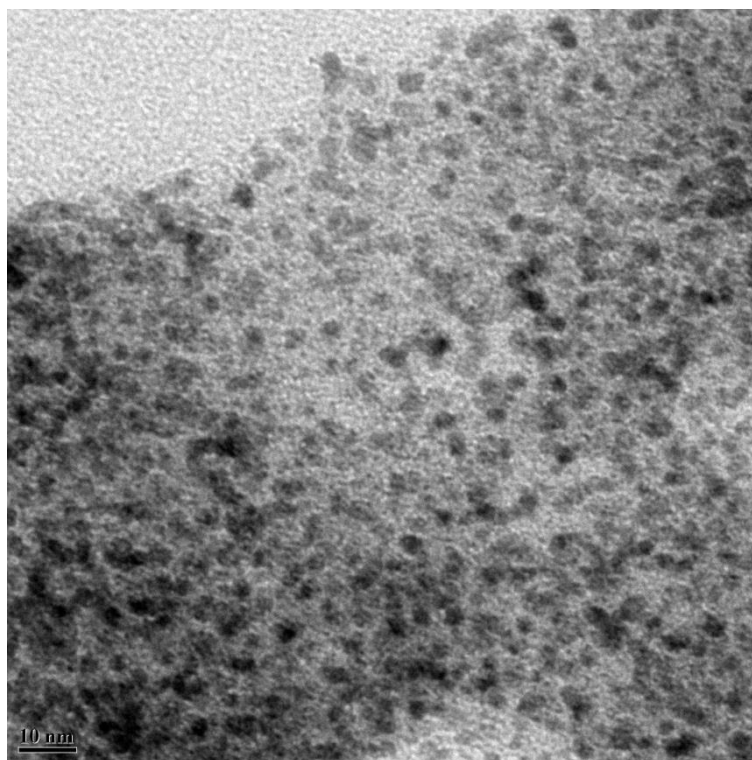
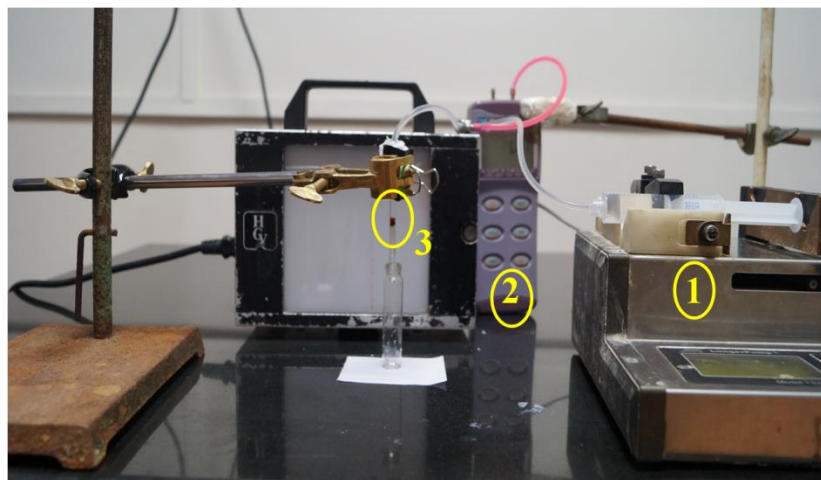
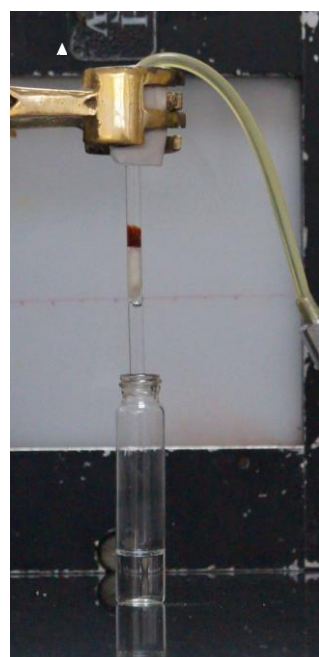


Figure C 8. TEM image of Pd@apoferritin scaffold after Suzuki - Miyaura coupling reaction

Continuous Flow for TMB (3, 3', 5, 5'-Tetramethylbenzidine) Oxidation Using Ferritin Scaffold



(A) Set-Up for continuous flow
(1) Syringe pump (2) Monometer (3) Capillary embedded with scaffold



(B) Before reaction



(C) After reaction

Figure C 9. (A) Set-up for continuous flow reaction (B) Before TMB oxidation reaction (C) Product formed after TMB oxidation reaction (3, 3', 5, 5'-Tetramethylbenzidine diimine)

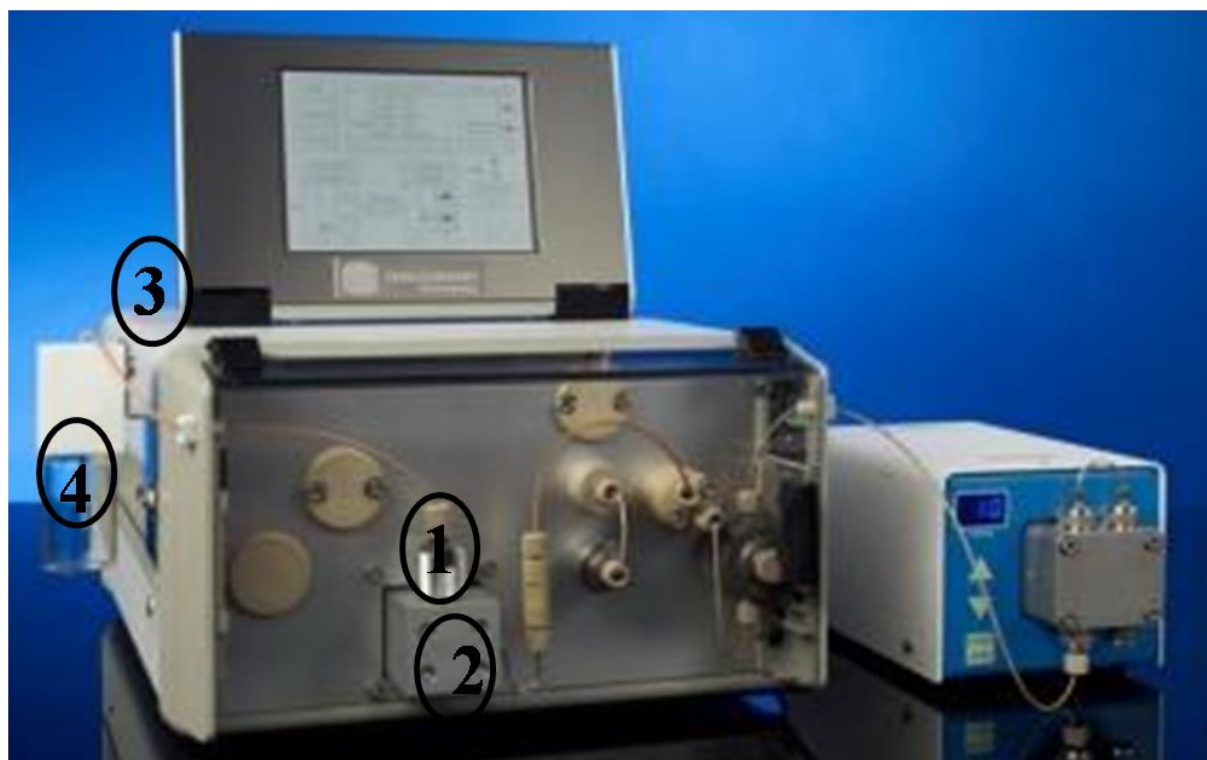
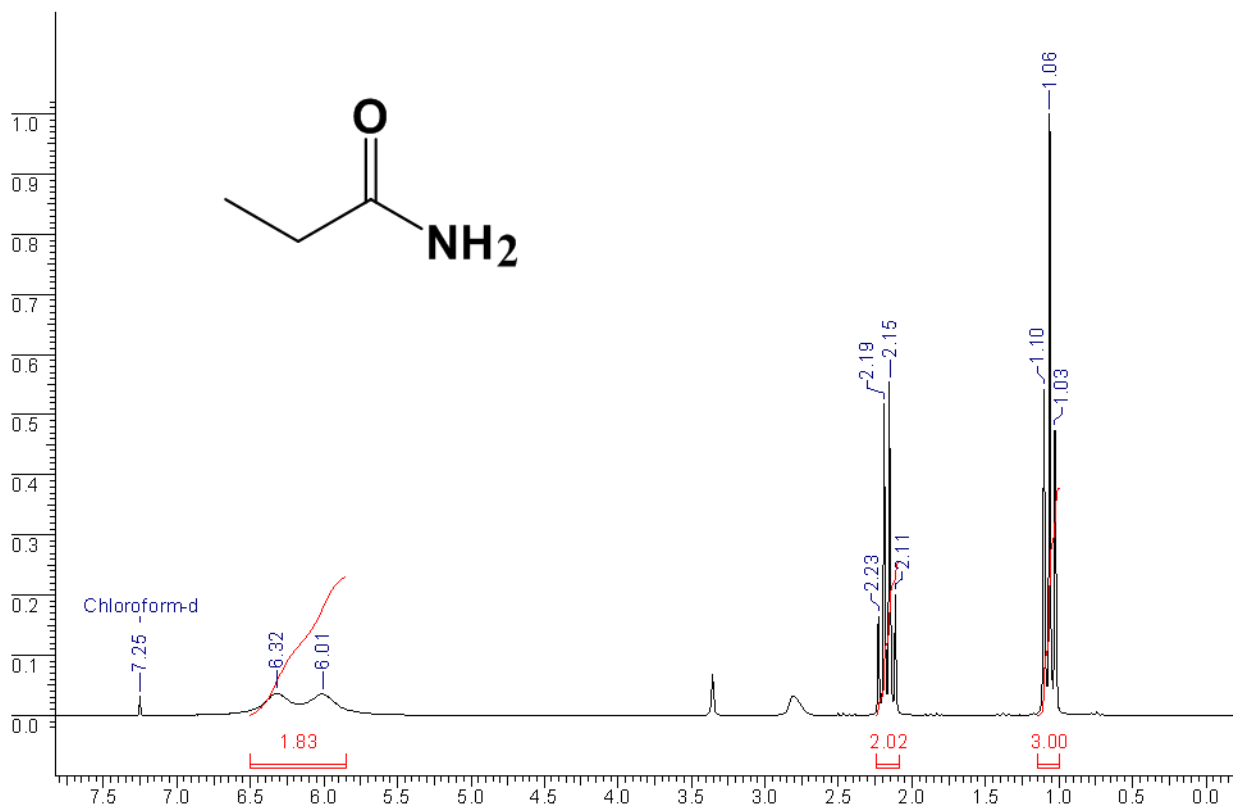
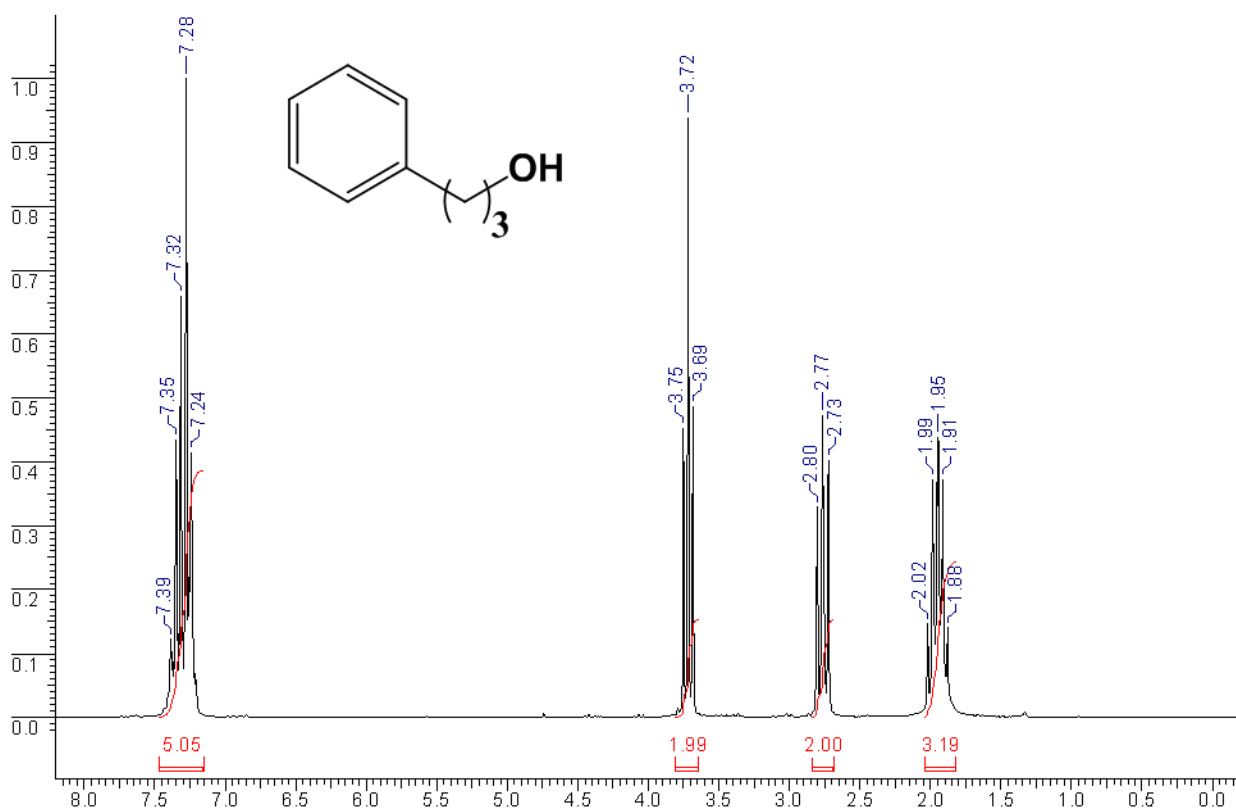


Figure C 10. Continuous flow hydrogenation set - up H³ system

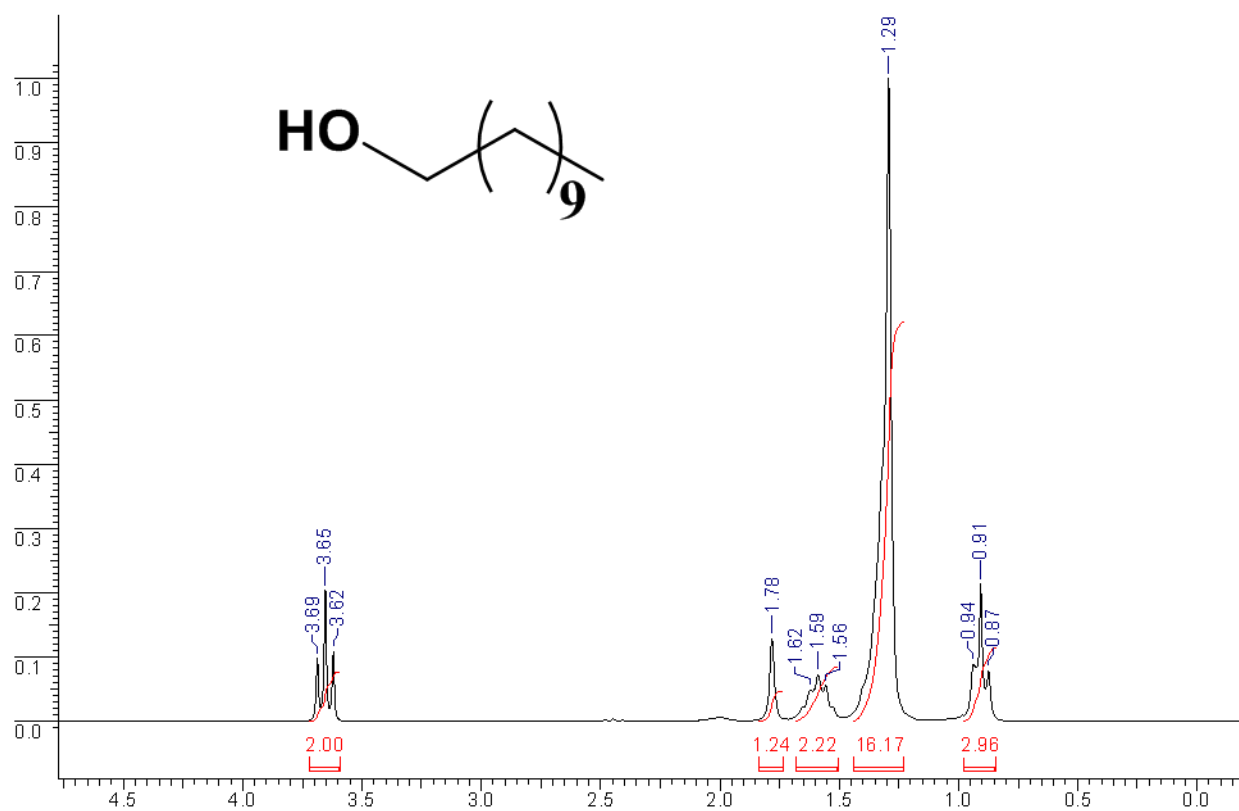
(1) Cartridge with Pd@apoferritin scaffold (2) heating unit (3) water reservoir (4) product collector

Figure C 11. ^1H NMR of 1-(λ^2 azanyl) propan-1-one

Yield (99%); ^1H NMR (200.13 MHz, CDCl_3): δ 1.03-1.10 (t, 3H), 2.11-2.23 (m, 2H), 6.01-6.32 (d, 2H)

Figure C 12. ^1H NMR of 3-phenylpropan-1-ol

Yield (99%); ^1H NMR (200.13 MHz, CDCl_3): δ 1.88-2.02 (m, 3H), 2.73-2.80 (t, 2H), 3.69-3.75 (t, 2H), 7.24-7.39 (m, 5H)

Figure C 13. ^1H NMR of undecan-1-ol

Yield (99%); ^1H NMR (200.13 MHz, CDCl_3): δ 0.87-0.94 (t, 3H), 1.29 (s, 16H), 1.56-1.62 (m, 2H), 1.78 (s, 1H), 3.62-3.69 (t, 2H)

Appendix IV

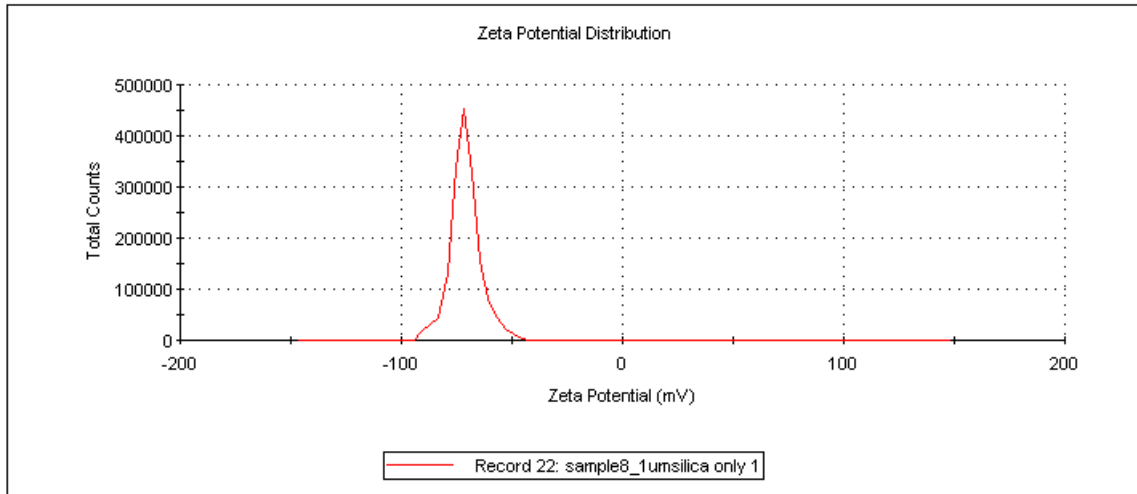


Figure D.1 (a) Zeta potential for 1 μ m silica with peak at -71.1 mV.

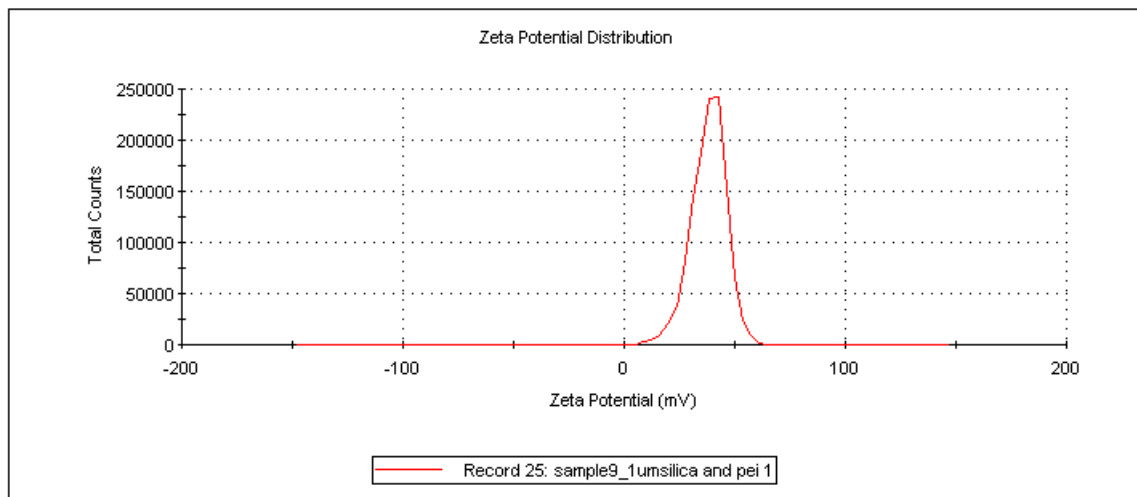


Figure D.1(b) Zeta potential for 1 μ m silica with 25kDa PEI coated showing peak at 38.1mV.

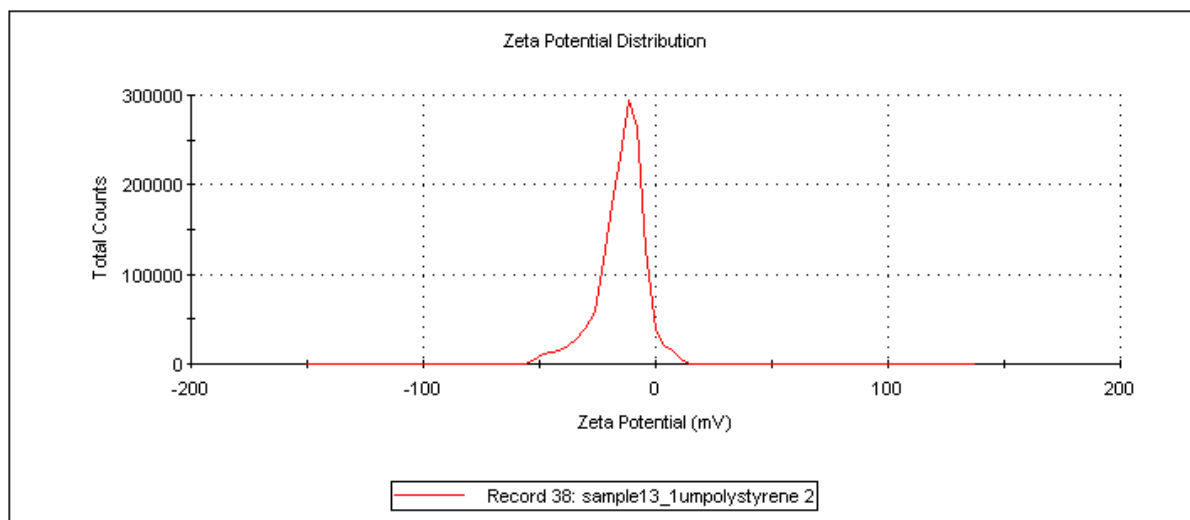


Figure D.1(c) Zeta potential for 1µm polystyrene particles with peak at -14.6mV.

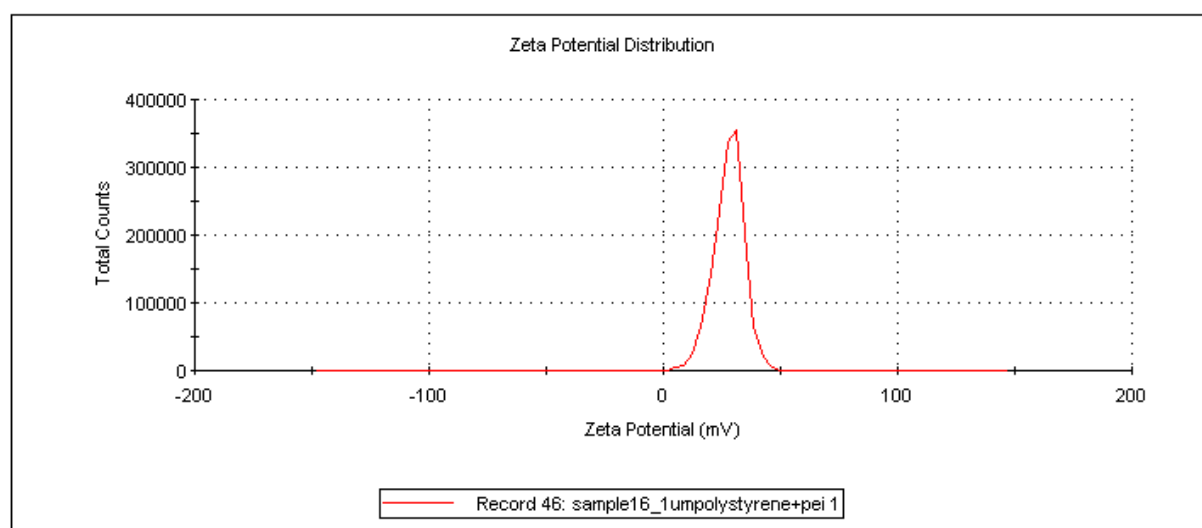


Figure D 1 (d) Zeta potential for 1µm polystyrene with 25kDa PEI coated showing peak at 28.0mV.

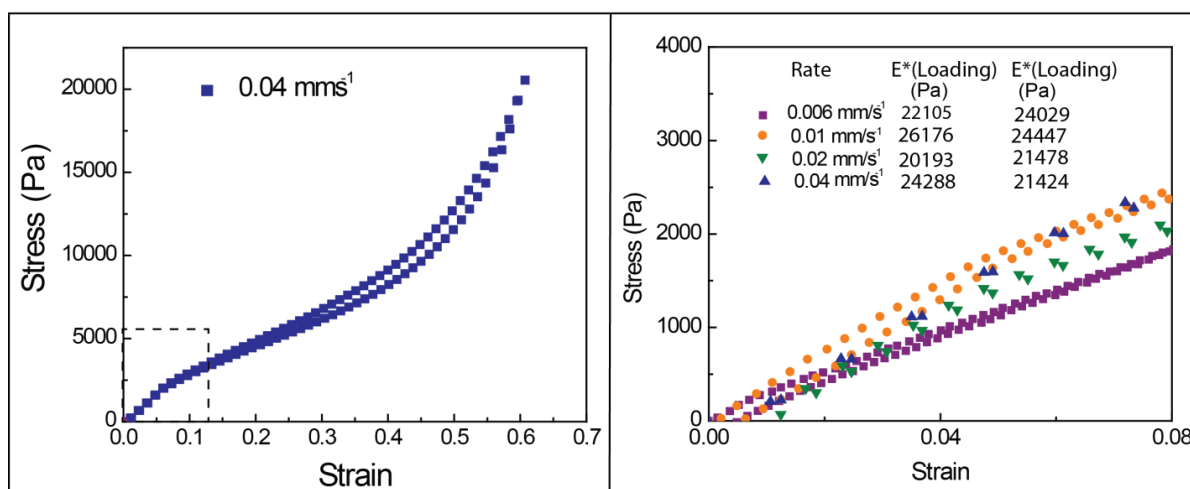


Figure D 2. Compression rate dependence of the compression test on scaffolds prepared using 1 μm silica colloids ice templated from a $\phi = 10\%$ w/v dispersion (with 25 kDa PEI and polyethylene-glycoldiglycidyl ether). The compression rates (in $\text{mm}\cdot\text{s}^{-1}$) are given in the legend. These measurements were made on a TA Instruments DMA (RSA-III) in the controlled rate mode. We calculate moduli during loading and unloading cycles, and varied the compression rate by about 7-fold. We note that there is no systematic trend for the moduli with compression rate. The average value of the modulus obtained during loading is 23 200 Pa and that during unloading is 22 800 Pa. Therefore, there is no experimentally significant difference in the values of E^* obtained for loading and unloading, and these compare well with that obtained using the TA Instruments ARES rheometer during loading (24 000 Pa). Therefore, in this work, all values reported are from loading curves on the scaffolds, performed using the TA ARES rheometer.

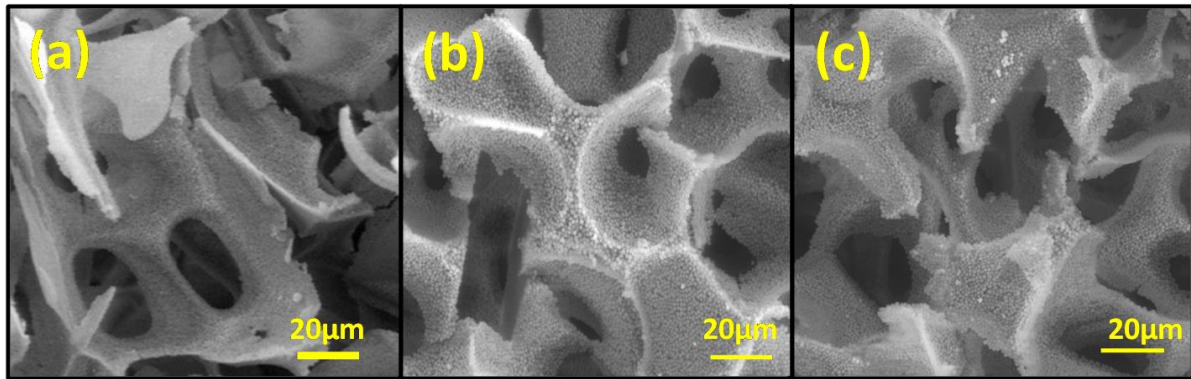


Figure D 3. SEM images of scaffolds prepared by ice templating (a) $\phi = 10\%$, (b) $\phi = 20\%$ and (c) $\phi = 30\%$ w/v aqueous dispersions.

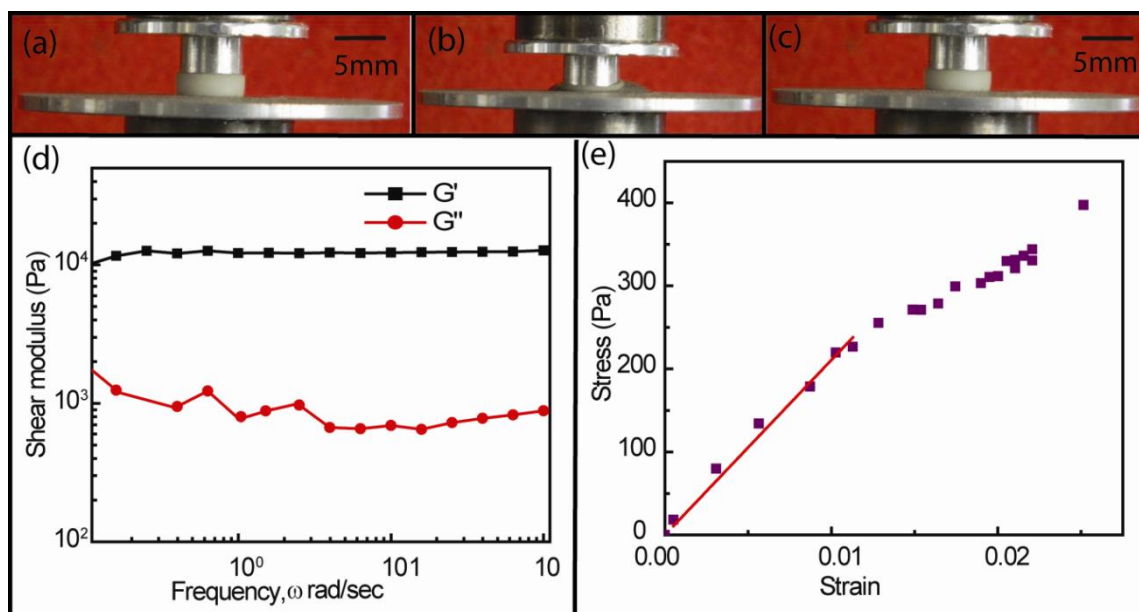


Figure D 4. Photographs that show the compression of scaffold prepared by ice templating a 10% w/v dispersion of 1 μm silica particles, with 25 kDa PEI and polyethyleneglycoldiglycidyl ether as the cross-linker. The compression/recovery test is done in 1 M NaCl solution. The photographs show (a) the initial state (b) the compressed state (strain = 85%) and (c) recovery on release of stress. (d) Frequency sweep for these scaffolds. We observe that $G' = 12\,198$ Pa at $\omega = 1$ rad/s. (e) Stress versus strain for compression test on the same scaffold. The elastic modulus, $E^* = 21\,071$ Pa, is obtained as the slope of the initial linear region of the stress-strain data.

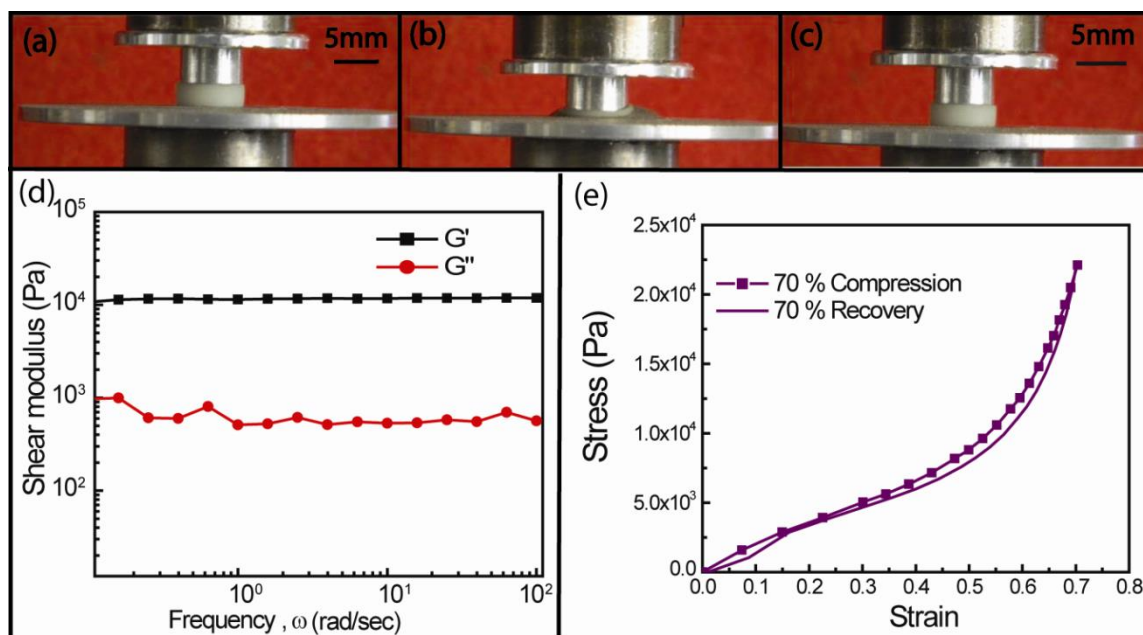


Figure D 5. Photographs that show the compression of scaffold prepared by ice templating a 10% w/v dispersion of 1 μm silica particles, with 25 kDa PEI and polyethylene-glycoldiglycidyl ether as the cross-linker. The compression/recovery test is done in water at pH = 4 solution. The photographs show (a) the initial state (b) the compressed state (strain = 85%) and (c) recovery on release of stress. (d) Frequency sweep for these scaffolds. We observe that $G' = 11\,447$ Pa at $\omega = 1$ rad/s (e) Stress versus strain for compression test (70%) on the same scaffold. The elastic modulus, $E^* = 18\,220$ Pa, is obtained as the slope of the initial linear region of the stress-strain data.

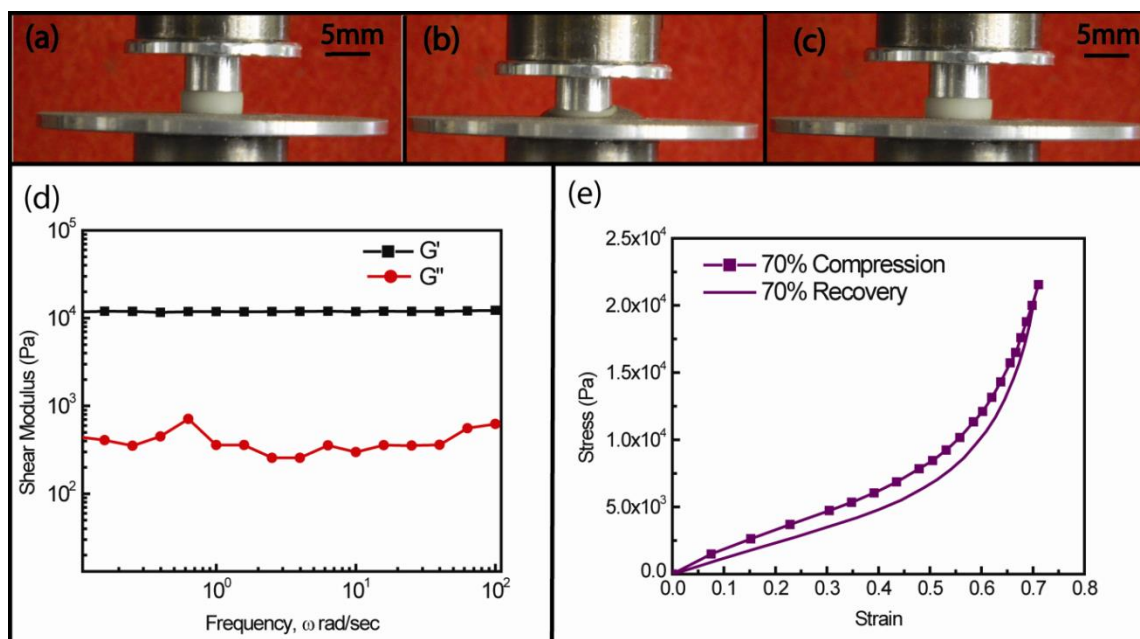


Figure D 6. Photographs that show the compression of scaffold prepared by ice templating a 10% w/v dispersion of 1 μm silica particles, with 25 kDa PEI and polyethylene-glycoldiglycidyl ether as the cross-linker. The compression/recovery test is done in water at pH = 10. The photographs show (a) the initial state (b) the compressed state (strain = 85%) and (c) recovery on release of stress. (d) Frequency sweep for these scaffolds. We observe that $G' = 11\,935$ Pa at $\omega = 1$ rad/s. (e) Stress versus strain for compression test (70%) on the same scaffold. The elastic modulus, $E^* = 17\,738$ Pa, is obtained as the slope of the initial linear region of the stress-strain data.

List of Research Credentials, Awards and Conferences

List of Publications

1. “Functionalization of SBA-15 Mesoporous Materials using “Thiol–Ene Click” Michael Addition Reaction” **Sushma Kumari**, B. Malvi, A. K. Ganai, V. K. Pillai, S. Sen Gupta, *The Journal of Physical Chemistry C*, 2011, 115, 17774.
2. “Synthesis of functional hybrid silica scaffolds with controllable hierarchical porosity by dynamic templating” A. K. Ganai, **Sushma Kumari**, K. P. Sharma, C. Panda, G. Kumaraswamy, S. Sen Gupta, *Chemical Communications*, 2012, 48, 5292.
3. “Large Centimeter-Sized Macroporous Ferritin Gels as Versatile Nanoreactors” **Sushma Kumari**, A. Kulkarni, G. Kumaraswamy, Sayam Sen Gupta, *Chemistry of Materials*, 2013, 25, 4813.
4. “Fe-TAML Encapsulated Inside Mesoporous Silica Nanoparticles as Peroxidase Mimic: Femtomolar Protein Detection” **Sushma Kumari**, B. B. Dhar, C. Panda, A. Meena, S. Sen Gupta, *ACS Applied Materials & Interfaces*, 2014, 6, 13866.
5. “Soft Colloidal Scaffolds Capable of Elastic Recovery after Large Compressive Strains” R. Rajamanickam[†], **Sushma Kumari**[†], D. Kumar, S. Ghosh, J. C. Kim, G. Tae, S. Sen Gupta, G. Kumaraswamy, *Chemistry of Materials*, 2014, 26, 5161 (†equal authorship).
6. “Self-templated Chemically Stable Hollow Spherical Covalent Organic Framework” Sharath Kandambeth, V. Venkatesh, D. B. Shinde, **Sushma Kumari**, A. Halder, S. Verma, R. Banerjee, *Nature Communications*, 2015. DOI: 10.1038/ncomms7786

List of Manuscripts under preparation

1. “Molecular Fe-complex as a catalyst probe for in-gel visual detection of proteins via signal amplification” **Sushma Kumari, C. Panda, S. Mazumdar, Sen Gupta**, (2015): Chemical Communications, Manuscript submitted.

Awards

1. Best poster presentation award in Physical and Material Chemistry division at “National Science Day” organized by CSIR-National Chemical Laboratory, Pune from 27-28 February 2014.
2. Best poster presentation award in Chemical Engineering and Process Development division at “National Science Day” organized by CSIR-National Chemical Laboratory, Pune from 27-28 February 2014.

Contributions to National/International Symposia/Conferences

1. “RSC-WEST INDIA SECTION Ph.D STUDENTS SYMPOSIUM” held during 3-4th September, 2010 at Goa University, Goa, India.
2. “Third International Conference on Multifunctional, Hybrid and Nanomaterials” from 3-7th March 2013 held in Sorrento, Naples, Italy.
3. “16th CRSI National Symposium in Chemistry (NSC-16)” held at Indian Institute of Technology Bombay, Powai, Mumbai from February 7-9, 2014.
4. Indo-German Conference on “Bioinspired Chemistry (IGCBIC-2014)” held at Indian Institute of Science, Bangalore from September 10-12, 2014
5. International Symposium on Bioorganic Chemistry (ISBOC-10) held at Indian Institute of Science Education and Research, Pune (www.iiserpune.ac.in), India, during January 11-15th, 2015.
6. “17th CRSI National Symposium in Chemistry” from February 06-08, 2015 at CSIR-NCL, Pune

ABOUT THE AUTHOR

Sushma Kumari, daughter of Shri Ramashray Singh and Harmuna Devi, was born in Rohtas district, Bihar, India, in 1986. She received her secondary and higher secondary education from Kendriya Vidyalaya No.1, Lohegaon Pune. She completed her B.Sc. from Nowrosjee Wadia, Pune. After the completion of her B.Sc. she joined Department of Chemistry, University of Pune, Maharashtra to pursue her M.Sc. She joined Department of Chemical Engineering and Process Development division, CSIR NCL, Pune to pursue her Ph.D. degree in August 2009. She was awarded research fellowship by Council of Scientific and Industrial Research (SRF) for 2012-2015. She has received best poster award in Material Chemistry and Chemical Engineering and Process Development division (CEPD) from CSIR-NCL Pune.